An Intelligent Framework For Distributed Satellite Operations

Advancing Autonomy for Space Traffic Management

A thesis submitted in fulfilment of the requirements for the degree of Doctor of Philosophy

Samuel Hilton

BApp Sci, RMIT University Australia

MEng Aerospace, RMIT University Australia

ORCID

School of Engineering

College of Science, Engineering and Health

RMIT University

Australia

December 2024

DECLARATION

I certify that except where due acknowledgement has been made, this research is that of the author alone; the content of this research submission is the result of work which has been carried out since the official commencement date of the approved research program; any editorial work, paid or unpaid, carried out by a third party is acknowledged; and, ethics procedures and guidelines have been followed.

In addition, I certify that this submission contains no material previously submitted for award of any qualification at any other university or institution, unless approved for a joint-award with another institution, and acknowledge that no part of this work will, in the future, be used in a submission in my name, for any other qualification in any university or other tertiary institution without the prior approval of the University, and where applicable, any partner institution responsible for the joint-award of this degree.

I acknowledge that copyright of any published works contained within this thesis resides with the copyright holder(s) of those works.

I give permission for the digital version of my research submission to be made available on the web, via the University's digital research repository, unless permission has been granted by the University to restrict access for a period of time

Samuel Mitchell Hilton

11/12/2024

Acknowledgements

My academic journey would have ended long ago without crossing paths with Roberto (Rob) Sabatini. Your dedication to your craft has shown me what is possible when you put your mind to something. The knowledge and insights I have gained from you will continue to profoundly influence my growth as an engineer - thank you for the motivation, guidance and support since day 1.

This thesis would never have been completed without the help from Alessandro (Alex) Gardi –I thank you for the countless late-night exploratory and edge-case conversations, debugging code and getting papers over the line. What I cherish most, however, is your unwavering support and encouragement throughout this journey.

Thank you to my family for all your support, most importantly my beautiful wife Alex. Through your patience, love and care you made this all possible for me. I owe it all to you.

To my colleagues:

Nichakorn (Nicha) Pongsakornsathien who started this PhD marathon with me – thank you for your friendship, technical input and of course your delicious Thai snacks.

Federico (Fede) Cairola & Enrico (Enrico) Lagona, thank you for your friendship, and technical input. I will continue to think fondly of our time together in Bundoora discussing Italian idiosyncrasies.

Finally thank you SmartSat CRC Australia & Northrop Grumman Missions Systems USA for funding this project.

Table of Contents

List of Tables

List of Figures

In loving memory of Andrew Hilton

...

Summary

The increasing complexity of space operations, driven by the proliferation of satellites and growing risks of orbital congestion, necessitates advancements in Distributed Satellite Systems (DSS) and Space Traffic Management (STM). This thesis presents a comprehensive framework that integrates next generation autonomy methods using distributed coordination and supervisory control to ensure mission assurance, resilience, and adaptability in DSS Space-Based Space Surveillance (SBSS) missions in support of STM.

Key Contributions:

Holistic Framework for Intelligent DSS in STM:

This research develops a unified framework for DSS operations, emphasizing distributed mission planning, task coordination, and real-time adaptability. It highlights the critical architectural elements and autonomy features required to optimize satellite collaboration in surveillance and STM tasks.

Distributed Mission Planning and Resource Optimization:

The thesis introduces a distributed, multi-agent mission planning strategy leveraging advanced optimization techniques to coordinate observation tasks effectively across satellite networks. These strategies, maximize global utility, and adapt dynamically to changing operational requirements.

Real-Time Adaptive Trajectory and Attitude Optimization:

A robust onboard optimization framework is designed to manage satellite manoeuvres and resource constraints. The algorithms enable satellites to autonomously adapt to evolving mission scenarios, ensuring timely and efficient execution of SBSS operations and collision avoidance.

Supervisory Control and Mission Assurance:

The research proposes an integrated approach of providing supervisory control mechanisms based on dynamic system reliability assessment. This ensures robust oversight of autonomous DSS operations through intelligent plan selection enhancing mission resilience under uncertainty and operational disruptions.

Uncertainty Management and Probabilistic Modelling:

The thesis addresses the challenges of uncertainty in RSO tracking and collision prediction by developing unified methods for quantifying and resident space object uncertainties to support collision avoidance activities

Impact and Applications:

The proposed frameworks and methodologies significantly enhance DSS capabilities in autonomous decision-making, distributed task coordination, and uncertainty management. These contributions support critical STM goals, including collision

avoidance, resource optimization, and mission resilience. The research has broad applications in managing the increasing demands of DSS operations, ensuring safe and sustainable use of space for future generations.

Chapter 1
Introduction

1.1. Background and Motivation

The mitigation and avoidance of collisions remain pressing challenges for Space Traffic Management (STM) systems. Current collision prediction methods, though widely used, are limited by delays in obtaining observational data. This highlights the necessity for advanced cyber-physical Communication, Navigation, and Surveillance (CNS) Systems that integrate cutting-edge networking, computational, and control technologies. These systems are crucial for transitioning from traditional Space Situational Awareness (SSA) to Space Domain Awareness (SDA). SDA encompasses a thorough understanding of all activities within the space domain, including satellites, debris, and the use of diverse CNS space-based systems. By providing deeper insights into space operations, SDA enables the detection of threats, mitigation of risks through informed decisions regarding STM, resource allocation, and mission planning.

Emerging Distributed Satellite Systems (DSS) architectures play a pivotal role in achieving these objectives. By moving from single, large-scale spacecraft to constellations of smaller, specialized platforms, DSS architectures offer scalable, resilient, and cost-effective solutions to address evolving STM goals.

Enhanced autonomy in DSS platforms further supports SDA by enabling adaptive mission execution and re-planning based on real-time environmental data. The shift from ground-controlled operations to autonomous, goal-driven systems allows DSS architectures to respond dynamically to changing mission needs and environmental conditions. With onboard capabilities such as trajectory optimization and autonomous mission planning, DSS platforms gain the agility required to tackle emerging cyber-physical threats while promoting the safe and sustainable management of space traffic.

However, unlocking the full potential of DSS requires addressing key research challenges, including the development of self-adaptive autonomy, efficient dynamic coordination, and robust supervisory control. These advancements will ensure that DSS systems effectively support the evolving needs of SDA and STM, enabling the efficient utilization of space resources while minimizing risks.

How can autonomy in Distributed Satellite Systems (DSS) be designed and coordinated to enable dynamic and collaborative SDA operations? Coordinating a DSS to cooperatively meet system goals optimally and adaptively represents a significant technical challenge. This includes developing algorithms and frameworks that allow DSS platforms to autonomously perform key mission functions, and coordinate behaviour to collectively optimize STM goals.

What strategies are required to effectively supervise autonomous decision-making in DSS? As DSS platforms achieve higher levels of autonomy, the role of human operators shifts to one of a more supervisory nature. This transition requires equipping space operators with a suite of intelligent tools capable of summarizing low-level information and providing actionable inputs to align with mission goals.

1.2. Research Questions

- How can autonomy in Distributed Satellite Systems (DSS) be designed and coordinated to enable dynamic and collaborative SDA operations?
- What strategies are required to effectively supervise autonomous decision-making in Distributed Satellite Systems (DSS)?

1.3. Research Objectives

1. Identify the evolving goals of Space Traffic Management (STM) focusing on operational challenges and technological drivers that enable a safe and sustainable use of the space environment
2. Develop an integrated operational framework for intelligent Distributed Satellite Systems (DSS) that integrates key system autonomy functionalities
3. Develop an integrated approach to quantify and propagate uncertainty in Resident Space Object (RSO) tracking and establish probabilistic models for collision prediction and avoidance
4. Develop and implement onboard optimization algorithms for adaptive trajectory and attitude planning in Space-Based Space Surveillance (SBSS) mission and collision avoidance operations
5. Design a distributed mission planning strategy for Space-Based Space Surveillance (SBSS) operations, to optimize task allocation, minimize duplication, and maximize global utility across collaborative satellite platforms
6. Develop a comprehensive framework that integrates supervisory control mechanisms with dynamic system reliability models to ensure mission assurance, operational reliability, and resilience in Distributed Satellite Systems (DSS)

1.4. Research Methodology

The research methodology is designed to address the central questions and objectives of this thesis, providing a structured approach to developing and validating

advancements in Distributed Satellite Systems (DSS) for Space-Based Space Surveillance (SBSS) and Space Traffic Management (STM). Each chapter of the thesis aligns with a specific research objective, presenting a progression from theoretical foundations, algorithmic development and simulation-based validation to ensure a comprehensive examination of key autonomy functions and their interaction within an intelligent DSS mission architecture.

Chapter 2: Identifying Evolving Goals in Space Traffic Management (Obj 1)

The research begins by addressing Objective 1: 1. Identify the evolving goals of Space Traffic Management (STM) focusing on operational challenges and technological drivers that enable a safe and sustainable use of the space environment

The methodology includes:

- Literature Review and Historical Analysis: A comprehensive review of the STM domain, tracing the evolution of SSA to SDA.
- Gap Analysis: Identifying critical gaps in current STM strategies, emphasizing the need for advanced autonomy in Distributed Satellite Systems (DSS).
- Foundation for Subsequent Research: This chapter lays the groundwork for the development of operational frameworks and autonomy models in the following chapters.

Chapter 3: Developing an Operational Framework for Intelligent DSS (Obj 2)

Chapter 3 corresponds to Objective 2, which involves the development of an integrated operational framework for Intelligent DSS, key system autonomy functionalities. This serves as the reference architecture for the remainder of the thesis. Key methods include:

- Functional Analysis: Expanding STM goals identified in Chapter 2 into specific autonomy requirements for DSS.
- Hierarchical Control Structure Design: Developing a multi-layered framework with feedback control loops for task coordination and decision-making.

Chapter 4: Trajectory Optimisation Model Design (Obj 4)

Aligned with Objective 4, this chapter focuses on developing and implementing onboard optimization algorithms for adaptive orbital and attitude manoeuvres in Space-Based Space Surveillance (SBSS) missions. The methodology involves:

- Dynamic Modelling: Developing equations of motion with key perturbation factors for spacecraft dynamics.
- Optimization: Solving trajectory optimization problems with adaptive metaheuristic methods.

Chapter 5: Collision Avoidance Autonomy Design (Obj 3)

This chapter addresses Objective 3, developing an integrated approach to quantify and propagate uncertainty in Resident Space Object (RSO) tracking and establishing probabilistic models for collision prediction and avoidance. The methods include:

- Covariance Analysis: Evaluating the accuracy and limitations of uncertainty models for RSOs.
- Integration with Trajectory Optimization: Incorporating uncertainty quantification into onboard decision-making algorithms for collision avoidance.

Chapter 6: Distributed Mission Planning for SBSS Operations (Obj 5)

Addressing Objective 5, this chapter focuses on designing a distributed mission planning strategy for SBSS operations to optimize task allocation, minimize duplication, and maximize global utility across collaborative satellite platforms. Key methodologies include:

- Platform Coordination: Developing a distributed optimisation algorithm for autonomous SBSS mission planning and coordination among satellites.
- Integration with On-board Trajectory Optimization autonomy: Incorporating Trajectory optimisation into SBSS mission planning
- Case Study Validation: Evaluating the performance of the mission planning strategy in a representative SBSS operational scenario.

Chapter 7: Supervisory Control and Mission Assurance in DSS (Obj 6)

The final chapter corresponds to Objective 6, which involves developing a framework that integrates supervisory control mechanisms to ensure mission assurance through operational reliability, and resilience in DSS. The methodology includes:

- Decision Support for Intelligent Plan Selection: Development of Mission Level reliability models based on system autonomy outputs to achieve optimal mission plan selection
- Simulation Case Study Validation: Demonstrating the effectiveness of the approach under dynamic and uncertain mission

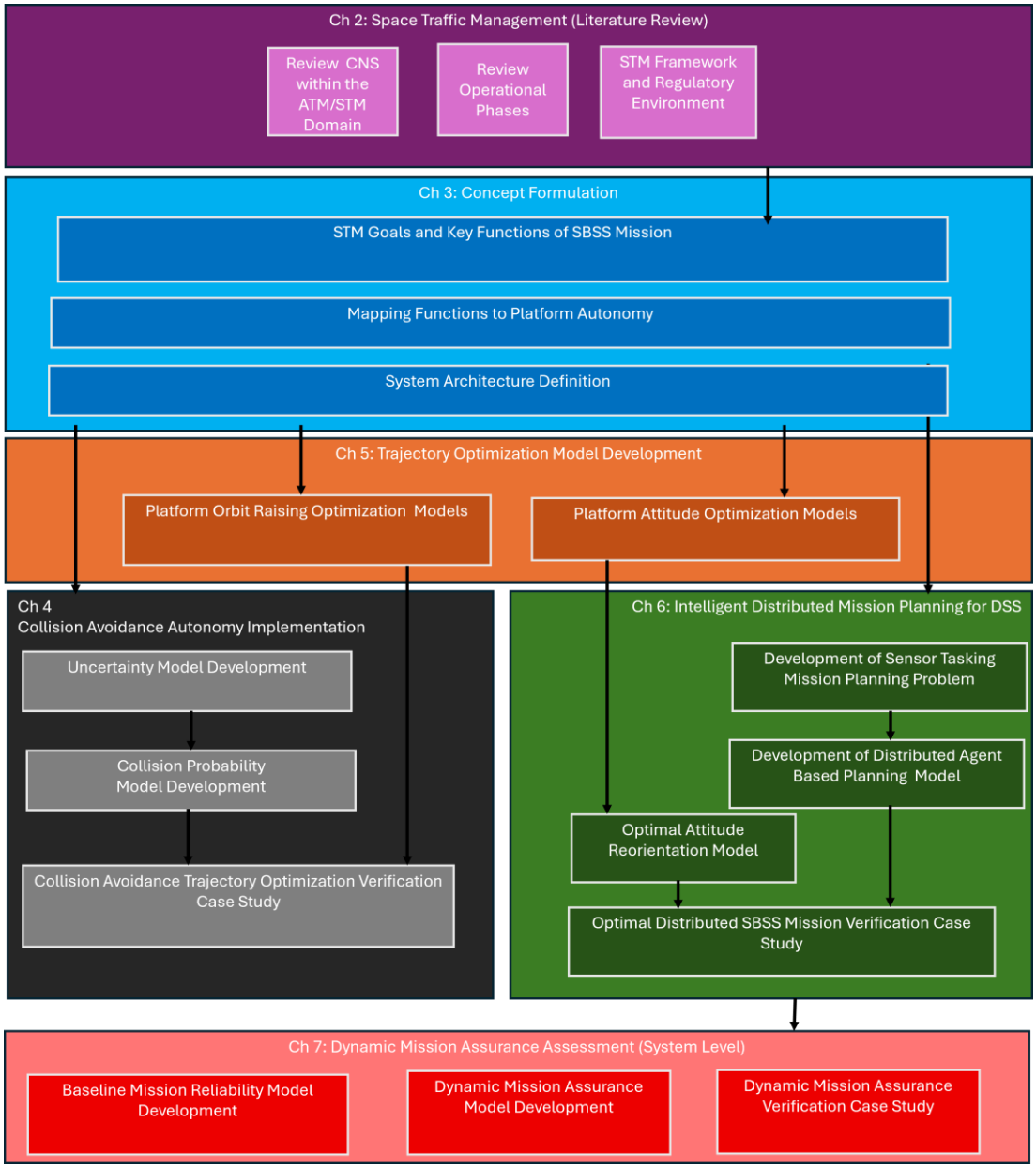

Figure 1. Thesis Structure

Chapter 2

Literature Review

This chapter provides a holistic literature review of the evolving technological advancements and operational strategies that shape the development of Space Traffic Management (STM) systems. The challenges posed by all phases of spaceflight, including launch, re-entry, and on-orbit operations are discussed while linking these challenges to STM goals such as collision avoidance, debris mitigation, and operational sustainability. By examining the transition from Space Situational Awareness (SSA) to Space Domain Awareness (SDA), the review sets the stage for a globally harmonized STM framework supported by DSS capabilities. This discussion serves as the foundation for the thesis by identifying the critical role DSS plays in achieving STM goals, particularly in advancing space-based surveillance, reducing uncertainty, and supporting safe and sustainable use of the space environment.

The contents of this chapter have been published in the following:

- **S. Hilton**, R. Sabatini, A. Gardi, H. Ogawa, and P. Teofilatto, "Space traffic management: towards safe and unsegregated space transport operations," (in English), Prog Aerosp Sci, Review vol. 105, pp. 98-125, 2019, doi: 10.1016/j.paerosci.2018.10.006.

- K. Thangavel, R. Sabatini, A Gardi, K. Ranasinghe, **S. Hilton**, P. Servidia, D.Spiller "Artificial Intelligence for Trusted Autonomous Satellite Operations," Prog Aerosp Sci, vol. 144, p. 100960,

2.1. Introduction

Capitalising on lessons learned from the Space Shuttle era, various manned and unmanned reusable space vehicle concepts have been proposed in recent years and some of these concepts are now being developed and successfully tested. Moving away from the traditional approach of expendable launch vehicles, the capability of reusable launch systems is currently being demonstrated by companies such as SpaceX and Virgin Galactic. Reusable platforms provide clear economic advantages and are now widely recognised as an integral component of a sustainable space transportation industry. These so-called “new-entrants” push the envelope regarding how the various flight phases are accomplished, introducing concepts such as Vertical Take-Off and Landing (VTOL), Horizontal Take-Off and Landing (HTOL) and hybrid approaches [1-5].

As the new-entrant technologies are being increasingly realised, the aviation and space industry (to a lesser extent) are undergoing large-scale modernisation processes towards increasing capacity, safety and efficiency. It is well understood that this will require the establishment of a Space Traffic Management (STM) system as well as a

significant evolution from ground-based legacy systems to realizing an advanced global network of Communication, Navigation and Surveillance (CNS) technologies [6-8]. As such, the integration of avionics CNS technologies into new-entrant platforms will be a critical aspect, associated with the simultaneous development of new air/ground mission planning and decision support tools that harmonize future Air Traffic Management (ATM) and spacecraft operational procedures. Within the orbital domain, Space Situational Awareness (SSA) is being provided by a network of ground-based surveillance systems known as the Space Surveillance Network (SSN) operated by the US Department of Defence. Nonetheless, a shift is now being pursued towards establishing a more "global" surveillance approach through both spaceborne measurements and Resident Space Object (RSO) data sharing from other commercial and governmental entities [9-11]. Emerging capabilities such as this pave the way for implementing the evolutionary changes required for a globally harmonised ATM/STM system.

Unlike conventional aircraft, new-entrants will operate in severe environments at extremely high velocities and as such the design and development of future ATM/STM operational procedures must consider the limitations each phase/environment imposes. The launch and re-entry environment is characterized by significant platform constraints regarding aerodynamic loading and thermal stresses [12-14]. Since the shuttle orbiter, re-entry planning schemes based on the use of the Quasi Equilibrium Glide Condition (QEGC) [15-19] and energy methods [20, 21] have been developed and tested.

During the on-orbit phase, spacecraft are subject to an environment that distinctly differs from that on Earth. Space weather phenomena are not only hazardous to human life [22-24] but have the potential to significantly degrade the performance of advanced CNS equipment [14, 25-28]. The highly non-linear dynamics of perturbed orbital motion is also a principal issue that must be considered, especially because it affects the validity of the long-term predictions required to assure separation from other spacecraft (operational and non-operational) and debris. Thus adequate measures must be implemented to accurately describe position uncertainty and its propagation over time. Common approaches to this problem are identified and discussed, including novel methods that aim to unify the approach to uncertainty representation in the interest of STM/ATM harmonization and platform interoperability [29, 30].

In place of a harmonized ATM/STM system, various international and national organizations have developed guidelines and standards to mitigate the risks associated with spaceflight operations [31-35]. Within the atmospheric domain, safety criteria have been met to date through ad-hoc approaches that segregate space transport vehicles from atmospheric aircraft during the launch and re-entry phases. Although relatively effective in current airspace, the applicability of such conservative approaches to future mixed flow operations is questionable. As a result, novel methods

have been proposed to achieve an optimized hazard volume based on spacecraft design characteristics and predetermined trajectories [36, 37]. Alongside promising Air Traffic Flow Management (ATFM) concepts [38] these methods have the potential to be strongly beneficial to future mixed-flow operations. However, the increasingly problematic situation of space debris has raised concerns about the sustainability of the orbital environment [39, 40]. As a consequence, mitigation guidelines outlining disposal strategies have been developed to slow the growth of debris within the Low Earth (LEO) and Geosynchronous (GEO) regions. These strategies are now evolving to meet both current and predicted operational compliance requirements [41-43]. However, as of now, it is clear that active measures must be also taken by spacecraft operators to identify potential on-orbit collisions and perform timely de-confliction manoeuvres.

Based upon on-orbit uncertainty modelling, various analytical tools have been developed to allow spacecraft operators to assess risk and meet the required operational criteria [44-50]. However, recent events, such as the 2009 collision between the Iridium 33 and Cosmos spacecraft, have demonstrated that unreliable observational data introduce significant additional uncertainties that impact the overall validity of current safety assessment methods. This chapter identifies the common modelling approaches taken to conduct on-orbit collision avoidance analysis addressing both the challenges and the necessary evolutions to increase the transparency and traceability of observational data required for future STM operations.

2.2. Communication, Navigation and Surveillance within the ATM/STM Domain

Aviation is undergoing a large-scale modernisation process, in which state-of-the-art aeronautical technology and higher levels of automation and information sharing are exploited to increase the safety, capacity, efficiency and environmental sustainability of air traffic [38, 51, 52]. Several major programs were launched to guide and support this modernisation, including the US Next Generation Air Transportation System (NextGen) and the Single European Sky ATM Research (SESAR) and other programs such as CARATS (Collaborative Actions for Renovation of Air Traffic Systems) in Japan and OneSky in Australia. These programs focus on novel operational capabilities and enabling technologies to meet future air transportation challenges including civil/military air traffic harmonisation and, more recently, UAS access to all classes of airspace. The NASA UAS Traffic Management (UTM) research initiative is currently leading the way in this direction, working with various academic, industrial and government institutions on prototype CNS/ATM and Avionics (CNS+A) technologies addressing airspace integration requirements for safe and efficient UAS operations [53-58]. The new services conceived in the UTM concept-of-operation will provide UAS pilots information for maintaining separation from other aircraft by

reserving airspace portions, with consideration of special use airspace and adverse weather conditions [56]. Consequently, the current operational concept mostly relies on opportune provisions for airspace design and management, geo-fencing, congestion management, authenticated operations and weather prediction services to provide an effective and seamless integration of UAS in the current ATM network. These provisions aim at reducing the potential risks to an acceptable level but it is now clear that a certifiable Sense-and-Avoid (SAA) capability is integral to the proper management of the risks throughout the entire operational spectrum of UAS platforms [59-61].

All these research initiatives are driving the advancement of CNS/ATM and Avionics (CNS+A) technologies towards allowing increased operational efficiency and safety in the management of air traffic and airspace resources, thereby providing technically viable and effective long-term solutions to cope with the global increase in air transport demand [6-8]. A key challenge for the future will be the global harmonisation of the ATM/UTM and STM frameworks, including the development of a cohesive certification framework for future CNS+A systems simultaneously addressing safety, security and interoperability requirements [62].

2.2.1. Towards Performance-Based Operations

Continuing rapid advances in aerospace sensor and computing technologies are stimulating the development of integrated and multisensor systems capable of providing to the pilot, in a synthetic form, all information required for safe and accurate navigation. Furthermore, automatic control and networking technologies have been extensively applied to Unmanned Aircraft Systems (UAS), allowing the development of multi-sensor systems for fully automated aircraft guidance. The recent introduction of Performance-Based Navigation (PBN) is the first step of an evolutionary process from equipment-based to Performance-Based Operations (PBO). PBN specifies that aircraft navigation systems performance requirements shall be defined in terms of accuracy, integrity, availability and continuity for the proposed operations in the context of a particular airspace when supported by an appropriate ATM infrastructure. The full PBO paradigm shift requires the introduction of suitable metrics for Performance-Based Communication (PBC) and Performance-Based Surveillance (PBS). The proper development of such metrics and a detailed definition of PBN-PBC-PBS interrelationships for manned and unmanned aircraft operations represent one of the most exciting research challenges currently faced by the avionics research community, with major impacts on air transport safety, airspace capacity and operational efficiency.

Despite being a core technology enabler for high-density and uncertainty-resilient operations, advanced communication systems have not experienced the same rapid

uptake observed in aeronautical navigation and surveillance technologies. For instance, current communications between conventional aircraft and ground entities (ATM, airlines and airport authorities) are still heavily reliant on analogue voice channels. The progressive introduction of digital data links and other networking technologies is now allowing enhanced timeliness and reliability of traffic flow information, increasing productivity and streamlining system capacity. At the core of this transformation, System-Wide Information Management (SWIM) will constitute the backbone of the data communication concept, providing the network to share strategic and tactical information, enabling new modes of decision-making for safety-critical air/space traffic management concepts such as Trajectory Based Operations (TBO).

Surveillance systems are designed to support traffic separation assurance and collision avoidance functions. Cooperative surveillance systems use a combination of Time and Space Position Information (TSPI) and communication links to share traffic information between aircraft and ground-based ATM systems. Non-cooperative systems can include radar, electro-optical and other kinds of active/passive sensors using various working principles and operating in various portions of the radiofrequency, infrared and/or visible spectrum [59, 63, 64]. The state-of-the-art in avionics surveillance is the Automatic Dependent Surveillance Broadcast (ADS-B) system. This is a cooperative system using TSPI from Global Navigation Satellite Systems (GNSS) and existing aeronautical data links. ADS-B provides significantly higher amounts of information compared to conventional Primary Surveillance Radar (PSR) and Mode-C Transponders, hence supporting a greatly enhanced situational awareness for air traffic controllers and pilots.

The integration of the above CNS+A technology into spacecraft platforms will be a critical aspect in performing more "aircraft-like" operations, allowing the transition from segregated to mix flow operations. Understandably, spaceflight will not only require CNS equipment to be highly reliable and light weight but also highly robust due to the extreme operating environments experienced through various flight phases.

2.2.2. Space Situational Awareness

Space Situational Awareness (SSA) refers to the knowledge of the near space environment, which in the context of STM is largely concerned with the knowledge of Resident Space Object (RSO) information. Effective SSA requires constant surveillance and tracking of the space environment, a task traditionally performed by a network of ground-based observation facilities known as the Space Surveillance Network (SSN), owned and operated by the US Department of Defence (DoD). However, over the past decade, a shift towards a global surveillance approach of SSA data sources has been possible as commercial entities and other countries exhibit SSA capabilities that match or exceed the US DoD [9].

2.2.3. Enhancing Global CNS Infrastructure

A future harmonised ATM/STM system will require unprecedented levels of situational awareness, which can only be achieved with new data analytics methods and a globally connected infrastructure. In the aviation context, the distinct advantages of employing global satellite systems have been widely demonstrated by GNSS (with its augmentation systems), allowing airspace capacity, route efficiency and safety to be significantly increased [65-67]. Similarly, for the full potential of advanced surveillance and communication technology to be realised, the development of new global satellite-based services will be required. These systems are collectively known as Distributed Satellite Systems (DSS)

2.2.3.1. Distributed Satellite Systems

The evolving needs of the scientific community and defence sector require larger-scale satellite systems to provide a lower-cost, more responsive and resilient option when compared to traditional monolithic spacecraft systems. Taking inspiration from multi-satellite systems such as the TerraSAR-X & TanDEM-X [68] and FireBird Missions [69], the concept of DSS shifts away from the use of monolithic platforms towards larger systems of smaller, specialised platforms that interact, and communicate through Inter Satellite Links (ISL) [70], and function collectively to provide an inherently commercially and economically viable approach due to the low size weight, power, and cost (SWaP-C) of small satellite technology. These next-generation satellite systems are collectively described as Distributed Satellite Systems (DSS), and encompass constellation, train, cluster, swarm, fractionated and federated mission architectures [71] [72]

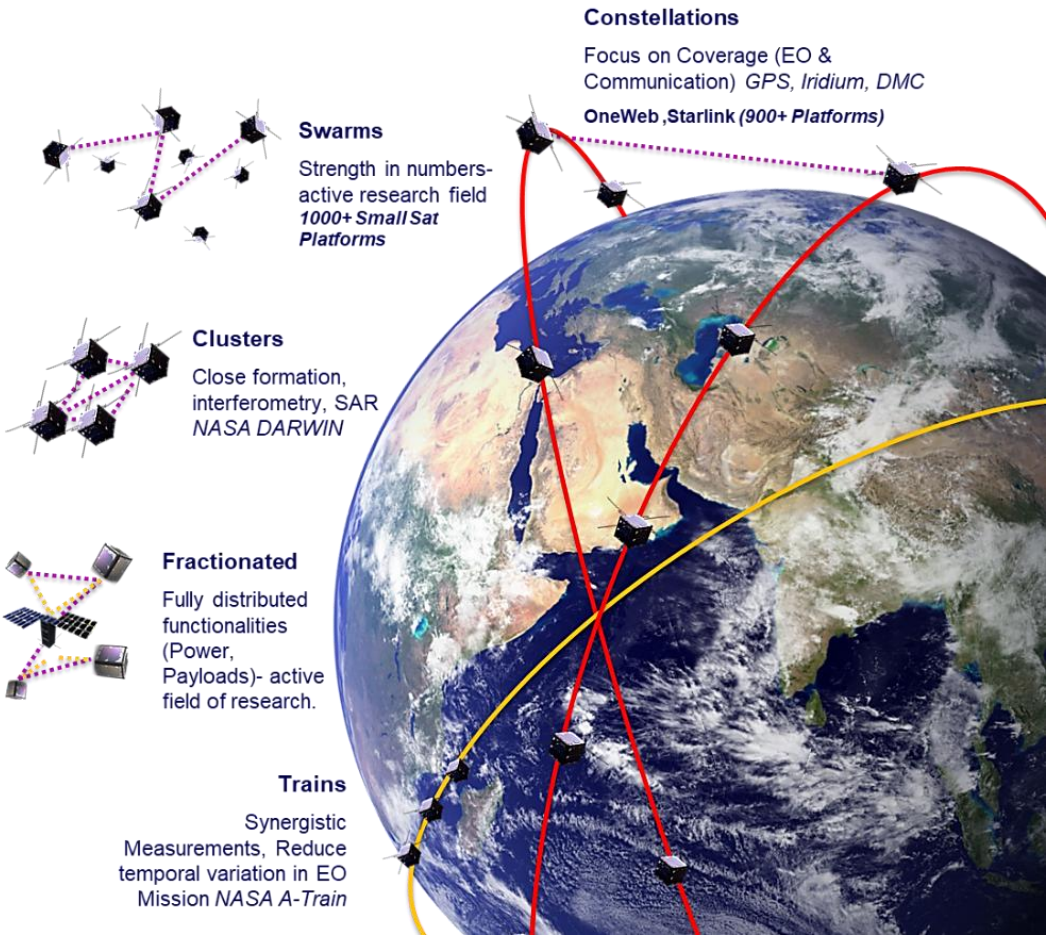

Figure 2 DSS Mission Architectures [73]

Constellation

A satellite constellation consists of multiple spacecraft, either homogeneous or heterogeneous, that work together as a unified system. The primary goal of the constellation is to provide continuous global or near-global coverage. These satellites are typically arranged across a series of orbital planes, designed to complement one another, and are linked either directly or through inter-satellite communication to one or more ground stations located around the globe. [72]

Train

In a Train formation, satellites are positioned along the same orbital path, following one another in a sequence. These satellites are configured to maintain a fixed relative angular separation throughout their orbit. In circular orbits, this angular spacing remains constant. However, in elliptical orbits, the relative angular separation varies depending on the satellite's position within the orbit. Typically, these angular separations are established when a designated primary satellite is at the perigee of its orbit, serving as the reference point for the formation [74].

Cluster

A cluster configuration refers to a group of satellites organized in a compact formation, where the satellites are positioned in orbits that keep them close to one another. Unlike trailing formations, where satellites are spaced along a common orbital path, satellites in a cluster typically travel together in tight formation, maintaining a relatively small spatial separation throughout their orbits.[75]

Swarm

Satellite swarms consist of distributed autonomous satellite modules that perform their designated tasks independently, without resource sharing, such as data exchange. Each module in the swarm is homogeneous, and the swarm's overall functionality can be enhanced by increasing the number of modules, thereby introducing redundancy. This redundancy improves the system's robustness by increasing the number of modules that conform to the desired constellation configuration.

For instance, in an Earth observation (EO) mission, the failure of a sensor in one module does not impede the overall mission's ability to collect images. However, in such cases, the transfer of resources (e.g., power, computational capacity) between modules is minimal. Despite individual module failures, the distributed spacecraft maintain the ability to communicate with one another to preserve the formation and share critical trajectory information, such as collision avoidance data. The system operates autonomously, with modules interacting primarily with their local neighbours, and resource transfer between modules is not required for operation.[76]

Fractionated

In fractionated systems, a spacecraft is divided into smaller, interdependent units that work together to achieve a common mission goal. These systems consist of co-dependent modules that rely on shared resources, such as data processing, power, and communication links, to function collectively [77]. While all fractionated systems require a common infrastructure to support these functions, the level of cooperation between modules can vary across a spectrum.

At one extreme, different tasks are assigned to distinct spacecraft units, with minimal collaboration between them. In this setup, each unit remains highly dependent on the shared infrastructure to perform its specific function. At the other extreme, fully fractionated systems feature modules that actively collaborate to complete the same task, contributing collectively to the overall mission objectives. Fractioned systems are still in their infancy and yet to be flown.

Federated Systems

In a federated system, a group of satellites collaborates to deliver a specific service, while each satellite operates independently with its own mission and communication capabilities. A Federated Satellite System (FSS) is a network of self-contained

satellites, each possessing the necessary infrastructure to function autonomously, unlike in fractionated systems where modules share resources. Each satellite in a federated system is independently launched and tasked with specific objectives, but they can opportunistically combine their resources and capabilities to contribute to a larger, distributed mission. [78]

While federated satellites differ from fractionated in that each satellite is fully equipped to operate independently. These systems are often heterogeneous, with satellites transferring underutilized resources to support shared mission goals. This flexibility allows federated satellite systems to be categorized as a distinct type of distributed satellite mission, combining both independent operations and resource-sharing for collective mission success. [72]

2.2.3.2. DSS For Space Based Space Surveillance

The needs of the scientific community largely stem from the provision of more accurate, reliable and timely Earth Observation (EO) and astronomical data. This data is used to inform the measurement and prediction of global meteorological events, natural disasters and fauna migration movements as a result of climate change [79]. Recent examples include the 2019-2020 Australian bushfire season and the critical role the Sentinel spacecraft constellation played in hotspot detection [80]. Nonetheless, as the frequency and degree of extreme climate events continue to increase, responsive space architectures offered by DSS will be key to optimizing manned assets to increase environmental sustainability and the safety of life on the ground. In parallel to the scientific EO endeavours, increased remote sensing capability requirements are being placed upon the maritime defence sector. Increasing threats posed by piracy, illegal fishing, sea terrorism, illegal immigration and blockades have cemented maritime domain awareness as an essential component to protect maritime assets. To form situational awareness of the maritime environment traffic entities must be identified with determination of intent requiring the use of maritime Intelligence, Surveillance and Reconnaissance (ISR) systems. Traditionally, manned platforms have been employed to classify and characterise maritime activity, however, there is now a significant shift in research and development towards the use of DSS ISR platforms to provide persistent and responsive wide area coverage of the maritime domain to obtain decision superiority over adversaries [81].

EO technologies enabled by DSS are just a subset of the possible critical mission capabilities that can be provided. By using DSS architectures we can begin to further address the pressing environmental and commercial sustainability problems within the Space Domain, one of which is the uncertainty around the ever-increasing number of Resident Space Objects (RSO) within the on-orbit environment. This condition is perpetuating the irrefutably hazardous probability of collision between RSOs, with increasing concerns of initiating an irreversible, cascading debris-generating process

widely recognised as Kessler syndrome [39, 40]. Historically the state vector of large orbiting objects (>10 cm) can be estimated and predicted with reasonable confidence, based on data accrued by the SSA Space Surveillance and Tracking (SST) segment and other non-government-owned ground-based sensors.

The feasibility of Space-Based Space Surveillance (SBSS) missions is being explored to monitor the Low Earth Orbit (LEO) [82] and Geosynchronous Orbit (GEO) regions [10, 83] due to the advantage of persistent tracking of smaller-sized RSOs (<10cm) elusive to traditional ground-based systems.

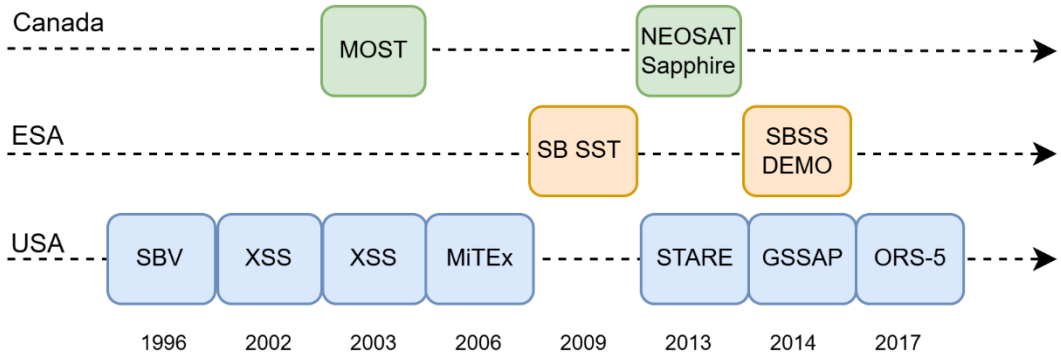

Figure 3. Timeline of SBSS Missions by Canada, European Space Agency and the United States. Adapted from [84]

This is credit to onboard sensors' ability to offer greater performances in terms of accuracy, larger field of view and weather independency allowing space-borne measurements to provide a wider set of useful observations [85]. Further, space-based observation systems are not subject to the scattering, diffraction, turbulences and aberrations that exist within the atmosphere [86]. The use of radar sensors to provide space-borne measurements has been explored in the past, however, due to challenges associated with size & power consumption, there has been a shift in research towards optical-based systems. Technological advancements in optical sensor principles (e.g., Coupled Charged Device (CCD) [11], complementary metal–oxide–semiconductor (CMOS), photon counting sensors [85, 87]) have significantly increased optical detection performance, demonstrating the ability to track a 3cm diameter object at a 3000km range [85, 88]. Figure 3 illustrates the various European and North American SBSS programs proposed based on monolithic mission architectures, each of which is discussed in detail in [89]. Nonetheless, monolithic approaches to SBSS inherently faced with issues relating to coverage and timelessness of RSO observation information [84], effective & timely coverage of the space environment requires SBSS platforms under sophisticated tasking and control strategies to meet key STM goals and performance requirements [90]. The DSS paradigm aims to meet these requirements [85] using a constellation of coordinated spacecraft to work in synergy

and compile tracking and estimation data to obtain more accurate and complete situational awareness. By providing a mission architecture that is resilient, responsive and acts cooperatively to reduce uncertainty about RSOs and facilitate safe on-orbit operations.

2.2.3.1. Platform Autonomy

In the context of the described SBSS missions, some form of centralized control is essential, as the ultimate objective of these missions is to serve ground-based human users[91]. In this framework, user-defined system-wide goals [92] are broadcast from the ground station to the DSS, where the spacecraft autonomously determine the course of action to achieve these objectives. This operational scenario aligns with what the European Space Agency (ESA) defines as a goal-oriented system, representing the highest level of spacecraft autonomy (E4) [93].

LEVEL	DESCRIPTION	FUNCTIONS
E1	Mission execution under ground control; limited on-board capability for safety issues	• Real-time control from the ground for nominal operations • Execution of time-tagged commands for safety issues
E2	Execution of pre-planned, ground-defined, mission operations on-board	• Capability to store time-based commands in an on-board scheduler
E3	Execution of adaptive mission operations on-board	• Event-based autonomous operations • Execution of on-board operations control procedures
E4	Execution of goal-oriented mission operations on-board	• Goal-oriented mission re-planning

Table 1:ESA defined levels of spacecraft autonomy [93].

*A Goal is a specification of operational intent***.** It describes what we want a system to do, not how to do it [94]. As such, Goal-Based Operations (GBO) represent a paradigm shift from traditional command sequencing operations. In terms of DSS autonomy, GBO facilitates the desirable reactive behaviour of DSS mission architectures by allowing replanning based on the sensed environment. In practice, this autonomy evolution describes a shift from typical satellite operational functions performed on

the ground segment to the space segment. A flagship study conducted by the French Space Agency (CNES) identifies the functions expected in this evolution [95]:

1. **Long term on-board programming:** Long-term platform activities on-board tele command (TC) stack, long-term mission plan upload
2. **Automation of TC generation – Automated Ground TM/TC loop:** Automated generation of TC for getting detailed telemetry, automated update of mission plan on reception of new hot spots and new targets
3. **On-board orbit determination and orbit control**
4. **Payload independence**
5. **Event-driven on-board execution:** Automated routine platform activities, automated image acquisition on newly detected hot spots
6. **Independent Control Centre and Mission Centres:** Direct link from Mission Centre to TT&C stations, reception of payload telemetry to the mission centre
7. **Condensed telemetry** Global satellite and mission status is condensed on-board and transmitted at regular intervals to the ground through GEO relays using a very low bandwidth. Detailed telemetry is downloaded only on demand when the overall status is not nominal.
8. **On-board mission planning from targets:** Detailed mission planning is performed on-board. Based on target observation.
9. **Automated on-board mission loop – Dynamic reprogramming:** Automated detection of hot spots in wide-FOV instrument images, on-board analysis of image quality and reprogramming of defective images
10. **Extended Fault Detection, Isolation and Recovery (FDIR)** (Integrated Vehicle Health Monitoring)

2.3. Categorisation of New Entrant Platforms

A variety of new space platforms have been recently proposed that bend the traditional image and classification of space vehicles [1-5]. Space platforms can be categorized into expendable launch vehicles (ELVs) and reusable launch vehicles (RLVs). Historically, a vast majority of space missions have relied on ELVs but RLVs are recently drawing great interest due to the remarkable potential economic savings [96, 97]. For instance, important savings were eventually achieved by the Falcon 9 (SpaceX) that now stands as a successful case study and is setting the new standard for space access costs [98, 99]. Development of other cost-effective reusable systems is currently underway including endeavours by Virgin Galactic (SpaceShipTwo + WhiteKnightTwo) and Reaction Engines (Skylon) [100, 101]. In addition to the RLV/ELV classification, space systems are also categorised based on their take-off and landing operational layout, as detailed in the following sub-sections.

2.3.1. Vertical Take-off and Landing

Vertical take-off is regarded as the traditional approach for space launch. In multistage configurations (*e.g.*, Space X Falcon 9) the upper stage can achieve orbital insertion while the first stage is recovered via vertical landing [98, 99], as schematically depicted in Figure 4 for a typical two-stage VTOL platform. Unmanned RLVs such as the SpaceX Falcon 9 and Blue Origin's New Shepard achieved reusability by incorporating platform-stabilizing fins and retrograde propulsion techniques to support vertical landing via thrust control [2, 12, 98]. A suborbital VTOL vehicle concept recently proposed is the hyper-velocity intercontinental transport system recently announced by SpaceX [102-104].

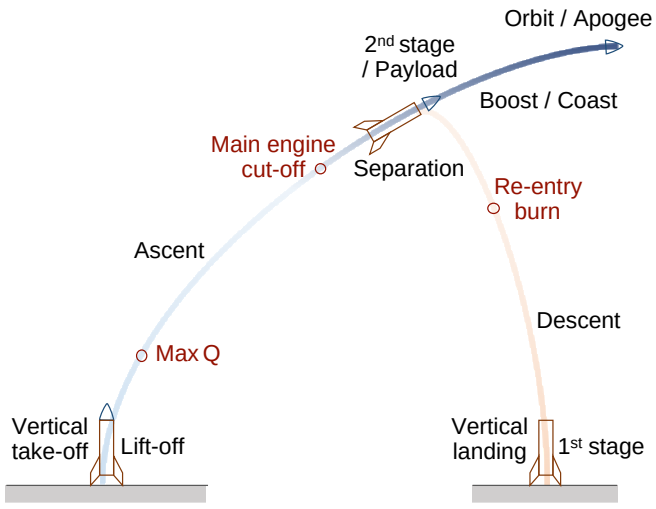

Figure 4. VTOL Platform Schematic (Two Stages).

VTOL spacecraft concepts for suborbital transport mostly entail a ballistic phase and are considered a staple case for future space traffic management [104]. From the atmospheric ATM perspective, the main advantage of the VTOL vehicles is that the atmospheric transits during both ascent and descent occur in the quickest possible manner, so that their interference with atmospheric traffic is relatively limited in time, as further discussed later. However, the launch, ballistic and re-entry phases of VTOL platforms offer very limited manoeuvring margins as these platforms do not rely on aerodynamics for lift, stability or flight control and their thin-shelled structure would potentially disintegrate in case of significant lateral accelerations, therefore their manoeuvrability is negligible [105], and cannot be considered an active player in any online de-confliction or collision avoidance processes.

In orbital flight, the spacecraft and/or payload transported by launch vehicles are typically placed in the low-Earth orbit (LEO) as the final orbit for LEO missions. For non-LEO missions, LEO serves as a parking orbit from which the spacecraft/payload is further transferred to a larger elliptic orbit including MEO, HEO and GEO, or parabolic/hyperbolic transfer orbit for lunar, interplanetary and deep-space missions. This decade has seen growing interest in low-mass payload launchers to transport mini/micro satellites for scientific and academic missions (*e.g.*, CubeSats) and constellation satellites primarily for commercial and strategic applications. Low-cost launchers for small payloads are actively developed worldwide including, Rocket Lab's Electron, Firefly α, and Virgin Galactic's LauncherOne [106, 107].

2.3.2. Horizontal Take-off and Landing

In contrast to VTOL, horizontal take-off and landing (HTOL) platforms are significantly more accommodating in their integration with conventional air traffic. Suborbital HTOL platforms are expected to enable next-generation, point-to-point transport systems for intercontinental travel, as explored extensively in past programs for suborbital aeroplanes such as NASP and HOTOL [102-104]. Figure 5 shows a schematic of a generic HTOL platform comprising two stages.

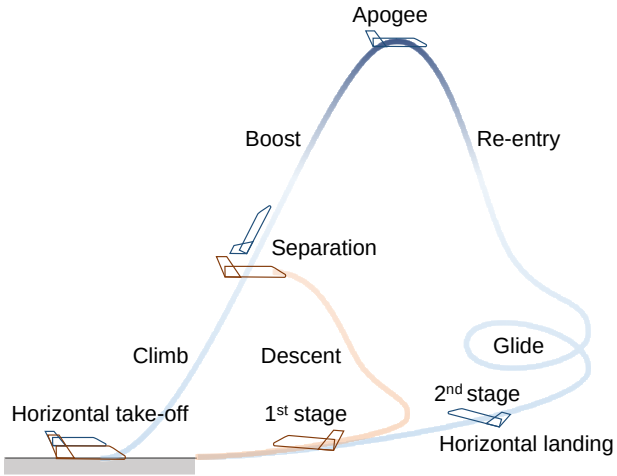

Figure 5. HTOL Platform Schematic (Two Stages).

Increasing commercial attention to affordable space tourism and small payload launch capabilities has led to renewed interest in HTOL platforms. Examples of contemporary HTOL concepts include XCOR and Skylon platforms under development by XOR Aerospace and Reaction Engines, respectively, as well as the SpaceLiner concept by DLR [5, 12, 108]. Unlike the ballistic nature of suborbital VTOL platforms, the SpaceLiner and Skylon HTOL concepts exploit aerodynamics to generate lift and control forces in their atmospheric transits both during ascent and during re-entry. The Earth's atmosphere is also exploited for air-breathing propulsion, which relieves the platform from the need to carry vast amounts of oxidiser.

HTOL platforms, like all other vehicles, typically rely on multi-stage launch systems, especially for orbital flight. Air launch systems are a subclass of multi-stage HTOL launch systems. Examples include North American X-15, Virgin Galactic's SpaceShipTwo and Orbital ATK's Pegasus, where a subsonic/transonic aircraft with air-breathing propulsion is used as a carrier (first stage), and the second/upper stage(s) is separated and launched in air to space, powered by solid/hybrid propellant rocket motors [100, 107, 109] [100, 110, 111]. Reaction Engines' Skylon concept is an exception of orbital HTOL, targeting single-stage-to-orbit (SSTO) by using the SABRE combined-cycle propulsion technology consisting of a turbo-ramjet and rocket engines [101, 112].

2.3.3. Hybrid

By definition, hybrid platforms are a combination of the VTOL and HTOL approaches, examples being the Space Shuttle Orbiter and Sierra Nevada Corporation's Dream Chaser platforms [98-100, 110, 111]. Requiring a vertical take-off with solid rocket boosters, these platforms are limited in manoeuvrability during their ascent, however during re-entry and subsequent gliding flight below FL600 their lifting body and control surfaces allow a significant level of manoeuvrability (Figure 6). Hybrid platforms typically utilize winged configurations for the reusable stage to exploit aerodynamic forces for flight stability and control.

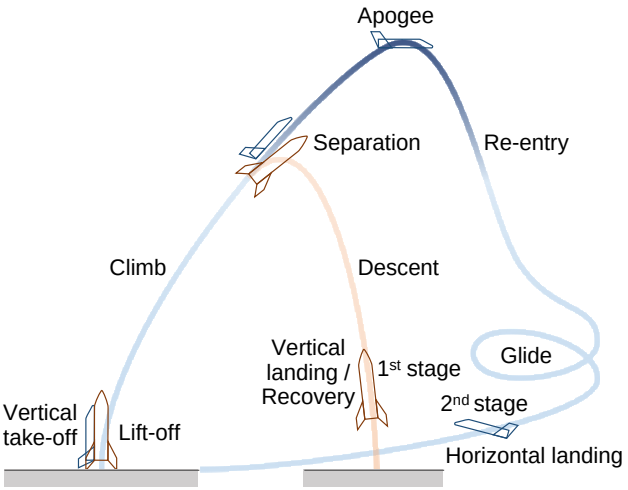

Figure 6. Hybrid Platform Schematic (Two Stages).operational Phases

2.4. Operational Phases

Beyond the highly vertical flight envelope – as opposed to atmospheric traffic – technical difficulties of integrating space vehicle activities with the conventional ATM infrastructure primarily originate from the significantly higher energy requirements, which exacerbate airworthiness certification challenges, as well as with the inherent manoeuvrability limitations discussed so far. Space platforms are designed to operate at extremely high velocities in severe environments and frequently feature reduced manoeuvrability due to a lack of aerodynamic controls and/or scarce propellant. Other important technical challenges include high position uncertainties due to complex aerothermal interactions and the high variability of the atmospheric environment, orbital perturbations associated with space weather and environment and the increasing probability of collision with space debris and the ever-growing government and commercial space activities [23, 24].

These and other specificities must be thoroughly considered as part of the technological requirements for ATM/STM integration and shall be carefully considered in all planning and operational processes. As a consequence, a solid understanding of the physical characteristics of each flight phase is a prerequisite for achieving ATM/STM harmonization.

2.4.1. Launch

In the course of launch and ascent, space vehicles are subjected to severe dynamic, aerodynamic, and thermodynamic environments, as described below, which crucially constrain the design and operation of the launch vehicles and payload [14]. Manned launch systems require careful assessment of the risk of ascent aborts associated with

failure environments such as debris strikes and blast overpressure from explosion in the event of a launch vehicle failure during the ascent phase [113].

2.4.1.1. Propulsion Systems

The propulsion systems of launch vehicles can be categorized into two classes, namely rocket and air-breathing engines, depending on the source of the oxidizer, *i.e.*, if it is carried as a propellant (rocket) or supplied by oxygen in the atmosphere (air-breathing).

Rocket engines produce thrust by burning liquid or solid propellants, or their combination (hybrid propellant). Air-breathing engines are necessarily combined or integrated with rocket engines to climb beyond the stratopause of the atmosphere, as thin air contains virtually no oxygen.

TBCC (turbine-based combined cycle) and RBCC (rocket-based combined cycle) systems are being developed as such integrated propulsion systems, where TBCC typically comprises turbojet, ramjet, and rocket engines, while RBCC involves ramjet, scramjet, and rocket engines [114-116]. Examples of TBCC include Skylon by Reaction Engines and SR-72 by Lockheed Martin [101, 117].

The flight path is constrained by dynamic pressure in structural consideration for launch vehicles whether powered by rockets or air-breathing engines. The latter is characterized by additional restrictions on dynamic pressure because thrust production for air-breathing engines in supersonic regimes crucially depends on the dynamic pressure to enable combustion as a result of aerodynamic and aerothermal interactions (*e.g.*, shock waves, and boundary layers). Dynamic pressure can also have a significant impact on the operation of the air intake, which requires a certain range of dynamic pressure to start and remain started.

The types of propulsion and propellants have considerable influence on the management and operation of space vehicles in both pre-launch and launch phases. For instance, liquid propellants require cryogenic systems and often turbopumps, whereas solid propellants offer ease of handling but difficulty in throttle control during flight, thus requiring careful design and planning of the trajectory and propellant charge (grain) [14].

The performance inevitably deviates from the optimal at off-design altitudes due to over- or under-expansion for rocket engines equipped with fixed geometry nozzles, while adaptive nozzles such as plug, expansion-deflection, and aerospike nozzles can effectively compensate for the atmospheric density variation with altitude change [118].

Space access with air-breathing propulsion, on the other hand, features self-compensation for altitude owing to air-breathing nature and external expansion (*e.g.*, SERN scramjet configuration) [119], but thermal management plays a key role in the success of sustainable flight; TBCC for hypersonic operation essentially requires pre-

cooling of incoming airflow, while RBCC requires effective wall cooling particularly for the combustor section [114, 120].

2.4.1.2. Launch Trajectory Dynamics

The point mass dynamics of a launch vehicle travelling over a spherical rotating earth can be described by the following set of 3 degrees of freedom (3DOF) equations of motion [121]:

$$\dot{r} = V \sin\gamma \tag{1}$$

$$\dot{\theta} = \frac{V \cos\gamma \sin\psi}{r \cos\phi} \tag{2}$$

$$\dot{\phi} = \frac{V \cos\gamma \cos\psi}{r} \tag{3}$$

$$\dot{V} = T - D - g\sin\gamma + r\Omega^2 \cos\phi(\sin\gamma\cos\phi - \sin\phi\sin\psi\cos\gamma) \tag{4}$$

$$\dot{\gamma} = \begin{bmatrix} (T\sin\alpha + L)\cos\sigma - g\cos\gamma + \frac{V^2\cos\gamma}{r} + \\ +\Omega\cos\phi\left(2V\sin\psi + \Omega r(\cos\gamma + \sin\gamma\sin\phi\cos\psi)\right) \end{bmatrix} \tag{5}$$

$$\dot{\psi} = \frac{1}{V}\begin{bmatrix} \frac{T\sin\alpha + L\sin\sigma}{\cos\gamma} + \frac{V^2\cos\gamma\sin\psi\tan\phi}{r} + \\ -2\Omega V(\tan\gamma\cos\phi) + \frac{\Omega^2 r}{\cos\gamma}\sin\phi\cos\phi\sin\psi \end{bmatrix} \tag{6}$$

$$\dot{m} = -\frac{m\,T}{g\,I_{sp}} \tag{7}$$

where r is the radial distance from the Earth centre to the vehicle, V is the Earth-relative velocity, θ and ϕ are the geodetic longitude and latitude, respectively, α is the angle of attack (incident angle), γ is the flight-path angle, and ψ is the velocity heading (track) angle. g is the gravitational acceleration, and Ω is the Earth's self-rotation rate. σ is the bank angle (positive to the right). T is the thrust acceleration, I_{sp} is the specific impulse of the propulsion system and m is the vehicle mass. L and D are the lift and drag accelerations, respectively:

$$L = \frac{1}{2m}\rho V_R^2 S C_L(\alpha, Ma) \tag{8}$$

$$D = \frac{1}{2m}\rho V_R^2 S C_D(\alpha, Ma) \tag{9}$$

Here ρ is the air density, S is the reference area, C_L, C_D are the lift and drag coefficients respectively and V_R is the velocity relative to the wind: $V_R = V - V_{wind}$. The dependency of the aerodynamic coefficients on the Mach number Ma is also highlighted.

2.4.1.3. Path Constraints

Launch vehicles undergo steady acceleration by engine thrust to achieve the target final velocity ΔV requirement. In addition, they must endure instantaneous peak accelerations including mechanical shocks characterized by extremely high acceleration levels and high-frequency local loading with a duration in the order of milliseconds. The peak acceleration is higher for loss-mass payload launchers, while it is lower for larger launch vehicles [122]. Vibration and aeroacoustics can also have severe impact during launch, including peaks from rocket motor firing of main engines and turbopump operation for liquid propellants at lift-off, and aerodynamic buffeting due to unsteady flow motion in transonic flight [12, 13].

Dynamic pressure is a crucial factor due to its potential impact on the vehicle structure especially when it peaks at a certain speed and altitude (as shown by the "Max Q" point in Figure 4). It also plays a critical role in air-breathing propulsion systems, as described in Section 2.4.1.1, and needs to be maintained in a suitable range to enable efficient engine operation and avoid engine unstart, which can lead to catastrophic failure. Aerothermal heating from skin friction and shock waves becomes significant at higher velocity in supersonic and hypersonic flight, necessitating appropriate thermal management accounting for heat transfer and materials [123]. The payload, which is often stored in the launch shroud where the maximum temperature is reached, requires particular care against not only aerothermal and mechanical effects but also the pressure environment which steadily decreases with the altitude [14].

The constraints imposed on launch vehicles can be summarised as follows:

$$n = \sqrt{L^2 + D^2} \leq n_{max} \tag{10}$$

$$q_{min} \leq q = \frac{1}{2}\rho V^2 \leq q_{max} \tag{11}$$

$$\dot{Q} = K_Q \rho^{0.5} V^{3.15} \leq \dot{Q}_{max} \tag{12}$$

where n is the magnitude of L and D acceleration forces, q is dynamic pressure, ρ is atmospheric density, $\dot{Q}$ is the heating rate, and K_Q is a constant specific to spacecraft material.

To reduce the aerodynamic loads on the structure of a space launcher the first two constraints are often summarized by the following constraint:

$$q\,\alpha < (q\,\alpha)_{max} \tag{13}$$

$Q\,\alpha$ is proportional to the aerodynamic load. This constraint is fulfilled during the first phase of the launch because the velocity V is low, then large α angles are allowed to rotate the launcher from its initial vertical attitude and implement the so-called pitch manoeuvre. At "pitch over" the angle α becomes zero and it is kept very low during the atmospheric flight to guarantee the $q\alpha$ constraint. This constraint disappears during the ascent since the density of the air decreases exponentially with the altitude.

To maintain the angle α close to zero the local wind velocities V_{wind} are taken into account. Wind velocities are measured at different altitudes around the launch base till a few minutes before the launch to update the nominal zero-lift trajectory (also called gravity turn trajectory). An ascending (safety) corridor is designed around the nominal trajectory: possible perturbations due to wind gusts and small model discrepancies as well as small hardware failures can produce moderate displacements from the nominal trajectory that can be recovered by the launcher control system. However if the launcher exits the ascending corridor a destruction command is actuated either by the Launch Officer, who tracks the trajectory on the ground, or by the autonomous destruction system located on board. Namely, linear-shaped charges are placed at the surface of the launcher case along the longitudinal axis. This arrangement limits the debris produced by the charge explosion: models of the mass and velocity distribution of the fragments are developed. For instance, the velocity distribution of the fragments of the third stage of Ariane V is modelled by the formula:

$$D_V = \mathrm{rand}(0,1)\, A\, m_F^{-B} \text{ km/s} \tag{14}$$

where rand(0,1) are random numbers between 0 and 1 chosen according to a Gaussian distribution, m_F is the mass of the fragment (in kg) and A, B are the numbers: A = 0.2154, B=0.1590 . The mass of the fragment is related to its dimension d_F according to an empirical formula:

$$m_F = f\, d_F^G, \qquad f = 45, \qquad G = 2.26 \tag{15}$$

From this formula, the ballistic coefficient of each fragment is estimated by:

$$B = \frac{1}{2} S\, C_D / m_F \tag{16}$$

With C_D ranging from 0.2 to 2. Considering different values of f ranging from 10 to 60, G ranging from 2.25 to 2.50, and the velocity variations D_V, the trajectories of the fragments are computed till the impact to the ground. All the possible values of altitude, velocity and flight path angles of the nominal trajectory are considered as the initial state of the fragments, corresponding to all the possible points where the destruction command can be activated. In this way regions surrounding the nominal trajectory are computed: these regions must be avoided during the launch activity.

2.4.2. Re-entry

Historic catastrophic losses during re-entry procedures highlight the significant limitations imposed by physical phenomena such as aerothermal heating, dynamic pressure and structural loading. A future STM/ATM system will have to support both safe and unsegregated re-entry operations and accommodate the projected increase of de-orbiting LEO supply spacecraft among sub-orbital re-entry trajectories intended for global point-to-point transport operations. The following sections provide a concise outline of the evolution of common re-entry planning methods, highlighting the limiting features that will inevitably affect STM/ATM coordination.

2.4.2.1. Re-Entry Dynamics

The control of the re-entry capsule is provided by aerodynamic torque. This torque depends on several parameters and on two control variables: the incidence angle α and the bank angle σ. The incidence angle is changed by a rotation in the symmetry plane of the capsule (pitch rotation) and the bank angle is changed by rolling the capsule around its longitudinal axis. To implement these rotations, different actuators are used corresponding to different re-entry capsule configurations. Ballistic capsules (having small aerodynamic efficiency C_L/C_D) generally use movable masses to change the static margin, which is the distance between the capsule centre of mass and the aerodynamic centre of pressure. This changes the stable attitude of the capsule, i.e., the value of α (α_{trim}) needed to ensure the flight in equilibrium condition. The bank angle can be changed by the rotation of the capsule around its longitudinal axis, generally implemented by cold gas jets generating a roll manoeuvre. On the other hand, lifted re-entry capsules (high aerodynamic efficiency) are endowed with movable aerodynamic surfaces to control the capsule in pitch and roll.

2.4.2.2. Shuttle Guidance Concept

Since its publication, the Shuttle guidance and trajectory design developed by Harpold has been used as the baseline for the majority of research regarding the re-entry problem, and hence outlining the underlying principles will be instrumental to identifying the progressions in re-entry design that followed. The primary objectives of the shuttle guidance are [124]:

- To guide the orbiter along a path that minimizes the demands on the orbiter system design throughout the orbiter missions
- To deliver the orbiter to a satisfactory energy state and vehicle altitude at the initiation of the terminal guidance system

During re-entry, the above constraints limit the orbiter's altitude at a given velocity, which can be expressed in terms of drag and acceleration. These constraints when visualized in a velocity/drag acceleration space produce what is known as a re-entry corridor. Figure 7 demonstrates the bounds of the shuttle re-entry scenario.

The shuttle guidance entry concept assumes the hypersonic portion of the flight is considered a great circle arc extending from the initial entry interface to the terminal area energy management (TAEM) interface. Terminal and entry points are specified by longitude, latitude, altitude above mean sea level (AMSL) and speed [20]. This assumption allows an initial estimate of the range to be flown ($S_{\mathrm{Togo}}{}^{*}$). A calculated guess of $S_{\mathrm{togo}}{}^{*}$ is an important parameter in designing the shuttle drag profile as the following will demonstrate. In constructing the appropriate drag profile the shuttle orbiter uses five drag reference segments. By connection of these segments a 2 dimensional "flight path" is then constructed from the entry interface to the terminal area.

Figure 8 shows the five drag reference segments. The first 2 segments are a quadratic function of (r,V) and are used during the period of high heating on the orbiter, followed by a quasi-equilibrium glide (QEGC) and an linear energy segment. Note that these segments lie within the entry corridor, and therefore satisfy the given constraint. The use of the former two segments in re-entry guidance (QEGC, Energy) is extremely convenient and has been the subject of numerous studies on the matter. The use of these conditions are further discussed in 2.4.2.4 and 2.4.2.3.

The drag profile now acts as the reference drag acceleration profile, that is, the profile that the orbiter follows to match a desired speed at a given altitude. Further, each point on the reference profile can be described in terms of S_{togo}^{*} Using solutions to the equations of motion. Under the QEGC condition, earth-relative speed is treated as the independent variable. In the latter section where a strong monotonic drag profile is employed, energy is treated as the independent variable.

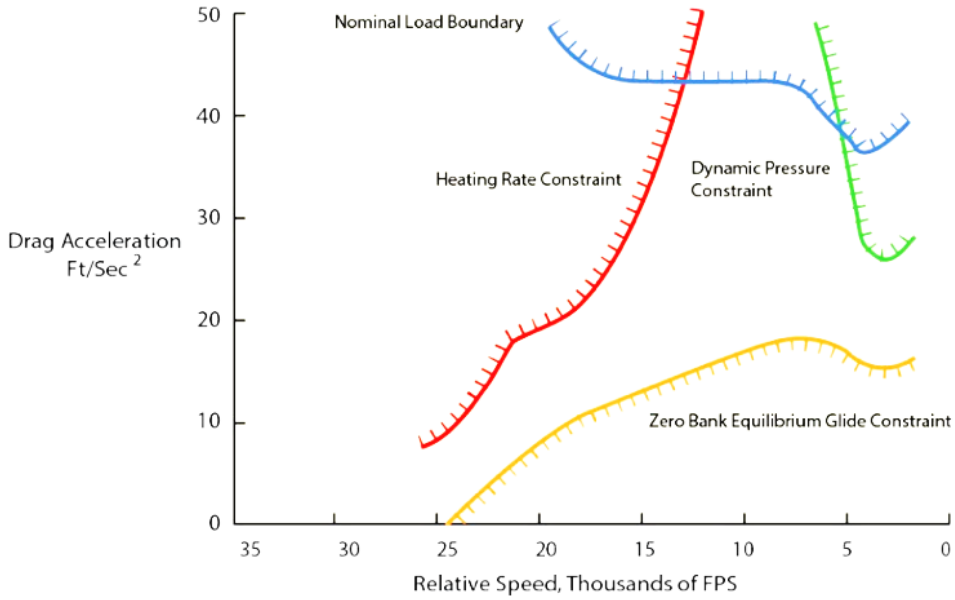

Figure 7. Orbiter guidance corridor [124].

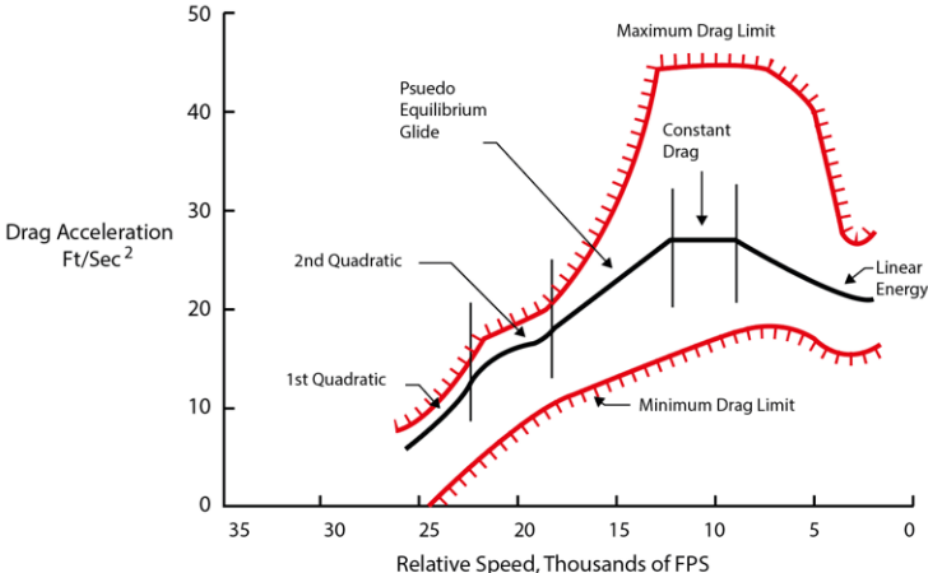

Figure 8. Orbiter drag segments [124].

Understandably for the orbiter to achieve objective 2, S_{togo} calculated from the reference S_{togoD} must closely match the estimated $S_{togo}{}^{*}$ otherwise, the orbiter will not meet the desired terminal conditions.

To accommodate for deviations in the reference profile during the re-entry phase, the magnitude of the drag profile is frequently updated so that $S_{togo}{}^{*} \approx S_{togoD}$ while maintaining the original reference shape to avoid any constraint breaches. For the orbiter to follow the constructed drag profiles, reference parameters are established to relate the lift and drag acceleration forces to each drag segment through the appropriate independent variable.

In following the desired reference profile, controllable inputs; bank angle σ, and angle of attack α , are scheduled as a function of the acceleration forces. Bank angle is chosen as the primary trajectory control parameter, where its magnitude dictates the total downrange while the sign of the bank angle commands the orbiter heading. An obvious consequence of a sustained bank will be heading deviation from the desired terminal interface, therefore a pre-defined heading error is set to schedule a reverse in the bank angle sign. Further, conducting a bank reversal requires the bank angle to roll through zero, directing the lift vector upwards. A temporary increase in the in-plane component of lift results in a deviation from the desired drag level and introduces phugoid motion. To minimise these transient effects modulation of the angle of attack compensates for the brief period of deviation from the nominal drag profile.

The Shuttle guidance concept outlined above has proven extremely successful through flight tests multiple shuttle missions and additional performance analysis [125], however, it is subject to the main assumption of a 2 Dimensional Trajectory [20]. The relatively coarse lateral motion planning severely limits its applicability in achieving mixed TBO operations envisioned for a future ATM/STM system.

Subsequent publications have focused on improving the Shuttle guidance's shortcomings while still retaining the attributes that made it highly effective. The following sections briefly recapture some of these successful approaches that have stemmed from the traditional Shuttle method.

2.4.2.3. Evolved Acceleration Guidance for Entry

Comparable to the linear energy drag segment in the Shuttle planning method, the Evolved Acceleration Guidance for Entry (EAGLE) method formulates the re-entry problem as a monotonically decreasing energy problem beginning at the re-entry interface and terminating at the TAEM point. Total Energy (E) is defined as the sum of kinetic and potential components:

$$E = \frac{1}{2}V^2 - \left(\frac{\mu}{r} - \frac{\mu}{r_s}\right) \tag{17}$$

where r_s is the radial distance from the planet's surface to the spacecraft's centre of mass.

The five state variables described by the equations of motion (γ ,θ φ, ψ , r_s/r) are then scheduled as a function of decreasing energy E through the velocity components found in each equation of motion. Subsequently, the reference variables used by the planning function (σ, α) are defined as normalized functions of energy $\widehat{E}$.

$$\widehat{E} = \frac{(E - E_i)}{(E_f - E_i)} \tag{18}$$

where E_i , E_f are the initial and desired final energy values respectively. By definition, $\widehat{E} = 0$ at the entry interface and terminating at $\widehat{E} = 1$ at the TAEM interface. Similar to the Shuttle method, EAGLE imposes the constraints described in 2.4.1.3 while also highlighting the importance that the trajectory and controls should maintain sufficient margins from the given hard constraints to allow for dispersions [20].

The fundamental extension of the Shuttle planning method is that EAGLE accounts for the lateral motion of the spacecraft during re-entry. This is achieved by assuming the re-entry path to be taking place on the surface of a sphere as opposed to the planar assumption taken by the shuttle method [20]. Further, the equations of motion are simplified from 5th to 3rd order by the assumption that *γ=0* throughout the hypersonic portion of the flight. The advantage of eliminating vertical dynamics from the equation of motion lies in avoiding phugoid-type behaviour due to fluctuations in the kinetic and potential energy terms as well as decreasing algorithm computation time [21].

EAGLE breaks down the re-entry problem into the following sub-problems [20]:

1. estimate the trajectory length and obtain the initial drag profile;
2. using the estimate of the drag profile, solve the trajectory curvature sub-problem;

3. based on the solution to the trajectory curvature sub-problem, adjust the trajectory length and resolve the trajectory length sub-problem and obtain a revised drag profile.

Sub-problem 1 is solved comparably to the Shuttle guidance concept, where a drag profile extends from an initial value through to a final value, corresponding to a longitude, latitude, velocity and altitude. In contrast to the Shuttle planning method, all the segments of the reference profile are represented by a function of monotonically decreasing energy [21]. Sub-problem 2 determines the curvature of the trajectory by calculating the lateral forces that occur as a consequence of following the drag profile. The magnitude and direction of these forces are extracted from the command history of the bank and angle of attack modulation [21]. Once the curvature is known, the total length is then determined and then the trajectory length (sub-problem 1) is updated. This process continues until the value of the estimated trajectory length (from entry to final point) converges with the extracted length of the 3-dimensional drag profile the re-entry planning problem is solved.

The objective of EAGLE was to develop a planning method that would be capable of achieving more aircraft-like operations through an on-board planning system that allowed significant cross-range entries as well as the ability to accommodate abort scenarios. This added benefit of the EAGLE over the traditional shuttle method demonstrates its capability in a future STM system [21].

2.4.2.4. Quasi-Equilibrium Glide Condition

The Quasi-Equilibrium Glide Condition (QEGC) has been the centrepiece of multiple research efforts regarding the re-entry planning problem. The following is a brief outline of the most well-known QEGC re-entry planning methods proposed and published by Shen and Lu. [15-19].

2.4.2.5. QEGC Concept

For a considerable portion of the re-entry trajectory, the flight path angle γ of a lifting body spacecraft is very small and therefore negligible in determining in spacecraft position and velocity. By ignoring the Earth's rotation and setting $\cos\gamma$=1 and $\dot{\gamma} = 0$ the equation of motion describing the rate of change of flight-path angle is simplified to [126]:

$$0 = \mathrm{L}\cos\sigma - \mathrm{g} + \frac{\mathrm{V}^2}{\mathrm{r}} \tag{19}$$

The assumption of the QEGC applies to a given cut-off velocity where the magnitude of this velocity is dependent on the $\frac{\mathrm{L}}{\mathrm{D}}$ of the re-entry vehicle. For instance, a re-entry vehicle with $\frac{\mathrm{L}}{\mathrm{D}} \leq 1$ such as the X-33, X-38 the QEGC assumption is only valid $\mathrm{V} \geq$ 2000 m/s, however for re-entry with $\frac{\mathrm{L}}{\mathrm{D}} \geq 1$ such as the Shuttle orbiter the QEGC provides a valid estimate of spacecraft position/velocity until a cut-off velocity

associated with desired TAEM conditions condition [19]. On closer inspection of the QEGC condition, it is clear that at any point on the re-entry trajectory where a distance r and velocity V are specified, σ will be adjusted to satisfy the QEG condition. Further, the QEGC allows a simple and effective way to construct the re-entry corridor within the velocity/altitude space if:

$$\sigma_{EQ}(V) \leq \sigma(V) \leq \sigma_{max}(V) \quad (20)$$

Where if $\sigma_{EQ}(V), \sigma_{max}(V)$ are chosen to satisfy the QEGC and the hard path constraints, the corresponding trajectory will satisfy all the imposed constraints [15]. Figure 9 depicts the key characteristics of the QEGC.

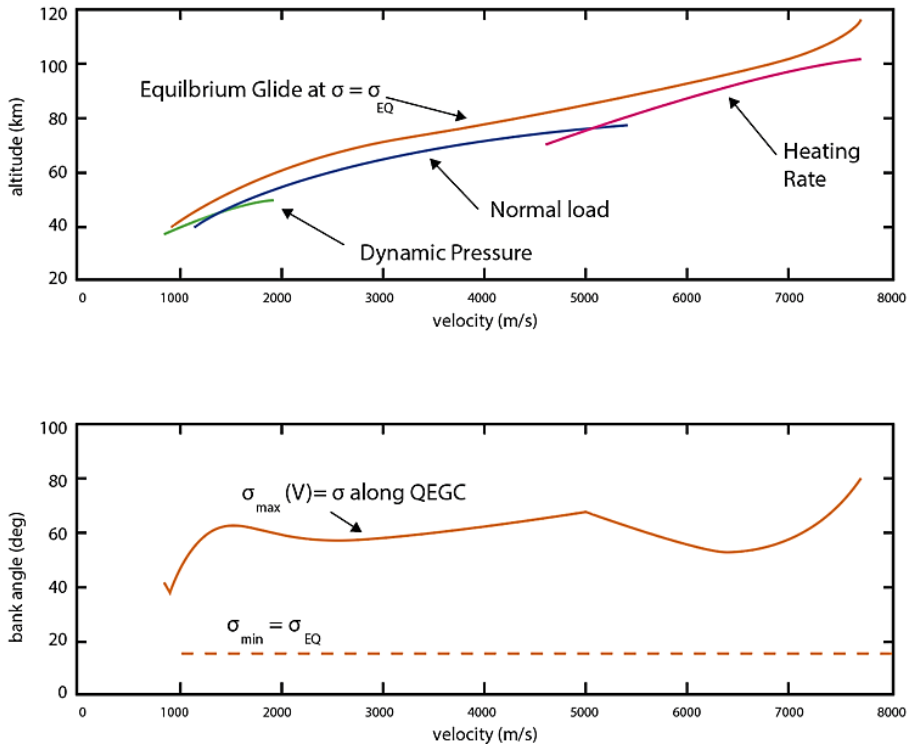

Figure 9: QEGC: (a) Re-entry corridor; (b) Bank angle Corresponding to path constraints [15].

2.4.2.6. QEGC Algorithm

Shen (2002) [15] divides the re-entry trajectory into the following three distinct phases.

1. Initial Descent Phase
2. QEG Phase
3. Pre-TAEM Phase

The initial descent phase extends from the entry interface to an altitude where the QEG condition becomes valid (120km - 80km). Up until this point, the QEGC is not an accurate estimate of the velocity and position of the vehicle as the lack of air

density at higher altitudes does not provide sufficient dynamic pressure required for the generation of lift and subsequent trajectory controllability. Until the re-entry vehicle can satisfy the QEGC it is in somewhat of a controlled fall. During this phase, a nominal angle of attack profile and constant bank angle are chosen to ensure a smooth transition to the QEGC phase. As discussed, the QEGC phase is subject to all constraints and the length of its validity is determined by the magnitude of the re-entry vehicle's L/D. Depending on the bounds of the QEGC there may be no need assess phase 3. In the case of a re-entry vehicle with $\frac{L}{D} \leq 1$, the pre-TAEM phase is evaluated as a fourth-order polynomial of (r,V), a similar approach to the first phase of the shuttle entry scheme [15]. Figure 10 presents the phases in the velocity/altitude space, while Figure 11 presents the top-level QEGC.

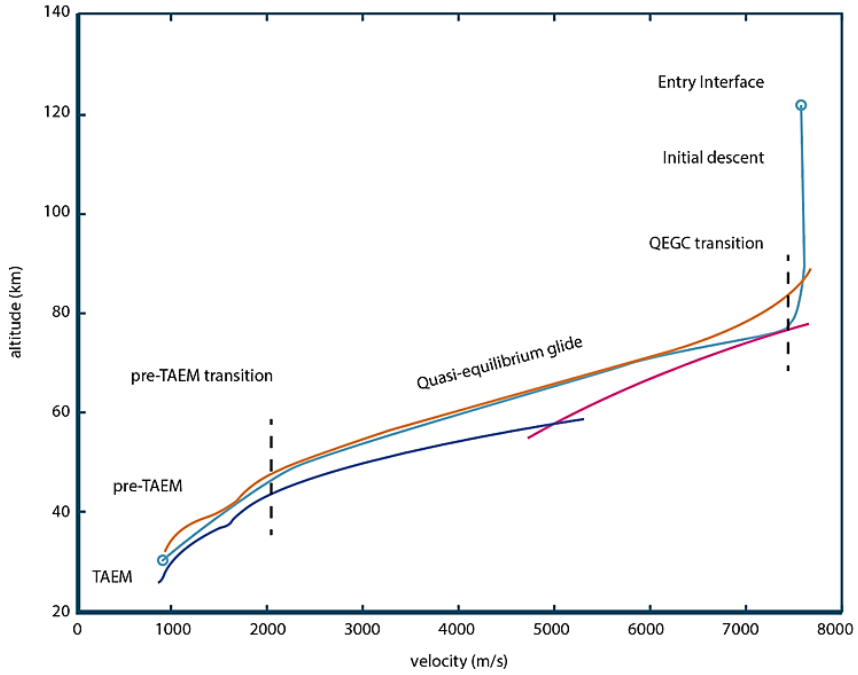

Figure 10: Re-entry phases [15].

Analogous to the EAGLE and shuttle methods, the point at which the bank reversal occurs is chosen to minimize the heading error at the TAEM interface. If the bank reversal is performed too early or late, the final heading error has the potential to be quite large. Once a suitable bank reversal point is located, the equations of motion are integrated to obtain a full 3DOF trajectory.

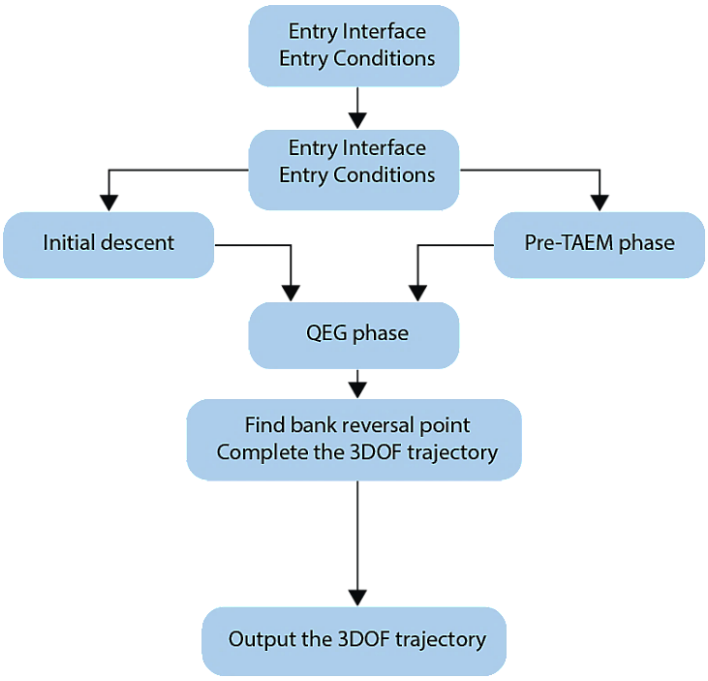

Figure 11. QEGC algorithm [15].

2.4.2.7. Suborbital Re-Entry Planning

Suborbital re-entry differs from orbital in that the re-entry interface begins at a significantly lower velocity and altitude in contrast to traditional re-entry procedures beginning from LEO. As a consequence the validity of re-entry trajectory generation methods based on the QEGC is questioned: if the spacecraft platform does not have an exceptionally high $\frac{L}{D}$ ratio the QEGC condition may not be satisfied due to the lower velocities associated with suborbital entry. Nevertheless, Shen and Lu proposed a method to extend the (r, V) polynomial from the TAEM interface to the end of the initial descent phase permitting suborbital trajectory generation for spacecraft platforms that exhibit lower $\frac{L}{D}$ ratios [16]. Future point-to-point spacecraft platforms associated with suborbital operations will most likely not succumb to the shortcomings associated with a low $\frac{L}{D}$ ratio as identified platforms are intended to operate tactically alongside traditional atmospheric aircraft.

2.4.2.8. Waypoints and No-Fly Zones

The use of waypoints and geofences such as no-fly zones (NFZ) during re-entry will most likely be a cornerstone requirement for re-entering spacecraft achieving mixed operations with traditional atmospheric aircraft, as these relatively simple geometric entities provide a means to accurately constrain the re-entry trajectory. As discussed, traditional re-entry methods first design the longitudinal profile and then command the bank angle to follow the reference profile, where the full 3DOF trajectory is obtained by integration of the equations of motion. This approach however is not appropriate when considering no-fly zones and waypoints as lateral motion is an

indirect function of the longitudinal planning and therefore may breach desired waypoints and geofences. Notwithstanding, re-entry planning methods have been proposed that simultaneously design the lateral and longitudinal motion to meet NFZ-like and waypoint constraints. However, the proposed algorithms can take multiple minutes to produce a valid solution deeming it somewhat ineffective for online trajectory generation, a capability that will be required for tactical de-confliction scenarios in mixed flow TBO [127].

2.4.3. On-Orbit Phase

As spacecraft travel beyond the Earth's atmosphere, they become subject to an environment that is distinctly different from that on Earth. Space weather events generally shielded by the Earth's atmosphere now become hazardous. Aerodynamics surfaces become ineffective, requiring the use of non-air-breathing propulsive forces. Trajectories begin to follow initially somewhat deterministic ballistic and orbital paths, however uncertainty in there prediction begins to grow due to the highly non-linear dynamics that govern the motion. This aspect becomes particularly problematic for long-term predictions required for separation assurance between other spacecraft (operational and defunct) and debris in the on-orbit environment. A future STM system must fully consider these elements when developing operational procedures and decision support tools. Because of this, in the following sections we briefly summarise orbital dynamics modelling and subsequently review in detail the most relevant factors affecting the on-orbit phase and finally discuss how these can be captured when calculating long-term estimations.

2.4.3.1. Orbital Dynamics

Cowell's method is a well-known deterministic approach for modelling orbital motion, for which the spacecraft trajectory can be estimated by direct integration of the equations of motion including all relevant perturbations and propulsion accelerations. Historically, numerical solutions to Cowell's method had issues with accuracy due to the limited floating point precision in legacy computing technology; however advances in computing allowed this method to be a reliable, simplistic and accurate approach for orbital simulation.

The equations of motion for the two-body problem with initial conditions can be written as:

$$\ddot{\mathbf{r}} = -\frac{\mu}{r^3}\mathbf{r}\,(\mathbf{r}, \dot{\mathbf{r}}, t) \qquad t_0, \mathbf{r}_0, \dot{\mathbf{r}}_0 \tag{21}$$

where:

$$r = \sqrt{x^2 + y^2 + z^2} \tag{22}$$

$$\mathbf{x} = \begin{Bmatrix} x \\ y \\ z \\ v_x \\ v_y \\ v_z \end{Bmatrix} \tag{23}$$

$$\dot{\mathbf{x}} = \begin{Bmatrix} v_x \\ v_y \\ v_z \\ \dot{x} \\ \ddot{y} \\ \ddot{z} \end{Bmatrix} = \begin{Bmatrix} v_x \\ v_y \\ v_z \\ -\frac{\mu}{r^3}x \\ -\frac{\mu}{r^3}y \\ -\frac{\mu}{r^3}z \end{Bmatrix} \tag{24}$$

$$\dot{\mathbf{x}} = f(\mathbf{x}, t) \tag{25}$$

2.4.3.2. Orbital Perturbations

When predicting the short-term evolution of orbital motion in the proximity of a relatively large gravitational attractor, the simplified two-body problem is sufficient; however, when estimating long-term orbital evolutions, the effect of perturbations must be considered. Orbital perturbations in the proximity of Earth can be classified in the three following categories [128]:

Perturbations due to the presence of other large celestial bodies and mainly:

- the Moon, $\mathbf{a}_m$
- the Sun, $\mathbf{a}_s$
- Perturbations due to the Earth not being a perfect point-mass
    - Oblate Earth (such as the J_2 term), U
- Perturbations due to non-gravitational sources:
    - Residual atmospheric drag, $\mathbf{a}_d$
    - Solar radiation pressure $\mathbf{a}_{SRP}$

The total perturbation in proximity of Earth ($\mathbf{a}_p$) is then simply summed into the two-body problem using the Cowell formulation:

$$\mathbf{a}_p = \mathbf{a}_d + \mathbf{a}_s + \mathbf{a}_m + \mathbf{a}_{SRP} \tag{26}$$

$$\ddot{\mathbf{r}} = -\frac{\mu}{r^3}\mathbf{r}U + \mathbf{a}_p\,(\mathbf{r}, \dot{\mathbf{r}}, t) \tag{27}$$

The following sections provide the analytical expressions for these perturbations, expressed each as accelerations.

Non-Gravitational Sources

The perturbing acceleration due to atmospheric drag is expressed as:

$$\mathbf{a}_d = -\frac{1}{2}\rho(\mathbf{r}, t)|\mathbf{v}_r|\mathbf{v}_r\frac{C_d A}{m} \tag{28}$$

where:

$\mathbf{v}_r$ = space object velocity vector relative to the atmosphereρ
ρ = atmospheric densityC_d = drag coefficient of the space object$A$
= atmospheric densityC_d = drag coefficient of the space object$A$
C_d = drag coefficient of the space object$A$
A = reference area of the space object$m$ = mass of the space object
= reference area of the space object$m$
= reference area of the space object$m$
= reference area of the space object$m$
m = mass of the space object
= mass of the space object
= mass of the space object
= mass of the space object

The relative velocity vector $\mathbf{v}_r$ is given by the space object velocity minus the cross product of the inertial rotation vector of the Earth's velocity, **w**, and the position vector of the satellite, **r**.

$$\mathbf{v}_r = \mathbf{v} - \mathbf{w} \times \mathbf{r} \tag{29}$$

$$\mathbf{w} = \omega_e[0\ 0\ 1]^T \tag{30}$$

$$\mathbf{v}_r = \begin{bmatrix} \mathbf{v}_z + \omega_e x \\ \mathbf{v}_y + \omega_e y \\ \mathbf{v}_z \end{bmatrix} \tag{31}$$

The solar radiation pressure constant can be expressed as:

$$C_{SRP} = \gamma P_s {A_u}^2 - \frac{A}{m} \tag{32}$$

where:

γ = reflectivity constant of the space objectP_s = solar radiation constantA_u
P_s = solar radiation constantA_u = astronomical unit
A_u = astronomical unit
= astronomical unit
A = surface area normal to the incident radiation$m$
= mass of the space object

$m =$ mass of the space object

The acceleration vector due to solar radiation pressure is then given by:

$$\mathbf{a}_{SRP} = C_{SRP} \frac{\mathbf{r}_{b-s}}{|r_{b-s}|^3} \tag{33}$$

where:

$\mathbf{r}_{b-s} = \mathbf{r}_b - \mathbf{r}_{e-s}$
$\mathbf{r}_b =$ geocentric inertial position vector of space object $\mathbf{r}_{e-s}$
$\mathbf{r}_{e-s} =$ geocentric inertial position vector of the sun
$=$ geocentric inertial position vector of the sun

Non-Spherical Earth

The zonal perturbations given by the non-spherical Earth can be expressed as:

$$U = \left[1 - \sum_{n=2}^{\infty} J_n \left(\frac{R_E}{r_E}\right)^n P_n(\cos\theta)\right] \tag{34}$$

where:

$r_E =$ distance from the earths centre$R_E =$ equatorial raduis of the earthθ
$R_E =$ equatorial raduis of the earth$\theta =$ colatitudeJ_n
$\theta =$ colatitude$J_n =$ zonal harmonic coefficient of the earth of degree nP_n
$=$ colatitudeJ_n
$J_n =$ zonal harmonic coefficient of the earth of degree nP_n
$=$ zonal harmonic coefficient of the earth of degree nP_n
$=$ zonal harmonic coefficient of the earth of degree nP_n
$P_n =$ Legendre polynomial of degree n
$=$ Legendre polynomial of degree n
$=$ Legendre polynomial of degree n
$=$ Legendre polynomial of degree n
$=$ Legendre polynomial of degree n

Corresponding zonal harmonic coefficients and Legendre polynomials are outlined in Table 3

Table 2: Zonal harmonic coefficients and Legendre polynomials.

n	J_n	$P_n(\cos\theta)$
2	1082.63	$\frac{1}{2}(3\cos^2(\theta - 1))$
3	-2.53215	$\frac{1}{2}\cos\theta(5\cos^2(\theta - 3))$

4	-1.61099	$\frac{1}{8}(35\cos^4\theta - 30\cos^2\theta + 3)$

Large Celestial Bodies

The perturbing acceleration from the Moon can be expressed as:

$$\mathbf{a}_m = -\mu_m \left(\frac{\mathbf{r}_{m-b}}{|\mathbf{r}_{m-b}|^3} + \frac{\mathbf{r}_{e-m}}{|\mathbf{r}_{e-m}|^3} \right) \quad (35)$$

Where:

μ_m = Gravitational constant of the moon$\mathbf{r}_{m-b}$
$\mathbf{r}_{m-b}$ = Position vector from the moon to the space object$\mathbf{r}_{e-m}$
= Position vector from the moon to the space object$\mathbf{r}_{e-m}$
$\mathbf{r}_{e-m}$ = Position vector from the Earth to the moon
= Position vector from the Earth to the moon
= Position vector from the Earth to the moon

Similarly, the perturbing acceleration from the Sun is given by:

$$\mathbf{a}_s = -\mu_s \left(\frac{\mathbf{r}_{s-b}}{|\mathbf{r}_{s-b}|^3} + \frac{\mathbf{r}_{e-s}}{|\mathbf{r}_{e-s}|^3} \right) \quad (36)$$

where:

μ_s = Gravitational constant of the sun$\mathbf{r}_{s-b}$
$\mathbf{r}_{s-b}$ = Position vector from the sun to the space object$\mathbf{r}_{e-s}$
= Position vector from the sun to the space object$\mathbf{r}_{e-s}$
$\mathbf{r}_{e-s}$ = Position vector from the Earth to the sun
= Position vector from the Earth to the sun
= Position vector from the Earth to the sun

2.5. Space Weather and Other Factors

The near-Earth space environment primarily comprises Earth's upper atmosphere, ionosphere, magnetosphere, and radiation belts, whereas the deep space environment can include heliosphere and other planetary and small body regions in interplanetary space [25]. The near-Earth environment has a crucial impact on the design and performance of space vehicles, which consistently operate in proximity to the Earth [14, 25].

The Earth's atmosphere becomes thinner with altitude within the lower atmosphere ($h \lesssim 85$ km), where its pressure and density decrease exponentially while maintaining a homogeneous composition mainly consisting of oxygen and nitrogen. In this altitude range, the pressure and viscous forces acting on the vehicle surfaces cause atmospheric drag to the spacecraft. Above this altitude, *i.e.*, the thermosphere, which extends up to $\lesssim 500$ km, the atmosphere becomes rarefied. The neutral atmosphere

in the thermosphere is characterized by the photoionization of molecules or atoms as well as absorption of UV photons radiated from the Sun, which leads to the dissociation of molecules (constituent species of the atmosphere are fully decoupled at $h \gtrsim 120$ km) [129]. The mean free path of the species becomes considerably large (significantly larger than the vehicle size at $h \gtrsim 180$ km), but their influence cannot be ignored. The cumulative effects of atomic and molecular impact on the vehicle and its orbit must be considered due to the large kinetic energy associated with hypervelocity, as it represents a driving effect for altitude decay and associated along-track dispersions [130]. Density variations in the neutral thermosphere are linked with temperature variations in close relation to geomagnetic activities (*e.g.*, magnetospheric storms) and solar events, particularly solar winds with an 11-year cycle [130, 131]. Reference [132] provides a comprehensive overview of approaches and modelling techniques available to estimate the drag encountered by space vehicles in the free molecular regime.

Plasma consisting of charged particles exists in the ionosphere at $h \gtrsim 85$ km (overlapping with the thermosphere), generated when neutral species are deprived of electrons by incident X-ray and photons from the Sun (photoionization), particularly on the dayside hemisphere. Energetic photons and electrons trapped in the Earth's magnetic field constitute the Van Allen radiation belt, presenting hazards such as degradation of spacecraft paints and protective glasses as well as surface temperature rise. Protons can cause greater damage due to larger mass hence momentum especially for LEO spacecraft operating in the South Atlantic Anomaly ($h \lesssim 500$ km). Electrons can trigger differential charging of spacecraft components, disrupting electronic components. High-energy electrons can penetrate the spacecraft and produce electrostatic discharges by bulk charging, disrupting subsystem signals and operation [133]. Such charge can subsequently harm electronic components in the form of single-event phenomena including single-event upset, latch-up, and burnout in a severe event [133, 134]. Ionospheric plasma can also cause significant dispersion to electromagnetic radio waves by reflecting low-frequency waves, increasing propagation errors and thus causing inefficiencies in telecommunication systems [135]. Ionospheric disturbances and scintillations, in conjunction with geomagnetic storms, can subsequently have a crucial impact on the GNSS performance, and thus require the development of proper mitigation techniques, in consideration of uncertainties that remain in density irregularities of highly dynamic, strong ionospheric plasma [26-28].

Atomic oxygen results from the photoionization of molecular oxygen by solar UV radiation in the atmosphere at $200 \lesssim h \lesssim 600$ km and becomes most predominant at $h \sim 200$ km due to gravitational influence, requiring particular consideration for the design and operation of LEO spacecraft. Solar arrays and sensor performance can be degraded irreversibly due to the interactions of atomic oxygen with materials such as composites, organic films, and metallized surfaces [136, 137]. Outgassing (sublimation) of organic materials can occur when surface atoms are vaporized, and subjected to very low ambient pressure, and they can represent a hazard to optically

and electrically sensitive devices when deposited to the surface [138]. Space debris originating from various components such as spacecraft/instrument parts and rocket exhaust particles can cause severe damage to the space vehicles upon impact due to high kinetic energy carried by the objects, depending on the debris size and relative collision velocity [139].

The radiation environment associated with solar particle events and galactic cosmic radiation represents serious hazards to humans, necessitating appropriate shielding structures and materials for manned spaceflights [140, 141]. Zero/microgravity environment can pose health risks in various aspects including blood pressure, and muscular, locomotor and vestibular systems [14].

The near-Earth environment is thus characterized by both static and dynamic conditions (i.e., *space weather*), due to the combined effects of atmosphere, thermosphere, magnetosphere, ionosphere, and gravity, in conjunction with the solar events, geomagnetic activities and other variations. Such conditions and phenomena can have a crucial impact on space-borne and ground-based systems and also may endanger human health or life [134]. It is therefore essential to take the influence of space weather into account for space traffic management [22-24].

2.5.1.1. A Case for Space Weather Services as part of STM?

When particularly referring to dynamic/unsteady phenomena, the term "space weather" is pertinent because these processes could be hazardous to spaceflight in a manner not dissimilar to severe atmospheric weather phenomena such as thunderstorms, tropical depressions, icing, turbulence and wind shear, which affect spacecraft during their atmospheric transits equally if not more substantially than aircraft. These severe weather phenomena can have safety-critical impacts on flight operations and are anyway cause of massive disruptions to operational regularity. These considerations equally apply to aircraft and spacecraft, with the added disadvantage that space vehicles are affected by both atmospheric and space weather. For instance, low-pressure systems and tropical revolving storms are known to cause significant disruptions to space launch and re-entry operations. Spacecraft operators rely on an increasing number of commercial space weather providers for SSA due to the significant hazards and disruptions caused by nature in their operations.

On the other hand, weather forecast uncertainty is the single greatest challenge to denser 4D-TBO, as it can have opposite effects on inbound traffic from different directions, disrupting arrival sequences and/or compromising the scheduling and demand-to-capacity balance. Accurate and continuously updated weather information is therefore essential to mitigate perturbations in high-density 4D-TBO. This section briefly reviews the current aeronautical weather standards and planned evolutions before discussing the opportunity for STM to accommodate space weather information services.

The most relevant standards for Meteorological (MET) services are the Radio Technical Commission for Aeronautics (RTCA) DO-308, 324 and 340, as well as the

International Civil Aviation Organization (ICAO) Annex 3. RTCA DO-340 specifies MET data link services in terms of service category, method of delivery and the weather information involved [142]. Category 1 services are safety-critical and comprise both MET and Aeronautical Information Service (AIS) data links, whereas category 2 services are useful for decision support. In terms of timeframe and operational need, weather decision services are classified as either: Planning – supporting strategic long-range decision-making; Near-term – conceived for tactical avoidance of hazardous weather cells, particularly in terminal arrival/departure operations; and Immediate – supporting emergency avoidance and take-off/landing abortion. Longer timeframes correspond to larger geographic extents. All the services are supported by three delivery modes: Broadcast, which involves continuous regular transmissions to all aircraft within range, as opposed to Demand and Contract, which instead involve an active request for specific MET information. Table 3 illustrates the typical information provided by the three decision support services.

Table 3. MET information is classified according to decision service [105].

MET Service	***Planning***	***Near-term***	***Immediate***
Time horizon	Greater than 20 mins	3 mins to 20 mins	Less than 3 mins
Intended application	Offline and strategic online operations	Tactical online operations	Emergency avoidance, landing & take-off abortion
Airport Equivalent	METAR, TAF		Visibility, gusts and wind shear

RTCA DO-324 specifies the Required Communication Performance (RCP) for MET service delivery in terms of Transaction Time (TT) [143]. Different TT requirements are defined for airport, terminal and en-route domains. RTCA DO-308, on the other hand, specifies the MET data formats: point data, area data, vector graphics and gridded data, and also identifies a list of candidate MET products [144]. Point data include, for example, the conventional Meteorological Aerodrome Report (METAR) and Terminal Aerodrome Forecast (TAF) – for which ICAO Annex 3 defines the recommended measurement and forecast accuracies [145] – as well as Snow Notice-To-Airmen (SNOWTAM), whereas examples of area data include Significant Meteorological Information (SIGMET). Gridded data consists of a 3D structured grid with a forecast time dimension.

ICAO's Aviation Systems Block Upgrade (ASBU) roadmap notably acknowledged that further improved meteorological services are required to implement advanced functionalities such as 4D-TBO, and indeed strategic planning services are already being supplemented by *nowcasting*, which uses sophisticated algorithms to track and extrapolate individual storm cells from weather surveillance sensors up to 6 hours into the future, with sub-kilometre spatial resolution and a temporal resolution in the

order of minutes. Aviation weather service providers are increasingly supplementing this information with satellite imagery and ground-based sensors such as lightning detectors [146]. Some of these advanced weather services are already acknowledged by RTCA in DO-308, as shown in Table 3. The most recent standards also accommodate the capability of aircraft to downlink their locally-sensed weather information, which can augment ground-based data.

Table 4. Advanced METLINK products for flight planning in the USA and Europe [103].

	Data Format	***Refresh Rate***	***Validity (hours)***
	US National Weather Service (NOAA)		
National Convective Weather Forecast (NCWF)	Gridded/ Vector	5 min	1
Graphical Turbulence Guidance (GTG)	Gridded	15 min	0.25
Current Icing Product (CIP)	Gridded	1 hr	N/A
Forecast Icing Potential (FIP)	Gridded	1 hr	3
	WIMS (FLYSAFE)		
WIMS thunderstorm	Gridded/ Vector	5 min to 6 hr	0.2-1
WIMS turbulence	Gridded/ Vector	6 hr	36
WIMS icing	Gridded/ Vector	15 min to 12 hr	0.24-24
WIMS wake vortex	Gridded/ Vector	1 to 6 hr	2-12

Drawing a parallel between STM and its atmospheric counterpart, it is important to note that ATM entail some AIS and MET services to accomplish its safety-critical air navigation mission, including for instance local winds and pressure dispatches, METAR, TAF, SNOWTAM as well as aircraft/pilot reports (AIREP/PIREP). More advanced ("*premium*") aeronautical weather information is instead available through non-ATM services and/or by subscription. These premium services are increasingly cherished by airlines as they allow them to more effectively mitigate operational disruptions and optimise flight routes. Although the current breakdown between basic (safety-critical) and premium aeronautical weather service categories, as captured by RTCA DO-340, was largely due to their historical evolution, it proves highly opportune when considering their different performance requirements. In particular, while fulfilling safety-critical requirements is feasible for basic weather services, it would prove inconvenient and unnecessary for premium services, which are increasingly based on sophisticate evolutionary and machine-intelligent-based forecast and extrapolation models to provide high-resolution global coverage at all altitudes.

Whether the future STM system shall also cater to atmospheric and space weather information services like ATM is certainly a worthwhile debate. While space weather-avoidance limitations of spacecraft may weight against such choice, essential orbital and sub-orbital estimations would be greatly benefited by a coordinated ground-based service. For instance, consistency in the 4DT planning and negotiation/validation processes and traffic synchronisation require consistency between the weather data in ground-based systems and the one handled by airborne/spaceborne systems as far as practical. This consideration strongly favours the introduction of a ground-based/centralised space weather service to support the functional air/ground integration being pursued as part of the CNS+A technological roadmap, which should be ideally extended to space. We suggest that by adopting or adapting the operational, level-of-service and timeframe categorisations introduced in RTCA DO-340 it would be easier to identify a baseline subset of information that could be delivered as part of the STM service.

2.6. Uncertainty in the Orbital Environment

The precise knowledge of an RSO position and velocity is, and will continue to be an ever increasingly crucial factor for future air and space traffic management programs. These estimations are provided by cooperative and non-cooperative systems, most of which are already fully accounted for as part of the CNS+A technological pathway. Cooperative systems rely on state estimates from on-board navigation systems (e.g. GNSS, IMU) and their proactive exchange with all other vehicles in a potential collision course, whereas non-cooperative surveillance is generally provided by tracking systems such as ground- and air-/space-based radar or electro-optical systems, which do not require response by the tracked object. These systems are subject to errors that are a function of physical phenomena or from the mathematical extrapolation itself. Navigation and tracking errors are the differences between the measured states and the actual states of the space vehicle. Errors can particularly arise from discrepancies within the reference coordinate system, from effects such as precession and polar motion or from errors specific to the position measurement such as clock accuracy, and atmospheric effects (ionospheric and tropospheric refraction) [29]. Tables 5-9 illustrate the performance of common spacecraft navigation and ground tracking-related systems.

Table 5: Spaceborne attitude sensor(s) performance.
Reproduced from [147].

Spaceborne Attitude Sensors	***Accuracy [mrad]***	***Limitations***	***FoV [rad]***
Sun Sensor	0.2 ~ 200		1 x 1
Earth Horizon Sensor	1 ~ 20	Accuracy is limited by the horizon uncertainty. Applicable to LEO spacecraft	

Star Tracker	0.005 ~ 0.30 (NEA)	Angular Rotation, Sun, Earth, and Moon stray light. Bias due to body frame misalignment.	≤ 0.45 x 0.45
Magnetometer	9 ~ 50	LEO Satellites, Accuracy is limited by the Earth's magnetic field uncertainty	

Table 6: Spaceborne Inertial Sensor(s) Performance. Reproduced from [147].

Spaceborne Inertial Sensors	***Accuracy***	***Limitations***
Single-Axis Gyroscope (Fibre Optic, Ring Laser)	Angular random walk: 0.035~1 [μ rads / $\sqrt{s}$]	Subject to short and long term bias instability
Linear Accelerometer	20 ~ 400 μm/s^2	Subject to short and long term bias instability

Table 7. Reference spaceborne GNSS performance.

Spaceborne GNSS Sensors	***Accuracy (3σ)***		
GPS (GOES-R Spacecraft) [33]	Radial (R)	In-Track (S)	Cross-Track (W)
	20 m	13m	7.3m

Table 8. Reference ground-based radar tracking accuracy

Ground Based Radar Station	***Accuracy (1σ)***		
	Azimuth	Elevation	Range
AN/FPS 16 Single Object Tracking Radar [35]	0.1 mrad	0.1 mrad	5.4 m
AN/MPS 39 Multiple Object Tracking Radar [34]	0.2 mrad	0.2 mrad	2 m

Table 9: Ground-based optical tracking accuracy.

Ground Based Optical Station	***Accuracy (1σ)***		
	Azimuth	Elevation	Range
Super RADOTS Kwajalein Missile Range [148]	0.04 mrad	0.04 mrad	-
RADOTS Kwajalein Missile Range[148] [148]	0.07 mrad	0.07 mrad	-

Commonly, the error in state vector measurements is expressed in the RSW satellite-based orbit coordinate system as shown in Fig. 9. The origin of the RSW of the coordinate system is located at the nominal position of the ECI state vector. The Radial (R axis) always points from the earth centre along the radius vector towards the satellite. The S-Axis is directed in the along-track direction, where in the case of elliptical orbits is only parallel to the velocity vector at apogee and perigee. The W (cross-track) is normal to the orbital plane and completes the right-hand triad.

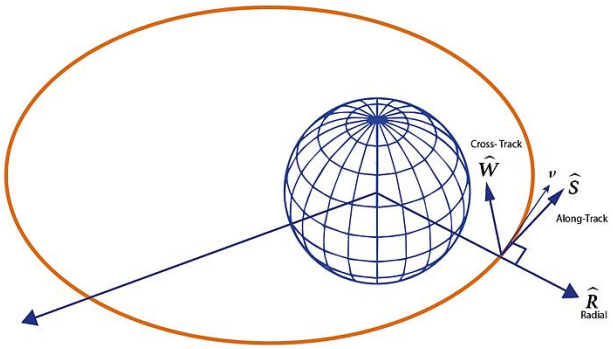

Figure 12: RSW Coordinate Frame

The RSW coordinate system can be easily related to the commonly adopted ECI coordinate system through the following unit vector transformation:

$$\hat{\boldsymbol{R}} = \frac{R_{ECI}}{|R_{ECI}|} \tag{37}$$

$$\widehat{\boldsymbol{W}} = \frac{R_{ECI} \times V_{ECI}}{|R_{ECI} \times V_{ECI}|} \tag{38}$$

$$\hat{\boldsymbol{S}} = \widehat{\boldsymbol{W}} \times \hat{\boldsymbol{R}} \tag{39}$$

The transfer matrix(s) between the RSW and ECI coordinate systems is the following:

$$M_{RSW \to ECI} = \left[\hat{\boldsymbol{R}}\ \hat{\boldsymbol{S}}\ \widehat{\boldsymbol{W}}\right] \tag{40}$$

$$M_{RSW \to ECI} = \left[\hat{\boldsymbol{R}}\ \hat{\boldsymbol{S}}\ \widehat{\boldsymbol{W}}\right]^{T} \tag{41}$$

Moreover, modelling errors occur from discrepancies in the orbital dynamic model. Errors included in the dynamic model are classified as the differences between the nominal model parameters and the real model parameters, which can be further categorised as rather gravitational or non-gravitational. Typical gravitational parameters include the mass of the Earth, geopotential coefficients, solid earth and ocean tide perturbations, mass and position of the moon and planets, as well as general relativistic perturbations. Drag (due to atmospheric density), solar and Earth radiation pressure, magnetic perturbations and spacecraft thrusting (actuating errors) are the non-gravitational accelerations required for consideration in orbital modelling [29].

2.6.1. Orbital Uncertainty Propagation Methods

Orbit propagation begins with an estimation of a space object's state vector. State measurement(s) are given by ground or on-board surveillance and navigation systems, for which measurement uncertainties can be assumed to be Gaussian and described by a mean and covariance matrix or PDF unless otherwise recommended. From this initial state measurement, the orbit is propagated using one of the various

approaches, inflating the position uncertainty ellipsoid with respect to time until the next measurement, which is commonly dictated by the update rate or availability of the navigation and/or surveillance system. The estimation of state can be seen as a convergent process that shrinks the volume of the ellipsoid at each observation epoch. Additionally, if any actuation is performed by the spacecraft the associated uncertainties should be included in the propagation at the time of manoeuvre [29].

An intuitive and rigorous empirical technique to propagate uncertainties and to reconstruct a statistical distribution is to perform the well-known Monte Carlo simulation, which involves the perturbation of initial states and of the dynamic coefficients in all their possible combinations. Nonetheless, conducting this approach with high fidelity is computationally expensive and can be deemed impractical in evaluating most collision scenarios.

A theoretical treatment of stochastic uncertainty propagation in dynamic systems was attempted as early as 1914 and led to the Fokker-Plank Equation (FPE), which describes the evolution of the PDF in time for a problem that satisfies the Itô stochastic differential equation. This approach augments the original deterministic flight mechanics equations with statistical moments. Although extensive efforts were targeted at the development of a computationally efficient solution method for the FPE, the high dimensionality and the significant nonlinearities of rigid-body (6-DoF) orbital mechanics so far encumbered these efforts and forced to make extensive use of linearity and Gaussian statistics [149]. To overcome the challenges associated with the rigorous statistical treatment of nonlinearities and high-dimensionality, it is necessary to employ approximation methods. Lou and Yang [29] provide a comprehensive review on the available uncertainty propagation methods for spaceflight mechanics. Their ontology is recaptured in Figure 13.

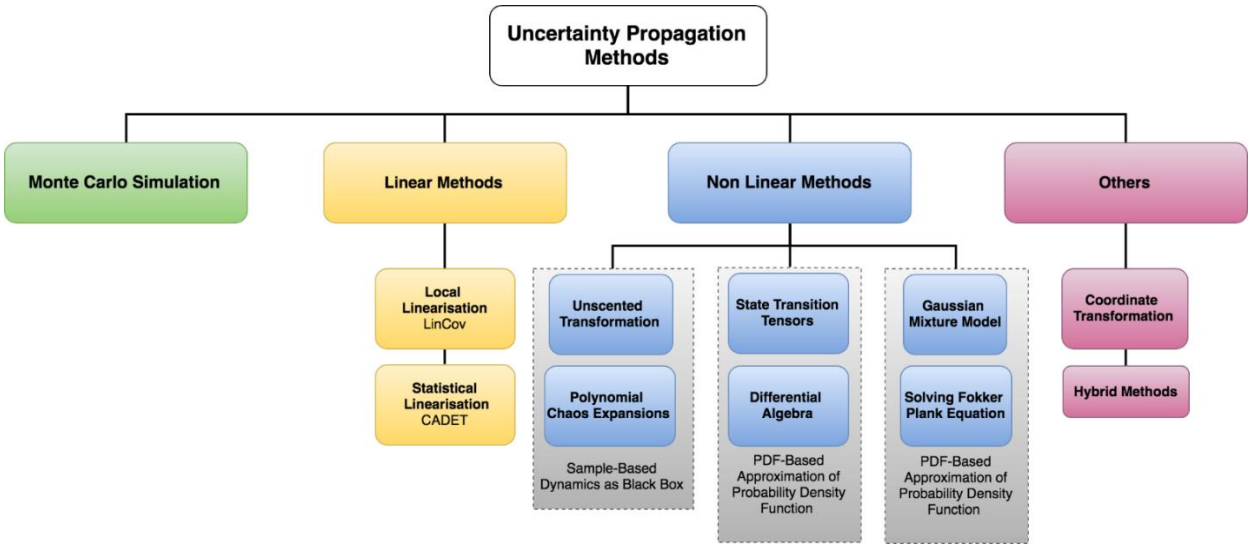

Figure 13. Ontology of uncertainty propagation methods, reproduced from [29]

Of these, linear methods provide the user with a convenient approach as only the mean position and covariance matrix need to be propagated when the following assumptions are taken [29]:

1. A linearized model sufficiently approximates the dynamics of neighbouring trajectories with respect to a nominal trajectory
2. The uncertainty can be completely characterised by a Gaussian probability distribution.

The dynamics can then be linearized via local or statistical means under the well-known Linear Covariance analysis (LinCov) and CADET [150, 151] techniques, respectively.

2.7. STM Framework and Regulatory Environment

The development of the STM system will require the implementation of policy, rules and regulations, standards, guidelines and best practices, a task that will not be without significant legal and political barriers. In any case, policy-related decisions will have considerable influence on the chosen technology and operational framework employed in an STM system. The technology domain acts to provide an STM system with Space Situational Awareness (SSA), which at a minimum, will enable an acceptable level of space-flight safety. This requires the necessary integration of products and services, applications, computing platforms, data sensors and other related technological aspects that together curtail the risks associated with existing and projected increases in orbital traffic. How these SSA-related tools are controlled and maintained will be subject to the systematic steps, activities and actions defined within the operational domain. The level of autonomy that will exist in executing these processes and procedures will be dictated by the complexity of required decisions and the effectiveness of Human Machine Interaction (HMI) within the operational environment. Decisions made within the policy domain shall capitalise on historical lessons, proven research, technical considerations, and operational limitations and time-lines.

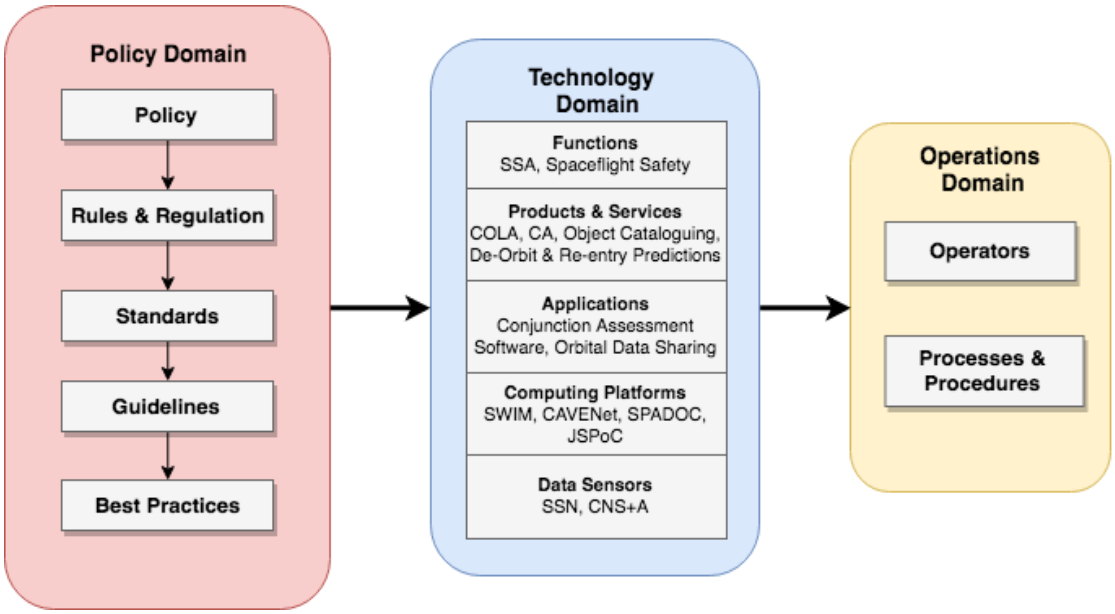

Figure 14. STM framework. Reproduced from [152]

The *outer space treaty* developed by the United States, the United Kingdom, and the Soviet Union provides the basis of an STM framework. Comprised of 17 articles, the treaty addresses fundamental concerns including the non-ownership of orbits and appropriation of space (Articles I, II), operator responsibilities in situations of distress (Article V) and damage liabilities from in space accidents (Article VII) among others. Although foundational, the Outer Space Treaty at present does not provide the necessary framework to assign space traffic management functions to new international decision-making STM authorities [153]. To accommodate such an aspect, it has been recommended that the treaty should be amended to establish a standing international organisation for STM, equivalent to ICAO and related atmospheric traffic standards and services [153]. Nevertheless, fast-forward 50 years and the problematic scenarios associated with the absence of a central STM authority are now becoming increasingly tangible.

In the interest of mitigating such events, many international and national organisations have developed various operational strategies, recommendations and requirements in the form of published guidelines and standards. The information contained in these documents addresses the specific hazard(s) present during each operational phase (launch, re-entry, on-orbit). The launch and re-entry phases are principally concerned with range safety which is addressed by Standard 321-07 “Common Risk Criteria Standards for National Test Ranges”. Standard 321-07 also extends to the on-orbit environment where separation and collision probability requirements are provided. Moreover, the on-orbit phase is subject to the irrefutably hazardous space-debris environment, with increasing concerns of initiating an irreversible, cascading debris-generating process widely recognised as Kessler syndrome [39, 40]. In consideration of the hazards imposed by space debris, mitigation guidelines and strategies have been issued by the IADC (Inter-Agency Space Debris Coordination Committee). The growth of space-based infrastructure

has also introduced a different type of congestion - the frequency spectrum. As such the ITU (International Telecommunication Union) has developed a regulatory framework to mitigate frequency interference between spacecraft operating in the on-orbit environment. The following sections review these guidelines that form the basis of STM operational procedures.

2.7.1. Space Debris Mitigation Guidelines

Founded on the common findings and recommendations of a wide range of international and nationally recognised agencies such as NASA, DLR, JAXA, ESA, and AIAA, the IADC "Space Debris Mitigation Guidelines" provides a comprehensive reference on recommended orbital debris mitigation strategies [31]. Focusing specifically on the following aspects, the IADC aims to guide all operational phases within the orbital environment.

1. limitation of debris released during normal operations;
2. minimisation of the potential for on-orbit break-ups;
3. post-mission disposal;
4. prevention of on-orbit collisions.

whereby spacecraft operation is comprised of the following phases (as defined by IADC):

Launch Phase *"Begins when the launch vehicle is no longer in physical contact with equipment and ground installations that made its preparation and ignition possible (or when the launch vehicle is dropped from the carrier-aircraft, if any), and continues up to the end of the mission assigned to the launch vehicle."*

Mission Phase *"The phase where the spacecraft or orbital stage fulfils its mission. Begins at the end of the launch phase and ends at the beginning of the disposal phase"*

Disposal Phase *" Begins at the end of the mission phase for a spacecraft or orbital stage and ends when the space system has performed the action to reduce the hazards it poses to other spacecraft and orbital stages"*

Additionally, guidelines are also provided in regards to the End of Mission/life phase, detailing relevant pacification measures that a spacecraft shall perform after its "useful" life.

Figure 15 illustrates the IADC framework, highlighting common causes of orbital debris and recommended mitigation practices across both operational and end of mission phases. Distinction is also made between the typical categories of space debris associated with different causes. Mission-related debris, fragments and spacecraft/rocket bodies are designated yellow, red and green respectively. Table 10 provides some examples associated with each debris category.

Table 10:IADC Space debris categories, common causes and examples [154].

Main Categories	***Causes***		***Examples***
Mission-Related Objects	Objects released intentionally	General Operation	Fasteners, covers, wires
		Experimental	Needles, balls, Tethers cut after experiments
	Objects released Unintentionally	General Operation	Tether systems cut by debris or meteoroids, Objects released before retrieval to ensure safety, Liquids, Solid motor particles
On-Orbit Break Ups	Intentional destruction	Scientific/Military Experiments	Debris fragments
		Prior to re-entry (Minimise ground casualty)	
		Security Assurance of on-board devices	
	Accidental Breakup	During Mission	Debris Fragments
		Post-Mission	
	On-Orbit Collison	Catalogued/Uncatalogued Objects	Debris Fragments
Mission-terminated systems	Incorrect/Not-actioned disposal manoeuvre		Spacecraft and rocket bodies

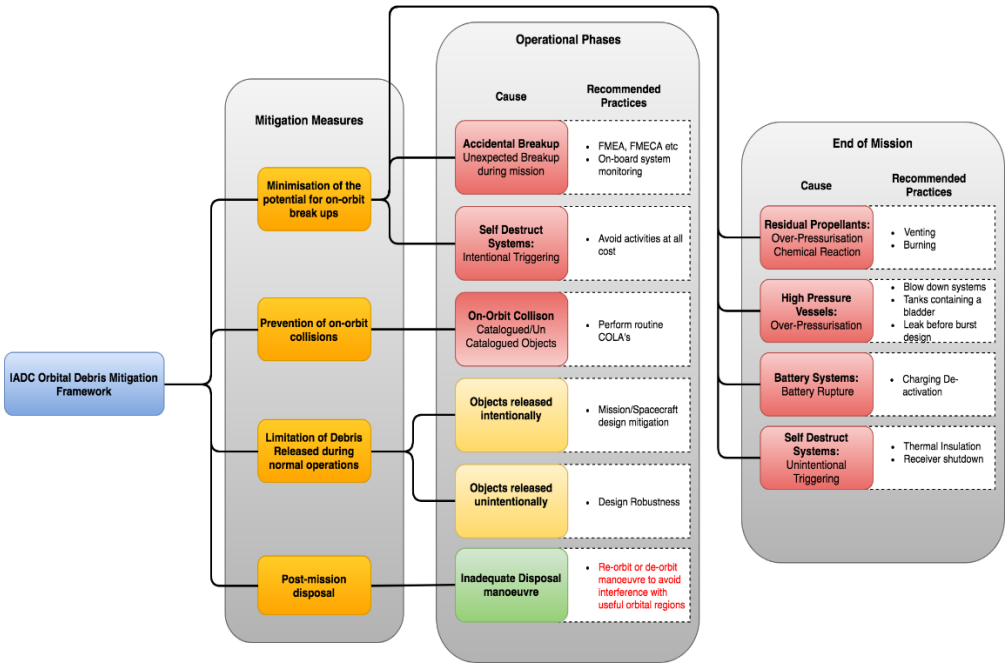

Figure 15. IADC Orbital debris mitigation framework.

2.7.2. Protected Orbital Regions

Certain orbital regimes provide unique opportunities to conduct specific operational applications. As such the number of RSOs under geosynchronous (GEO) and low earth orbit (LEO) regimes continues to grow rapidly due to their distinct advantage in providing global communication, navigation, scientific and surveillance services. While a detailed discussion regarding the GEO regime is beyond the scope of this paper due to its limited relevance for space transport applications, some key aspects including the debris mitigation provisions developed by IADC are worthy of consideration. Understandably, maintaining the useful life of both of these regions is of high priority to ensure acceptable levels of safety for space operations and the sustainability of critical global CNS infrastructure. In doing so, the IADC has designated LEO and GEO-protected regions regarding the generation of space debris. Protected zones provide a basis for post-mission disposal operations and therefore are an inseparable component of a future STM system. Table 11 provides a spatial description of the IADC-defined LEO (A) and GEO (B) protected regions which are then shown graphically in Figure 16. In contrast, a protected Medium Earth Orbit (MEO) region has not yet been warranted due to its low spatial density and rare use as a disposal zone. Nevertheless, it is recommended that where possible MEO operators should take a collaborative approach to mitigate the generation of space debris [155]. The following sections outline the recommended disposal strategies for spacecraft operating within the LEO and GEO regions.

Table 11: Protected orbital regions as defined by IADC.

Region	***Description***
Region A: Low Earth Orbit	Spherical region that extends from the Earth's surface up to an altitude of 2000 km
Region B: Geosynchronous Region	A segment of the spherical shell defined by the following: Altitude Bounds = Geostationary altitude (Z_{GEO}) ± 200km within -15° ≤ latitude ≤ +15° Z_{GEO} = 35786 km

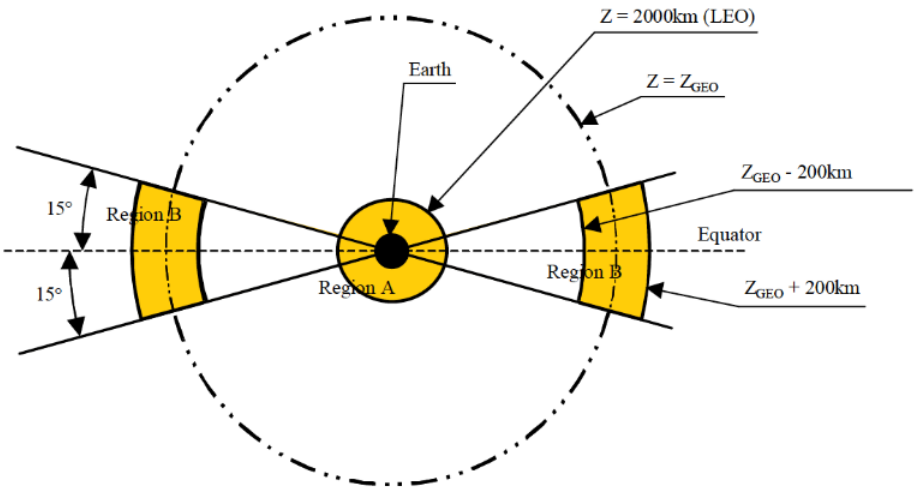

Figure 16. Overview of LEO and GEO-protected regions as per IADC. [154].

2.7.2.1. Geosynchronous Disposal Guidelines

The IADC states the following for mission-terminated spacecraft operating in the GEO-protected region [31]:

"*Spacecraft that have terminated their mission should be manoeuvred far enough away from GEO so as not to cause interference with spacecraft or orbital stage still in geostationary orbit. The manoeuvre should place the spacecraft in an orbit that remains above the GEO-protected region."*

Studies conducted by the IADC have found effective post-mission GEO disposal manoeuvres can be conducted by fulfilling two specific conditions [31]. The first of these conditions is a minimum increase in perigee altitude of:

$$235\ \text{km} + (1000 \cdot C_{SRP} \cdot \frac{A}{m}) \tag{42}$$

Where 235 km corresponds to the sum of the upper altitude of the GEO-protected region (200km) and the compensation required for altitude reduction due to lunisolar and geopotential perturbations (35km). C_{SRP}, $\frac{A}{m}$ is the solar radiation pressure coefficient and aspect area to dry mass ratio respectively. The second condition is a re-orbit eccentricity that satisfies the following:

- An eccentricity ≤ 0.003, or
- An eccentricity vector is pointed so that the longitude of periapsis, ϖ, is pointed towards the winter or summer solstice. i.e.

$$\varpi = \omega + \Omega \approx 90° \text{ or } 270° \tag{43}$$

Where ω is the argument of periapsis and Ω is the longitude of the ascending node. The implementation of these requirements will result in the space vehicle not re-entering the protected zone over 40 years. Under the assumption that a spacecraft

meets the minimum perigee altitude (condition 1), the graph shows that an operator may need only to consider the direction of the vector if the value of eccentricity (of the re-orbit) is above the prescribed value of 0.003. In the case of small eccentricities, the IADC states that a smaller increase in perigee may be chosen if a sun-pointing vector is chosen due to the diminishing effect solar radiation pressure will have on perigee height variation. Nevertheless, the IADC states that for all re-orbit strategies, it is highly advantageous to carry out further simulation studies to assess manoeuvre suitability. This is especially the case when eccentricity values > 0.003 are chosen due to the increased sensitivity between the pointing angle and successful post-mission disposal.

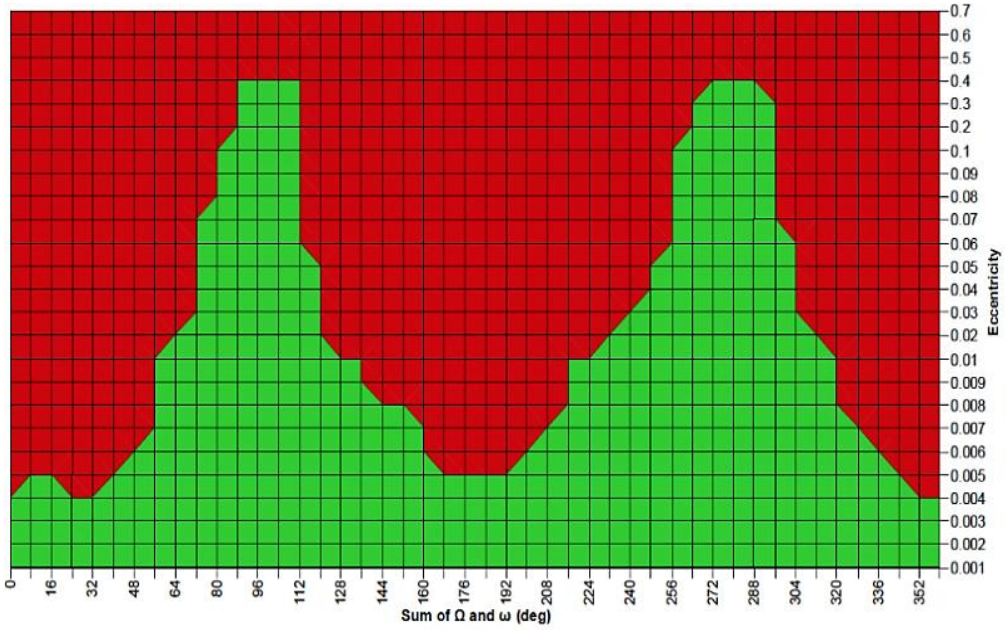

Figure 17: Combinations of Eccentricity Vector directions and Values that will cause spacecraft to re-enter GEO protected zones (red) [154].

2.7.2.2. Low Earth Orbit Disposal Guidelines

To maintain a balance between increased collision risk associated with extended post-mission life and the substantial costs associated with reducing it, the IADC recommends the following guidelines:

Post-mission lifetime should be limited to 25 years for any spacecraft that passes through or has the potential to interfere with the LEO region.

Although direct post mission re-entry would be the most effective method in reducing LEO traffic and satisfying the above, it is by far the least efficient as it imposes a significant weight fraction penalty on spacecraft mission design. As such the exploitation of natural orbital perturbations is suggested as the primary mechanism to enforce eventual re-entry and ideally complete burnup.

Table 12: Propellant requirements for 25-year LEO post-mission lifetime, reproduced from [154]. I_{SP}= 200 sec, A/m = 0.05 m^2/kg

Initial Circular Orbit Altitude	*Final Perigee Altitude*	*Delta Velocity*	*Mass Fraction (propellant/dry mass)*
800 km	730 km	18 m/s	0.8%
1000 km	630 km	88 m/s	4.3%
1500 km	535 km	236 m/s	11%
2000 km	495 km	349 m/s	17%

Adhering to the 25-year policy requires post-mission disposal to be fully considered in mission and spacecraft design, most notably the propellant mass fraction associated with required manoeuvres. Inversely proportional to altitude, the effectiveness of atmospheric drag to decay a space object orbit primarily depends on the final perigee of the spacecraft (after post-mission manoeuvre) and as such spacecraft operating in the outer periphery of the LEO region are imposed with heavier propellant weight penalties. Table 12 demonstrates this effect. For spacecraft that cannot perform de-orbit manoeuvres, the IADC recommends the following:

"Satellites without de-orbiting capability should not be launched to the orbits within the LEO protected region if their post-mission lifetime is greater than 25 years"

Obviously, by decreasing the altitude of post-mission spacecraft congestion in the lower altitudes of the LEO region will eventually occur. Historically this region has been populated by manned spacecraft missions, a trend that is set to grow with envisioned commercial spaceflight operations. Nonetheless, the IADC guidelines state that the collision risk associated with an increasing population of disposed spacecraft is unjustified considering current tracking and collision avoidance capabilities within the LEO region [154].

2.7.2.3. Post-Mission Disposal Compliance

Building upon the IADC guidelines, a suite of new space debris focussed standards have been published by the International Organisation for Standardisation (ISO) [32]. Consequently, identifying operational compliance with these standards is becoming an increasingly important topic of research. In particular, this research focuses on monitoring LEO & GEO operational lifecycle trends as these actions can be observed somewhat conclusively through publicly available surveillance data.

Findings from studies conducted by NASA (2012) [41] indicate a strong trend towards operational compliance with IADC guidelines with approximately 80% of end-of-mission spacecraft manoeuvring into GEO disposal orbits over the 2001-2010 period. Moreover, a 2014 ESA/European Space Operation Centre (ESOC) study [42] reaffirms these findings identifying that only approximately 10% of spacecraft are left abandoned, and 2/3 of disposal manoeuvres that are conducted are in full

compliance with IADC guidelines. Nonetheless, there has been a shift towards the use of inclined GEO orbits due to the reduced propellant requirement associated with East-West station keeping [41], introducing higher relative velocities and subsequently an increased collision probability [156]. Additionally, highly inclined spacecraft such as the Chinese Beidou (55 degrees) and U.S Sirius, (65 degrees) operate a significant portion of their mission well outside the currently designated GEO protected regions.

In contrast, IADC compliance in the LEO region is more concerning. A 2014 study conducted by ESA [42] found that less than 50% of end-of-life (EOL) spacecraft (post-mission) *without* active de-orbit capabilities were under an orbital regime that would naturally decay within 25 years. Similarly, less than 50% of spacecraft *with* active de-orbit capability meet the post-mission lifetime criteria through either active or natural deorbit means. Upper stages left In LEO are the most compliant with approximately 75% meeting the 25-year criteria. In all cases, natural decay due to orbital perturbations was identified as by far the most common mechanism in meeting the 25-year criteria. Nevertheless, when considering the densely occupied areas between 800 and 1100 km altitude, successful implementation of the 25-year strategy cannot solely rely on natural perturbations. As such the study recommends that considerably more effort is required from future EOL spacecraft residing within higher LEO altitudes to perform post-mission disposal manoeuvres to ensure operational sustainability of the LEO region [42].

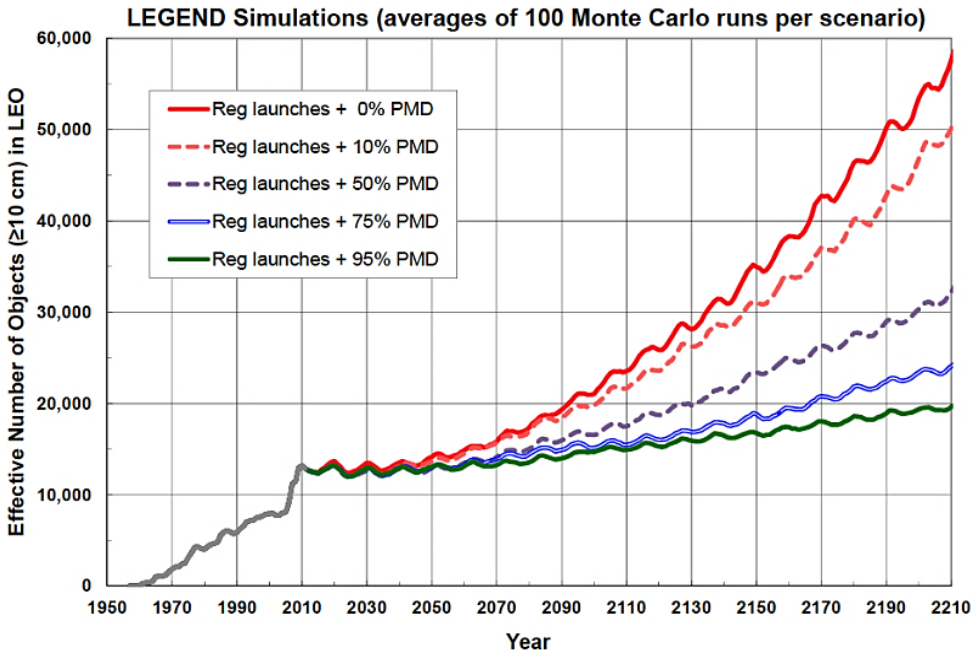

Figure 18. Predicted LEO orbital debris evolution at various PMD compliance levels [43].

Providing an updated view of the IADC guidelines first formulated in the 1990s, a study undertaken by NASA in 2013 [43] also highlights concerns with the LEO

operational environment. Using predictive analytics in the form of Monte Carlo simulations of NASA's state-of-the-art orbital debris evolutionary tool LEGEND (LEO-to-GEO ENvironment Debris model), the study aims to identify the growth of the LEO population under varying levels of IADC 25-year post-mission disposal (PMD) compliance. When considering the case of 95% PMD compliance, the study found that the average LEO debris population increase is limited to 54% over 200 years, with a collision occurring on average every 4.4 years [43]. However, when bearing in mind PMD compliance values reported by recent studies [42], 50% provides a realistic, if not, the best-case representation of current operational compliance. Under this assumption, the debris growth rate is estimated at an alarming rate of 150% over the next 200 years with collisions occurring every 2.6 years. The results from this study highlight two critical points. Firstly, PMD can be an effective tool in reducing the growth of orbital debris, if and only if there is a dramatic shift towards increased operational compliance levels. Secondly, current PMD operations can only reduce the growth rate of LEO debris, whereas the total number would still increase in most scenarios, calling for novel active debris removal techniques to be urgently developed targeting the LEO environment [43].

2.7.3. International Telecommunication Union

The International Telecommunication Union (ITU) is a sub-agency of the United Nations aimed at preserving the operational sustainability of satellite-based communication infrastructure. As described by the ITU, "radio frequencies and orbital slots are limited natural resources that must be used rationally, efficiently and economically". In favour of interference-free orbital slots and radio frequencies, the ITU has developed a complex framework to promote safe and secure satellite operations. All civilian spacecraft are required to be registered with the ITU which is achieved through either a "first come – first served" or an "a priori" scheme [157]. In the former case, a request is made by the spacecraft operator that outlines the volume of orbit and spectrum resources required to satisfy their *actual* operational requirements [158]. Allocation and coordination of spacecraft orbit/spectrum activities are then performed with the aim of efficient integration into the current orbital environment. Alternatively, the "a priori" approach is intended to optimise *planned* orbital position and frequency allotment to reduce future congestion most commonly in the GEO region. The reservation of orbit/spectrum resources also ensures "equitable access" to all countries. This approach is particularly significant for developing countries that currently do not have the means to exploit space-based assets [158].

2.7.4. Standard 321-07: Common Risk Criteria Standards for National Test Ranges

With 1% of probability of fatality per flight [159], spaceflight has shown to be an inherently dangerous undertaking. This risk does not only apply to the people aboard the spacecraft, but to the general public also, with one-quarter of all failures occurring during the first stages of operation [160]. To curb the risk associated with space flight, Standard 321-07, "Common Risk Criteria Standards for National Test Ranges" provided by the Range Commanders Council outlines the requirements and guidelines to provide adequate levels of safety during all flight phases, and as such is treated by the US Federal Aviation Administration (FAA) as the principal resource for space flight operation risk management [161]. The following section provides a top-level description of important definitions and the risk management criteria outlined in Standard 321-07 [33-35].

Standard 321-07 identifies the following "at risk" categories during space vehicle operations:

1. manned spacecraft
2. active satellites
3. general public
4. non-mission aircraft criteria
5. mission-essential aircraft
6. non-mission ship

Each category is assigned an allowable level of "risk", expressed in terms of individual probability of individual casualty or fatality (public), collision (manned spacecraft and active satellites), or impact (non-mission and mission-essential aircraft and ships) occurring for any single mission (Table 13)

Table 13: Standard 321-07 Risk Criteria

Category	*Max Acceptable*	*Undesired Event*
1. Manned Spacecraft	1E-7	Individual Probability of Collision
	Ellipsoidal Miss Distance of 200km in track and 50x50km Cross Track and Radial	
	Spherical Miss Distance 200km	Collision
2. Active Satellites	1E-4	Individual Probability of Collision
	Ellipsoidal Miss Distance of 25km in track and 7x7km Cross Track and Radial	Collision
	Spherical Miss Distance 25km	Collision

3. General Public	1E-6	Individual Probability of Casualty
	1E-7	Individual Probability of Fatality
4. Non-Mission Aircraft	1E-7	Probability of Impact
5. Mission-Ess. Aircraft	1E-6	Probability of Impact
6. Non-Mission Ship	1E-5	Probability of Impact

Excluding manned spacecraft and active satellite categories, the maximum acceptable risk associated with the undesired event is fundamentally based on debris field dispersion – simply, the probability of casualties and or fatalities from debris due to the spacecraft undergoing a planned or unplanned catastrophic failure at any point in the mission.

Understandably, to quantify this risk, additional assessments must be carried out. These include (but are not limited to) modelling space vehicle breakup, debris distribution, and impact probability within the atmospheric environment (As discussed in 2.4.1.3). In contrast, the undesired events associated with manned spacecraft and active satellites are aimed at reducing the risk within the orbital environment. Similarly, manned spacecraft (including those on route too or in support of manned missions) and active satellites are bound by "miss-distances" as well and the maximum probability of impact of 1E-7 with any other spacecraft or orbital debris is 1mm or greater. [33-35] Hence, accurate orbital insertion and comprehensive situational awareness of the space environment are crucial in conforming to the acceptable limits.

The Risk Criteria specified in Table 13 are calculated on a "per mission" basis, i.e., total risk over all flight phases, naturally imposing highly stringent requirements on the space vehicle. However, if certain conditions are met, separate risk budgets can be applied to each phase of flight. To explore this concept further it is necessary to outline the following definitions [34]:

Beginning of Flight *"Flight begins at a time in which a launch vehicle normally or inadvertently lifts off from a launch platform. Lift-off occurs with any motion of the launch vehicle concerning the launch platform"*

Beginning of Mission Risks *"The beginning of mission risks may not always start at the beginning of flight phases, depending on the nature of the spacecraft"*

End of Flight for Expendable Launch Systems *"ELV end of flight occurs when orbital insertion is completed. Orbital insertion takes place when a launch vehicle achieves an orbital state or when its drag-corrected instantaneous impact point leaves the earth without intending to re-establish on the earth before entry, and thrust has been discontinued"*

End of Flight Involving Re-entry *"RLV end of flight commences at the point of payload deployment, thus ending the "launch phase" of the RLV mission. Re-entry is defined as the event occurring when a spacecraft or other object comes back into the sensible atmosphere after going to higher altitudes, or the actions involved in this event"*

If a "decision point" exists between each distinct phase of flight, and where all the following conditions are met, separate risk budgets can be applied for each phase of flight:

1. The Vehicle has sufficient controllability to allow operational options that could reduce the risk posed by a subsequent phase (or phases) significantly.
2. The decision as to whether or how to proceed with a subsequent phase is based on a risk assessment that is conducted or validated just before each phase of flight.
3. The risk assessment for subsequent phases is made or validated using updated vehicle status and updated predictions of flight conditions

Nonetheless, a risk assessment undertaken previously can be considered valid if the assumptions made closely follow the current conditions of the mission. Further, the use of separate risk budgets is increasingly legitimate if the various flight phases pose hazards to distinctly different population groups [34].

2.7.5. Meeting Space Vehicle Operation-Risk Criteria

Understandably, meeting the requirements associated with the various “at risk” categories mandates the implementation of phase-specific procedures. i.e., the operational procedures put in place for categories 3, 4, 5, and 6 are bound to the physical limitations of the launch and re-entry phases. Conversely, categories 1, and 2 (manned spacecraft, active satellites) are bound by the confines of the orbital environment discussed in 2.4.3. The following sections provide insight into current operational procedures to meet the risk criteria, in addition to promising Air Traffic Flow Management (ATFM) concepts and research initiatives that aim to optimise the design and handling of space operation-related hazards.

2.7.5.1. Launch and Re-entry Operations

At present, the integration of space traffic into traditional airspace is being treated with a somewhat ad hoc approach. Temporary Flight Restrictions (TFR) and Special Use Airspace (SUA) are issued through Notice to Air Mans (NOTAMS), resulting in exaggerated sections of airspace segregated from traditional atmospheric traffic during launch and re-entry operations. Considering the low frequency and remote locations of current spacecraft operations, the existing approach safely separates traditional air traffic from space vehicles with minimal impact on traditional air traffic flow.

Improvements to the current segregation methods could be achieved through the implementation of the Flexible Use of Airspace (FUA) Concept during space operations [162]. Developed by EUROCONTROL in the 1990s, the FUA concept moves away from designating airspace as either "civil" or "military" airspace but considering it as one continuum and allocated according to user requirements. In the

context of space operations, this would increase the flexibility of SUA restrictions by only temporarily closing sections of airspace sectors that pose a hazard.

2.7.5.2. ATM / Space Operation Integration Concepts

Figure 19 illustrates an excerpt of an aeronautical chart, where the exclusion zone in the airspace surrounding the US Kennedy Space Center is represented. When considering the projected demand of future space operations [163], the static, inflexible and over-conservative nature of current airspace sector closure methods severely limits future applicability. As such new strategies are being developed to appropriately size the hazard area, including Space Transition Corridors (STC) and 4 Dimensional Compact Envelopes (4DCE).

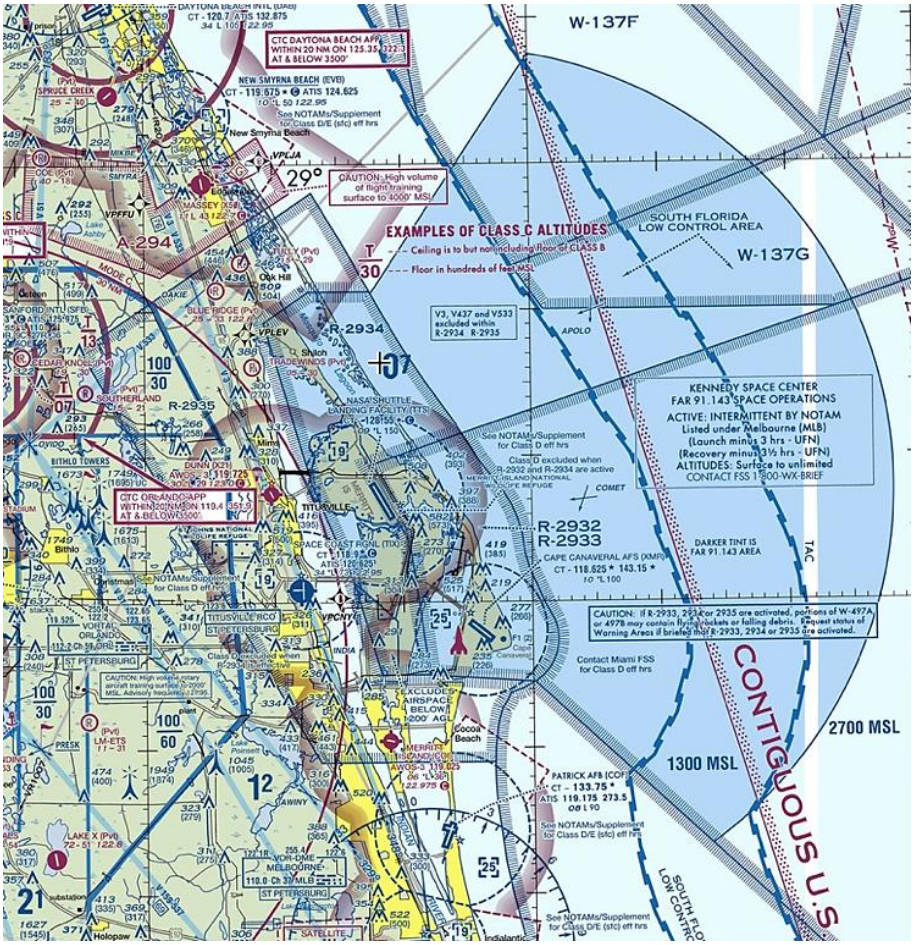

Figure 19: Detail of aeronautical chart depicting the exclusion zone around Kennedy Space Centre during Spacecraft Launch [164].

Space Transition Corridors (STC) is a concept developed by NASA to facilitate the growing demand for future space launches while simultaneously reducing the overall impact launch and re-entry operations have on the affected airspace. In contrast to the current method of space and atmospheric traffic segregation where exaggerated

portions of airspace are cordoned off during launch and re-entry phases, the STC concepts focus on employing three spatial (length, width, azimuth) and two temporal parameters (duration and midpoint of the airspace closure time window) to create a "transition" corridor [165]. This approach has been used in sub-orbital trajectory simulations of SpaceShipTwo [166]. Unlike current airspace segregation methods, the bounds of the transition corridor are defined to equal the acceptable risk during an off-nominal event (Standard 321-07). However, like current segregation methods, the restricted airspace (transition corridor) remains static throughout the entire flight phase, limiting its viability for next-generation spacecraft-integrated air traffic operations. Proposed by Stanford University Aerospace Design Lab, 4 Dimensional Compact Envelopes are based on individual probabilistics of nominal spacecraft conditions during launch and the re-entry phases adhering to the maximum acceptable risk outlined in Standard 321-07 [36, 167]. By knowing the nominal trajectory, debris catalogue, and probability of failure distribution of the spacecraft, 4D Compact Envelopes enforce only the closure of airspace that is at risk at each epoch [37]. By appropriately sizing and timing the hazard area 4D envelopes offer an elegant solution in safeguarding spacecraft operations from traditional air traffic in contrast to current airspace segregation methods. This concept is depicted in Figure 20. Moreover, simulations using NASA's Future ATM Concepts Evaluations Tool (FACET) demonstrate that 4D Envelopes present little to no impact on traditional traffic during launch and re-entry procedures [36, 37].

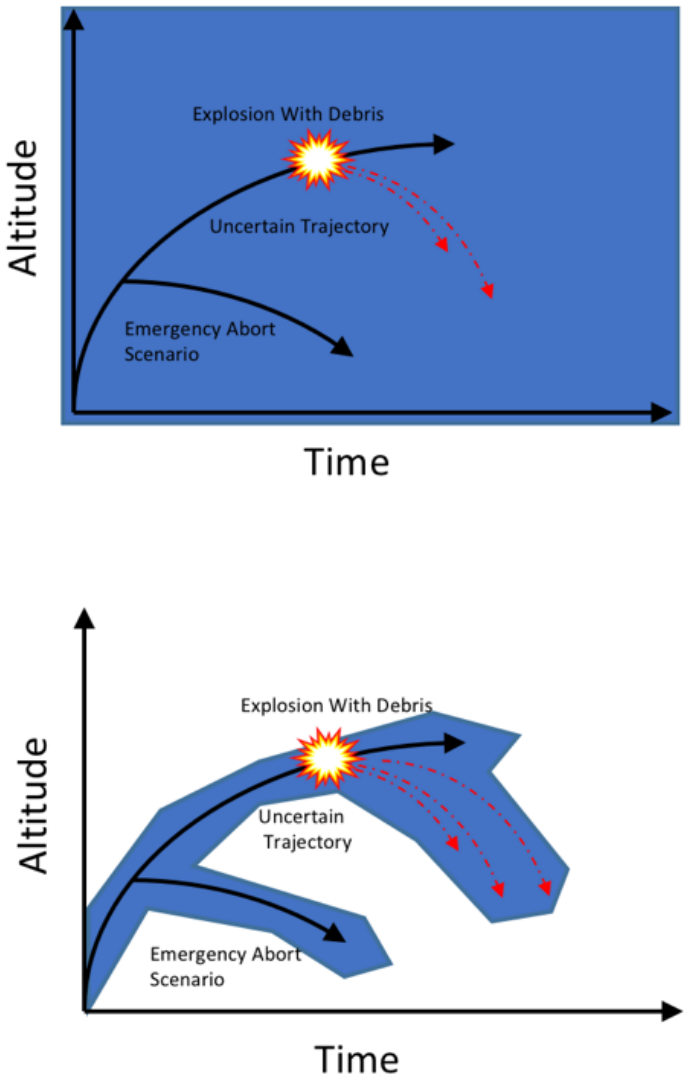

Figure 20: 4-Dimensional Compact Envelopes (bottom) vs Current Airspace Segregation Methods (top). [37].

In practice, advanced tools that spatially and temporally optimise hazard volumes will require space vehicles to transmit accurate and timely TSPI information, requiring high-performance global CNS and interoperability between all parties – an assumption that is in-line with the envisioned CNS+A enabled SWIM/TBO environment. This will also allow emerging TBO-based ATFM techniques such as *dynamic sectorisation* to become applicable. As the name implies, the dynamic sectorisation concept introduces the capability of real-time airspace sector morphing with the aim of better-exploiting airspace capacity and increasing efficiency while reducing the operator's workload. The underlying approach is that the airspace structure adapts to future traffic flow which is inherently more predictable in the TBO environment. Based upon the current ATC sector requirement of a right prism layout, automatic two-dimensional sectorisation algorithms have demonstrated their capability of supporting real-time sector re-design, however, significant issues lie in the disruptive changes that neighbouring sectors often undergo when these methods are used. An alternative approach that aims to mitigate the unfamiliarity of operators

to ATC sector changes is to introduce “Splitting and Merging” functionality, depicted in Figure 21. Emerging research is showing, on the other hand, that an optimal control formulation based on Eulerian flow theory allows realising a 2D plus time (2D+T) sector morphing to accommodate envisioned spatiotemporal shifts in traffic density (demand) [38]. Employing dynamic sectorisation concepts alongside advanced hazard volume tools like 4D compact envelopes has the potential to further increase spacecraft integration efficiency within the atmospheric domain [162, 168]

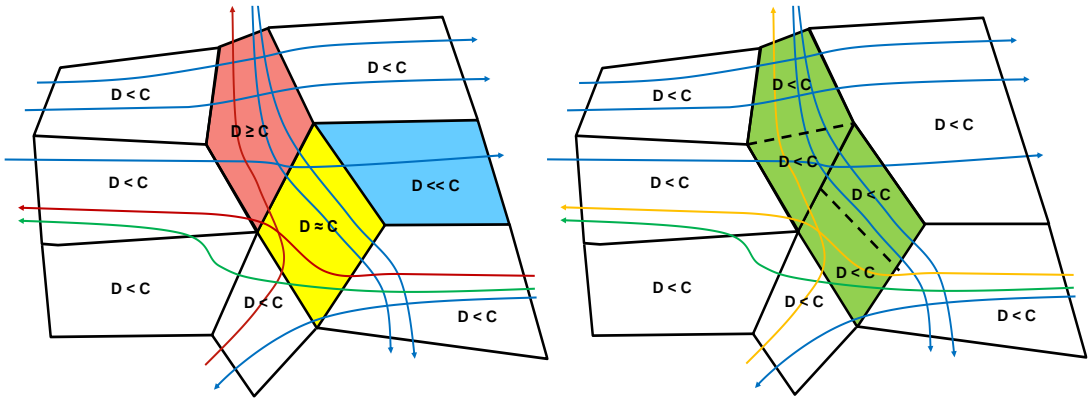

Figure 21: Sector splitting and merging – airspace demand and capacity (D, C) before and after (left, right) sector re-design.

2.7.6. On-Orbit Collision Avoidance

Due to the non-cooperative nature of space debris, an inherently higher threat exists between a spacecraft-debris pair as a collision with space objects 10 cm or larger has the potential to cause widespread damage. As a consequence, novel methods have been proposed for the capture and/or removal of space debris. However, due to the considerable operational and technical challenges associated with these methods, a single piece of debris is yet to be removed from orbit [169]. Until these methods reach operational maturity, performing evasive manoeuvres is the single most important technique in managing the risk associated with space object collision [40]. Formerly (as first used by the Space Shuttle orbiter), the strategy adopted to reduce the risk of on-orbit collisions was to manoeuvre whenever an “intruding” object violated a 5×2×2km volume centred on the orbiter. This approach required the orbiter to expend 11 to 14kg of propellant on average to avoid a potential collision, eventually making this approach over-conservative and operationally inadequate. Increasing research in the field of on-orbit deconfliction confirmed that significant operational advantages could be achieved if the uncertainty in a space object's position were considered when generating a “keep out” volume [170]. Specifically, this allowed state vector errors to be represented as a covariance ellipsoid centred on the object's nominal position [44]. This concept has led to what is now commonly known as a Space Object Collision Analysis (COLA). COLAs are routinely

performed by spacecraft operators to characterise potential on-orbit collision generally either in terms of the miss distance between orbiting objects or in a statistical nature expressed as a probability of collision.

2.7.6.1. Modelling Approach

In modelling a spacecraft collision scenario the following assumptions are typically made in the literature [50, 171]:

1. Position uncertainty can be described by a 3D Gaussian distribution
2. The target and risk object move along straight lines at constant velocities.
3. The uncertainties in space object velocities can be neglected.
4. The target and risk object position uncertainties are Gaussian and non-correlated, therefore the covariance matrixes of both objects can be summed.
5. The position uncertainties during the encounter are constant, with corresponding covariances as at the time of closest approach.
6. The space object size can be expressed as the sum of both radii

Figure 22 displays the 3-dimensional collision condition, where a "collision tube" (of the sum of both spacecraft radii) is formed through the covariance ellipsoid. Figure 23, on the other hand, depicts the two-dimensional encounter plane view. The magnitude of ellipsoid inflation is user-defined, but corresponds to an 8-sigma distribution to provide 99.999999% position assurance.

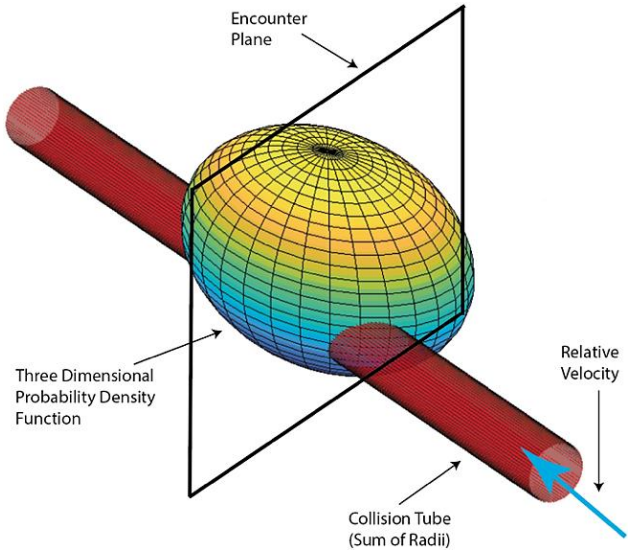

Figure 22: 3-Dimensional encounter [172].

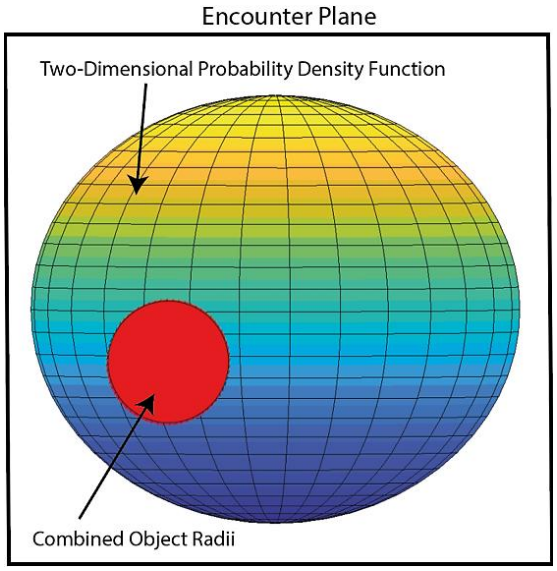

Figure 23: 2-Dimensional encounter plane [172].

Evaluating the encounter probability can become a cumbersome task due to its high dependency on the complex dynamics of each space object and the general inability to evaluate a 3-dimensional integral of any closed-form formula [50]. However, it can be shown that the probability of collision may be reduced to a two-dimensional integral within the combined radii on the plane perpendicular to the relative velocity at the time of closest approach [172]. This is known as the short-term encounter model. The short-term encounter model is used to describe a collision scenario within the LEO environment where the typical encounter geometry of two space objects is characterised by high relative velocities and the period of encounter is in the order of seconds. Mathematically, the short-term condition is expressed as the following double integral:

$$P = \frac{1}{2\,\pi\,\sigma_x\,\sigma_y}\int_{-OBJ}^{OBJ}\int_{-\sqrt{OBJ^2-x^2}}^{\sqrt{OBJ^2-x^2}} \cdot \exp\left[-\frac{1}{2}\left[\left(\frac{x-x_m}{\sigma_x}\right)^2+\left(\frac{y-y_m}{\sigma_y}\right)^2\right]\right] dy\,c \quad (44)$$

Where OBJ represents the combined object radii, x_m and y_m are the respective miss distance components, and σ_x σ_y are the corresponding standard deviations.

Multiple schemes have been developed to compute the two-dimensional collision probability integral, taking both numerical (Foster [45], developed for NASA ISS & Shuttle operations, Patera [44], used by Aerospace Corporation's Collision Vision Tool and Satellite Orbit Analysis Program (SOAP) [46], Alfano [47], used by Analytical Graphics STK) and analytical (Chan [48], used by Analytical Graphics STK, Garcia [50, 173]) approaches. Comparative studies undertaken have provided further insight into these methods in terms of their validity, accuracy [172] and speed [174]. In any case, analytical methods demonstrate much higher performance in terms of computational speed but with decreased accuracy (however acceptable for practical purposes), whereas numerical methods provide the contrary. The method chosen by the user (i.e. accuracy vs time) should be driven by the specifics of the

potential collision scenario in hand which extends from the planning to the operational phase of spacecraft coordination. [44-48, 50, 173]

2.7.6.2. Eliminating Assumptions in Collision Avoidance Analysis

As stated, the general approach outlined above is limited in that the assumptions made are only applicable to assessing the short-term encounter. This assumption is generally appropriate when considering LEO as the relative motion between the two space objects can be assumed linear and positional errors are zero-mean, uncorrelated, Gaussian and constant during the encounter [175]. However when considering the case of Geosynchronous orbits, where the relative velocity between a spacecraft pair is significantly lower than what is observed in LEO, and is now appropriately measured in the order of meters per second. The encounter region may now potentially extend up to 24 hours and therefore the direction & magnitude of the relative velocity and combined covariance ellipsoid cannot be considered constant [48]. To account for the non-linear dynamics of the described scenario, a reformation of the overall approach is required to compute the collision probability. Alfano [175] provides a comprehensive review of the techniques that can be employed to account for non-linear encounters. Each approach follows an underlying principle of dividing the encounter into specific finite linear regions (small discs, elongated discs, parallelepipeds) which when summed provide a total collision probability for the extended encounter.

As previously defined, the collision tube is assumed to be the combined hard-body radius of both the primary and secondary spacecraft, assuming constant altitude throughout the encounter. However, depending on the miss-distance and values of covariance of the given confliction, the need to consider the actual, 'complex' geometry of both objects may become apparent. Pulido et al [176] demonstrate this case when covariance values are small (high orbital accuracy) compared to object size. To overcome the assumption of a combined hard-body radius, one method proposed is to calculate the Minkowski sum of the two objects [173, 177].

2.7.7. On-Orbit Collision Assessment Issues

As discussed, on-orbit collision analysis is achieved through the propagation of orbital observational data where a collision warning is issued if separation criteria or collision thresholds are breached. Proportional to the growth of orbital traffic, collision warnings are continually being treated as false alarms due to the high amount of uncertainty associated with current observational data [9]. The February 10th 2009 (UTC) collision between the Iridium-33 and Cosmos 251 spacecraft, provides insight into the shortfalls of current SSA capabilities [178]. Figure 24 displays the predicted minimum range at the time of the Iridium-Cosmos collision in terms of the closest:

1. Conjunction (within the report)

2. Iridium Constellation conjunctions
3. Iridium 33 specific conjunctions
4. Iridium 33/Cosmos 2251 conjunctions

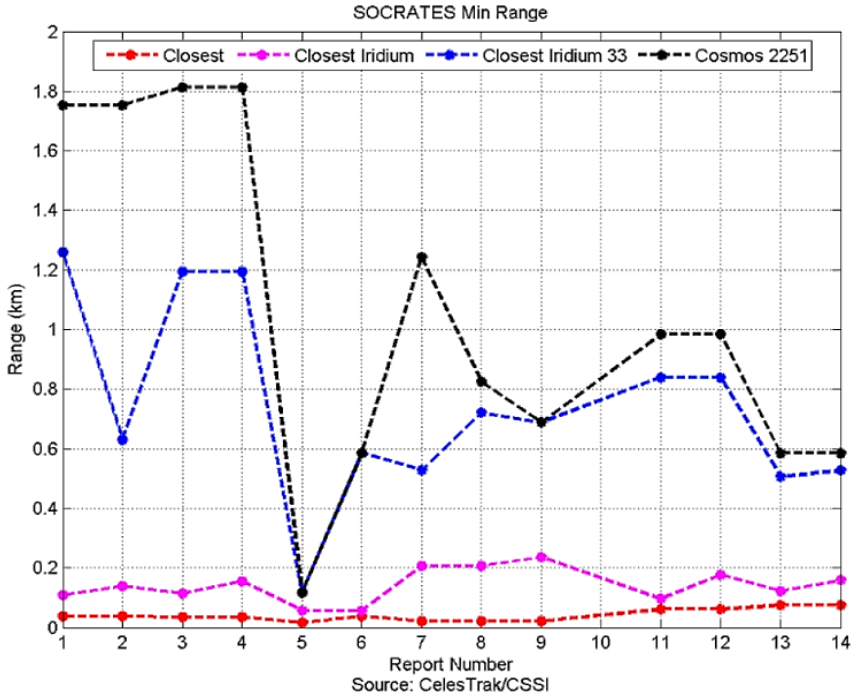

Figure 24: Predicted Close Approaches of Iridium [179] Constellation, Iridium 33 and Cosmos 2251 from February 4th - 10th, 2009 [179].

Each of the 14 reports (2 per day) was generated by the Centre for Space Standards and Innovation (CSSI) conjunction assessment tool, SOCRATES [180] spanning from the 4th-10th February. Close approaches between Cosmos and Iridium 33 were estimated in reports 4, 5, ranging from 117m to respectively, however, the problem therein lies that the identified conjunctions between Cosmos/Iridium 33 were consistently overshadowed by the smaller miss distances estimated in all other considered scenarios.

When interpreted by the SOCRATES ranking system (a service provided by the SOCRATES tool to identify the more probable collision scenarios), the Iridium 33/Cosmos collision is effectively concealed from operator awareness due to the greater risk of conjunctions between other objects during that period, including other Iridium spacecraft. This is displayed in Figure 25 where the Cosmos/Iridium conjunction rank is shown in terms of the total number of collision warnings, against all other iridium-related conjunctions and any other Iridium-33 collision warning (within each specified report).

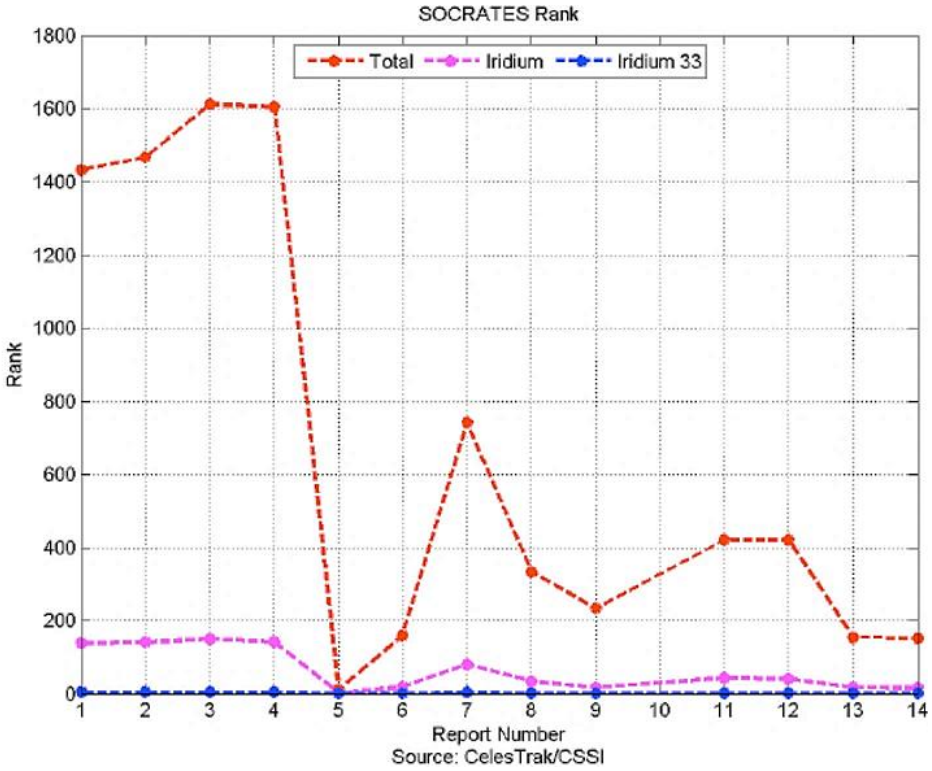

Figure 25. Ranking of Predicted Close Approaches of Iridium, Iridium 33 and Cosmos 2251 from February 4th - 10th, 2009 [179]

Nonetheless, the statistical inconsistencies observed in both Figure 24 and Figure 25 that effectively led to the Iridium 33/ Cosmos collision are no fault of the SOCRATES tool but due to unreliable orbital observation data. In this instance, orbital data was provided by the North American Aerospace Defence (NORAD) in the form of a Two Line Element Set (TLE). TLEs are a specific data format used regularly by satellite operators to assess potential collision scenarios and conduct orbital manoeuvres if required. TLEs contain the following object-related information at a given epoch:

- Line Number
- Satellite Number
- Classification
- International Designator
- Epoch
- Mean Motion Derivative(s)
- Drag Term
- Element Set number
- Checksum
- Inclination
- Right Ascension of the ascending node
- Argument of Perigee
- Mean Motion
- Revolution Number

TLE data structure is specific to the use of simplified perturbation models SGP4, and SDP4, where the former is tailored for near-space object propagation (orbital period of less than 225 minutes) and the latter for deep space (orbital period greater than or

equal to 225 minutes). Detailed information on the algorithms employed in special perturbation models can be found in [181]. TLEs are generated from measurements made by the US Space Surveillance Network (SSN), a global network of predominantly ground-based optical and radar (mechanical and phased array) sensors. The SSN plays a critical role in tracking and cataloguing non-cooperative RSOs, however, the required accuracy for credible collision detection cannot be reached using TLEs and associated propagators exclusively [179, 182, 183].

Despite well-documented shortfalls, the advantage of providing a compact, easily attainable form of RSO information has led to TLEs' widespread use in the satellite industry. As such there have been continued research efforts to improve the fidelity of TLEs and related applications [184]. Nonetheless, a lack of meaningful covariance and planned manoeuvre information introduces significant uncertainty (particularly for long-term predictions), and as such it is best practice amongst satellite operators to treat assessments purely based on TLEs as a coarse indication of collision risk initiating what is known as the "two-tier" model. To overcome the shortfalls of TLE data, the satellite operator will then commonly use the precise owner-operator ephemeris data, and in the case of a non-cooperative collision scenario, special perturbation (SP) information of the "intruding object" can be requested when possible from the Joint Space Operations Centre (JSpOC). As a result of more precise orbital data, the additional screening will then reduce the severity of the collision risk and if necessary, more pertinent manoeuvre(s) can be performed [185].

In exchange for more authoritative data comes the additional delays associated with the manual collection process and the reduced effectiveness of any actionable protocol that may be required. Because of this, the risk associated with a two-tier process is still seen as overall insufficient and an ineffective way to perform collision screening [182]. In the interest of improved SSA capabilities, considerable progress has been made for more effective data-sharing methods amongst the satellite community. SOCRATES-GEO, an automated conjunction analysis process offered by the Centre for Space Standards and Innovation (CSSI), generates conjunction analysis using owner-operator-supplied ephemeris data. Originally developed in mind for GEO operations, SOCRATES-GEO has now extended to the LEO environment with a total of 286 operational satellites (as of 2010) sharing precise ephemeris data [186].

A user-centric approach to data collection reduces the frequency of a two-tier model as user-cooperative conjunction scenarios can be managed with a single forecast. Sharing precise satellite ephemeris data is under the discretion of the owner-operator, as in some circumstances disclosing planned manoeuvre information may compromise the mission of the spacecraft. Nonetheless, complete ephemeris data must be shared whenever possible due to the implications that almost certain intermediate manoeuvres have on collision assessment validity[186]. In any case, there is a consensus that a sensor and mission-centric information-sharing scheme akin to the current services provided by CSSI will be an essential aspect of an STM system.

Of utmost importance will be the *transparency* and *traceability* of all available data - An increase alone will not solve the current issue of RSO ambiguity and COLA subjectivity, confidence building measurements must also be readily available to all operators. This would include (but not be limited to); the amount, type and performance of the sensor(s), chosen coordinate systems and time (including clock accuracy), and where possible physical states and parameters, functional characteristics and mission objectives. To effectively distribute this information[187, 188] and support the use of big data analytics, standardised RSO ontologies have been proposed [187, 188]. Further, using high-definition photometry and the principles of biometrics, novel methods are being developed that aim to uniquely characterise RSOs in the form of "fingerprints" and progress towards a **Unique** Resident Space Object (URSO) database [189].

Through the realisation of the above elements, the traditional SSA approach can be elevated to *"Encompass all elements in the space environment as well as operators and human decision-makers and ground-based elements that affect space activities"* [9]. Which in practical terms will allow *"The actionable knowledge required to predict, avoid, deter, operate through, recover from, and/or attribute cause to the loss and/or degradation of space capabilities and services"* [9]. This vision encapsulates a concept that is described as Space Domain Awareness (SDA).

In essence, an SDA approach to a future STM system will enable intelligent decision-making tools to ensure timely, reliable threat and hazard identification and prediction within the orbital domain [9] [178, 190] while also harmonising the interfaces between the atmospheric and near-space environment in the context of safe and unsegregated future space transport operations.

2.8. Conclusions

Significant progress is being made toward advancing spacecraft platforms that redefine both atmospheric and orbital operations. In the atmospheric domain, new entrants, such as point-to-point spacecraft, highlight the necessity for global, interconnected spaceport networks to support mixed-flow Trajectory-Based Operations (TBO). The operational concepts of Space Transition Corridors (STC) and Four-Dimensional Compact Envelopes (4DCE) leverage advanced Communication, Navigation, and Surveillance/Air Traffic Management (CNS+A) systems, optimising hazard volumes and enhancing airspace efficiency. However, these concepts remain nascent, necessitating further research in Air Traffic Management/Space Traffic Management (ATM/STM) harmonisation and spacecraft-focused Air Traffic Flow Management (ATFM) techniques. Additionally, there is a pressing need to address the environmental sustainability of atmospheric operations, especially regarding emissions and noise from spacecraft.

In the on-orbit phase, the avoidance and mitigation of collisions remain critical challenges for STM. Efforts to enhance compliance with post-mission disposal

standards in Low-Earth Orbit (LEO) and Geostationary Orbit (GEO) are pivotal to ensuring the long-term sustainability of space operations. Current collision prediction methodologies, although industry standard, are hindered by unreliable observational data and false alarms. This underscores the need for cyber-physical STM architectures leveraging advanced networking, computing, and control technologies to ensure data fidelity and reliable space object tracking. Additionally, there is an urgent need to establish a globally recognised STM code of conduct and certification standards for CNS+A systems operating above FL600 to fully integrate and harmonise the ATM/STM network.

The transition from Space Situational Awareness (SSA) to Space Domain Awareness (SDA) is being driven by technological advancements within Communication Navigation and Surveillance (CNS) systems, facilitated by next-generation mission architectures supported by Distributed Satellite Systems (DSS). DSS architectures provide resilient, cost-effective, and scalable solutions for space-based space surveillance (SBSS) by shifting from monolithic spacecraft to constellations of smaller, specialised platforms. These architectures, which include constellations, swarms, clusters, and federated systems, are well-suited to meet evolving STM goals by reducing the collective uncertainty through persistent monitoring of Resident Space Objects (RSOs).

DSS enhances Space-Based Space Surveillance (SBSS) by addressing limitations of monolithic systems, such as coverage gaps and timeliness of observations. Constellations of DSS-equipped satellites, operating with advanced optical sensors like CMOS and photon-counting technologies, offer unprecedented precision in tracking RSOs, including smaller debris (<10 cm). These systems mitigate the challenges of atmospheric aberrations and extend surveillance capabilities beyond the limitations of ground-based sensors. The DSS paradigm plays a pivotal role in reducing uncertainties around RSO trajectories and mitigating collision risks, thereby contributing to a safer orbital environment.

The increasing levels of autonomy of DSS systems further reinforce their role in achieving SDA. Leveraging Goal-Based Operations (GBO) principles, DSS platforms can autonomously re-plan and execute missions based on sensed environmental conditions. This shift in autonomy levels—from ground-controlled operations to goal-oriented mission execution—enables DSS systems to dynamically respond to evolving mission requirements. By integrating advanced onboard functions, such as autonomous mission planning and trajectory optimisation (orbit and attitude), DSS architectures provide the reactive and adaptive capabilities necessary to adapt to the increasing cyber-physical threats while supporting future safe and sustainable STM.

In conclusion, DSS architectures exemplify the technological drivers facilitating the paradigm shift from SSA to SDA. By providing a robust, scalable, and autonomous approach to space surveillance, DSS enhances situational awareness, optimises collision avoidance strategies, and supports the development of an integrated, global

STM infrastructure. These advancements will be instrumental in addressing the growing challenges of STM, ensuring operational sustainability, and mitigating the cascading risks posed by increasing RSO densities.

Chapter 3

Intelligent Distributed Satellite Systems for Space Traffic Management

Building on the key findings from Chapter 2, the STM goals are expanded through functional analysis, forming the basis for the operational framework of intelligent distributed satellite systems. This analysis is applied to a representative DSS space-based surveillance mission, where the functions are mapped to autonomy elements. This process highlights the integration of intelligent technologies, such as orbit and attitude optimization, mission planning, and decision support at the supervisory level.

Each autonomy element is then introduced within the operational architecture of intelligent distributed satellite systems, framed within a hierarchical control structure. This structure consists of multiple feedback control loops that manage satellite operations and ensure system goals are met within operational constraints. At each level, specific satellite functions are controlled, enabling organized decision-making and the achievement of both short-term and long-term mission objectives. The hierarchical control structure serves as the reference architecture for the proposed system and sets the foundation for the remaining chapters of the thesis.

The contents of this chapter have been published in part in the following:

- **S. Hilton**, A. Gardi, R. Sabatini, N. Ezer, and S. Desai, "Human-machine system design for autonomous distributed satellite operations," in 2020 AIAA/IEEE 39th Digital Avionics Systems Conference (DASC), 2020: IEEE, pp. 1-8

3.1. Functional Definition

Safety and sustainability are the fundamental drivers behind an effective Space Traffic Management System. As space activities continue to grow, the management of orbital traffic becomes increasingly crucial to prevent collisions and ensure the long-term viability of space operations. Central to this effort is the mitigation of space debris, which poses a significant threat to both active satellites and future space missions. By developing systems that track and manage debris, implement debris removal technologies, and establish guidelines for debris creation, we can minimize the risk of catastrophic collisions and ensure a sustainable orbital environment.

In achieving this goal, the development of a global CNS (Communication, Navigation, and Surveillance) infrastructure is paramount, particularly through the implementation of Distributed Satellite Systems. These systems, especially when enhanced by responsive, space-based surveillance capabilities, can provide timely tracking and

monitoring of objects in orbit. This distributed network of satellites would enable a more accurate collision prediction, through reduction of collective RSO uncertainty, and support coordinated debris mitigation efforts on a global scale.

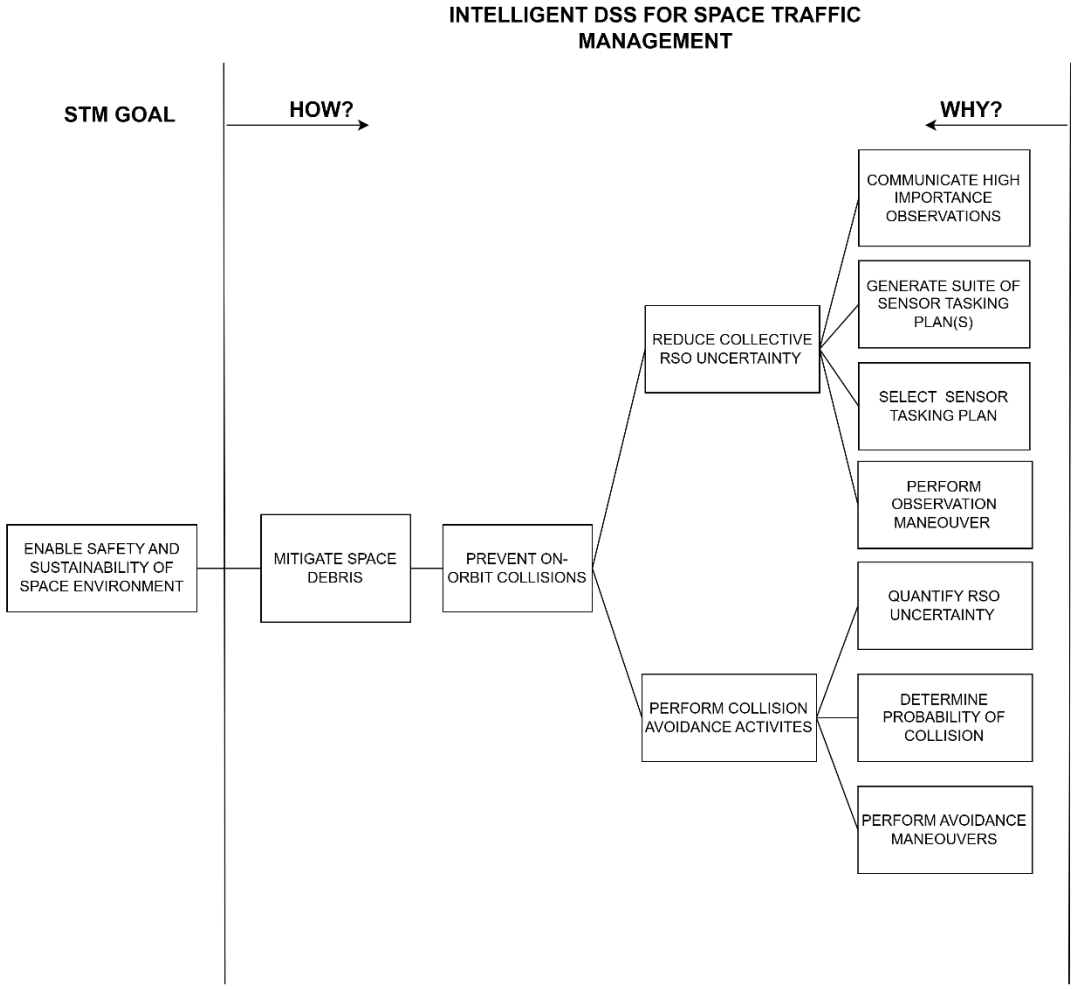

Figure 26 Functional Breakdown from Central STM Goal through to key system functions.

To further this objective, a functional breakdown is performed based on the central goal of enabling the safety and sustainability of the space environment**.** This involves analysing the How/Why logical relationships between key system elements to identify the essential functions required for effective Space Traffic Management (STM). The analysis identifies key functions such as communicating high-priority observations**,** generating and selecting optimal sensor tasking plans, performing observation manoeuvres, quantifying RSO uncertainty, determining the probability of collision and executing avoidance manoeuvres. These functions form the foundation of the space-based surveillance system architecture. In the next section, these functions are mapped to specific platform system elements, to illustrate how each function contributes to achieving the broader STM and debris mitigation goals.

3.1.1. Function to System Element

In Figure 27, each function is mapped to specific system elements within the Distributed Satellite System architecture, where a description of each system element is then provided.

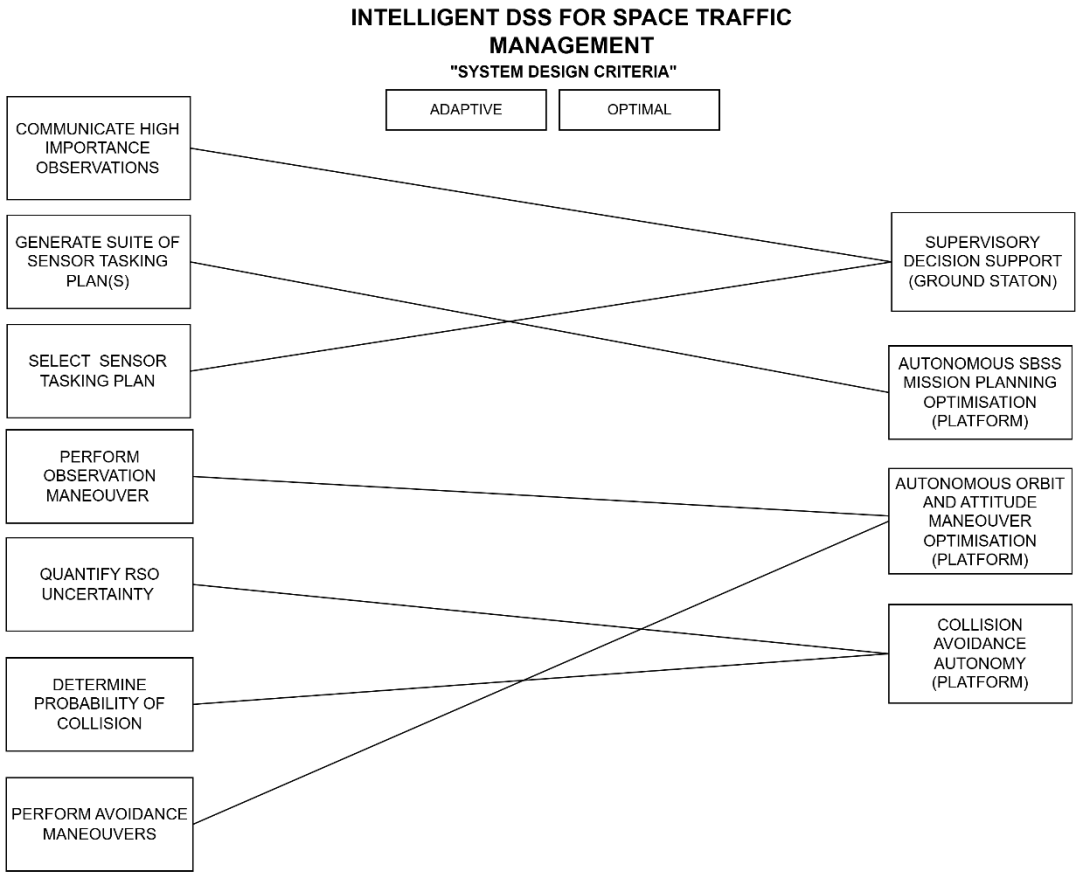

Figure 27 Function to System Allocation

3.1.1.1. SBSS Mission Planning Autonomy

Spacecraft mission planning serves as a primary function in the planning and scheduling of dynamic space systems, requiring the careful coordination and modelling of all contributing assets and their specific constraints. When considering the scope of both ground and space-based systems required to successfully perform a space-based surveillance mission, the planning problem becomes multi-dimensional and highly complex. This complexity is amplified by the need to coordinate heterogeneous sensor networks, each with unique capabilities and constraints. Distributed Satellite Systems performing Space-based surveillance rely on various sensors—such as optical, radar, and infrared—which must be tasked effectively to monitor objects in space. The detectability of each object is time-dependent,

influenced by the observation geometry and object-specific properties such as attitude motion, shape, and surface reflectivity.[191]

To manage these complexities, Mission Planning Systems (MPS) are developed to optimally achieve surveillance goals. This requires careful coordination of different sensors, each operating under a distinct set of constraints. At the heart of these systems lies a generalized timeline, represented as a Sequence of Events (SoE), which ensures that sensor tasking is conflict-free and as optimal as possible for the specific mission objectives.

The first in the mission planning process is pass prediction, which is necessary to populate the sensor's field of view (FoV). In this context, pass prediction refers to the process of determining the trajectory and time window during which a sensor will have line-of-sight access to a target object. This involves modelling the motion of both the sensor platform (such as a satellite) and the target object, accounting for orbital perturbations, and predicting when and where the sensor will be in position to observe the target. These predicted passes are then used to populate the sensor's FoV, ensuring that each sensor is tasked to observe the relevant objects at the appropriate times.

The general input to the planning process includes the pass prediction, which provides a time- and location-specific estimate of when a sensor will be in position to observe a target. Once the pass prediction data is generated, the FoV is discretised into a grid of possible viewing directions, considering the sensor's field of view (FoV) and specific constraints such as minimum elevation angles. These viewing directions, referred to as grid fields, are defined relative to the chosen coordinate system for each sensor. The output of this process is a suite of Sequence of Events (SoE), which specifies the optimal viewing directions for each sensor at specific times, ensuring that the mission's surveillance objectives are achieved optimally while accommodating all sensor constraints and operational limitations.

3.1.1.2. Collision Avoidance Autonomy

Due to the non-cooperative nature of space debris, an inherently higher threat exists between a spacecraft-debris pair as a collision with space objects 10 cm or larger has the potential to cause widespread damage. Consequently, novel methods have been proposed for the capture and/or removal of space debris. However, due to the considerable operational and technical challenges associated with these methods, performing evasive manoeuvres is the single most important technique in managing the risk associated with space object collision [40]

Onboard collision avoidance autonomy is a critical capability to support this approach, as it enables the spacecraft to react dynamically to the threat of collision with space debris. The key functions of this autonomy involve quantifying both the current and future position uncertainty of the spacecraft and the intruder (debris), allowing for the estimation of their trajectories. This uncertainty of each is then used to evaluate the probability of a conjunction**.** With this information, an appropriate orbital manoeuvre

reduces the probability of collision to an acceptable level, helping to ensure the safety and operational continuity of the spacecraft in an increasingly RSO filled environment.

3.1.1.3. Orbit and Attitude Manoeuvre Optimisation Autonomy

Trajectory optimization plays a crucial role in ensuring the efficient and safe operation of spacecraft by generating trajectories that satisfy mission-specific criteria while adhering to prescribed initial and final conditions. It serves as a key supporting function for mission planning autonomy and collision avoidance, enabling dynamic and responsive spacecraft operations in complex orbital environments. By enabling the identification of optimal manoeuvres under time and energy constraints, trajectory optimization contributes to the spacecraft's ability to mitigate collision risks, efficiently execute orbital adjustments, and support task coordination in distributed satellite systems. These capabilities are increasingly essential in ensuring the safety and continuity of spacecraft operations amidst the growing complexity of space traffic and mission demands.

3.1.1.1. Supervisory Level Decision Support

A common misconception is that the more "autonomous" a spacecraft becomes (i.e. functions usually performed on the ground transferred to spacecraft) that these roles will disappear from the ground segment. The classical ground segment processes shift from a lower level (command sequence) to a higher supervisory role (autonomous goal-based operations). This predicted evolution of ground station roles is further described as pertaining to the following high-level operator tasks [192]:

Commanding and monitoring of on-board autonomous (decisional) processes (Monitoring and Control (M&C) of on-board orbit control, onboard mission planning, FDIR)

On-ground automation, that participates in the global system autonomy (automation of Telemetry/Telecommands Loop, mission plan assessment and update)

Support to on-board autonomous processes. Enhanced autonomy induces a new repartition of processes between Ground and Space. Nonetheless, on-board autonomy should rely on high-level supervisory decisions of the ground operator.

Together these tasks form the expected supervisory nature of next-generation DSS operations. The third point highlights the capability of the ground station to verify the autonomous outputs on board to maintain mission assurance. This places an explainability criteria on the autonomous onboard processes, to allow the operator to verify system autonomy outputs and provide guidance when required. In the context of GBO, the operator must be able to express their intentions in the form of goals, interpret the effect of these intentions and include mechanisms to recognize and understand when these intentions are being performed, and more importantly when

they are not [91, 193-195]. This includes interdiction measures to initiate lower-level commands when required [196]. This requires the design and development of supporting Human-Machine Systems (HMS) for decision support, a topic that is now gaining well-deserved attention in the space sector [197-201] due to the mission and safety-critical tasks performed by space systems

3.2. System Architectural Definition

3.2.1. Approach

A control structure is a system model composed of feedback control loops that work together to manage and regulate processes. In this context, a hierarchical control structure is utilized, as defined in the STPA (Systems-Theoretic Process Analysis) framework[202]. This structure consists of multiple control loops arranged in a hierarchy, where each level is responsible for specific decisions and actions to achieve defined goals while enforcing constraints on the overall system behaviour.

A hierarchical control structure typically comprises at least five distinct types of elements:

1. **Controllers**: Entities that make decisions based on their process models to achieve specific goals, determining the necessary control actions to regulate the system's behaviour.
2. **Control Actions**: Commands or adjustments issued by controllers to influence the behaviour of controlled processes, guiding the system toward desired states.
3. **Feedback**: Information provided from the controlled processes back to the controllers, is crucial for assessing the effectiveness of control actions and updating the controllers' process models.
4. **Other Inputs and Outputs**: Signals or data that do not fall under control actions or feedback, representing various influences or interactions between components necessary for comprehensive operation.
5. **Controlled Processes**: The systems or entities being regulated by the controllers, which receive control actions and generate feedback that informs the controllers about their current state.

In this hierarchical framework, controllers operate by providing control actions to manage processes while maintaining feedback mechanisms to observe and adjust these processes. Each controller has an internal process model that reflects its understanding of the controlled process, incorporating beliefs about system dynamics and environmental factors. These process models are updated through feedback, ensuring that controllers can make informed decisions.

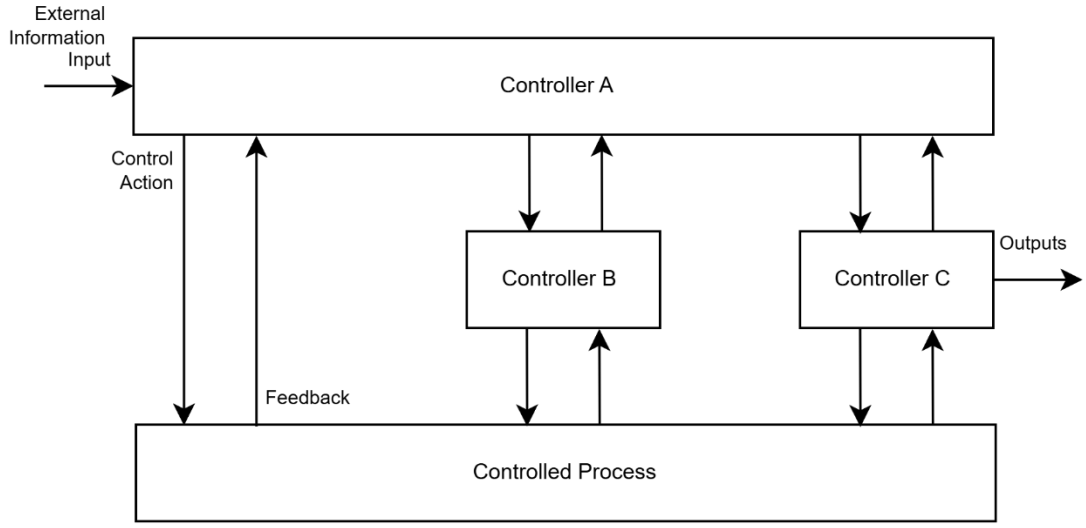

Figure 28. Generic Hierarchical Control Structure. Adapted from [203]

The vertical axis of the hierarchical control structure signifies levels of control and authority, with higher-level controllers overseeing the actions of lower-level entities. Each entity at a given level has authority over those directly beneath it and is subject to control from those above.

3.2.2. Definition

In the following section, each defined system element is placed within DSS architecture, detailing their interactions in the context of a Space-Based Surveillance System (SBSS) mission. The interactions between each element are described through the following operational loops, each with specific control and feedback elements (see Figure 2):

3.2.2.1. Supervisory Loop

The outermost loop defines the interaction between ground and space segments. It provides high-level goals and decision-making (control) to guide the emergent behaviour (feedback) of the DSS. Fundamentally, this relates to the interface between the supervisory-level decision support function and the DSS system. In the context of the described SBSS mission, the supervisory loop shall enable the communication of SBSS mission goals (CA1), and the ability to observe DSS autonomy outputs (FB1) and guide autonomous system behaviour through intelligent plan selection (CA2).

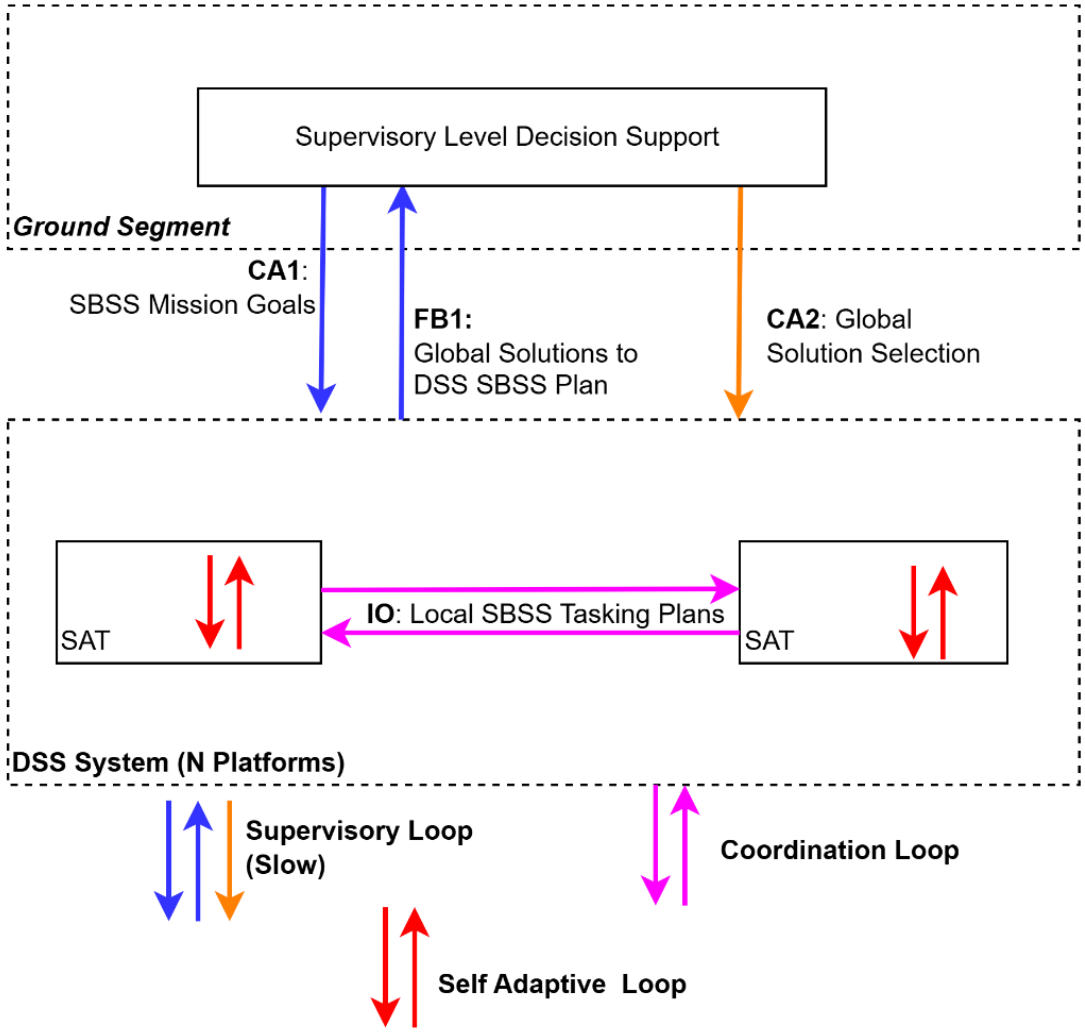

Figure 29. System Level Architecture detailing high-level interactions between the DSS System, Satellite Platforms and ground station elements

3.2.2.1. Coordination Loop

A DSS-level loop that enables intelligent coordination across the DSS. It shall provide a mechanism for the DSS platforms to coordinate key aspects of the SBSS mission to enable a globally optimal sensor tasking solution.

3.2.2.1. Self-Adaptive Loop:

A platform-level loop that enables the system to handle both internal and external environmental uncertainties and unplanned events. In the context of the SBSS mission, this includes the provision of proposed SBSS observation plans (CA3) is achieved of and the corresponding validation feedback (FB3) to validate mission planning outputs considering dynamic constraints on supporting platform systems. This high-level interaction is detailed in Figure 27.

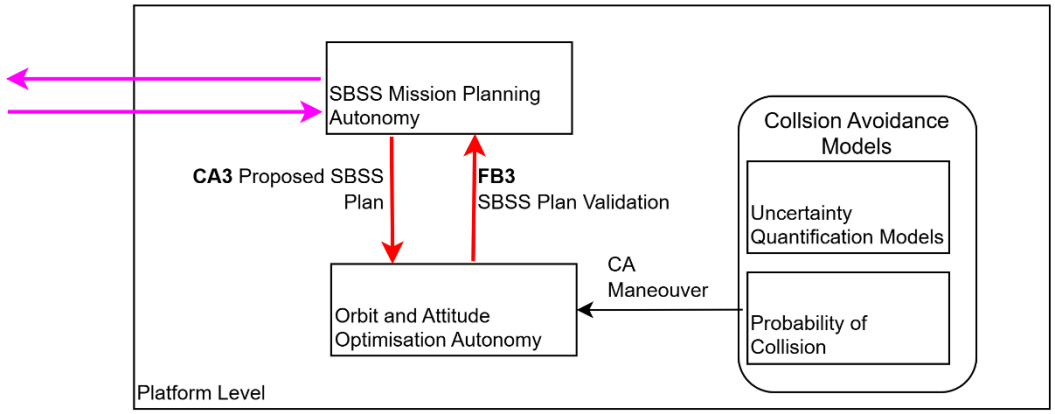

Figure 30. Platform Level Architecture detailing high-level interactions between Mission Planning and Orbit/Attitude trajectory optimisation.

For each defined operational loop, Table 14 describes each control and corresponding feedback and interaction with the intelligent mission planning module and the corresponding chapter where the detailed design of these interfaces and interactions is presented and simulated through verification case studies.

Table 14. High-Level DSS Operational Loops and their corresponding interactions

	Control		**Feedback**		
Operational Loop	ID	Name/Description	ID	Name/Description	**Thesis Chapter**
Supervisory	CA1	**Mission Goals**: A control action provided from the ground segment that influences the tasking behaviour of the DSS SBSS mission planning autonomy	FB1	**Global Solution Feedback:** Feedback provided to the ground station that contains a set of global solutions to the SBSS mission planning problem	**6**
	CA2	**Global Solution Selection:** A control action provided from the ground segment that selects a solution provided by FB1			**7**
Self-Adaptive	CA3	**Proposed Attitude Plan:** A control action provided from each local mission planning autonomy output to a local attitude optimisation engine.	FB3	**Attitude Plan Validation:** Feedback on attitude constraint violation provided to the Mission Planning autonomy from the local attitude optimisation autonomy	**6**
Coordination	**IO**	**Local SBSS Tasking Plan:** A broadcasted output from each satellite to the DSS network to coordinate RSO observation allocation			**6**

3.3. Conclusions

This chapter has addressed Objective 2 by developing an integrated operational framework for Intelligent Distributed Satellite Systems (DSS), incorporating - system autonomy to support Space Traffic Management (STM). Building on the foundational STM goals established in Chapter 2, the framework formulates these goals into specific autonomy functions for DSS, supporting both the safety and sustainability of space operations.

Through functional analysis, key DSS autonomy elements were identified, including mission planning, collision avoidance, and orbit/attitude optimization. These functions were integrated into a hierarchical control structure comprising multi-layered feedback loops for task coordination, supervisory control and self-adaptive behaviour. This structure enables clear interaction between intelligent system behaviour to be studied in this thesis.

The operational framework defined in this chapter serves as the reference architecture for the remainder of the thesis where verifications and simulation studies of the framework's components and behavioural interactions are presented in subsequent chapters.

Chapter 4

Trajectory Optimisation Model Design

This chapter outlines the development of key trajectory optimization models for both attitude and orbital manoeuvres, which form the foundation for collision avoidance, autonomy, and attitude reorientation in space-based surveillance missions. The relevant dynamic equations are introduced, including perturbation factors that influence spacecraft motion. Using a particle swarm optimization (PSO) approach, trajectory optimization is implemented, incorporating optimality criteria and constraints for both orbit and attitude control.

The contents of this chapter have been published in part in the following:

- E. Lagona, **S. Hilton**, A. Afful, A. Gardi, and R. Sabatini, "Autonomous Trajectory Optimisation for Intelligent Satellite Systems and Space Traffic Management," *Acta Astronautica*, 01/25 2022, doi: 10.1016/j.actaastro.2022.01.027.

4.1. Trajectory Optimisation Approaches

Spacecraft trajectory involves generating a trajectory that satisfies specific criteria while meeting prescribed initial and final conditions [204]. Typically, trajectory optimization problems (TOPs) are formulated in state-space representation, making them equivalent to optimal control problems (OCPs). To solve these problems numerically, the infinite-dimensional OCP must first be transformed into a finite-dimensional version, a process that can be accomplished using either direct or indirect methods [205, 206].

In direct methods, the continuous TOP is discretised into a finite number of intervals. While this approach guarantees a feasible solution, it does not necessarily ensure that the solution is optimal[205]. Direct methods integrate the discretised system dynamics either explicitly or implicitly, converting the TOP into a non-linear programming (NLP) problem by generating non-linear constraint equations that the parameters attempt to satisfy[207].

A particularly efficient class of direct methods for solving OCPs in aerospace trajectory optimization are pseudospectral methods (PM)*)* [204, 208, 209]. PMs have been successfully applied to a variety of problems, including optimized manoeuvres [208-211] problems. These methods use an efficient, and sometimes adaptive, discretization of the problem domain into intervals where state and control variables are parametrized with polynomials of appropriate order. This transformation converts the TOP into an NLP, which is then solved using gradient-based search algorithms. However, gradient-based algorithms face a key limitation: the requirement for initial guesses that are sufficiently close to the globally optimal solution, especially in non-

convex search spaces. Without a good initial guess, the optimization routine may be slow to converge or may settle at a suboptimal local solution.

An alternative to gradient-based methods is the class of metaheuristic optimization algorithms, which include evolutionary algorithms (EAs) such as genetic algorithms (GAs), particle swarm optimization (PSO), and various insect colony algorithms. Unlike gradient-based methods, metaheuristics are not limited by local convergence issues, making them suitable for solving highly nonlinear problems. These algorithms adapt dynamically to explore the solution space effectively and can be categorized into single-solution and population-based methods [212, 213]. Population-based methods, such as EAs, are particularly well-suited for trajectory optimization. However, they also have limitations: they are stochastic, producing potentially different results in different runs, and their convergence performance is not formally guaranteed. Nevertheless, EAs have been successfully applied to many space domain problems, including rendezvous, interplanetary transfers, and orbit adjustments [204].

As the viability of onboard, real-time trajectory optimization depends heavily on computational time and cost. Particle Swarm Optimization (PSO) is chosen in this study as the primary numerical optimizer for orbital and attitude manoeuvres due to its ability to provide time-constrained (responsive) solutions. PSO offers robust global convergence capabilities, adaptability to highly nonlinear problems, and strong parallelization efficiency, making it a suitable choice for onboard applications in dynamic and time-sensitive mission environments.

4.2. Model Development

This section introduces the particle swarm optimisation algorithm, all the adopted models for the spacecraft dynamics, bright object avoidance, optimality criteria and constraints and collision avoidance requirements.

4.2.1. Particle Swarm Optimisation

Introduced in 1995 by Kennedy and Eberhart [214], PSO is a metaheuristic algorithm able to reproduce a natural swarm behaviour, with markedly simple evolutionary logics. In PSO the candidate solutions to the problem are individuals in a population, and the cost function describes the quality of this solution. As in most optimisation algorithms, it is desirable to restrict the search domain size to improve the computation times. This population-based optimiser is initialized randomly using a set of possible solutions (particles), then an optimal solution is iteratively searched by then moving the particles within the problem space.

The swarm is composed by p particles representing possible solutions in the problem search space. The position of each particle advances as

$$x_{k+1}^i = x_k^i + v_{k+1}^i \tag{45}$$

Where x is the i^{th} particle position at the increment of time k and v is the velocity expressed by

$$\begin{aligned} v_{k+1}^i = v_k^i + c_1 \cdot r_1 \cdot \left(p_k^i - x_k^i\right) + \\ c_2 \cdot r_2 \cdot \left(p_k^g - x_k^i\right) \end{aligned} \tag{46}$$

p_k^i is the best position of the particle i at the time k and p_k^g is the global best position of all the particles at the time k; r_1 and r_2 are random numbers between 0 and 1, while c_1 and c_2 represent the cognitive and social scaling parameters respectively; these are equal to 2 to give a mean of 1 when multiplied by r_1 and r_2. Let us denote f_{best}^i and f_{best}^g As best fitness value for the i^{th} particle and global solution respectively. The pseudocode for PSO is provided below.

1. Initialization

Set constant $_{max}$, c_1 and c_2

Initialization of particle positions in the problem space x_0^i for p particles

Initialization of particle velocities in the problem space v_0^i for p particles

Set $k = 1$

2. Optimization

Evaluate the function value f_k^i

If $f_k^i \leq f_{best}^i$ then $f_{best}^i = f_k^i, p_k^i = x_k^i$

If $f_k^i \leq f_{best}^g$ then $f_{best}^g = f_k^i, p_k^g = x_k^i$

If the stopping criterion is satisfied go to step 3

Particle velocities are updated

Particle positions are updated

Time is updated $k = k + 1$

Go to step 2(a)

3. Termination

Due to the high computational parallelisation, efficiency and robustness of the PSO algorithm, it is possible to resort to explicit integration of the Ordinary Differential Equations (ODEs) for attitude and vehicle dynamics adopting the Dormand-Prince Runge-Kutta method, although implicit integration methods could potentially yield more efficient implementations.

4.2.2. Orbital Manoeuvre Models

In general, orbital motion models can be formulated using Gaussian variational equations based on classical orbital elements However, these models may encounter singularities, particularly when dealing with low eccentricities or inclinations where sine and cosine values approach critical points (e.g. 0, π/2, π, …) . To overcome these singularities, a new model has been developed [215, 216] that employs modified equinoctial elements (MEE). This model includes J_2 perturbation effects allowing it to account for the regression of the right ascension of the ascending node (RAAN) and the argument of perigee over time. The attitude model, on the other hand, is formulated using parametric curves, where the coefficients are optimized to achieve the optimal solution through inverse dynamics[217-219].

To avoid singularities, the set of MEE developed by Kechichian [216] is therefore adopted to solve a low-thrust earth orbit transfer.

The relationship between classical orbital elements and modified equinoctial elements can be described by the following equations:

$$\mathrm{p} = \mathrm{a}(1 - \mathrm{e}^2) \tag{47}$$

$$\mathrm{f} = \mathrm{e}\cos(\omega + \Omega) \tag{48}$$

$$\mathrm{g} = \mathrm{e}\sin(\omega + \Omega) \tag{49}$$

$$\mathrm{h} = \tan\left(\frac{\mathrm{i}}{2}\right)\cos(\Omega) \tag{50}$$

$$\mathrm{k} = \tan\left(\frac{\mathrm{i}}{2}\right)\sin(\Omega) \tag{51}$$

$$\mathrm{L} = \Omega + \omega + \nu \tag{52}$$

Where p is the semiparameter, a the semi-major axis, e orbital eccentricity, i orbital inclination, ω argument of perigee, Ω right ascension of the ascending node (RAAN), L true longitude.

The inverse relationship between classical and modified equinoctial elements is described by the following equations:

$$\mathrm{a} = \frac{\mathrm{p}}{1 - \mathrm{f}^2 - \mathrm{g}^2} \tag{53}$$

$$\mathrm{e} = \sqrt{(\mathrm{f}^2 + \mathrm{g}^2)} \tag{54}$$

$$\mathrm{i} = 2\,\mathrm{atan2}\left(\sqrt{(\mathrm{h}^2 + \mathrm{k}^2)}, 1 - \mathrm{h}^2 - \mathrm{k}^2\right) \tag{55}$$

$$\omega = \mathrm{atan2}(\mathrm{gh} - \mathrm{fk}, \mathrm{fh} + \mathrm{gk}) \tag{56}$$

$$\Omega = \mathrm{atan2}(\mathrm{k}, \mathrm{h}) \tag{57}$$

$$\nu = \mathrm{L} - \Omega - \omega \tag{58}$$

In these equations, the expression "atan2" indicates the four-quadrant inverse tangent calculation [220]. The relationship between the ECI state vector and modified equinoctial elements is

$$\mathbf{r} = \begin{bmatrix} \frac{r}{s^2}(\cos(L) + \alpha^2\cos(L) + 2hk\sin(L)) \\ \frac{r}{s^2}(\sin(L) - \alpha^2\sin(L) + 2hk\cos(L)) \\ \frac{2r}{s^2}(h\sin(L) - k\cos(L)) \end{bmatrix} \tag{59}$$

$$\mathbf{v} = \begin{bmatrix} -\frac{1}{s^2}\sqrt{\left(\frac{\mu}{p}\right)}(\sin(L) + \alpha^2\sin(L) - 2hk\cos(L) + g - 2fhk + \alpha^2 g) \\ -\frac{1}{s^2}\sqrt{\left(\frac{\mu}{p}\right)}(-\cos(L) + \alpha^2\sin(L) + 2hk\sin(L) - f + 2ghk + \alpha^2 f) \\ \frac{2}{s^2}\sqrt{\left(\frac{\mu}{p}\right)}(h\cos(L) + k\sin(L) + fh + gk) \end{bmatrix} \tag{60}$$

where

$$\alpha^2 = h^2 - k^2 \tag{61}$$

$$s^2 = 1 + h^2 + k^2 \tag{62}$$

$$r = \frac{p}{q} \tag{63}$$

$$q = 1 + f\cos(L) + g\sin(L) \tag{64}$$

The dynamic system can be described in terms of the new state variables.

$$[\mathbf{y}^T, w] = [p, f, g, h, k, L, m] \tag{65}$$

Where m is the mass of the satellite. Using the MEEs, the equations of motion are defined as

$$\dot{\mathbf{y}} = A(\mathbf{y})\boldsymbol{\Delta} + \mathbf{b} \tag{66}$$

$$\dot{w} = -T/I_{sp} \tag{67}$$

The equinoctial dynamics is defined by the matrix A, the perturbations $\boldsymbol{\Delta}$ and the vector **b**. More details for the matrix A are found in [215]. In general, the motion of the spacecraft can be described by a system of second-order ODEs

$$\ddot{\mathbf{r}} + \mu\frac{\mathbf{r}}{r^3} = \mathbf{a}_d \tag{1}$$

Her r represents the magnitude of the inertial position, and $\boldsymbol{a}_d$ denotes the disturbing acceleration. This equation is commonly referred to as the Gaussian form of the variational equations. Since the disturbing acceleration is typically small, the orbital

elements can be approximated as quasi-constant over time. In the case of low-thrust manoeuvres, the thrust applied to the spacecraft is also small and can be treated as a perturbation, incorporated into the disturbing acceleration.

When modified equinoctial elements are used, the disturbing acceleration is replaced by **Δ.** The contributions to the perturbations include effects from Earth (e.g., gravitational harmonics) and the spacecraft thrust (when applied).). $\boldsymbol{a}_d$ Is expressed in a rotating radial frame (RSW) where the principle axes are defined by

$$\mathrm{Q_r} = [\mathbf{i}_\mathrm{r} \quad \mathbf{i}_\mathrm{s} \quad \mathbf{i}_\mathrm{w}] = \left[\frac{\mathbf{r}}{|\mathbf{r}|} \quad \frac{(\mathbf{r}\times\mathbf{v})\times\mathbf{r}}{|(\mathbf{r}\times\mathbf{v})\times\mathbf{r}|} \quad \frac{(\mathbf{r}\times\ \mathbf{v})}{|(\mathbf{r}\times\ \mathbf{v})|}\right] \tag{69}$$

When the disturbing acceleration is zero, the problem becomes a two-body problem. The J_2 perturbation is modelled with the following equations:

$$\mathrm{f_r} = -\frac{3\mu \mathrm{J_2 R^2}}{2\mathrm{r^4}}\left[1 - 12\frac{(\mathrm{h\sin L - k\cos L})^2}{\mathrm{s^4}}\right] \tag{70}$$

$$\mathrm{f_s} = -\frac{12\mu \mathrm{J_2 R^2}}{2\mathrm{r^4}}\left[\frac{(\mathrm{h\sin L - k\cos L})(\mathrm{h\cos L - k\sin L})}{\mathrm{s^4}}\right] \tag{71}$$

$$\mathrm{f_w} = -\frac{6\mu \mathrm{J_2 R^2}}{2\mathrm{r^4}}\left[\frac{(\mathrm{h\sin L - k\cos L})(1 - \mathrm{k^2} - \mathrm{h^2})}{\mathrm{s^4}}\right] \tag{72}$$

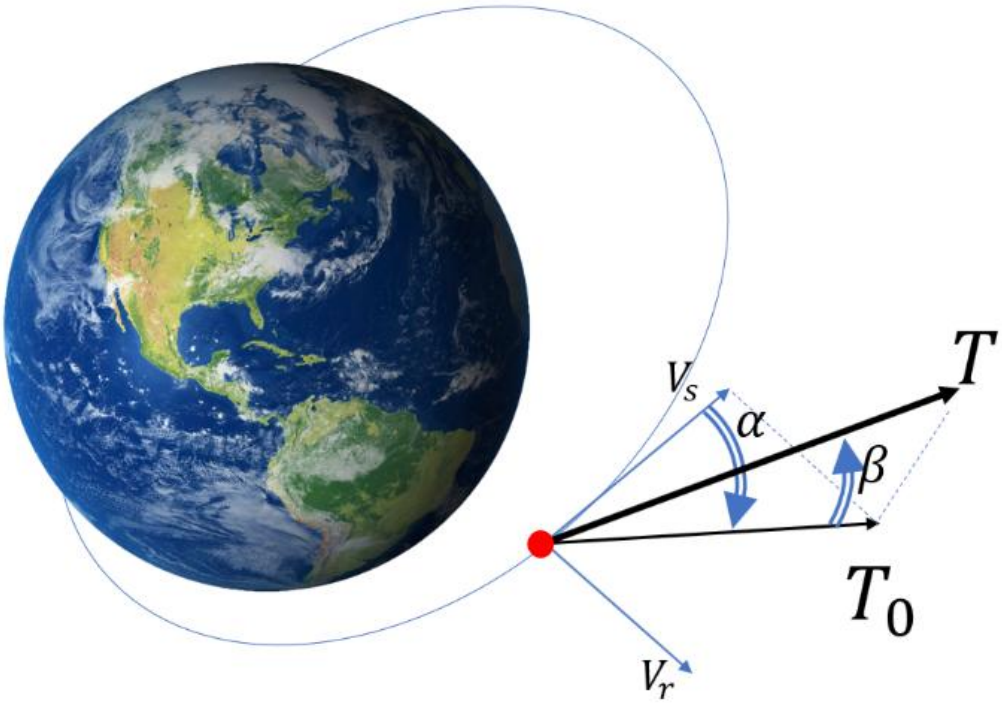

Figure 31 Thrust Vector Spherical Coordinates

The thrust is treated as a perturbation due to its relatively small magnitude.

$$\boldsymbol{\Delta} = \boldsymbol{\Delta}_{\mathbf{pert}} + \boldsymbol{\Delta}_{\mathbf{T}} \tag{73}$$

where $\boldsymbol{\Delta}_{\mathbf{pert}}$ is due to J_2, $\boldsymbol{\Delta}_{\mathbf{T}}$ is the thrust.

Thrust acceleration is represented as

$$\mathbf{a}_{\mathbf{T}} = \frac{\mathrm{T}}{\mathrm{m}}\mathbf{u} \tag{74}$$

with $\mathbf{u}$ control vector In this context, the spacecraft is assumed to provide a constant thrust rather than a constant acceleration [205], The control vector represents the direction of the applied thrust, and the thrust-to-mass ratio can be expressed as:

$$\frac{\mathrm{T}}{\mathrm{m}} = \frac{\mathrm{cn}_0}{\mathrm{c} - \mathrm{n}_0\mathrm{t}} \tag{75}$$

Where c is the effective exhaust gas velocity, n_0 the thrust-to-mass ratio at the initial time. Constant acceleration is not assumed because of the variable mass of the spacecraft during the manoeuvre.

The control time history is parameterized using shape functions, which allow the thrust profile to be flexibly adjusted over the manoeuvre duration. The thrust vector is expressed in spherical coordinates, making it possible to define the direction of the thrust using control angles. The control angles are expressed with the following polynomial shape functions:

$$\alpha(\mathrm{t}) = \mathrm{a}_0 + \sum_{\mathrm{i}=1}^{6} \mathrm{a}_\mathrm{i} \left(\frac{\mathrm{t}}{\mathrm{t}_\mathrm{f}}\right)^\mathrm{i} \tag{76}$$

$$\beta(\mathrm{t}) = \mathrm{b}_0 + \sum_{\mathrm{i}=1}^{6} \mathrm{b}_\mathrm{i} \left(\frac{\mathrm{t}}{\mathrm{t}_\mathrm{f}}\right)^\mathrm{i} \tag{77}$$

where a_i and b_i are the control parameters that PSO uses to modify the control time history. The extended form for α is as follows:

$$\alpha(\mathrm{t}) = \mathrm{a}_0 + \mathrm{a}_1\frac{\mathrm{t}}{\mathrm{t}_\mathrm{f}} + \mathrm{a}_2\left(\frac{\mathrm{t}}{\mathrm{t}_\mathrm{f}}\right)^2 + \mathrm{a}_3\left(\frac{\mathrm{t}}{\mathrm{t}_\mathrm{f}}\right)^3 + \mathrm{a}_4\left(\frac{\mathrm{t}}{\mathrm{t}_\mathrm{f}}\right)^4 + \mathrm{a}_5\left(\frac{\mathrm{t}}{\mathrm{t}_\mathrm{f}}\right)^5 + \mathrm{a}_6\left(\frac{\mathrm{t}}{\mathrm{t}_\mathrm{f}}\right)^6 \tag{78}$$

Alternative parameterizations, such as trigonometric functions, are also feasible and can sometimes provide more advantageous formulations for highly periodic functions. However, in many practical scenarios, the desired control function lacks sufficient periodicity to fully benefit from trigonometric parameterizations. As a result, polynomial parameterizations are often preferred due to their flexibility and effectiveness in capturing a wide range of non-periodic or irregular control profiles. The three components of thrust acceleration in the RSW frame are

$$\boldsymbol{a}_{T_{RSW}} = \frac{T}{m}\begin{Bmatrix}\sin\alpha\cos\beta\\ \cos\alpha\cos\beta\\ \sin\beta\end{Bmatrix} \tag{79}$$

Where the RSW frame is defined using the following unit vector approach:

$$\mathrm{M}_{\mathrm{RSW}\rightarrow\mathrm{ECI}} = [\mathbf{i}_{\mathrm{r}} \quad \mathbf{i}_{\mathrm{s}} \quad \mathbf{i}_{\mathrm{w}}] = \left[\frac{\mathbf{r}}{|\mathbf{r}|} \quad \frac{(\mathbf{r}\times\mathbf{v})\times\mathbf{r}}{|(\mathbf{r}\times\mathbf{v})\times\mathbf{r}|} \quad \frac{(\mathbf{r}\times\ \mathbf{v})}{|(\mathbf{r}\times\ \mathbf{v})|}\right] \tag{80}$$

And the transformation matrix from the RSW frame to the ECI frame.

$$\boldsymbol{u}_{T_{ECI}} = M_{RSW\rightarrow ECI}\boldsymbol{u}_{\boldsymbol{T_{RSW}}} \tag{81}$$

Due to the low altitude of the satellite, aerodynamic drag effects cannot be neglected. Within the RSW frame, the drag force is expressed as:

$$\begin{bmatrix}\Delta_{D_r}\\ \Delta_{D_s}\\ \Delta_{D_w}\end{bmatrix} = \frac{1}{2}\rho S C_D v_R \begin{bmatrix}v_r\\ v_s\\ 0\end{bmatrix} \tag{82}$$

where ρ is the atmospheric density [221, 222], S the aerodynamic reference area, C_D the drag coefficient, v_R the velocity magnitude. v_r and v_s are expressed as

$$\mathrm{v_r} = \sqrt{\frac{\mu}{\mathrm{p}}}(\mathrm{f}\sin\mathrm{L} - \mathrm{g}\cos\mathrm{L}) \tag{83}$$

$$\mathrm{v_s} = \sqrt{\frac{\mu}{\mathrm{p}}}(1 + \mathrm{f}\cos\mathrm{L} - \mathrm{g}\sin\mathrm{L}) \tag{84}$$

4.2.3. Attitude Reorientation Models

When reorienting the spacecraft's attitude, three fundamental requirements must be met: the manoeuvre should be time-optimal, the spacecraft must avoid pointing towards bright objects (e.g., the Earth or Sun) that could interfere with instrumentation performance, and the actuator torque constraints must be met. For this analysis, the fixed reference frame is the Radial-Transverse-Normal (RSW) frame, while the spacecraft's body frame is denoted as the XYZ frame.

The rotational motion dynamics are expressed as:

$$I\dot{\boldsymbol{\omega}} = T\boldsymbol{u} - \omega^{\times}I\boldsymbol{\omega} \tag{85}$$

where $\boldsymbol{u} = [u_1 \quad u_2 \quad u_3]^T$ is the control vector, I is the inertia matrix about its centre of mass in the body frame and $\omega^{\times}$ Is a skew-symmetric matrix defined as

$$\omega^{\times} = \begin{bmatrix}0 & -\omega_3 & \omega_2\\ \omega_3 & 0 & -\omega_1\\ -\omega_2 & \omega_1 & 0\end{bmatrix} \tag{86}$$

Two forbidden zones must be avoided: one delimited by a cone pointing toward the Sun and the other toward the Earth. The boresight vector of the instrument. $\boldsymbol{x}$ is s expressed in the spacecraft's body frame, while, θ s the angle between the negative radial direction $-\boldsymbol{r}$ and x. The cone angle of the forbidden zone is denoted as θ_F To ensure the boresight vector outside the forbidden zone the following inequality constraint is applied [217]:

$$-\mathbf{r}^{\mathrm{T}}\mathbf{x}' - \cos(\theta_{\mathrm{F}}) < 0 \tag{87}$$

where x' is the vector of the bright object expressed in the inertial frame, calculated as

$$\begin{bmatrix}0\\ \mathbf{x}'\end{bmatrix} = \mathbf{q} \otimes \begin{bmatrix}0\\ \mathbf{x}\end{bmatrix} \otimes \mathbf{q}^{*} \tag{88}$$

where $\boldsymbol{q}$ is the quaternion expressing the attitude with respect to the inertial frame and $\boldsymbol{q}^{*}$is the conjugate quaternion. The attitude forbidden zone constraint is therefore

$$\mathbf{q}^{\mathbf{T}}\mathrm{M}_{\mathrm{F}}\mathbf{q} < 0 \tag{89}$$

where M_F is

$$\mathrm{M}_{\mathrm{F}} = \begin{bmatrix}\mathrm{d} & \mathrm{b}^{\mathrm{T}}\\ \mathrm{b} & \mathrm{A}\end{bmatrix} \tag{90}$$

With $\mathrm{d} = -\mathbf{r}^{\mathrm{T}}\mathbf{x}' - \cos(\theta_{\mathrm{F}})$, $\mathrm{b} = \mathbf{x}' \times (-\mathbf{r})$,

$\mathrm{A} = -\mathbf{r}\mathbf{x}'^{\mathrm{T}} + \mathbf{x}'(-\mathbf{r})^{\mathrm{T}} - (-\mathbf{r}^{\mathrm{T}}\mathbf{x}' + \cos(\theta_{\mathrm{F}}))\mathrm{I}_{3\mathrm{x}3}$

In the same fashion, an attitude mandatory zone can be defined as

$$\mathbf{q}^{\mathbf{T}}\mathrm{M}_{\mathrm{M}}\mathbf{q} > \mathbf{0} \tag{91}$$

Where the matrix M_M Expressing the mandatory zone. M_M has the same form of M_F and θ_F is replaced by θ_M.

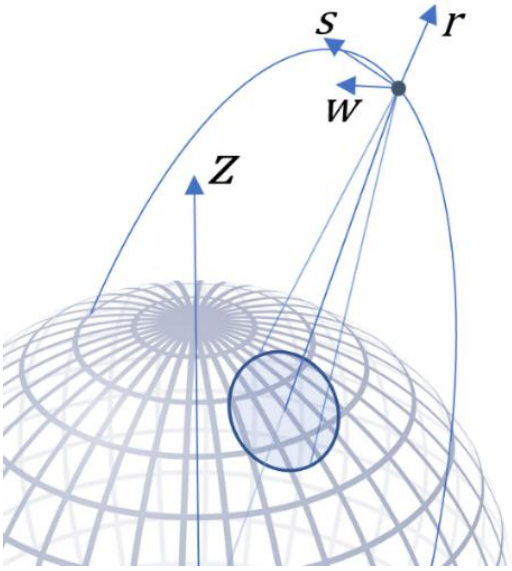

Figure 32 Forbidden Earth cone.

Given the vector $\boldsymbol{s}_{\oplus}$ In the Earth-Centered Inertial (ECI) frame, which points from the centre of the Earth toward the Sun, the vector as seen from the satellite is expressed as:

$$\mathbf{s} = \mathbf{s}_{\oplus} - \mathbf{r} \tag{93}$$

Where $\boldsymbol{r}$ is the satellite position in the ECI frame, and $\boldsymbol{s}_{\oplus}$ Is the position of the Sun, calculated from the astronomic Almanac [223].

When considering the effects of solar radiation pressure, it is essential to determine whether the satellite is in the Earth's shadow (umbra) to appropriately include or exclude these contributions. For simplicity, the shadow region is defined to encompass both the umbra and penumbra zones, assuming a solar radiation-free condition within this extended region.

The shadow region can be defined under the assumption that celestial bodies are perfectly spherical. Using this hypothesis, the Earth's shadow is modelled as a cone extending from the Earth in the direction opposite to the Sun, with its boundaries determined by the Earth's and Sun's radii and their relative positions [208].

Defining $\mathrm{d_P} = \mathrm{R_{Earth}} + 1\mathrm{AU} + \mathrm{R_{Sun}}$. The distance χ_P is

$$\chi_P = \frac{\mathrm{R_E d_P}}{\mathrm{R_E} + \mathrm{R_S}} \tag{94}$$

and the angle α_P

$$\alpha_P = \arcsin\left(\frac{\mathrm{R_E}}{\chi_P}\right) \tag{95}$$

In this study, the spacecraft position vector is considered in the ECI system. The solar unit vector is

$$\hat{\mathbf{s}} = \frac{\mathbf{s}}{|\mathbf{s}|} \tag{96}$$

Computing the projection of the spacecraft along $\hat{\mathbf{s}}$

$$\mathbf{r}_P = (\mathbf{r} \cdot \hat{\mathbf{s}})\hat{\mathbf{s}} \tag{97}$$

Where the distance between the axis of the penumbra cone and the spacecraft is then defined as

$$\boldsymbol{\delta} = \mathbf{r} - \mathbf{r}_P \tag{98}$$

and the distance between the centre of the penumbra cone axis and the penumbra termination point at the projected spacecraft location is

$$k_P = (\chi_P + |\mathbf{r}_P|) \tan \alpha_P \tag{99}$$

Two cases are now possible:

Shadow termination points are possible if $(\mathbf{r} \cdot \hat{\mathbf{s}}) < 0$. If $|\boldsymbol{\delta}| > k_P$ the spacecraft is still in sunlight

If $|\boldsymbol{\delta}| = k_P$ there are penumbra termination points and the spacecraft is in the penumbra cone if $|\boldsymbol{\delta}| < k_P$

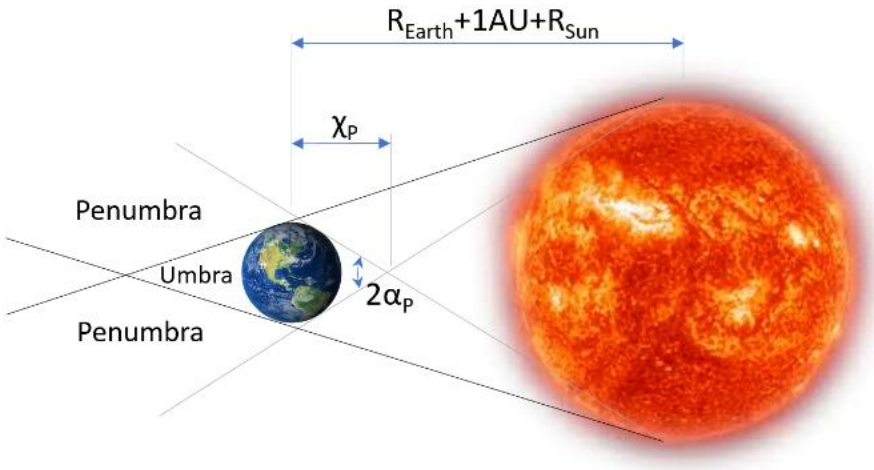

Figure 33 Umbra and penumbra model

4.2.3.1. Disturbance Torques

For attitude manoeuvres, the primary disturbance torques considered are those caused by atmospheric drag and solar radiation pressure. Drag is expressed as:

$$D_{drag} = \frac{1}{2}\rho S c_d V^2 \tag{100}$$

Where ρ is the atmospheric density [kg/m^3], S is the surface [m^2] considered for the drag (only the solar panel surface is considered), c_d is the drag coefficient (assumed to be 2.2), **V** is the velocity [m/s] of the spacecraft with respect to the atmosphere. For the attitude, the RSW frame is used as the inertial frame. The disturbance torque due to this drag is calculated as:

$$M_{drag}^{x} = \frac{1}{2}\rho S \cos(\vartheta)\, c_d V^2 d_z \tag{101}$$

$$M_{drag}^{y} = \frac{1}{2}\rho S \cos(\vartheta)\, c_d V^2 d_x \tag{102}$$

$$M_{drag}^{z} = \frac{1}{2}\rho S \cos(\vartheta)\, c_d V^2 d_y \tag{103}$$

Where ϑ is the angle between the velocity vector and the normal vector to the surface of the solar panel, d_x, d_y, d_z are the distance of the centre of mass of the solar panel with respect to the centre of mass of the satellite.

Disturbance torque due to the solar radiation pressure is then expressed as

$$M_{srp}^{x} = p_{\odot} S \cos\eta\, d_z \tag{101}$$

$$M_{srp}^{y} = p_{\odot} S \cos\eta\, d_x \tag{102}$$

$$M_{srp}^{z} = p_{\odot} S \cos\eta\, d_y \tag{103}$$

where η is the angle between the normal vector to the solar panel and the vector in the direction of the Sun and $p_{\odot} = 9.08 \cdot 10^{-6}$ N is the solar radiation pressure.

4.2.3.2. Attitude parametric path

A common approach to modelling attitude paths is through the use of parametric curves, such as B-splines [219] or Bézier curves [218]. In this paper, a Bézier curve-based approach is adopted due to its flexibility and smooth representation of trajectories. Bézier curves are defined in a virtual time domain τ, where τ ranges between 0 and 1. A mapping function is then introduced to convert the virtual time domain into the real-time domain, ensuring that constraints on control torque and angular velocities are satisfied by appropriately adjusting the mapping function.

A Bezier curve of order n , defined by n+1 control points is expressed as:

$$\bar{b}(\tau) = \sum_{i=0}^{n} \beta_{i,n}(\tau)\bar{p_i} \quad (0 \le \tau \le 1) \tag{104}$$

where $\bar{p_i}$s are the control points ($i = 0, \dots, n$), τ is the control variable of the curve varying from 0 to 1 corresponding to the initial and final point, $\beta_{i,n}$ is the Bernstein basis polynomials of degree n given by

$$\beta_{i,n}(\tau) = \binom{n}{i} (1-\tau)^{n-i}\tau^{i} \tag{105}$$

where the term $\binom{n}{i}$ indicates the binomial coefficient defined as

$$\binom{n}{i} = \frac{n!}{i!\,(n-i)!} \tag{106}$$

The attitude path in this work is modelled using Bézier quaternion curves, which provide a smooth and continuous representation of the spacecraft's orientation over the manoeuvre. To parameterize these curves, the control points are defined using the Modified Rodrigues Parameters (MRP) [224, 225]. Given a quaternion $\boldsymbol{q} = [q_0 \quad \boldsymbol{q_v}]$, where q_0 is the scalar component and $\boldsymbol{q_v}$ the vector component, we define

$$\boldsymbol{p} = \frac{\boldsymbol{q_v}}{1+q_0} = \boldsymbol{e}\tan\left(\frac{\Phi}{4}\right) \tag{107}$$

where $\boldsymbol{e}$ is the rotation axis and Φ the rotation angle. The inverse transformation is given by

$$q_0 = \frac{1-p^2}{1+p^2} \quad \text{and} \quad \boldsymbol{q_v} = \frac{2\boldsymbol{p}}{1+p^2} \tag{108}$$

with $p^2 = \boldsymbol{p}^T\boldsymbol{p}$. The type of manoeuvre is known as *rest-to-rest*: meaning the satellite has null initial and final angular velocities and accelerations. To impose these constraints, the first and second derivative of Bézier curve needs to be analysed. It is important to adopt curves with differentiability class C^4 to have smooth and continuous second derivatives, as the angular acceleration. Because of a *rest-to-rest* manoeuvre it is necessary to set just the first and the last control point. If the angular velocity is null, then the MRP are null. We use a 7th order curve, expressed as

$$\begin{aligned}\mathbf{p_7}(\tau) = \mathbf{p}_0(1-\tau)^7 + 7\mathbf{p}_1\tau(1-\tau)^6 + 21\mathbf{p}_2\tau^2(1-\tau)^5 + 35\tau^3(1-\tau)^4 \\ + 35\mathbf{p}_4\tau^4(1-\tau)^3 + \mathbf{p}_5\tau^5(1-\tau)^2 + \mathbf{p}_6\tau^6(1-\tau) + \mathbf{p}_7\tau^7\end{aligned} \tag{109}$$

Under the constraints

$$\boldsymbol{\omega}(\tau=0) = 0 \qquad \mathbf{p}_1 = \mathbf{p}_0 - \mathbf{p_7} \tag{110}$$

$$\boldsymbol{\omega}(\tau=1) = 0 \qquad \mathbf{p}_6 = \mathbf{p}_7 \tag{111}$$

$$\dot{\boldsymbol{\omega}}(\tau=0) = 0 \qquad \mathbf{p}_2 = \mathbf{p}_0 - \frac{35}{21}\mathbf{p}_7 \tag{112}$$

$$\dot{\boldsymbol{\omega}}(\tau=1) = 0 \qquad \mathbf{p}_5 = -14\mathbf{p}_7 \tag{113}$$

The derivative of the RMP are linked to angular velocities through

$$\dot{\mathbf{p}} = \frac{1}{4}\Psi(\mathbf{p})\boldsymbol{\omega} \tag{114}$$

where the matrix $\Psi(\mathbf{p})$ is

$$\Psi(\mathbf{p}) = [(1-\mathbf{p}^{\mathrm{T}}\mathbf{p})\mathrm{I} + 2[\tilde{\mathbf{p}}] + 2\mathbf{p}\mathbf{p}^{\mathrm{T}}] \tag{115}$$

For the development of inverse dynamics, angular velocity and acceleration need to be expressed in function of $\mathbf{p}$ and $\dot{\mathbf{p}}$.

$$\boldsymbol{\omega} = 4\Psi^{-1}(\mathbf{p})\dot{\mathbf{p}} \tag{116}$$

The inverse of Ψ is a near-orthogonal matrix because its inverse is proportional to its transpose; so, we have

$$\Psi^{-1}(\mathbf{p}) = \frac{\Psi^{\mathrm{T}}(\mathbf{p})}{(1+\mathbf{p}^{\mathrm{T}}\mathbf{p})^2} \tag{117}$$

From the previous equations, if the angular velocity is null, then $\dot{\mathbf{p}} = 0$. The angular acceleration is obtained by

$$\dot{\boldsymbol{\omega}} = 4\left(\dot{\Psi}^{-1}(\mathbf{p})\dot{\mathbf{p}} + \Psi^{-1}(\mathbf{p})\ddot{\mathbf{p}}\right) \tag{118}$$

where $\dot{\Psi}$ and $\dot{\Psi}^{-1}$ are

$$\dot{\Psi} = \left[-\left(\dot{\mathbf{p}}^{\mathrm{T}}\mathbf{p} + \mathbf{p}^{\mathrm{T}}\dot{\mathbf{p}}\right)\mathrm{I} + 2[\widetilde{\dot{\mathbf{p}}}] + 2\left(\dot{\mathbf{p}}\mathbf{p}^{\mathrm{T}} + \mathbf{p}\dot{\mathbf{p}}^{\mathrm{T}}\right)\right] \tag{119}$$

$$\dot{\Psi}^{-1} = \frac{\dot{\Psi}^{\mathrm{T}}}{(1+\mathbf{p}^{\mathrm{T}}\mathbf{p})^2} - \frac{2\Psi^{\mathrm{T}}}{(1+\mathbf{p}^{\mathrm{T}}\mathbf{p})^3}(\dot{\mathbf{p}}\mathbf{p}^{\mathrm{T}} + \mathbf{p}^{\mathrm{T}}\dot{\mathbf{p}}) \tag{120}$$

The advantage of these equations is the possibility to fully describe the attitude kinematics using the MRP. So, we have a mathematical formulation to express the torque as a function of the MRP.

$$\mathbf{M} = \mathrm{f}(\mathbf{p}, \dot{\mathbf{p}}, \ddot{\mathbf{p}}) \tag{121}$$

As described, a mapping function needs to be chosen to map the virtual domain τ to the time domain t.

$$\frac{d\tau}{dt} = c \tag{122}$$

where c is a constant parameter used to adjust the angular velocity along the attitude path.

Applying an inverse dynamic method, we can find the angular velocities and accelerations. Starting from the value of $\boldsymbol{p}$ we have

$$\dot{\boldsymbol{p}} = \frac{d\boldsymbol{p}}{\mathrm{d}t} = \frac{d\boldsymbol{p}}{\mathrm{d}\tau}\frac{\mathrm{d}\tau}{\mathrm{d}t} = \frac{d\boldsymbol{p}}{\mathrm{d}\tau}c \tag{123}$$

$$\ddot{\boldsymbol{p}} = \frac{d^2\boldsymbol{p}}{dt^2} = \frac{\mathrm{d}}{\mathrm{d}t}\left(\frac{d\boldsymbol{p}}{\mathrm{d}t}\right) = \frac{\mathrm{d}^2\boldsymbol{p}}{\mathrm{d}\tau^2}\frac{\mathrm{d}\tau}{\mathrm{d}t} + \frac{d\boldsymbol{p}}{\mathrm{d}\tau}\frac{\mathrm{d}^2\tau}{\mathrm{d}t^2} \tag{124}$$

If the mapping function is constant

$$\ddot{\boldsymbol{p}} = \frac{d^2\boldsymbol{p}}{dt^2} = \frac{\mathrm{d}^2\boldsymbol{p}}{\mathrm{d}\tau^2}\frac{\mathrm{d}\tau}{\mathrm{d}t} = \frac{\mathrm{d}^2\boldsymbol{p}}{\mathrm{d}\tau^2}c \tag{125}$$

4.2.4. Optimality Criteria and Constraints

The optimization of orbital and attitude manoeuvres plays a critical role in achieving overarching Space Traffic Management (STM) goals. For attitude manoeuvres, the primary aim is to support an SBSS mission and observe as many Resident Space Objects (RSOs) as possible, making the minimization of rest-to-rest manoeuvre time

a logical sub-objective. Shorter manoeuvres increase observation availability supporting responsiveness of space-based surveillance systems. In contrast, orbital manoeuvres are more closely aligned with the overarching goal of promoting the sustainability of the space environment. By minimizing propellant consumption, these manoeuvres extend the operational lifespan of satellite propulsion subsystems, ensuring their continued contribution to STM while reducing the risks associated with orbital debris. The following sections outline the specific cost functions and constraints adopted for these two types of manoeuvres.

4.2.4.1. Cost Function for Orbital Manoeuvres

Due to the limited fuel tanks onboard, orbital manoeuvres are always planned to minimise the propellant consumed, therefore a minimum fuel consumption criterion is adopted to define the initial cost function:

$$J_f = \frac{m_0}{m(t_f)} \tag{126}$$

where m_0 and $m(t_f)$ are the initial and final mass of the satellite respectively.

The MME dynamics (eq. 4-8) are treated as constraints in the optimisation problem formulation; hence they take the form:

$$\boldsymbol{\phi} = \begin{Bmatrix} p(t_f) - p_f \\ f(t_f) - f_f \\ g(t_f) - g_f \\ h(t_f) - h_f \\ k(t_f) - k_f \end{Bmatrix} = \mathbf{0} \tag{127}$$

Before being added to the cost function, these equality constraints are made nondimensional by dividing them by their initial value. Most optimisation algorithms do not natively handle constraints, therefore it is necessary to resort to Lagrangian relaxation, by which constraints are translated into cost elements with very heavy weightings (to penalise constraint violations) as in

$$G_i = w_L \, \nu_i(t_j) \tag{128}$$

where w_L is the heavy weighting introduced with the Lagrangian relaxation (here for simplicity assumed equal for all constraints) and ν_i is each difference in eq. 126.

When added to the cost function, nondimensional terms are sometimes squared to improve the rate of convergence during initial iterations. The final cost function for orbital manoeuvres includes both the fuel objective (J_f, eq. 85) and all the squared nondimensional constraints as in:

$$J = \frac{m_0}{m_f} + w_L \left(\frac{p(t_f)-p_f}{p_i}\right)^2 + w_L \left(\frac{f(t_f)-f_f}{f_i}\right)^2 + w_L \left(\frac{g(t_f)-g_f}{g_i}\right)^2 + w_L \left(\frac{h(t_f)-h_f}{h_i}\right)^2 + w_L \left(\frac{k(t_f)-k_f}{k_i}\right)^2 \tag{129}$$

4.2.4.2. Cost Function for Attitude Manoeuvre

In attitude control scenarios, minimizing the time required for a manoeuvre is often advantageous, as shorter manoeuvre durations typically equate to reduced mission downtime. However, accelerating the manoeuvre significantly can lead to excessively high angular accelerations and velocities. These are undesirable for two key reasons:

Attitude Control Concerns: High angular accelerations can shorten the lifespan of reaction wheels and cause saturation issues, compromising the spacecraft's ability to perform subsequent attitude adjustments effectively.

Attitude Determination Challenges: Rapid movements increase errors in inertial sensor readings, reducing the precision of attitude determination.

To address these issues, it becomes essential to impose a limit on the maximum torque output of the reaction wheels. This torque constraint adds to the set of avoidance constraints outlined in Section 2.3, which were designed to prevent electro-optical instruments from pointing toward sensitive directions, such as the Sun or Earth.

Avoidance constraints are typically expressed as inequality conditions. Handling such constraints within an otherwise unconstrained trajectory optimization framework requires the application of Lagrangian relaxation methods with binary penalty functions. In the case of torque constraints, violations are penalized using a specific penalty function, ensuring that the optimization respects the desired operational limits while still achieving feasible and efficient manoeuvre solutions.

[219]. In the torque case, the penalty function associated with constraint violations can be formulated as:

$$\nu_i(t_j) = \begin{cases} 0 & \text{if } |\boldsymbol{M_i}(t_j)| < \boldsymbol{M_{max}} \\ 1 & otherwise \end{cases} \tag{130}$$

Conversely, for quaternion-based path constraints, the penalty function can be formulated as:

$$\nu_i(t_j) = \begin{cases} 0 & \text{if } \boldsymbol{q^T}(t_j) M_F \boldsymbol{q}(t_j) < 0 \\ 1 & otherwise \end{cases} \tag{131}$$

By introducing these constraints, we can ensure that solutions will comply both with the maximum torque and with the bright object avoidance constraints. The cost function for the attitude manoeuvre is:

$$J = t_f + \sum_{i=1}^{N_{ineq}} G_i \tag{132}$$

4.3. Conclusions

This chapter has presented the development and implementation of trajectory optimization models tailored for adaptive orbital and attitude manoeuvres for Space-Based Space Surveillance (SBSS) missions, addressing Objective 4 of this study. The chapter outlined key methodologies, including the formulation of dynamic models incorporating perturbation effects and the application of adaptive metaheuristic optimization algorithms, with a specific focus on Particle Swarm Optimization (PSO). These models were designed to solve complex trajectory optimization problems for scenarios involving collision avoidance and attitude reorientation to minimise manoeuvre energy and time.

The solutions were developed to accommodate both orbital and attitude manoeuvres under real-world mission conditions, leveraging Bézier curves for attitude path planning and Modified Equinoctial Elements (MEE) for orbital dynamics to ensure robustness and accuracy. The integration of onboard optimization capabilities into the DSS platform demonstrates the potential for autonomous and responsive decision-making in space operations, which is vital for distributed satellite systems.

Verification studies to evaluate the proposed methodologies are performed in subsequent chapters. Chapter 5 focuses on validating the orbital manoeuvre optimization in the context of collision avoidance autonomy while Chapter 6 evaluates the attitude manoeuvre optimization within a SBSS mission.

Chapter 5

Uncertainty Quantification and Collision Avoidance Autonomy Design

This chapter presents the development of key models for uncertainty quantification and collision avoidance. The validity of these models is first assessed in terms of covariance realism to identify their limitations and ensure their accuracy in representing the inherent uncertainties of Resident Space Objects. These models are then integrated with an orbit-raising trajectory optimization approach to demonstrate onboard collision avoidance functionality. A particle swarm optimization (PSO) method is employed to solve the trajectory and avoidance problems, highlighting the effectiveness of this approach in support of autonomous decision-making. The chapter concludes with an analysis of the results, emphasizing the potential of the integrated system for improving spacecraft safety in uncertain DSS mission environments.

The contents of this chapter have been published in part in the following:

- **S. Hilton,** F. Cairola, A. Gardi, R. Sabatini, N. Pongsakornsathien, and N. Ezer, "Uncertainty quantification for space situational awareness and traffic management," *MDPI Sensors*, vol. 19, no. 20, p. 4361, 2019.
- E. Lagona, **S. Hilton**, A. Afful, A. Gardi, and R. Sabatini, "Autonomous Trajectory Optimisation for Intelligent Satellite Systems and Space Traffic Management," *Acta Astronautica*, 01/25 2022, doi: 10.1016/j.actaastro.2022.01.027.

5.1. Uncertainty Quantification

The ever-increasing number of Resident Space Objects (RSO) is strongly highlighting the need for an evolution from traditional Space Situational Awareness (SSA) capabilities towards Space Domain Awareness (SDA) [226, 227]. Analogous to its atmospheric counterpart (i.e., Air Domain Awareness) SDA aims to elevate current SSA capabilities through the dissemination of confidence-building measures, necessary to reliably estimate the future states of RSOs with the aim of optimal coordination and accommodation in a future Space Traffic Management (STM) system. Confidence-building measures ideally encapsulate the functional characteristics of an RSO (e.g., shape and size), and, when possible, mission objectives and planned operational activities of active spacecraft. Even so, an increase alone in the available data will not solve the current issues of RSO ambiguity and collision avoidance subjectivity – contextualizing information must be used together with transparent and traceable Time and Space Position Information (TSPI) reflective of sensor

performance. Cooperative RSO equipped with TSPI enabling systems such as GNSS and data sharing capabilities equivalent to the Automatic Dependent Surveillance Broadcast (ASD-B) system will be an important aspect in managing uncertainty in the on-orbit environment. Nonetheless, due to the inherently high threat of space debris, the notion of transparent and traceable TSPI information must extend to the classification of non-cooperative RSOs. In most cases, the position of a large orbiting object (>10 cm) can be predicted with reasonable uncertainty, based on data accrued by the SSA Space Surveillance and Tracking (SST) segment and other non-government-owned ground-based sensors. The performance of these systems is detailed in Table 15.

Table 15. Overview of Space Surveillance and Tracking (SST) ground-based radar systems [83].

Ground-Based Radar System	Devices	Description	Location
AN/FPS-85	UHF Phased-array radar	Maximum peak power: 30 MW, it can detect 1.0 m^2 objects in geosynchronous orbits	Florida, USA
Globus II	X-Band mono-pulse radar with 27m parabolic dish antenna	Track spacecraft of all types up to a range of 4,000 Km	Vardo, Norway
TIRA	L-band and Ku-band radar using a 34 m parabolic reflector	Radar images of space objects at a distance of up to 20,000 Km	Watchberg, Germany

Although ground-based systems will continue to be a vital aspect in filling the SST role, the feasibility of Space-Based Space Surveillance (SBSS) is being explored to monitor the Low Earth Orbit (LEO) [82] and Geosynchronous Orbit (GEO) regions [10, 228].due to the advantage of persistent coverage of smaller sized RSOs (<10cm) elusive to traditional ground-based systems. Understandably spaceborne tracking of RSOs is not a trivial matter [229, 230] – effective coverage of the space environment will require constellations of SBS platforms each under complex tasking regimes to overcome performance and physical constraints [90]. Given that true collisions are a rare space event, the cost of platforms devoted to debris detection may exceed their benefit given that there would be minimal power available for mission-oriented payloads. This is especially the case for spaceborne radar due to the higher power requirements associated with this sensor. For future SBSS platforms to be commercially and economically viable, it is imperative that a low size weight, power, and cost (SWaP-C) approach must be taken. Regardless of the sensor suite chosen, SBSS platforms will be subject to dynamic positional errors from onboard TSPI/Navigation systems, in contrast to traditional ground-based systems that perform observations from

accurately surveyed locations. As such, there is a compelling case for analysis on the effect of initial RSO position estimation based on both navigation and tracking system errors. Nevertheless, in both ground-based and SBSS applications, a sensor-focused approach must be taken to establish an unambiguous initial estimate of RSO uncertainty.

In the context of SSA, realistic orbital uncertainty directly underpins the effectiveness of operational activities that include the following: RSO Orbit determination, data or track association/correlation, manoeuvre detection, the computation of the probability of collision for conjunction assessment and sensor management [231, 232]]. Most importantly, these processes require the knowledge of how the uncertainty of RSOs will propagate over time subject to orbital dynamics and perturbations from residual atmospheric drag, solar radiation pressure, non-spherical Earth, and other celestial bodies. Largely, Orbital uncertainty propagation methodologies can be grouped under either Linear and Non-Linear Methods [29]. Typical Non-Linear methods include Unscented Transformations, Polynomial Chaos Expansions, and Fokker Plank Methods. Undoubtedly, these methods can capture well the non-linear growth of RSO uncertainty subject to orbital dynamics, however, are computationally burdening due to the high dimensionality of the problem especially for longer propagation periods. The mathematical derivation of these methods is beyond the scope of this chapter, the reader is referred to reference [29]. A popular alternative is to construct a linearized model of the dynamics so that the uncertainty about an RSO can be propagated in a computationally efficient manner. However, linearized propagation methods are not without shortcomings -which if not explicitly quantified have significant implications on the realism of subsequent analysis made based on the estimated uncertainty. Uncertainty quantification is defined as follows: ‘The process of determining the various sources of errors and uncertainties, properly characterizing these errors and uncertainties, and the roll up of these in the prediction of the quantities of interest”[232]. In the context of linearized uncertainty propagation methods, two fundamental assumptions are made:

1. A linearized model sufficiently approximates the dynamics of neighbouring trajectories with respect to a nominal trajectory.
2. The uncertainty can be completely characterized by a Gaussian probability distribution.

To quantify the uncertainty, we are interested in testing the uncertainty realism, which under Gaussian assumptions (linear), coincides with covariance realism – the characterization (size, shape, and orientation) of the (gaussian) uncertainty of the RSO in question. Various covariance realism tests and metrics have been used to assess realism with a primary focus on determining the length of Gaussian validity, i.e., the amount of time (commonly described

in orbital periods) a linearized uncertainty propagation method can be used to confidently and accurately describe the estimated position uncertainty of an RSO. Nonetheless, by the reiteration of the above assumption, linear propagation methods are only valid if the initial RSO uncertainty (input) is Gaussian. This presents the necessary case of applying covariance realism testing to the sensor level to quantify tracking and navigation system performance characteristics that support or do not, a linearized (Gaussian) method to describe initial RSO position uncertainty. By taking a sensor-level perspective to model tracking and navigation system uncertainty, this section first addresses two SST representative case studies of traditional ground-based radar and proposed Millimetre Wave (MMW) Space-Borne Radar (SBR) for the tracking of space debris aboard larger spacecraft platforms.

5.1.1. Model Development

Firstly, radar tracking (TRK) and navigation (NAV) error models are developed, including common transformations required to represent the uncertainty in a convenient frame. Attention is then turned to methods to assess the "realism" of the uncertainty under Gaussian assumptions using two common approaches - the Average Mahalanobis Distance (AMD) statistic metric and Cramer–von Mises (CVM). A Monte-Carlo framework is then presented to obtain the required Empirical Distribution of both tracking and navigation uncertainty.

5.1.1.1. Tracking and Navigation System Error Models

The SNR (Signal to Noise Ratio) of the radar is a key measure of its performance, which is defined as the ratio of signal power to noise power at the output of the radar receiver.

$$\mathrm{SNR} = \frac{\mathrm{P_r}}{\mathrm{P_n}} = \frac{\mathrm{P_p G_t \sigma A_r \tau}}{(4\pi)^2 \mathrm{R^4 k F T_0 L}} \tag{133}$$

Where:

$\mathrm{P_p}$: Peak transmitted power [W]

$\mathrm{G_t}$: Radar transmit antenna gain (power ratio)

$\mathrm{A_r}$: Radar receiver antenna effective aperture area [$\mathrm{m^2}$]

σ: Target radar cross-section (RCS) [$\mathrm{m^2}$]

R: Range from radar to target [m]

F: Noise figure of the receiver subsystem

L: Radar system losses

T0: Standard Temperature [290 K]

k: Boltzmann's constant [1.38064852 × 10^{-23} m^2Kg $s^{-2}K^{-1}$]

τ: Radar pulse duration [sec]

Target state vector information is measured relative to the radar site in a spherical coordinate system in range, elevation and azimuth ($r_{RDR}, \eta_{RDR}, \epsilon_{RDR}$ respectively) (Figure 2a) The measurements in each of the elements are prone to specific error sources that include the following [233]:

$$\sigma_{r_{RDR}}{}^2 = \sigma_{RN}^2 + \sigma_{RF}^2 + \sigma_{RB}^2 \tag{133}$$

where σ_{RN} Is an SNR-dependent random range measurement error, which can be calculated as:

$$\sigma_{RN} = \frac{c}{2B\sqrt{2(S\text{NR})}} \tag{134}$$

Where B is waveform bandwidth, c is the speed of light and signal-to-noise ratio (SNR). σ_{RF} is a random measurement error having a fixed standard deviation, due to noise sources in the latter stages of the radar receiver. σ_{RB} is a range bias error associated with the radar calibration and measurement process. We assume the Zero-mean condition, so. σ_{RB} and σ_{RF} are equal to zero.

Radar angular measurements are commonly made using monopulse receive antennas that provide a difference pattern characterized by a deep null on boresight. The difference pattern formed by these beams may be used to measure the target angular position with a single signal transmission. The measurement accuracy in each angular coordinate is characterized by the RMS of the SNR-dependent random angular measurement error, angular bias, and random measurement error. As with the range error, we assume angular bias and random measurement error to be 0 under the Zero-mean condition.

$$\sigma_{\epsilon_{RDR}}{}^2 = \sigma_{AN_\epsilon}^2 + \sigma_{AF_\epsilon}^2 + \sigma_{AB_\epsilon}^2$$
$$\sigma_{\eta_{RDR}}{}^2 = \sigma_{AN_\eta}^2 + \sigma_{AF_\eta}^2 + \sigma_{AB_\eta}^2 \tag{136}$$

As with the range errors, the SNR-dependent error dominates the radar angle error:

$$\sigma_{AN} = \frac{\vartheta}{k_m\sqrt{2(SNR)}} \tag{137}$$

Where: ϑ is the radar beamwidth in the angular coordinates and k_m is the monopulse pattern difference slope.

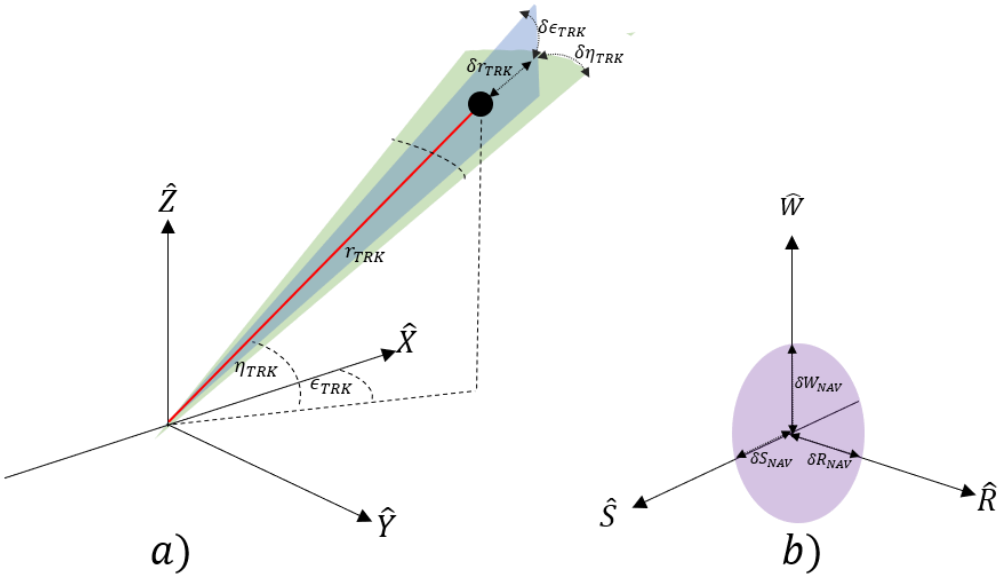

Figure 34 Generic Tracking (a) and Navigation (b) RSW coordinate systems detailing corresponding error geometry.

The RSW satellite coordinate system is chosen to express the position uncertainty of RSO. At the time of observation, we assume that the nominal spacecraft position (SP) is centred at the origin of the RSW axis The Radial (R) axis always points from the earth centre along the radius vector towards the satellite. The S-Axis is pointed tangentially to the track's direction, where, in the case of elliptical orbits, it is only parallel to the velocity vector at apogee and perigee. The W (cross-track) axis is normal to the orbital plane and completes the right-hand triad (Figure 34). The coordinate system can then be constructed through the following unit vector approach [222]:

$$\widehat{\boldsymbol{R}} = \frac{R_{ECI}}{|R_{ECI}|} \tag{138}$$

$$\widehat{\boldsymbol{W}} = \frac{R_{ECI} \times V_{ECI}}{|R_{ECI} \times V_{ECI}|} \tag{139}$$

$$\widehat{\boldsymbol{S}} = \widehat{\boldsymbol{W}} \times \widehat{\boldsymbol{R}} \tag{140}$$

The transfer matrix(s) between the RSW and ECI coordinate systems is then the following:

$$M_{RSW \to ECI} = \left[\widehat{\boldsymbol{R}}\, \widehat{\boldsymbol{S}}\, \widehat{\boldsymbol{W}}\right] \tag{141}$$

$$M_{ECI \to RSW} = \left[\widehat{\boldsymbol{R}}\, \widehat{\boldsymbol{S}}\, \widehat{\boldsymbol{W}}\right]^T \tag{142}$$

Positional errors from the on-board navigation system are then expressed as deviations, $\delta \boldsymbol{X_{NAV}}$, from the origin of the axis, defined as the difference between the true state, $\boldsymbol{X_{NAV}}$, and the nominal state $\bar{\boldsymbol{X}}_{\boldsymbol{NAV}}$ under the zero mean

$$\delta \boldsymbol{X_{NAV}} = \boldsymbol{X_{NAV}} - \bar{\boldsymbol{X}}_{\boldsymbol{NAV}} \tag{143}$$

$$\boldsymbol{X_{NAV}} = \begin{bmatrix} R_T \\ S_T \\ W_T \end{bmatrix}, \bar{\boldsymbol{X}}_{\boldsymbol{NAV}} = \begin{bmatrix} R_N \\ S_N \\ W_N \end{bmatrix} \tag{144}$$

Navigation uncertainty is assumed to be Gaussian, and can then be expressed in terms of covariance, where the assumption of zero main is made:

$$Q_{NAV}{}^{RSW} = E\left[\delta \boldsymbol{X_{NAV}} \delta \boldsymbol{X_{NAV}}^T\right] = \begin{bmatrix} \sigma_{R_{NAV}}{}^2 & 0 & 0 \\ 0 & \sigma_{S_{NAV}}{}^2 & 0 \\ 0 & 0 & \sigma_{W_{NAV}}{}^2 \end{bmatrix} \tag{145}$$

Similarly, tracking measurement errors are expressed as measurement deviations in the spherical dimension, $\delta \boldsymbol{X_{TRK}}$, defined as the difference between the true state, $\boldsymbol{X_{TRK}}$, and the nominal state $\bar{\boldsymbol{X}}_{\boldsymbol{TRK}}$ of the RSO [234].

$$\delta \boldsymbol{X_{TRK}} = \boldsymbol{X_{TRK}} - \bar{\boldsymbol{X}}_{\boldsymbol{TRK}} \tag{146}$$

$$\boldsymbol{X_{TRK}} = \begin{bmatrix} r_T \\ \epsilon_T \\ \eta_T \end{bmatrix}, \bar{\boldsymbol{X}}_{\boldsymbol{TRK}} = \begin{bmatrix} r_N \\ \epsilon_N \\ \eta_N \end{bmatrix} \tag{147}$$

The tracking error of the radar is then expressed in terms of covariance:

$$Q_{TRK_{SPH}}^{RDR} = E\left[\delta \boldsymbol{X_{TRK}} \delta \boldsymbol{X_{TRK}}^T\right] = \begin{bmatrix} \sigma_{r_{TRK}}{}^2 & 0 & 0 \\ 0 & \sigma_{\epsilon_{TRK}}{}^2 & 0 \\ 0 & 0 & \sigma_{\eta_{TRK}}{}^2 \end{bmatrix} \tag{148}$$

5.1.1.2. Transformation of Uncertainty to Common Coordinate System

To combine NAV & TRK uncertainty from the spacecraft and tracked RSO both covariance matrices must belong to the same coordinate frame. In this case, a transformation from the spherical to the Cartesian system must be performed. Position and velocity measurements (and uncertainty) should be expressed in a reference frame that is most convenient to the user, where in this case a Cartesian Earth-Centred Inertial (ECI) frame is chosen. As such, the navigation covariance matrix must be transformed to the Cartesian Earth-Centred inertial (ECI) frame. As this is a linear process (cartesian to cartesian), a simple coordinate transformation can be applied to the covariance matrix. Following the derivation of the RSW to ECI transformation matrix previously described, we can write:

$$Q_{NAV}{}_{CART}^{ECI} = M_{RSW \to ECI}\, Q_{NAV}{}_{CART}^{RSW} \cdot M_{RSW \to ECI}{}^T \tag{149}$$

$$Q_{NAV}{}_{CART}^{ECI} = \begin{bmatrix} {\sigma_{x_{NAV}}}^2 & \sigma_{xy_{NAV}} & \sigma_{xz_{NAV}} \\ & {\sigma_{y_{NAV}}}^2 & \sigma_{yz_{NAV}} \\ sym & & {\sigma_{z_{NAV}}}^2 \end{bmatrix} \tag{150}$$

In contrast, the tracking covariance matrix is expressed in a spherical coordinate system within the radar frame. This requires both a transformation from a spherical to the Cartesian system and then a translation to the ECI frame. As the transformation between these systems is nonlinear, a basic coordinate transformation is not sufficient, and mathematical tools such as the Jacobian of the spherical to Cartesian transformation matrix must be calculated to linearize the process. The spherical to Cartesian Jacobian (D) is expressed as the following, where c, s and represents the cosine and sine of the radar angular measurements.

$$D = \begin{bmatrix} -\,\mathrm{c}\,\epsilon_{TRK}\,\mathrm{c}\,\eta_{TRK} & r_{TRK}\,\mathrm{c}\,\epsilon_{TRK}\,\mathrm{s}\,\eta_{TRK} & r_{TRK}\,\mathrm{s}\,\epsilon_{TRK}\,\mathrm{c}\,\eta_{TRK} \\ \mathrm{c}\,\epsilon_{TRK}\,\mathrm{s}\,\eta_{TRK} & r_{TRK}\,\mathrm{c}\,\epsilon_{TRK}\,\mathrm{c}\,\eta_{TRK} & -r_{TRK}\,\mathrm{s}\,\epsilon_{TRK}\,\mathrm{s}\,\eta_{TRK} \\ \mathrm{s}\,\epsilon_{TRK} & 0 & r_{TRK}\,\mathrm{c}\,\epsilon_{TRK} \end{bmatrix} \tag{151}$$

The transformation from the spherical tracking error matrix in the Radar coordinate system to the Cartesian ECI is then given by the following:

$$Q_{TRK}{}_{CART}^{ECI} = (M_{RDR\to ECI} \cdot D) \cdot Q_{TRK}{}_{SPH}^{RDR} \cdot (M_{RDR\to ECI} \cdot D)^T \cdot \tag{152}$$

$$Q_{TRK}{}_{CART}^{ECI} = \begin{bmatrix} {\sigma_{x_{TRK}}}^2 & \sigma_{xy_{TRK}} & \sigma_{xz_{TRK}} \\ & {\sigma_{y_{TRK}}}^2 & \sigma_{yz_{TRK}} \\ sym & & {\sigma_{z_{TRK}}}^2 \end{bmatrix} \tag{153}$$

Where $M_{RDR\to ECI}$ is the transformation matrix from the chosen Radar (TRK) coordinate frame to the ECI frame. The covariance matrix of both the navigation and tracking can now be expressed geometrically as an ellipsoid centred about the nominal position in the ECI Frame. Due to the transformation and translations between the Radar Spherical and Cartesian coordinate systems to the ECI frames, the covariance terms within the error matrix (off-diagonal) are now non-zero. The geometric interpretation of ${Q_{TRK}}^{ECI}$ now requires that the ellipsoid considers both the variances about the principal axis but also the rotation within the cardinal system (ECI).

5.1.1.3. Assessing Covariance Realism at the Sensor Level

Within the SSA/Astrodynamics community, the assessment of covariance realism (also known as covariance consistency) has been focused on identifying the point at which Gaussian assumptions in the propagation of orbital uncertainty breakdown. As discussed, this chapter is interested in applying this approach to the sensor level and in turn validating when Gaussian assumptions of navigation and tracking error break down. In doing so, 2 commonly

used statistical metrics and goodness of fit tests have been adopted. The Mahalanobis distance [235] provides a convenient metric for testing covariance realism, where a set of empirically generated points, $\boldsymbol{x}_{\mathrm{mc}}$, from the measurement model are tested to see if it corresponds to the gaussian distribution defined by a covariance matrix P centred about the truth state, $\boldsymbol{x}_{\mathrm{truth}}$, of the target. The squared Mahalanobis distance between the estimated orbit state and the truth target is defined as:

$$\mathcal{M}((\boldsymbol{x}_{\mathrm{mc}}, \boldsymbol{x}_{\mathrm{truth}}, \mathbf{P}) = (\boldsymbol{x}_{\mathrm{mc}} - \boldsymbol{x}_{\mathrm{truth}})^T \mathbf{P}^{-1} (\boldsymbol{x}_{\mathrm{mc}} - \boldsymbol{x}_{\mathrm{truth}}) \tag{154}$$

The expected value of $\mathcal{M}$ is *n*, where *n* is the dimension of the state vector $\boldsymbol{x}_{\mathrm{truth}}$, which in the case of a cartesian coordinate system corresponds to 3. As an uncertainty realism metric, one can consider the values of $\overline{\mathcal{M}}$, averaged over each observation condition. Let $\mathcal{M}^{(i)}$ be the uncertainty realism metric computed in the *i*-th Monte Carlo trial. Let *k* be the total number of independent trials.

$$\overline{\mathcal{M}} = \frac{1}{nk} \sum_{i=1}^{k} \mathcal{M}^{(i)} \tag{155}$$

A stronger test for uncertainty realism is to consider the statistical distribution determined from the measurement model in the form of a physics-based Monte Carlo simulation. As such, the second covariance realism metric test used is the Cramer–von Mises goodness of fit test statistic [231, 232]. This test permits to verify the consistency of the sample and test how well the theoretical Gaussian distribution fits the empirical distribution. The Cramer–von Mises (CVM) test is based in a statistic of the type

$$Q_k = \int_{-\infty}^{+\infty} [F_n(x) - F^*(x)]^2 \varphi(F(x)) dF^*(x) \tag{156}$$

Where $F^*(x)$ is the cumulative distribution function (CDF) of the Mahalanobis distance $\mathcal{M}$ and $F_n(x)$ is the Empirical CDF of the AMD representing the *n* degree of freedom system being analyzed. Where the results are from a Monte Carlo simulation of the measurement error model with N samples. Specializing to $\varphi(F(x)) = 1$, the CVM test is then calculated by:

$$Q_k = \frac{1}{12N} \sum_{i=1}^{N} \left[\frac{2i-1}{2N} - F(\mathcal{M}^{(i)}) \right]^2 \tag{157}$$

Sorting the Mahalanobis squared distance of the samples, $\mathcal{M}^{(i)}$, from the smallest to largest, $F\left(\mathcal{M}^{(i)}\right)$ can be obtained by:

$$F\left(\mathcal{M}^{(i)}\right) = erf\left(\sqrt{\frac{\mathcal{M}^{(i)}}{2}}\right) - \sqrt{\frac{2\,\mathcal{M}^{(i)}}{\pi}}\,e^{-\frac{\mathcal{M}^{(i)}}{2}} \tag{158}$$

Given a significance level α, one can derive a two-sided 100(1- α)% confidence interval for the distribution $\overline{\mathcal{M}}\,(n)$**.** As with the averaged Mahalanobis distance (AMD), the acceptable degree of the CVM metric is determined by defining a confidence level. Table 16 outlines the acceptable ranges of the CVM and AMD for a commonly selected confidence level for measurement models of dimension 3.

Table 16 Confidence interval for Cramer–von Mises (CVM) [12] and Mahalanobis Distance (MD) for ∞ samples.

	90%	**95%**	**99%**	**99.9%**
AMD	[0.9655,1.0457]	[0.9578,1.0534]	[0.9427,1.0685]	[0.9106,1.1006]
CVM	[0,0.3430]	[0,0.46136]	[0,0.74346]	[0,1.16204]

As described the Squared Mahalanobis Distance Metric and the Cramer–von Mises distribution matching test require the generation of an Empirical Distribution. In doing so, a measurement model using the calculated uncertainty of the radar and tracking error models is constructed, generating N observation samples about the nominal measurement. Under the assumption that each measurement variable is independent (non-correlated):

The navigation Error contribution, (considered only for the SBSS platform), is given by:

$$\begin{Bmatrix} R_N = \sigma_{R_{NAV}} N \\ S_N = \sigma_{S_{NAV}} N \\ W_N = \sigma_{W_{NAV}} N \end{Bmatrix} \tag{159}$$

The tracking contribution is given by:

$$\begin{Bmatrix} r_T = r_0 + \sigma_{r_{TRK}} N \\ \epsilon_T = \epsilon_0 + \sigma_{\epsilon_{TRK}}\, N \\ \eta_T = \eta_0 + \sigma_{\eta_{TRK}} N \end{Bmatrix} \tag{160}$$

The total uncertainty about the object, when tracked from the space-based platform, is then described by:

$$\begin{Bmatrix} R_T = R_N + r_T\ cos(\eta_T)\, cos(\epsilon_T) \\ S_T = S_N + r_T\ cos(\eta_T)\, sin(\epsilon_T) \\ W_T = W_H + r_T\ sin(\epsilon_T) \end{Bmatrix} \tag{161}$$

Under the assumption, the position of observation is well known and therefore the error is negligible, the total uncertainty from the ground station is:

$$\begin{Bmatrix} S_T = r_T cos(\eta_T) cos(\epsilon_T) \\ E_T = r_T cos(\eta_T) sin(\epsilon_T) \\ Z_T = r_T sin(\epsilon_T) \end{Bmatrix} \quad (162)$$

5.1.1.4. Ground-Based Tracking Scenario

The first case studies applies the above framework for the typical scenario of RSO tracking from a radar ground station for the practical purpose of identification and assessment of a potential collision with an operational spacecraft (**Figure 35**). Typically ground-based tracking stations utilize the South East Zenith Topocentric Horizon Coordinate frame (SEZ). The SEZ coordinate system is defined for a given longitude and latitude at a local sidereal time and rotates with the site where the local horizon forms the fundamental plane. The S axis points due South from the site, The E axis points East from the site and the Z axis (Zenith) points radially outward from the site along the site position vector from the ECI origin.

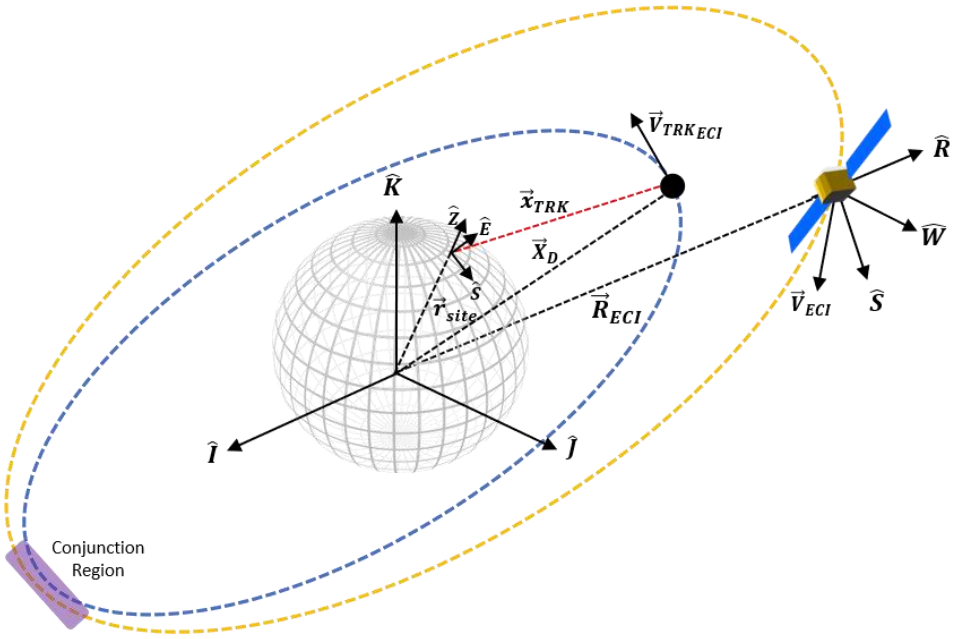

Figure 35. Illustration of ground-based tracking scenario and subsequent conjunction region with operational satellite.

The coordinate system is constructed using the site position vector, $\vec{r}_{SITE}$, in ECI frame:

$$\hat{\boldsymbol{Z}} = \frac{\vec{r}_{SITE}}{|\vec{r}_{SITE}|} \quad (163)$$

$$\hat{\boldsymbol{E}} = \hat{\boldsymbol{K}} \times \hat{\boldsymbol{Z}} \quad (164)$$

$$\widehat{\boldsymbol{S}} = \widehat{\boldsymbol{E}} \times \widehat{\boldsymbol{Z}} \tag{165}$$

The transfer matrix between the RSW and ECI coordinate systems is then following:

$$M_{SEZ \to ECI} = \left[\widehat{\boldsymbol{S}}\, \widehat{\boldsymbol{E}}\, \widehat{\boldsymbol{Z}}\right] \tag{166}$$

Within the SEZ coordinate frame the tracked RSO range, azimuth and elevation (ρ, ϵ, η) and their derivates are measured where then by implementing the SITE-TRACK algorithm [222] the position $\vec{X}_{TRK}$ and the velocity $\vec{V}_{TRK}$ in the ECI frame can be determined.

$$\vec{X}_{TRK} = \vec{r}_{SITE} + M_{SEZ \to ECI} \begin{bmatrix} \rho cos(\eta) cos(\epsilon) \\ \rho\, cos(\eta) sin(\epsilon) \\ \rho\, sin(\eta) \end{bmatrix} \tag{167}$$

$$\vec{V}_{TRK} = M_{SEZ \to ECI}\, \vec{v}_{SEZ} + \vec{\omega}\ x\, \vec{X}_{TRK} \tag{168}$$

Where: $\vec{v}_{SEZ}$ is the velocity vector determined from observations at the site in the SEZ coordinate frame and $\vec{\omega}$ is the Earth's rotation vector. Based on the calculated radar performance parameters using radar error equations , it is then necessary to transform the TRK uncertainty ($\sigma_{r_{TRK}}$, $\sigma_{\epsilon_{TRK}}$, $\sigma_{\eta_{TRK}}$) into the ECI coordinate system, $Q_{TRK}{}_{CART}^{ECI}$ as described in Section 2.3. Assuming the velocity measurement error to be zero we obtain the following 3 × 3 Covariance matrix for each observation.

$$Q_{TRK}{}_{CART}^{ECI} = (M_{SEZ \to ECI} \cdot D) \cdot Q_{TRK}{}_{SPH}^{SEZ} \cdot (M_{SEZ \to ECI} \cdot D)^T \tag{169}$$

$$Q_{TRK}{}_{CART}^{ECI} = \begin{bmatrix} {\sigma_{x_{TRK}}}^2 & \sigma_{xy_{TRK}} & \sigma_{xz_{TRK}} \\ & {\sigma_{y_{TRK}}}^2 & \sigma_{yz_{TRK}} \\ sym & & {\sigma_{z_{TRK}}}^2 \end{bmatrix} \tag{170}$$

5.1.1.5. Space-Based Surveillance Scenario

Based on proposed MMW SBR systems and documented GPS performance, we outline here a mathematical framework to combine tracking and navigation uncertainty to provide a rigorous methodology to describe and analyse the position uncertainty of a tracked RSO from an SBSS Radar platform. As with the ground-based scenario, we focus on the case of representing uncertainty expressed in a common satellite coordinate system to a convenient Earth-Centred Inertial (ECI) reference frame. In this case, the RSW coordinate system is used for both navigation and tracking observations, where the MMW radar (TRK) and GNSS (NAV) system is assumed to be centred on the origin. The reference geometry and the key symbols for this scenario are introduced in Figure 36, Figure 37.

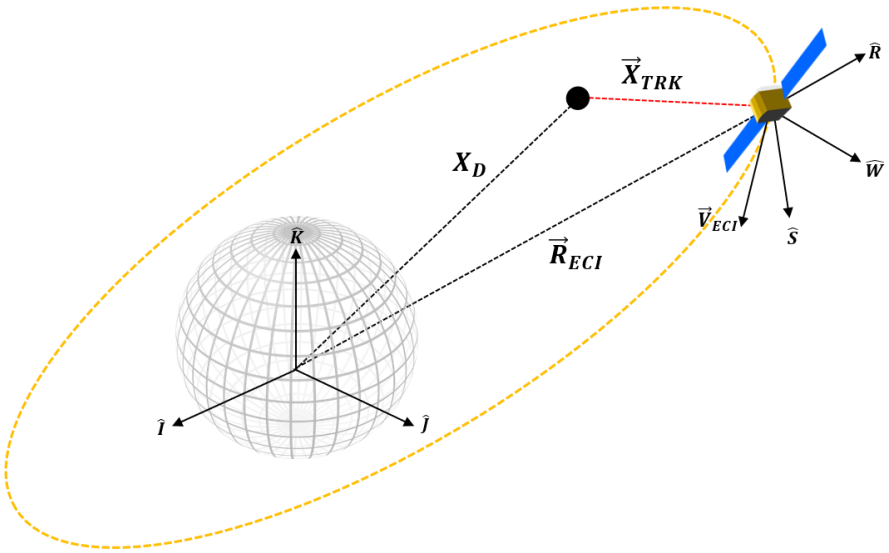

Figure 36. Reference geometry of the non-cooperative tracking and RSW coordinate system.

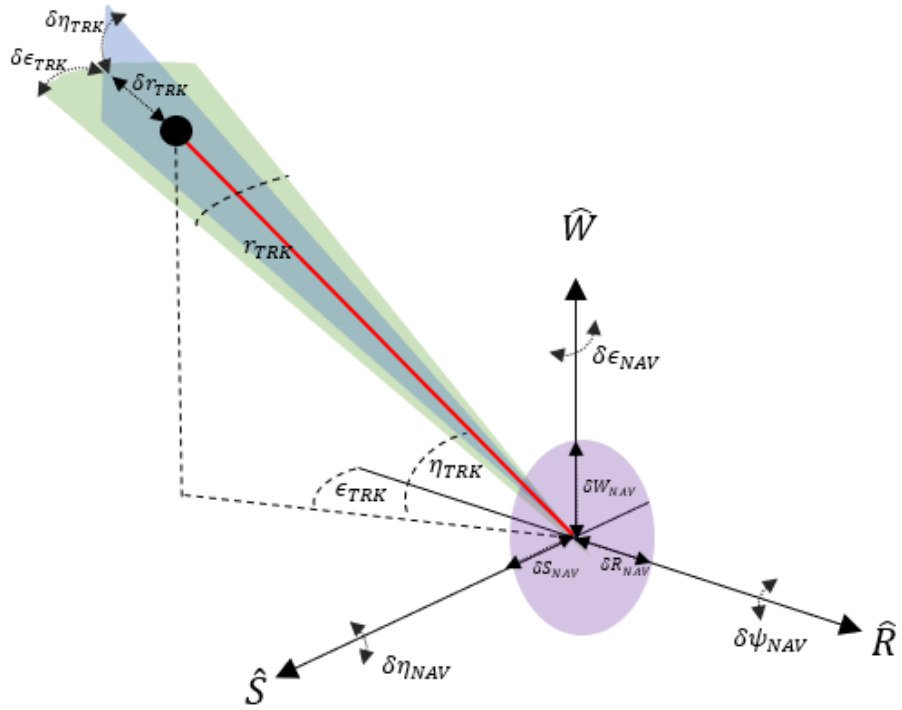

Figure 37. Space-based observation geometry and measurement deviations in RSW frame

To quantify the total error about the RSO position, we reformulate the framework described in Section 2.2 as an Errors in-variable model following the Gauss–Helmert method [236, 237]. In this case, we assume the attitude error of the spacecraft is zero ($\delta\epsilon_{NAV} = 0, \delta\eta_{NAV} =$

$0, \delta\psi_{NAV} = 0$). The generic Gauss–Helmert form consists in resolution of the following equation system:

$$\boldsymbol{F}(\boldsymbol{X}, \boldsymbol{l}) = \boldsymbol{0} \tag{171}$$

where $\boldsymbol{X}$, $\hat{\boldsymbol{l}}$ are estimated parameters and observation vector respectively. The linearized form of the previous equation is:

$$\boldsymbol{A\delta} + \boldsymbol{Br} + \boldsymbol{w} = \boldsymbol{0} \tag{172}$$

where $\boldsymbol{A} = \frac{\boldsymbol{\partial F}}{\boldsymbol{\partial \hat{X}}}$ and $\boldsymbol{B} = \frac{\boldsymbol{\partial F}}{\boldsymbol{\partial l}}$ are the matrix of partial derivates with respect to $\boldsymbol{X}$, $\boldsymbol{l}$ and **w** is the misclosure vector. $\boldsymbol{\delta}$ and $\boldsymbol{r}$, the parameter and observation correction vector respectively, are:

$$\begin{aligned} \hat{\boldsymbol{\delta}} &= -(\boldsymbol{A^T M A})^{-1} \boldsymbol{A^T M w} \\ \hat{\boldsymbol{r}} &= -\boldsymbol{C_r B^T M}(\boldsymbol{A\delta} + \boldsymbol{w}) \end{aligned} \tag{173}$$

Where $\boldsymbol{M} = (\boldsymbol{BC_r B^T})^{-1}$ and $\boldsymbol{C_r}$ is the covariance matrix of the observations. We obtain the covariance matrix of parameters:

$$C_{NAV+TRK} = (\boldsymbol{A^T M A})^{-1} \tag{174}$$

Equation (43) is then:

$$\boldsymbol{F}(\boldsymbol{X}, \boldsymbol{l}) = \boldsymbol{X_D} - \boldsymbol{M_{RSW \rightarrow ECI} X_{TRK}} - \boldsymbol{R}_{ECI} = \boldsymbol{0} \tag{175}$$

where:

$\boldsymbol{X_D} = \begin{bmatrix} X_D^{ECI} \\ Y_D^{ECI} \\ Z_D^{ECI} \end{bmatrix}$ and $\boldsymbol{R}_{ECI} = \begin{bmatrix} X_h^{ECI} \\ Y_h^{ECI} \\ Z_h^{ECI} \end{bmatrix}$ are the RSO and spacecraft position in ECI frame

$\boldsymbol{X}_{TRK} = \begin{bmatrix} -r_{TRK} cos(\epsilon_{TRK}) cos(\eta_{TRK}) \\ r_{TRK} cos(\epsilon_{TRK}) sin(\eta_{TRK}) \\ r_{TRK} sin(\epsilon_{TRK}) \end{bmatrix}$ is the nominal position of the target in RSW frame.

$\boldsymbol{l} = [r_{TRK}, \epsilon_{TRK}, \eta_{TRK}, x_{NAV}, y_{NAV}, z_{NAV}]^{\boldsymbol{T}}$ is vector of estimated observations, and

$$\boldsymbol{C_r} = \begin{bmatrix} \sigma^2_{r_{TRK}} & 0 & 0 & 0 & 0 & 0 \\ & \sigma^2_{\epsilon_{TRK}} & 0 & 0 & 0 & 0 \\ & & \sigma^2_{\eta_{TRK}} & 0 & 0 & 0 \\ & & & {\sigma_{x_{NAV}}}^2 & \sigma_{xy_{NAV}} & \sigma_{xz_{NAV}} \\ & & & & {\sigma_{y_{NAV}}}^2 & \sigma_{yz_{NAV}} \\ & Sym & & & & {\sigma_{z_{NAV}}}^2 \end{bmatrix} = \begin{bmatrix} {Q_{TRK}}_{SPH}^{RDR} & \boldsymbol{0} \\ \boldsymbol{0} & {Q_{NAV}}_{CART}^{ECI} \end{bmatrix}$$

is the covariance matrix of observations.

The assumption is made that all navigation and tracking observation errors are independent, so covariance terms between the 2 observation sets in the matrix $\boldsymbol{C_r}$ are set to zero. However, covariance terms between navigation uncertainty exist due to the transformation from the RSW to ECI coordinate frame described by equation 18. With $A_{(3\times3)} = \mathbb{1}$, the covariance matrix of observation is then computed by:

$$\boldsymbol{C}_{NAV+TRK\,(3\times3)} = (\boldsymbol{B}\boldsymbol{C_r}\boldsymbol{B^T}) \tag{176}$$

5.1.1.6. Collision Probability

To calculate the probability of collision, it is necessary to propagate the uncertainty volumes generated of the satellite and the intruder RSO (Q_{NAV}, Q_{TRK}) from the time of last position to the time of close approach. In doing so a linearized approach known as Markley's method[238, 239] is adopted.

Markley's method calculates the state transition matrix between two states, t_{k-1} and t_k. It accounts for Earth's flattening as the dominant factor, approximating the transition matrix via a Taylor series expansion for short propagation intervals Δt. The state transition's differential equation is given by:

$$\frac{\partial}{\partial \mathrm{t}}\boldsymbol{\Phi}(\mathrm{t},\mathrm{t}_0) = \mathbf{A_1}(\mathrm{t})\boldsymbol{\Phi}(\mathrm{t},\mathrm{t0})\begin{bmatrix}\mathbf{0} & \mathbf{I}\\ \mathbf{G(t)} & \mathbf{0}\end{bmatrix}\boldsymbol{\Phi}(\mathrm{t},\mathrm{t0}) \tag{177}$$

Where, the initial condition is given by:

$$\mathbf{I} = \Phi(\mathrm{t}_0,\mathrm{t}_0) \tag{178}$$

Cartesian state vectors are

$$\mathbf{r} = \{\mathrm{x\ y\ z}\}^{\mathrm{T}} \tag{179}$$

$$\mathbf{v} = \{\dot{\mathrm{x}}\ \dot{\mathrm{y}}\ \dot{\mathrm{z}}\}^{\mathrm{T}} \tag{180}$$

The gradient matrix,

$$\mathrm{G(t)} = \frac{\partial \mathrm{a}(\mathbf{r},\mathrm{t})}{\partial \mathbf{r}} \tag{181}$$

And the accelerations of the orbiting object,

$$\mathrm{a}(\mathbf{r},\mathrm{t}) \tag{182}$$

After successive derivates and simplifications [238], the state transition matrix is given by:

$$\boldsymbol{\Phi}(\mathrm{t},\mathrm{t0}) \approx \begin{bmatrix}\boldsymbol{\Phi}_{\mathrm{rr}} & \boldsymbol{\Phi}_{\mathrm{rv}}\\ \boldsymbol{\Phi}_{\mathrm{vr}} & \boldsymbol{\Phi}_{\mathrm{vv}}\end{bmatrix} = \tag{183}$$

were,

$$\mathbf{\Phi}_{\mathrm{rr}} = \mathbf{I} + (2\mathbf{G_0} + \mathbf{G})\frac{(\Delta \mathrm{t})^2}{6} \tag{184}$$

$$\mathbf{\Phi}_{\mathrm{rv}} = \mathbf{I}\Delta \mathrm{t} + (\mathbf{G_0} + \mathbf{G})\frac{(\Delta \mathrm{t})^3}{12} \tag{185}$$

$$\mathbf{\Phi}_{\mathrm{vr}} = (\mathbf{G_0} + \mathbf{G})\frac{\Delta \mathrm{t}}{2} \tag{186}$$

$$\mathbf{\Phi}_{\mathrm{vv}} = \mathbf{I} + (\mathbf{G_0} + \mathbf{2G})\frac{(\Delta \mathrm{t})^2}{6} \tag{187}$$

$$\Delta \mathrm{t} = \mathrm{t} - \mathrm{t0} \tag{188}$$

$$\mathbf{G_0} = \mathrm{G}(\mathrm{t}_0) \tag{189}$$

The Gradient Matrix, considering the central force and the oblate earth perturbation, J_2, is given by

$$\mathrm{G(t)} = \frac{\partial \mathbf{a}(\mathbf{r}, \mathrm{t})}{\partial \mathbf{r}} = \begin{bmatrix} \frac{\partial \mathbf{a_x}}{\partial_{\mathrm{x}}} & \frac{\partial \mathbf{a_x}}{\partial_{\mathrm{y}}} & \frac{\partial \mathbf{a_x}}{\partial_{\mathrm{z}}} \\ \frac{\partial \mathbf{a_y}}{\partial_{\mathrm{x}}} & \frac{\partial \mathbf{a_y}}{\partial_{\mathrm{y}}} & \frac{\partial \mathbf{a_y}}{\partial_{\mathrm{z}}} \\ \frac{\partial \mathbf{a_z}}{\partial_{\mathrm{x}}} & \frac{\partial \mathbf{a_z}}{\partial_{\mathrm{y}}} & \frac{\partial \mathbf{a_z}}{\partial_{\mathrm{z}}} \end{bmatrix} \tag{190}$$

And the accelerations due to the central force and the J_2 parameter

$$\boldsymbol{a_x} = \frac{-\mu x}{r^3}\left[1 + \frac{3}{2}\frac{J_2 R_e^2}{r^2}\left(1 - \frac{5z^2}{r^2}\right)\right] \tag{191}$$

$$\boldsymbol{a_y} = \frac{y}{x}a_x \tag{192}$$

$$\boldsymbol{a_z} = \frac{-\mu z}{r^3}\left[1 + \frac{3}{2}\frac{J_2 R_e^2}{r^2}\left(3 - \frac{5z^2}{r^2}\right)\right] \tag{193}$$

The partial derivatives are [240]:

$$\frac{d\boldsymbol{a_x}}{dx} = \frac{\mu}{r^5}\left[3x^2 - r^2 - \frac{3}{2}J_2 R_e^2 + \frac{15}{2}\frac{J_2 R_e^2}{r^2}(x^2 - z^2) - \frac{105}{2}\frac{J_2 R_e^2}{r^4}x^2 z^2\right] \tag{194}$$

$$\frac{d\boldsymbol{a_x}}{dy} = \frac{3\mu xz}{r^5}\left[1 + \frac{5}{2}\frac{J_2 R_e^2}{r^2} - \frac{35}{2}\frac{J_2 R_e^2}{r^4}z^2\right] \tag{195}$$

$$\frac{d\boldsymbol{a_x}}{dz} = \frac{3\mu xz}{r^5}\left[1 + \frac{15}{2}\frac{J_2 R_e^2}{r^2} - \frac{35}{2}\frac{J_2 R_e^2}{r^4}z^2\right] \tag{196}$$

$$\frac{d\boldsymbol{a_y}}{dx} = \frac{d\boldsymbol{a_x}}{dy} \tag{197}$$

$$\frac{d\boldsymbol{a_y}}{dy} = \frac{y}{x}\frac{d\boldsymbol{a_x}}{dy} + \frac{\boldsymbol{a_x}}{x} \tag{198}$$

$$\frac{d\boldsymbol{a_y}}{dz} = \frac{y}{x}\frac{d\boldsymbol{a_x}}{dz} \tag{199}$$

$$\frac{d\boldsymbol{a_z}}{dx} = \frac{d\boldsymbol{a_x}}{dz} \tag{200}$$

$$\frac{d\boldsymbol{a_z}}{dy} = \frac{d\boldsymbol{a_y}}{dz} \tag{201}$$

$$\frac{d\boldsymbol{a_z}}{dz} = \frac{\mu}{r^5}\left[-r^2 + 3(z^2 - \frac{3}{2}J_2R_e^2 + 15\frac{J_2R_e^2}{r^2}z^2 - \frac{35}{2}\frac{J_2R_e^2}{r^4}z^4\right] \tag{202}$$

Markley's Method is then used to propagate each object until the time of closest approach and under the assumption that covariance matrixes are uncorrelated, they can be summed directly when represented in the same reference system.

$$C = C_p + C_s \tag{203}$$

Where C_p is the covariance of the primary object (DSS Platform Navigation) and C_s is the secondary (tracked intruder) RSO. **Figure 38** illustrates the concept of a combined ellipsoid.

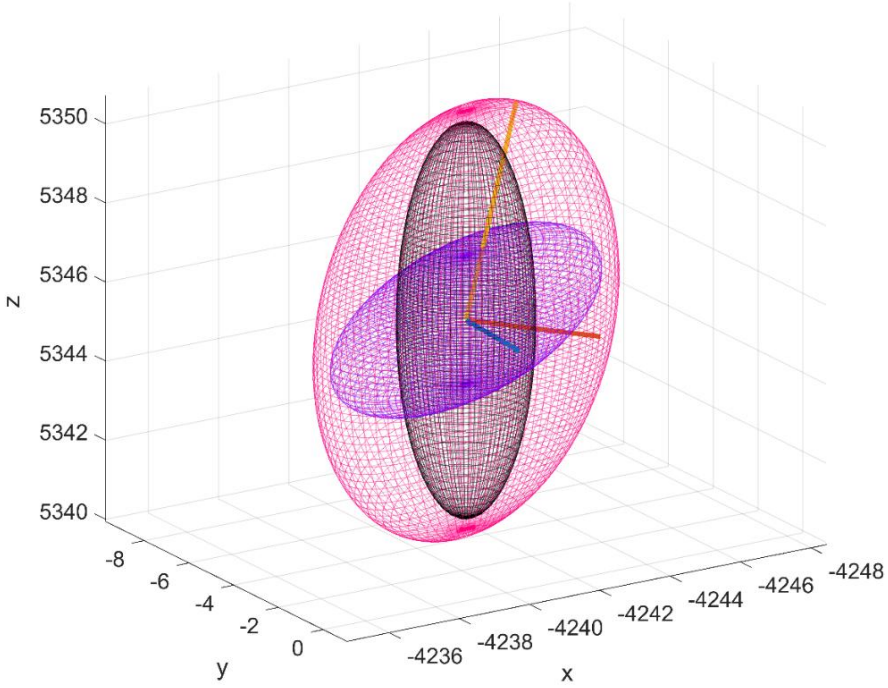

Figure 38 Conceptual illustration of DSS platform (purple), C_p, tracking (black) C_s, total uncertainty volume at the time of closest approach, C, (magenta) and major (orange), semi-major (red) and minor axis (blue) of total uncertainty volume

Following the summation of the uncertainty volumes, the general method to compute the collision probability consists in projecting the combined covariance matrix, C onto a conjunction plane. [241, 242]. A number of approaches exist to define the conjunction plane, where the following approach is taken.

The relative velocity, $\boldsymbol{v}_r$,of the primary object with respect to the secondary (debris) is:

$$\boldsymbol{v}_r = \boldsymbol{v}_s - \boldsymbol{v}_d \tag{204}$$

The encounter frame is then defined by the unit vectors.

$$\hat{\boldsymbol{e}}_{\boldsymbol{x}} = \frac{\boldsymbol{v_r}}{|\boldsymbol{v_r}|} \quad \hat{\boldsymbol{e}}_{\boldsymbol{y}} = \frac{\boldsymbol{v_s} \times \boldsymbol{v_d}}{|\boldsymbol{v_s} \times \boldsymbol{v_d}|} \quad \hat{\boldsymbol{e}}_{\boldsymbol{z}} = \hat{\boldsymbol{e}}_{\boldsymbol{x}} \times \hat{\boldsymbol{e}}_{\boldsymbol{y}} \tag{205}$$

The position of the DSS Platform with respect to the debris is

$$\boldsymbol{r_{ds}} = \boldsymbol{r_s} - \boldsymbol{r_d} \tag{206}$$

The probability of collision is then computed along this vector where the conjunction plane is the y-z plane. Rotating the summed covariance matrix into the encounter frame, is it possible to express the bivariate Gaussian pdf as

$$f(y,z) = \frac{1}{2\pi\sigma_y\sigma_z\sqrt{1-\rho_{yz}^2}} e^{-\frac{\left(\frac{y}{\sigma_y}\right)^2 - 2\rho_{xy}\left(\frac{y}{\sigma_y}\right)\left(\frac{z}{\sigma_z}\right) + \left(\frac{z}{\sigma_z}\right)^2}{2\left(1-\rho_{yz}^2\right)}} \tag{207}$$

and the probability of collision is

$$P_c = \int_A f(y,z)\, dA \tag{208}$$

For simplicity, a rotation is made to define the y-axis along the $\boldsymbol{r_{ds}}$ vector. The area A is a circle of radius $r_A = r_s + r_d$, primary plus secondary body, called hard body radius. The circle of integration is positioned in (y_e,0) where y_e is the distance from the origin, and thus from the nominal position of the debris. Collision plane geometry is illustrated in **Figure 39**.

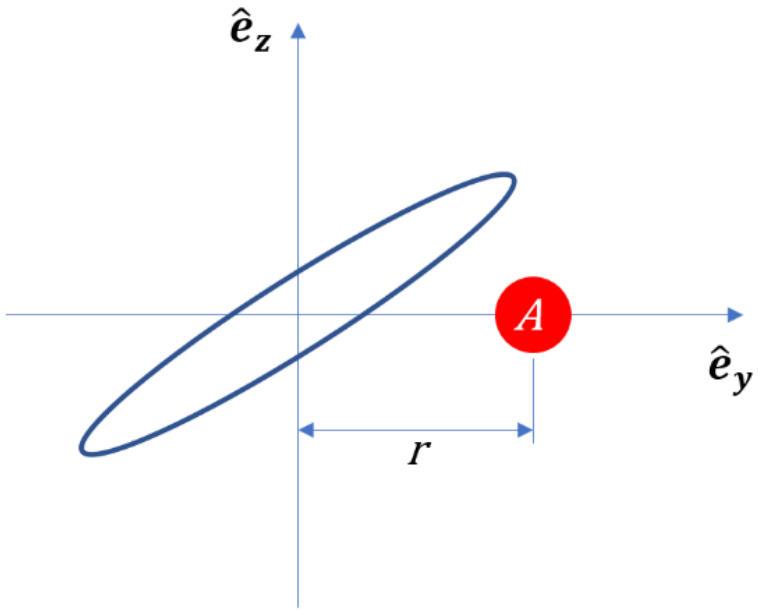

Figure 39. Encounter Plane and the Circle of Integration (hard-body radius).

5.2. Verification Case Studies

This section presents two verification case studies designed to validate the methodologies and algorithms developed for enhancing the safety and operational continuity of space missions in debris-laden environments. The first case study focuses on the uncertainty quantification models developed in Section 5.1.1, exploring the measurement and representation of position uncertainties for Resident Space Objects (RSOs). This study evaluates the performance of ground-based and space-based radar systems in tracking RSOs of varying sizes and distances, demonstrating how uncertainty realism impacts subsequent orbital analysis and decision-making processes. By assessing the limits of Gaussian assumptions in uncertainty modelling, the study highlights critical insights into the fidelity of covariance representations and their implications for Space Domain Awareness.

The second case study examines collision avoidance, utilizing the proposed Particle Swarm Optimization (PSO) based orbital manoeuvre algorithm to mitigate collision risks between a DSS platform and an intruding RSO. This study quantifies the initial uncertainty in position and propagates it to calculate the probability of collision at the Time of Closest Approach (TCA). Based on this analysis, an optimal orbit-raising manoeuvre is developed to reduce the collision probability to an acceptable level, ensuring the safe and efficient operation of the

DSS platform. Together, these case studies provide a comprehensive validation of the proposed methods, demonstrating their effectiveness in addressing key challenges in STM and autonomous spacecraft operation.

5.2.1. Uncertainty Quantification

In the first scenario, radar design parameters were selected based on ground-based radar tracking stations in the SSA SST network whereas in the second case, radar parameters were selected from proposed spaceborne MMW Radar designs. The second case implements an error in variables model under a Gauss–Helmert formulation to combine both tracking the navigation measurements when determining the total position uncertainty of the tracked RSO. In doing so, navigation measurements are assumed to be provided by an onboard GNSS system where corresponding uncertainty values are taken from a LEO GPS accuracy experiment found in the literature [243]. **Table 17** outlines the specific radar parameter and nominal tracking measurements (azimuth and elevation) values for both cases and the spacecraft orbital parameters (at measurement epoch) and associated uncertainty values within the RSW frame. To reflect the advantages of spaceborne MMW radar <10cm RSO size was selected for the simulation, as opposed to the larger debris sizes(>10cm) which have been chosen for the ground station scenario.

Table 17. Ground and Space-based tracking scenario inputs.

Spacecraft Position	**a= 6829km**	**e =0.00001**	**i = 51.6°**	**ω = 90°**	**Ω = 90°**
Navigation Error					
Radial (R) $\sigma_{R_{NAV}}$	13.81m				
In-Track (S) $\sigma_{S_{NAV}}$	4.15m				
Cross-Track (W) $\sigma_{W_{NAV}}$	3.0m				
Nominal Tracking Angle	**Space-Based Radar**		**Ground-Based Radar**		
ϵ_{TRK}	45°		45°		
η_{TRK}	45°		81°		
Fixed Radar Parameters					
Frequency	95 GHz (W band)		442 MHz (UHF)		
Peak transmit power	1200 W		36 MW		

Beamwidth	0.2°	1.3°
Aperture Dimension	1.0m	58.0 m
Noise Figure	4.5 dB	4.5dB
Radar pulse duration	1 μs	1 μs
Transmit antenna Gain	58 dBi	48dBi
Varied Parameters		
Debris Diameter	1, 3, 6 cm	10,20,30cm
Range to Target r_{TRK}	1:60 km	1:850 km

To test the covariance realism of the total position uncertainty the RSO the average Mahalanobis distance metric and the Cramer–von Mises test statistic is computed. Adapting the test procedure outlined in [232] for a sensor-level analysis, the following steps are performed for both cases:

1. Define a range to target and debris size, calculate the performance of the radar system and fuse the tracking + navigation errors using the approach outline in Section 2.1
2. Generate N Monte Carlo points based on the measurement model performance as described in Section 2.3. (10,000 points were chosen in the case of these simulations)
3. Calculate the corresponding average Mahalanobis distance metric (AMD) and Cramer–von Mises (CVM) goodness of fit statistic.
4. Repeat steps 1–3 for every range to target for each RSO size.
5. Plot the averaged uncertainty metric (AMD) and the Cramer–von Mises test statistic versus range to target for each tracked RSO size
6. Determine the range to target when the averaged uncertainty metric and the Cramer–von Mises test statistic first pierce a pre-defined confidence interval (Table 2)– and declare that the covariance realism has broken down under the corresponding sensor performance.

Figure 40 and Figure 41 display the results of the above uncertainty realism test procedure which can be interpreted as follows: The calculated degree of the CVM test and AMD metric are plotted for each range to target as well as the confidence interval for each. Until the first point of intersection from either realism test and the corresponding confidence interval, the uncertainty distribution can be assumed to represent the calculated RSO covariance matrix under the chosen level of confidence. In both the ground and space-based cases, a confidence level of 99% was chosen arbitrarily. Both figures demonstrate that for all tracked RSO sizes,

the CVM test statistic with the corresponding confidence interval provides a more restrictive statistical measure, when compared against the first-moment AMD metric. This is not a surprising result as the CVM test statistic is determined from the empirical CDF measurement model, giving more indication on the actual shape, size and orientation of the distribution. In turn the CVM test can distinguish finer discrepancies between the empirical (CDF) and the theoretical uncertainty distribution (covariance) when compared to the AMD metric. Table 18 outlines the difference in the range to target when between the CVM test statistic and AMD metric at the 99% confidence interval.

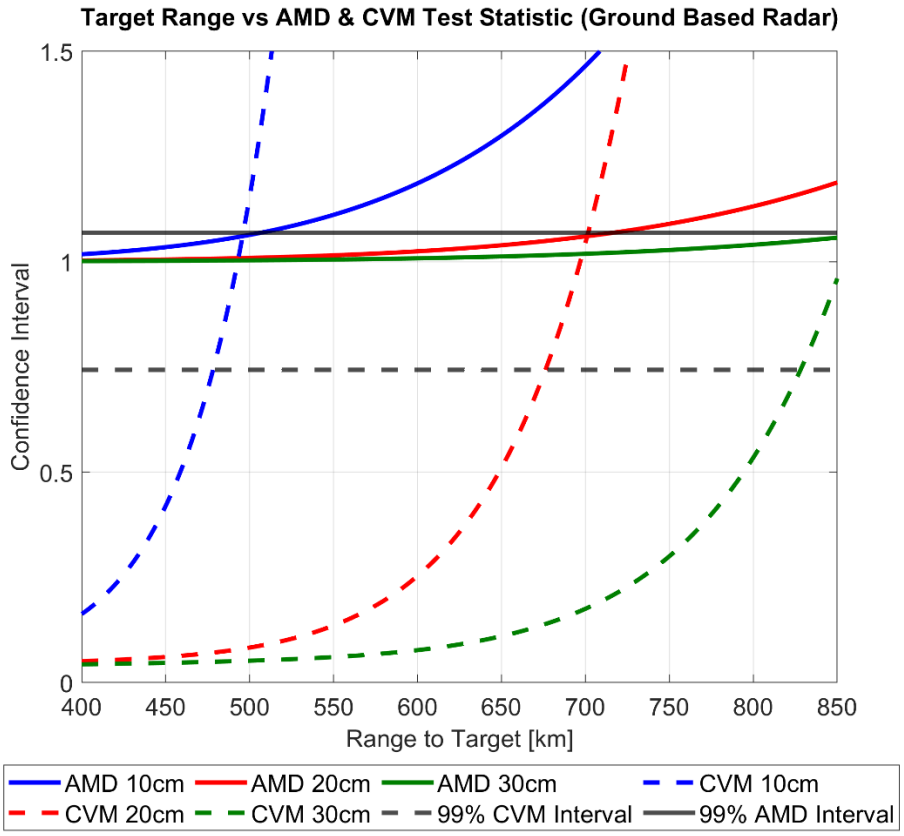

Figure 40 Covariance realism of theoretical uncertainty volume as a function of range to target for Ground-Based Radar.

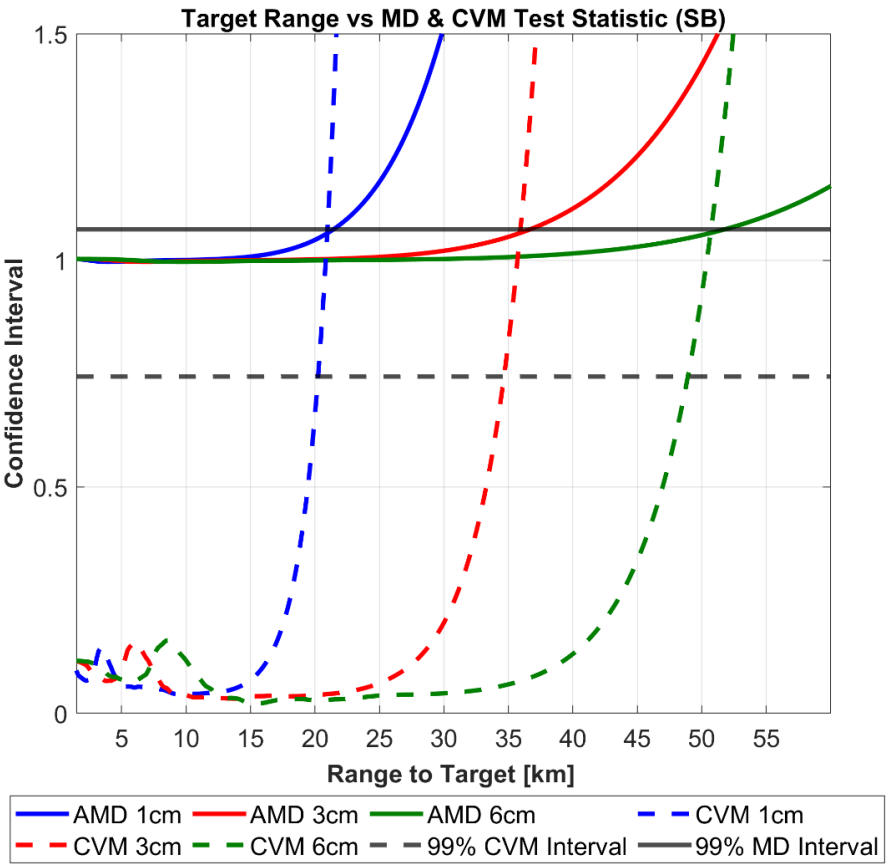

Figure 41. Covariance realism of theoretical uncertainty volume as a function of range to target for Space-Based Radar.

Table 18. Max Range-to-Target for 99% Average Mahalanobis Distance (AMD) and CVM Covariance Realism Test Statistic.

	Space-Based Tracking			**Ground-Based Tracking**		
RSO Size	**1cm**	**3 cm**	**6 cm**	10 cm	20 cm	30 cm
AMD range [km]	21.393	36.689	51.825	505.54	716.61	876.80
CVM range [km]	20.027	34.618	48.958	479.15	677.03	827.80
Δ range to target [km]	1.115	2.071	2.867	26.38	39.57	49

Due to the significant impact on the calculated SNR of the radar system, assessing the covariance realism in relation to the specific range to target and debris size provides a practical relationship to defining an acceptable magnitude of measurement errors. Figure 42 and Figure 43 illustrate this relationship for the ground and space-based case, where the magnitude of range and angular errors and corresponding 99% CVM interval are plotted against the range-to-target for each debris size.

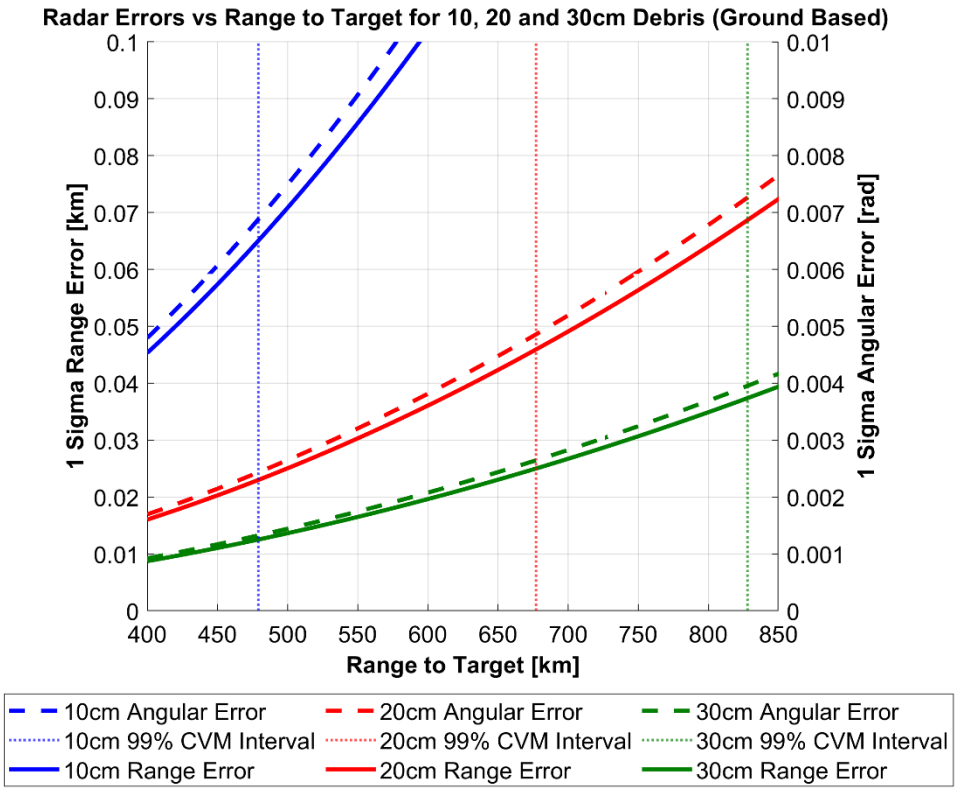

Figure 42. Ground Based Radar range and angular errors as a function of range to target

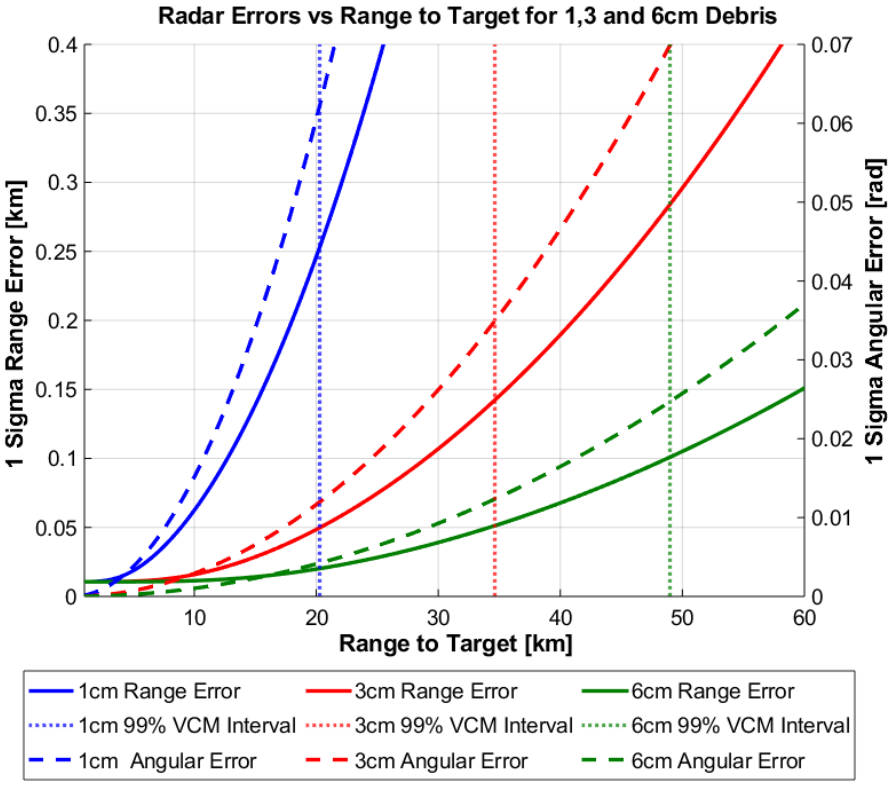

Figure 43. Space Based Radar range and angular errors as a function of range to target

The confidence interval represents the point at which the original curvilinear distribution described by the radars spherical uncertainty can no longer be truthfully represented as rectilinear covariance within the cartesian ECI system. To illustrate this point further; Figure 44 a) shows the generation of Monte Carlo points used to generate the empirical distribution for the 6cm RSO at the 99% CVM confidence interval for the 6cm debris size. The calculated Cartesian covariance matrix inflated to 3 sigma is then overlaid as an ellipsoid centred about the nominal RSO position. As expected, the corresponding contour map Figure 44 b) illustrates that the Monte Carlo points conform to a rectilinear Gaussian distribution and therefore the corresponding uncertainty can be represented in terms of covariance within the ECI cartesian frame. Conversely, Figure 44 c), d) illustrates the distribution corresponding to range to 6cm target far beyond the 99% CVM confidence interval. The distribution is now morphed from an ellipsoidal shape to a “bananoid”, a curvilinear Gaussian distribution inherent to the radar measurement uncertainty model. Although this demonstrates the extreme case, meaning practically that the radar would not be used under these conditions due to the large uncertainty of the measurements, the figures aim to show physically what it means when the distribution becomes non-gaussian at the sensor level (in the rectilinear sense) and therefore cannot be described in terms of cartesian covariance.

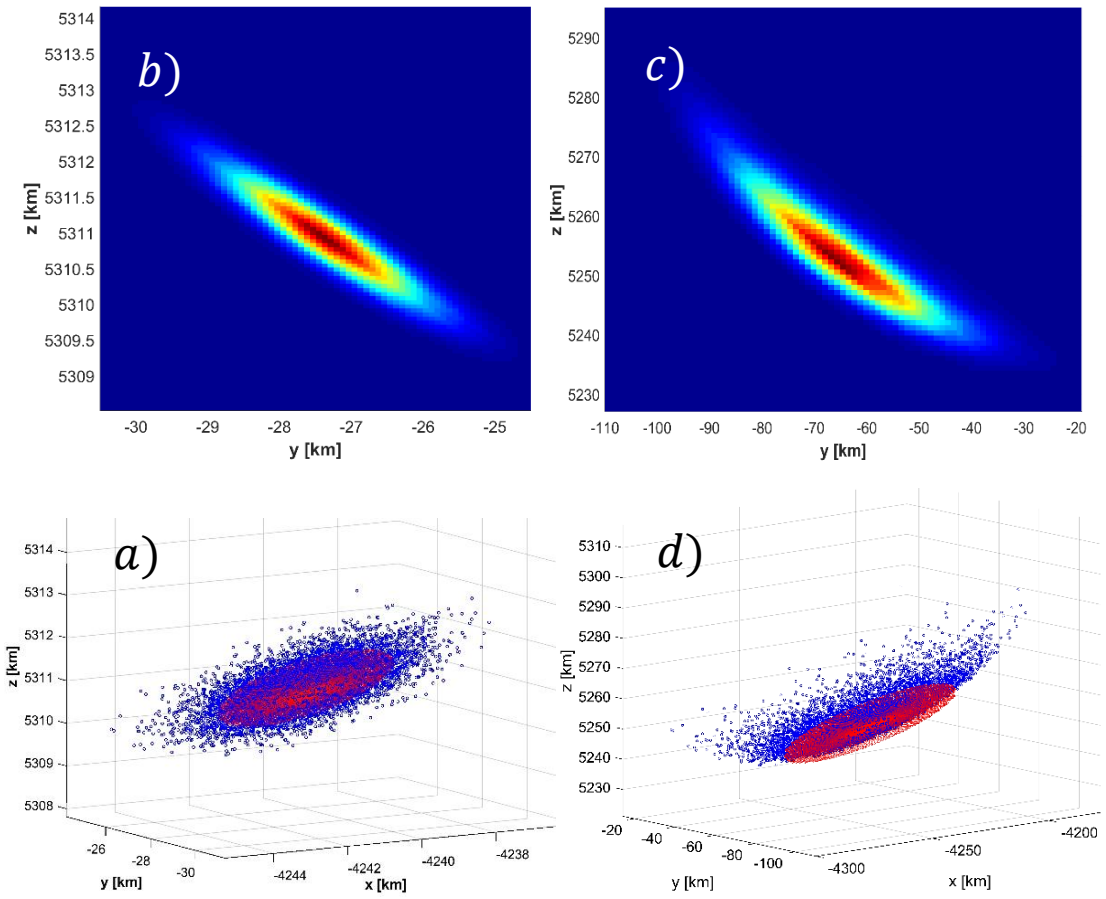

Figure 44 Monte Carlo generated distribution and corresponding contour maps for the 6cm debris. Clockwise from bottom left: (**a**) 99%CVM Monte Carlo distribution (**b**) 99%CVM Contour Map**,** (**c**) >>99% CVM Confidence Interval Contour Map (**d**) >>99% CVM Confidence interval Monte Carlo distribution.

As previously highlighted, the importance of quantifying uncertainty at the sensor level is to meet the required assumptions of covariance realism for SSA activities such as orbit determination and uncertainty propagation for RSO collision probability analysis and subsequent avoidance activities. In effect, covariance realism at the sensor level provides a means of covariance "fidelity" to these processes. Previously published studies on covariance realism for orbital propagation demonstrate that the initial AMD and CVM metric should tend unity and (1/12k) respectively to demonstrate that a large enough Monte Carlo sample size of the initial covariance matrix (of RSO position uncertainty) has been taken. Nonetheless, the sensor level analysis performed demonstrate that the initial covariance matrix used for these analyses may vary in its actual realism/gaussianity if its intrinsic observation uncertainties have been mapped from its original coordinate system. For example, if an observation is taken under a certain tracking performance (in the case of this

paper, RSO size and range-to-target), the subsequent covariance goodness of fit determined by the CVM test will lay somewhere along plot as shown in Figure 40 and Figure 41. Analysis of the effect of varying Gaussianity as inputs to typical SSA analysis(orbit determination, probability of collision) is beyond the scope of this paper and will be addressed in future research.

Turning attention now specifically to the second case of an SBSS platform. Using the Gauss–Helmert errors in variables framework a measurement model was produced that combines both navigation and tracking errors to generate a position uncertainty of the tracked RSO. We are interested in identifying the influence of the navigation error on the total position uncertainty and any effect on the covariance realism tests described previously. In doing so, plotting the range to target against the ratio between NAV+TRK (Q_{TOT}) and TRK (Q_{TRK}) uncertainty indicates the total effect of the navigation error on the total uncertainty of the RSO. This is done by taking the eigenvalues of each respective covariance matrix (Q_{TOT}, Q_{TRK}) and summing them in an RSS manner, where the ratio between the two is then calculated.

$$TOT_{RSS} = \sqrt{\lambda_{1_{Q_{TOT}}} + \lambda_{2_{Q_{TOT}}} + \lambda_{3_{Q_{TOT}}}} \tag{209}$$

$$TRK_{RSS} = \sqrt{\lambda_{1_{Q_{TRK}}} + \lambda_{2_{Q_{TRK}}} + \lambda_{3_{Q_{TRK}}}} \tag{210}$$

From Figure 45 , it is clear the navigation error uncertainty has a strong influence on the total error uncertainty volume at close target ranges, however as the range increases the ratio between the two uncertainty volumes decreases asymptotically to 1. This result is expected as the navigation error is assumed fixed during observation however the calculated radar performance is dynamic and heavily dependent on the range to target. Not surprisingly, Figure 7 demonstrates that navigation error has

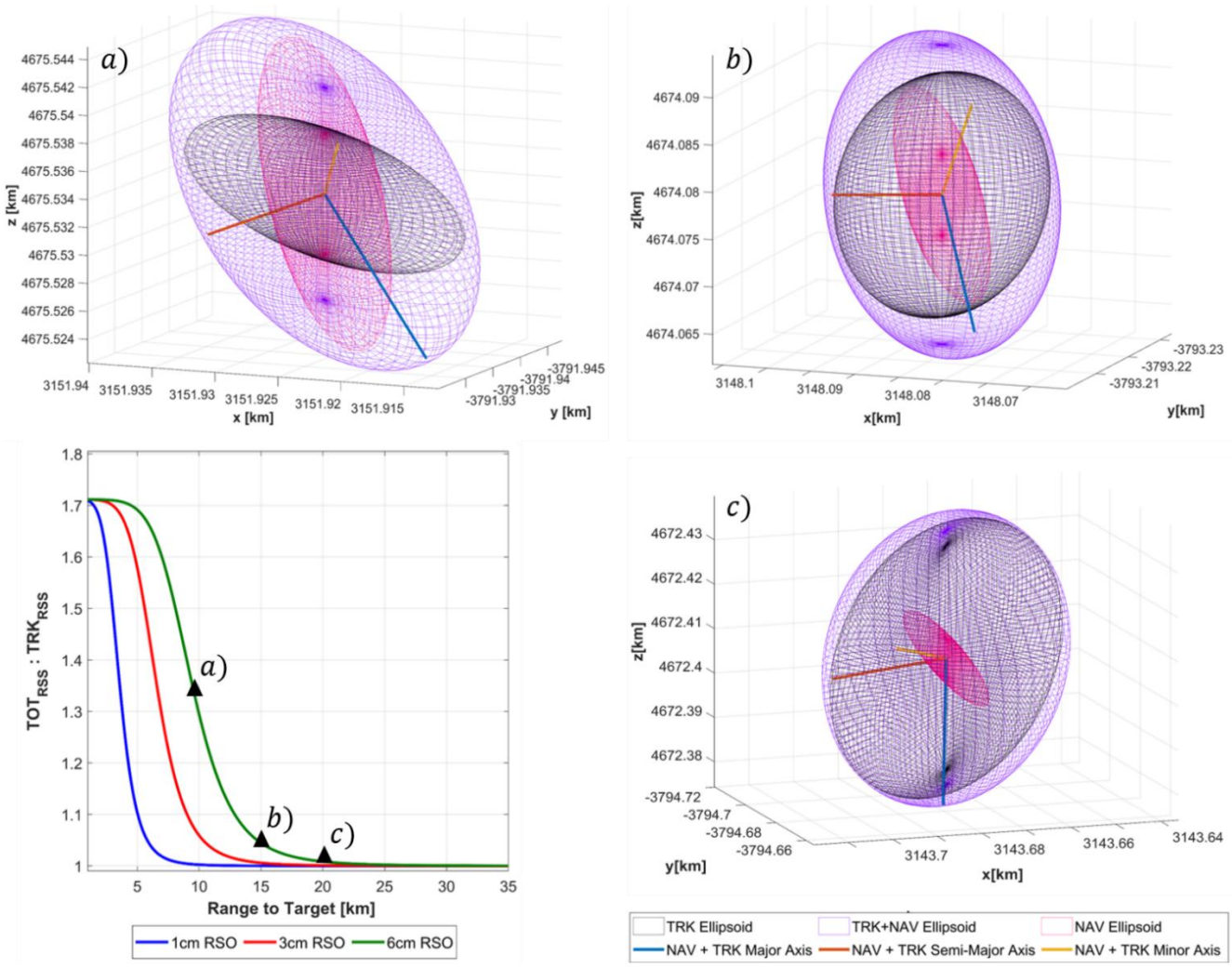

Figure 45. Effect of Navigation errors on total RSO uncertainty of tracked debris (clockwise from top left:). **a**)10 km **b**)15 km, **c**)20 km range to target. In each figure, the magenta, black and purple ellipsoids represent the Navigation, Tracking, and Total (NAV+TRK) uncertainty volumes respectively

.

A significantly larger influence when a higher performance radar configuration is used, which in the case of the SNR-dependent error corresponds to a larger size RSO being tracked. Figure 45 graphically illustrates the influence of navigation uncertainty error on the total uncertainty size and orientation at the 10, 15, 20km range to a 6cm target. At each range value, the navigation (NAV), tracking (TRK) and total (NAV+TRK) are represented as magenta, black and purple respectively. Regarding the effect of navigation uncertainty the covariance realism, we can see that the navigation uncertainty region of influence as defined by the ratio between TOT_{RSS} and TRK_{RSS} asymptotes to unity well before the range to target of the corresponding confidence interval. This indicates that under these specific simulation parameters, the navigation error is not a limiting factor in maintaining Gaussian assumptions.

5.2.2. Optimal Collison Avoidance

Using the models presented in the previous section, the performance of a typical ground-based radar is used to quantify the total uncertainty about an intruding RSO (debris). From this, the uncertainties of both the DSS Platform (based on LEO GPS navigation accuracy) and debris positions are propagated, and a probability of collision is calculated. Based on this analysis, an orbit-raising manoeuvre is calculated to reduce the probability of collision below an acceptable threshold.

To quantify the initial tracking uncertainty, radar parameters were chosen based on available sensor information on ground-based radar tracking stations in the Space Surveillance and Tracking (SST) network (Table 19)

Table 19 Radar performance data used to generate tracking uncertainty.

Radar Tracking Angle (SEZ)	
ε = -45 deg	η = 81 deg
Ground-Based Radar Fixed Parameters	
Frequency	442 MHz
Peak transmit power	36 MW
Beamwidth	1.3 deg
Aperture dimension	58 m
Noise figure	4.5 dB
Radar pulse duration	1 μs
Transmit antenna gain	48 dBi
Radar system losses	15 dB

Assuming the worst case of a single state vector measurement, an initial state vector of the RSO is and subsequent position uncertainty (covariance) is generated (**Table 20**)

Table 20 Ground-based radar tracking accuracy at 600 km of altitude

	Accuracy (1σ)			
Ground-based radar station	Azimuth	Elevation	Range	99% CVM Interval
	38mrad	38mrad	0.035km	TRUE

Assuming that a GNSS system provides navigation measurements for the DSS Platform, the position uncertainty values are taken from a LEO GPS accuracy experiment (Table 21).

Table 21 Spacecraft initial data and navigation errors [243].

Navigation error	
Radial (R) σ_R	13.81 m
In-Track (S) σ_S	4.15 m
Cross-Track (W) σ_W	3 m

By propagation of the nominal state vectors of the DSS Platform and intruder (debris), we can identify a Time and point of closest approach, TCA, PCA, respectively, simply by finding when a predefined distance threshold is breached between both objects. Following the methodology presented, and further outlined in [44], we are then able to propagate the position uncertainty of the DSS platform and secondary (debris) objects to the TCA, combine the covariance and evaluate the collision integral.

Based on a total rigid body radius of 0.85 m (when considering debris of 20 cm of diameter), a probability of collision, P_c, of 0.012 is calculated, well breaching the typically acceptable collision risk level of 10E-5 [244], and therefore an avoidance manoeuvre by the DSS platform is required. **Figure 46** illustrates the effects of moving along they–axis of the conjunction plane on the value of P_c, where the origin represents the estimated P_c with no manoeuvre (head on collision). To reduce the P_c to an acceptable level the DSS platform can either perform an orbit raising or lowering manoeuvre of $\Delta y \simeq 1.68$ km.

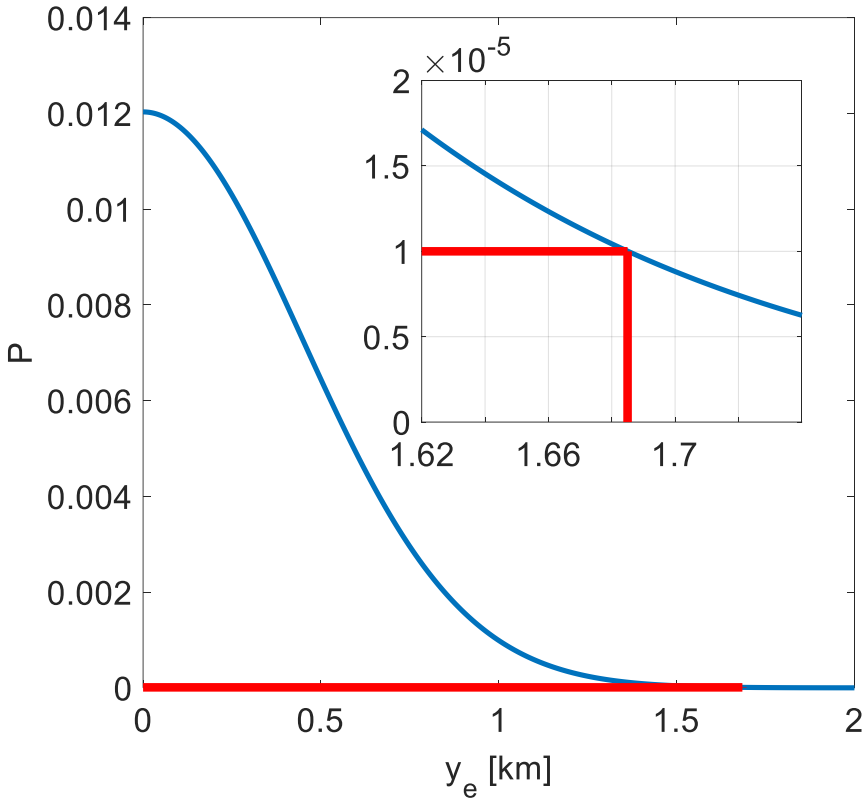

Figure 46 Change in probability of collision between primary and secondary objects with varying degree of orbit raising/lowering manoeuvre.

As identified, the satellite must either perform an orbit raising or lowering manoeuvre to reduce the Probability of collision (P_c) to a typical industry-acceptable level of 10E-5. In this case, an orbit-raising manoeuvre has been chosen, requiring an increase of 1.68km to the semi-major axis of the satellite. **Table 22** provides the initial and final orbital elements after the manoeuvre is performed.

Table 22 Initial and final orbital elements for Orbit raising case study

	Initial state	**Final State**
a	600 km	601.68 km
e	0.00001	0.00001
i	97.4°	97.4°
ω	0°	0°
Ω	0°	0°

In manoeuvring, the DSS is equipped with a Hall thruster producing a constant thrust of 13 mN with 1390 s of specific impulse. Using the proposed approach, an optimal low thrust orbit raising manoeuvre is calculated, The manoeuvre has an estimated

transfer time of 45.92 mins and a computational time of 72.75 seconds for 9240 iterations. **Table 23** outlines the generated control parameters for the constant thrust directions. α and β, that illustrated graphically in **Figure 49**. The subsequent change in the platform's semi-major axis as a fraction of total transfer time is illustrated in **Figure 48**, and the resultant trajectory in the ECI frame is illustrated in **Figure 47**.

The approach allows to formulate minimum fuel orbit raising manoeuvre considering actual conditions from any point on the orbit, considering all key perturbations and any chosen thrust profile. This approach facilitates a more responsive trajectory planning methodology required for autonomous, resilient space architectures.

Table 23 Thrust polynomial coefficients

a		**b**	
$\mathbf{a_0}$	0.3756	$\mathbf{b_0}$	-0.8205
$\mathbf{a_1}$	0.9976	$\mathbf{b_1}$	-0.6503
$\mathbf{a_2}$	0.9951	$\mathbf{b_2}$	-0.5606
$\mathbf{a_3}$	0.9969	$\mathbf{b_3}$	-1.0000
$\mathbf{a_4}$	-0.9969	$\mathbf{b_4}$	-0.9917
$\mathbf{a_5}$	-0.7569	$\mathbf{b_5}$	-0.9999
$\mathbf{a_6}$	-0.7845	$\mathbf{b_6}$	-0.1777

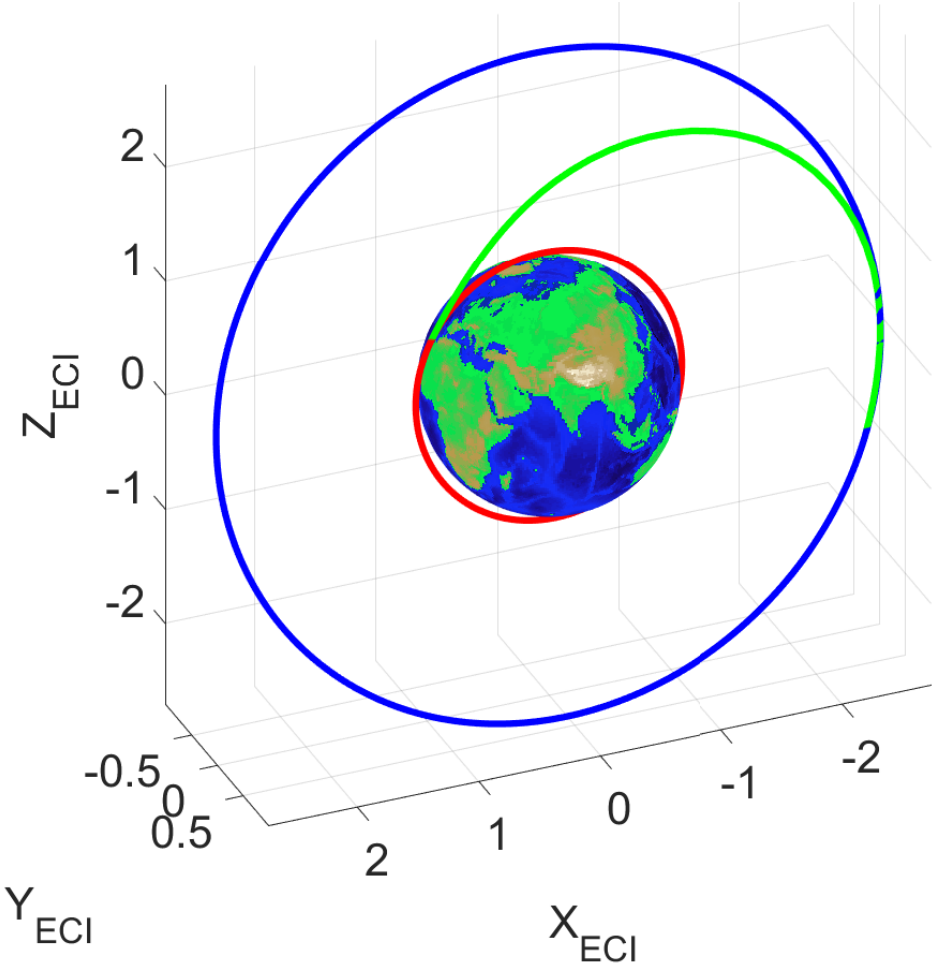

Figure 47 Low-thrust Optimal Orbit-raising maneuverer for collision avoidance- (not to scale)

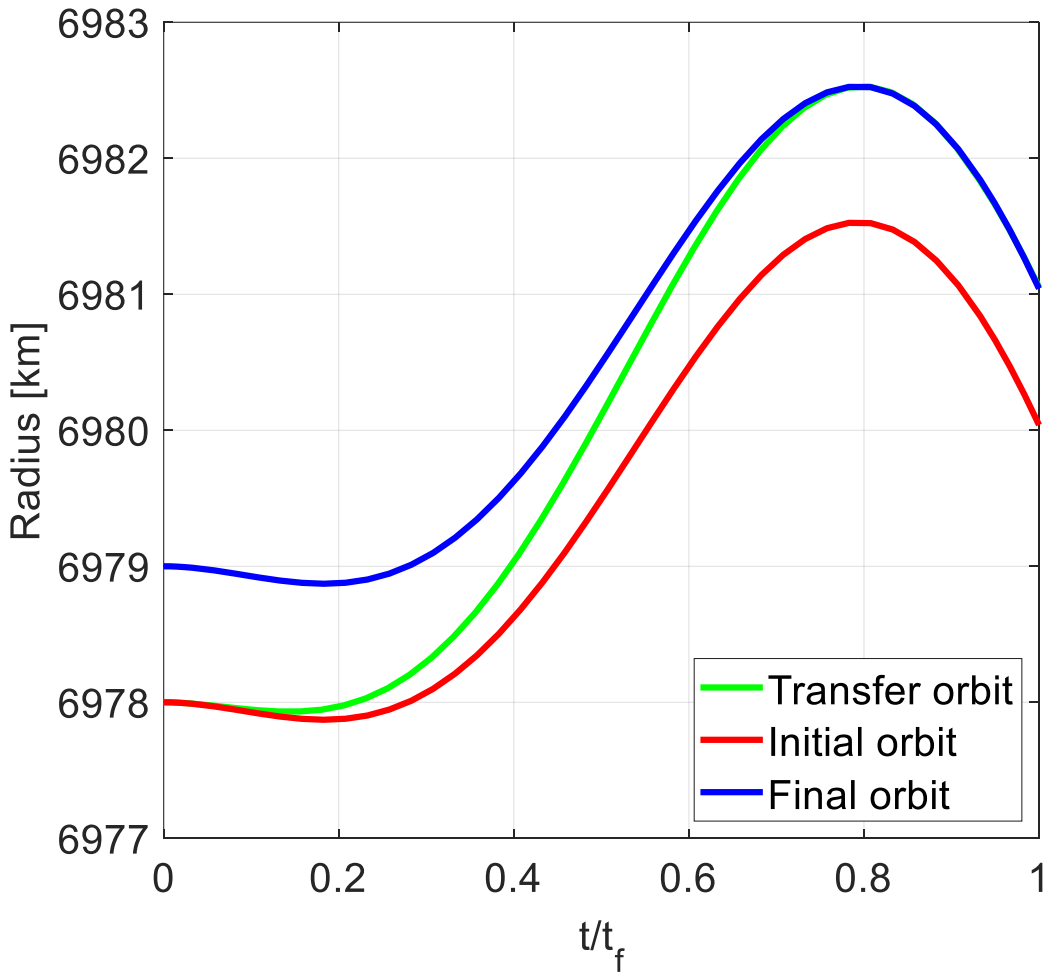

Figure 48 Semi-major axis of initial, final and performed transfer orbit against the fraction of total transfer time.

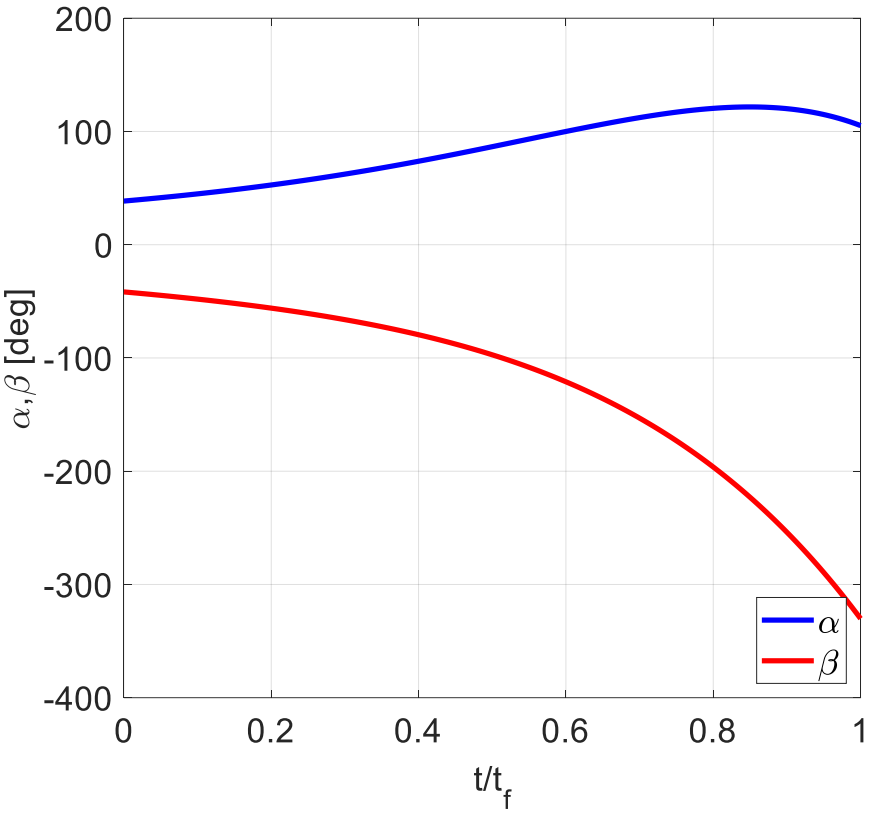

Figure 49 Orbit raising control angles against the fraction of the total transfer time

5.3. Conclusions

This chapter presented a comprehensive framework for collision avoidance autonomy, addressing Objectives 3 and 4 by integrating uncertainty quantification with onboard trajectory and attitude planning for Space-Based Space Surveillance (SBSS) missions. The proposed methodology establishes a robust foundation for accurate collision prediction and adaptive avoidance strategies by combining covariance analysis, probabilistic modelling, and trajectory optimization.

By accurately modelling both parameter value uncertainty (aleatoric) and sensor performance limitations, the framework ensures realistic uncertainty representation for Resident Space Object (RSO) tracking. Covariance realism studies provided critical insights into the influence of sensor performance on Gaussian uncertainty assumptions, delivering a dual perspective: top-down, through performance requirements, and bottom-up, through the explicit quantification of model-based uncertainty. This integrated approach not only enhances confidence in RSO positional accuracy but also facilitates building trusted autonomous systems capable of supporting future Space Traffic Management (STM) operations.

The chapter further demonstrated the integration of onboard trajectory optimization algorithms, such as Particle Swarm Optimization (PSO), with real-time uncertainty quantification. By leveraging high-order polynomial parameterizations, the proposed method ensures efficient and adaptive trajectory and attitude planning under dynamic mission conditions. This integration allows platforms to effectively respond to stochastic uncertainty and unforeseen events while maintaining mission goals and operational constraints.

Validation through case studies revealed the framework's effectiveness in reducing the risk of collision, improving RSO positional confidence, and ensuring safe satellite operations. The results highlighted the importance of dynamic sensor performance characterization, showing that tracking conditions significantly impact uncertainty realism and the quality of decision-making processes in STM and Space Domain Awareness (SDA).

Future work will extend these covariance realism studies to focus on space-based optical sensors under varying physical and geometric constraints. This will enhance understanding of sensor-specific uncertainty behaviour and its influence on the overall framework, further refining its capability to support SBSS missions and STM operations.

Chapter 6

Mission Planning Autonomy Design

This chapter outlines the design of an intelligent mission planning system intended to support increasing levels of onboard autonomy, to enable global coordination within a Space-Based Sensor System (SBSS) mission for enhanced Space Domain Awareness (SDA). The chapter then discusses the implementation of autonomous mission planning for SBSS using a distributed Ant Colony Optimization (ACO) method, which facilitates both self-adaptation and coordination between spacecraft. A representative verification case study is also presented to assess the system's performance, followed by a summary of key findings that highlight the system's potential benefits and areas for further development.

The contents of this chapter have been published in part in the following:

- **S. Hilton**, K. Thangavel, A. Gardi, and R. Sabatini, "Intelligent mission planning for autonomous distributed satellite systems," Acta Astronautica, vol. 225, pp. 857-869, 2024.

- E. Lagona, **S. Hilton**, A. Afful, A. Gardi, and R. Sabatini, "Autonomous Trajectory Optimisation for Intelligent Satellite Systems and Space Traffic Management," *Acta Astronautica,* 01/25 2022, doi: 10.1016/j.actaastro.2022.01.027.

6.1. Background

One of the core supporting functionalities for Trusted Autonomous Space Operations (TASO) is the parallel evolution of the control and coordination of spacecraft, directly reflected in the design and operation of increasingly intelligent Mission Planning Systems (MPS). MPS are complex cyber-physical systems that compile and translate the requests of the user(s) through to executable actions performed by the spacecraft [25]. Traditional MPS employ a deliberative (pre-planned) nature, allowing the production of highly optimal task sequences given estimated environmental conditions. Nonetheless, this approach does not provide the flexibility for a spacecraft to react truly autonomously to a dynamic, uncertain mission environment. Such an approach does not reflect the philosophy behind the use of DSS, and therefore the implementation of current ground station command and control system architectures will not be beneficial. To truly meet the needs of the defence sector and scientific community, DSS require an evolution of mission planning from deliberative approaches to one that enables adaptive Systems of Systems (SoS), DSS mission architectures [25][245] In the following sections we present the key aspects of the Intelligent mission planning approach. We first present the background on mission planning approaches, highlighting the key design features required for the architecture proposed in Chapter 4. The formulation of the mission planning problem for sensor

tasking is then presented which is then expand on the S-DSBSS architecture. Key adaptive interfaces to intelligent mission planning approach are then discussed in detail. The Ant Colony Optimisation algorithm for the single platform sensor tasking problem is then detailed, followed by its extension to a distributed multi-satellite agent approach to enable the coordination feedback loop presented in Chapter 3.

6.1.1. Planning Generation Philosophies

Timeline generation models can be distinguished broadly as either fixed, repeated, or incremental methods. Each of these methods represents a different underlying philosophy to MP and should be chosen to best reflect the specifics of the mission being performed [246].

- **Fixed Plan** is static in its implementation, providing no ability to update the plan during execution –this requires explicit a priori knowledge about the mission environment and a hard-coded approach of how best to navigate it to fulfil mission objectives. A fixed plan approach requires that MP tool be conservative with estimated resources, nonetheless, fixed plans can be of extremely high fidelity as they are generated from computationally expensive algorithms that are limited to offline use due to time constraints.
- **Repeated Planning** provides the MPS with dynamic capabilities. Planning is performed regularly and instantiated during downlink/uplink windows when updated planning requests and related mission information are collected. Repeated planning suits uncertain mission environments, where tactical replanning is required to meet evolving mission criteria. As such, a large amount of trust is placed in the planning automation and optimisation algorithms utilised as in many cases the operator may not be capable in overruling the SoE produced due to the timely, tactical nature of repeated planning. In contrast to fixed planning optimisation approaches, repeated planning is characterised by fast-running algorithms that typically require major modifications to the prior mission timeline.
- **Incremental Planning** concept is based on keeping modifications to the existing timeline to a minimum. Described simply, incremental planning is akin to a "First-come, first served" basis. When a planning request is sent to the MPS, the existing SoE is considered "rigid", and an assessment is made on what events and subsequent requests would have to be modified (moved or removed) to meet new requests. Based on this assessment, the spacecraft operator can then choose how to (or not) accommodate new requests. The obvious shortfall of an important level of supervisory control over timeline modification is the applicability of incremental planning to autonomous operations. This is due to the fact that incremental MP optimisation routines are highly constrained, as well as a general inability of optimisation routines to modify historic entries based on the relative importance of new planning requests.

6.1.2. Periodicity of Mission Planning

The periodicity of the planning process typically reflects the specific mission length itself. Under the definitions provided by the Consultive Committee for Space Data Systems (CCSDS), planning periodicity categories can be grouped under the following:

- **Long-Term Planning:** The planning cycle has a typical duration in the order of several years to several months or even weeks. This planning cycle could be concerned with the overall achievement of the mission objectives, impacted by the long-term spacecraft orbit and attitude planning, and with performing a first iteration of resources and constraints [247].
- **Medium-Term Planning:** This planning cycle has a typical duration in the order of several months to several weeks. This planning cycle could be concerned with the more detailed spacecraft orbit and attitude planning and the allocation of resources, such that the different entities in the mission planning can start the detailed planning, based on more accurate resources [247].
- **Short-Term Planning:** This planning cycle has a typical duration in the order of several weeks to several days or even hours. This planning cycle is typically concerned with the detailed planning of the spacecraft and payload activations based on the final orbit and attitude information, and with checking resources and constraints at the highest detail level, to ensure the output plan is conflict-free and can be executed [247].

A consistent theme among the above approaches is an increasing fidelity of planning outputs inversely proportional to the planning horizon. Although mission-specific, this is fundamentally due to the inability to accurately estimate the future state of an uncertain mission environment, typically limiting the practicality of producing long-term high-fidelity plans as they are likely to be obsolete by the time of execution. This drives the need for a flexible approach to mission planning, which is achieved by performing the planning process simultaneously at each hierarchal level (short, medium, and long term). From this perspective, the mission becomes much more flexible in its ability to dynamically adapt to an inherently uncertain space environment.

6.1.3. Resources and Constraints

Within the context of mission planning, resources are defined as an abstract object that encapsulates a system constraint, typically represented as a capacity [79], i.e. a profile of a physical resource or system variable over time [248]. Modelling of resources and their estimated capacity over the mission plays a significant role in the planning process, as it dictates the availability, capability and safety of a DSS to perform a given task(s). Given the diversity of tasks performed within a DSS system, resource modelling is a deep, heavily researched field. However, following the studies performed by NASA Jet Propulsion Laboratory (JPL) [249] and [248], we can characterise resources and constraints under the following:

- **Atomic Resources** refers to a resource with a binary capacity and can be thought of as defining an opportunity. This means that the resource can only serve one task at a time (in use, or available for use), i.e., the resource level is set to 0 for all other tasks preventing the simultaneous planning. A prime example of atomic resource allocation is the availability of up/down communication links, where a resource level of 1 or 0 would define link window visibility. Additionally, an atomic resource can be used to define an equipment resource, for example, the availability of an antenna for up/down link.
- **Consumable Resources** are resources that can be depleted by more than one task at a time, under the condition that the sum of the tasks does not consume more resources than available. The capacity of consumable resources is formulated as a normalized real number which can be renewable, such as power, energy, memory data storage, or finite such as gas propellent for station-keeping manoeuvres. These are by far the most important and commonly modelled consumable resources in operational and research MPS [68, 250-256]. Additionally, more complex modelling has embodied thermal [257] and attitude [252, 258] observables as a resource.
- **Spatial and Temporal Constraints** are used to further contextualise the (un)availability of atomic and consumable resources to perform tasks, such as timing, ordering and synchronisation activities of subsystems required to achieve cooperative tasks, thermal constraints [250] due to the adverse effect of the sun vector intensity over time, power usage based on predicted recharge capability, data volume, spacecraft pointing conditions for earth observation missions (e.g. cloud cover [259] and sunlight [260], estimated location and timing of up/down link windows.

6.1.4. Optimal Problem Formulation

In general, all MPS aims to solve the following problem: *"Given **m** resources with at least **m** corresponding constraints, fulfil **n** user requests, **i** in the most optimal way possible."* Mathematically, this problem can be formulated as a subset of the nondeterministic polynomial (NP)-hard travelling salesman's problem known as the Knapsack problem [255]:

$$\text{maximise } f(X) = \sum_{i=1}^{n} w_i x_i \tag{211}$$

Subject to resource constraints:

$$\sum_{i=1}^{n} r_i x_i \leq c \tag{212}$$

Where X is a vector of decision variables, x_i, that describes if a request has been scheduled ($x_i = 1$) or not $x_i = 0$. The Knapsack is the most common formulation of the MP problem, which is discussed in greater detail in [261, 262]. Nonetheless,

diversity exists in the literature regarding the exact or Approximate Methods (AM) used to solve the knapsack formulation [252].

- **Exact Methods (EM)** have a distinct advantage of finding the global optimum solution (if it exists). Notable exact methods include the use of Dynamic Programming (DP) methodologies that aim to recursively decompose the MP problem and have been applied to earth observation [251, 263] Nonetheless, DP methodologies have significant drawbacks of high computational cost and exploration time due to the large search spaces associated with complex distributed satellite systems[252].
- **Approximate Methods (AM)** In an attempt to overcome the shortcomings of exact methods, much MP research has been devoted to the use of AM that implement sub-routines that are far less computationally intensive to find a "good" solution to the MP problem within an acceptable runtime. In doing so, Research has focused on the use of traditional greedy [260, 263] and local search [250] methods as well as more contemporary approaches such as tabu search [264], simulated annealing [265], however the use of genetic algorithms and other metaheuristic methods [258, 266-269] is the most common approach. Nonetheless, the performance of approximate methods is strongly reliant on the specific heuristics that guide the search.

6.1.5. Deliberative, Reactive and Hybrid Approaches

The results of MP studies focusing on EO missions have shown that by applying the above optimisation methodologies (the majority using AM), it is possible to generate a mission plan of up to hundreds of heterogenous satellites. However, the studies are simplified by reducing (or removing) the dynamics of the mission, including the modelling of subsystems and operational modes. Most importantly, in these studies the fundamental ***coordination*** of the spacecraft assets (required to complete the mission) is achieved as a direct product of an offline optimisation engine, i.e., the explicit interactions and behaviours of individual platforms behaviours is pre-planned to provide a deterministic output, this is an important concept within MP research and is known as a ***Deliberative Approach***. Historically, MPS architectures for monolithic satellite systems have been deliberative [255, 258, 267], and are performed within the ground segment. Nonetheless, a deliberative architecture is well recognised amongst the MPS research community to not be the correct solution for the coordination and optimisation of future DSS [91]. DSS is envisioned to be resilient (no single point of system failure), mission robust, and provide timely information to users, each of which is based on the ability of some type of onboard autonomous capabilities. By adapting to a dynamic mission environment, spacecraft autonomy then permits a *reactive* to the mission (re)planning problem. In this sense, based on the level of autonomy within the system a mission planning framework ranges across a spectrum from reactive (spontaneous) to deliberative (highly planned) approaches. In practice, this requires platform-level mission planning autonomy that employs EM and AM optimisation methods to include feedback mechanisms that interface with

supporting platform autonomy to effectively adapt to the dynamic environment (internal and external) [252]. In summary the main advantages of introducing reactive elements into the space segment are as follows [69, 91]:

- **Ability to react to unforeseen events not captured in the prior planning process:** if an MPS is comprised only within a ground segment, the spacecraft cannot react to unforeseen events between contact periods with ground station infrastructure. For instance, real-time re-planning capabilities are particularly useful for EO missions that aim to react to dynamic environmental conditions.
- **Ability to measure onboard resources in real-time for optimal allocation**: on-ground planning requires the prediction of the available onboard resources during communication blackout periods. To meet mission safety criteria the prediction is performed under a worst-case scenario of resource consumption/availability, leading to conservative task structures and suboptimal mission performance. Onboard MP capability utilises the real-time monitoring of resources to permit lower-level tasks to be performed that typically could not be accommodated in the conservative pre-planned approach.

Reactive and deliberative DSS MP architectures represent two quite different paradigms. On the one hand, deliberative approaches can produce highly detailed plans of a well-defined problem space whereas reactive approaches are suited to adapting to and exploring a dynamic mission environment. This dichotomy represents a trade-off between optimisation versus adaptation [91] i.e. how a fully reactive DSS architecture can be efficiently coordinated in a dynamic mission environment. A promising solution to this problem is the use of an MP architecture that (smartly) exploits the benefits of both reactive and deliberative elements, this is known as a *Hybrid Approach* (HA). Within the literature, the most applied HA is the ability to re-plan the tasks of the individual spacecraft (deliberatively) based on some reactive capability (e.g., new observations, spacecraft health monitoring) [250, 251, 260, 261]. Nevertheless, individual planning based on individual reactivity is not the end game for DSS, where the real advantage is the ability to dynamically coordinate a constellation, swarm, train or cluster of spacecraft to meet global mission goals [91]. Goals. The DSS research community has recognised that these requirements directly reflect the basic philosophy of Multi-Agent Systems (MAS) [91, 270].

6.1.6. Multi-Agent DSS Mission Planning Systems

The European Space Agency (ESA) study on Distributed Agents for Autonomy (DAFA) aimed to demonstrate the advantages of a MAS framework for DSS where the objectives of the study can be summarised as the following [271]:

1. Demonstrate that agent technology, and in particular distributed agents, can be applied to increase mission performances
2. Demonstrate a methodology to allow the assessment of the impact of introduction of agents in a space system

The study first analysed multiple scenarios with differing mission requirements to quantify which would benefit the most from a MAS framework in terms of the following performance criteria: operational cost, scientific return, responsiveness, timeliness and reliability. The explored missions included a planetary exploration mission representative of the ExoMars programme[272], a formation flying mission similar to the SWARM[273] and DARWIN [274] missions, the Guidance, Navigation & Control (GNC) chain representative of the Deep Space-1 Mission[275], and finally the Global Monitoring for Environment and Security (GMES) programme that aims to provide global, timely information through the harmonization of remote image requests [276]. In all of the assessed performance criteria, it was determined that firstly the ExoMars and secondly the GMES programmes would benefit the most from a MAS framework. Ultimately the GMES scenario was chosen to as the MAS technology demonstration as the ExoMars scenario was deemed out of scope for the project. Nonetheless, by implementing a MAS framework a significant increase in scientific return and responsiveness in emergencies was demonstrated. Importantly, the study called for the use of MAS frameworks at both a space and ground-based autonomy level, where the former will allow spacecraft to perform decision making based on goals commanded from the ground stations, and the ability to react autonomously to complex “in-situ” earth observation situations. In contrast, ground-based agent autonomy will provide the capability to support automated processes, intelligent information management and fault tolerance capabilities. In conclusion, it was the opinion of the authors of the DAFA study that MAS frameworks will undoubtable become an integral part of the software used in operational systems [271].

6.1. System Development

This chapter extends the original architecture of Distributed Satellite Systems (DSS) by refining and expanding the operational loops to incorporate advanced control and feedback mechanisms that enhance the system's autonomy, adaptability, and coordination. Building upon the foundational structure outlined in Chapter 3, this extension introduces detailed interactions between the intelligent mission planning modules and the operational control loops. Figure 50 illustrates the lower-level architecture where each interaction is detailed **Table 24**.

Table 24 Intelligent DSS Operational Loops and extended interactions

	Control		**Feedback**	
Operational Loop	ID	Name/Description	ID	Name/Description
Supervisory	CA1	**Mission Goals**: A control action provided from the ground segment that influences the behaviour of the DSS mission planning autonomy	FB1	**Global Solution Feedback:** feedback provided to the ground station that contains a set of global solutions to the mission planning problem

	CA1a	**Track Importance Weighting:** a subset of the mission goal control action that provides a measure of observation importance on a given RSO	FB1a	**Observation List:** a subset of the global solution feedback that contains each satellites tasking plan (RSO, time of detection and track performance)
	CA1b	**Mission Assurance Constraint/Resource:** a subset of the mission goal control action that encodes a mission reliability-based global figure of merit to dynamically update uptime usage of attitude reorientation systems	FB1b	**Attitude Manoeuvre:** a subset of the global solution feedback that contains the corresponding attitude profile (torquing profile) for each satellite's observation list (torquing profile)
	CA1c	**Tasking Goal:** Tasking goal represented in the form of utility function common to all satellite platforms		
	CA2	**Global Solution Selection:** A control action provided from the ground segment that selects a solution provided by FB1		
Self-Adapting	CA4	**Torque Constraints, Time Thresholds**: a control action provided from the IHMM autonomy module that constraints torque and thresholds time of attitude reorientation systems.		
	CA3	**Proposed Attitude Plan:** a control action provided from each local mission planning autonomy output to a local attitude optimisation engine.	FB3	**Attitude Plan Validation:** feedback on attitude constraint violation provided to the Mission Planning autonomy from the local attitude optimisation autonomy
Coordination	**IO**	**Local SBSS Tasking Plan:** A broadcasted output from each satellite to the DSS network to coordinate RSO observation allocation		
	IOA	**Local Candidate Attitude Plan:** information broadcasted from the local satellite to the DSS network to coordinate RSO observation allocation		
	IOB	**Global Candidate Attitude Plan:** information from each satellite in the DSS network that contains the corresponding observation list		

The **supervisory loop** has been expanded to include granular control actions, such as track importance weighting (CA1a) to guide observation importance, mission assurance constraints (CA1b) to guide autonomous behaviour based on mission reliability assessment, and Mission Goals (CA1c) – a common utility function provided to all satellite platforms. Corresponding feedback mechanisms, such as observation lists (FB1a) and attitude manoeuvre profiles (FB1b), offer enhanced system insights to support supervisory level decision-making (discussed in chapter 7).

The **self-adaptive loop** introduces new control elements, such as torque constraints and time thresholds (CA4), enabling more efficient operation of attitude reorientation systems. Feedback on attitude plan validation (FB3) ensures that proposed plans remain compliant with dynamic operational constraints, further enhancing adaptability.

The **coordination loop** integrates mechanisms for broadcasting (IOA) and receiving (IOB) local candidate attitude plans across the DSS network. These additions facilitate more coordination and allocation of RSO observation tasks among satellites, optimizing system-wide performance.

By extending these operational loops, this chapter details the enhanced interfaces and interactions with the Mission Planning Autonomy, presenting simulation-based case studies to verify the design and evaluate the performance improvements.

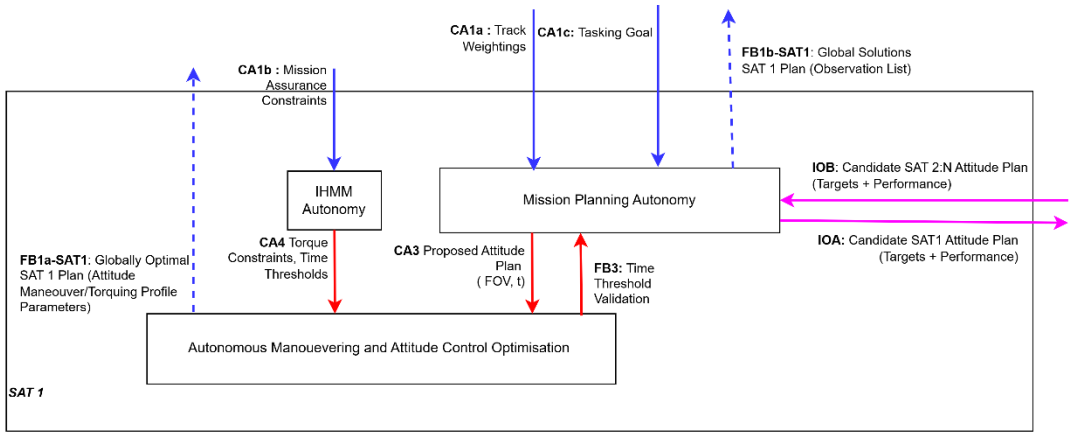

Figure 50. S-DSBSS Architecture detailing platform level control and feedback loops between supporting autonomy elements

6.1.1. Supervisory Loop

The supervisory loop provides a unified objective function that is applied consistently across all satellite platforms within the Distributed Satellite System (DSS). This common tasking objective ensures alignment among platforms, enabling coordination toward a shared mission goal. Similarly, the track weightings, which quantify the relative importance of observing specific Resident Space Objects (RSOs), are also standardized across the network, reinforcing a collective prioritization of current STM observation goals. This section introduces the specific tasking formulation used, based on established methods for sensor tasking in RSO catalogue follow-up, detailing how Field of View (FOV), observation data, and attitude manoeuvre sequences are modelled to achieve optimal task selection.

6.1.1.1. Tasking Goal and Track Weightings

In this article, we use a simplified version of the sensor tasking formulation presented by Bryan et.al [191] to represent the common tasking goal CA1c. This formulation is specific to the follow-up problem for a catalogue of known RSO.

$$U_p = \max \sum_{f=1}^{m_g} \left(\sum_{i=1}^{n} \mu(x_i) P_d(x_i) \right) \tag{213}$$

Equation 3, m_g is the number of viewing directions (field of view – FOV), and n is the number of RSO that can be observed in that FOV over the observation period. A common representation is the use of a directed graph *D* (digraph), where *D* consists of a non-empty finite set *V(D)* of elements called vertices (or nodes) and a finite set of

A(D) of ordered pairs of vertices called arcs (or edges) [277]. The digraph for the sensor tasking problem is as follows. Each vertex represents a different FOV, m_g, where the complete set of vertices make up the possible Field of Regard (FOR) of the platform to provide RSO measurements. The FOR is comprised of a discretised 10x10 grid of FOV where the centre of each FOV represents a specific spacecraft boresight angle of the optical payload. For each FOV, a RSO pass prediction is performed, that extends to the end of the planning horizon. The results from the pass prediction populate the FOV vertex with observation information including an RSO ID, x_i, an estimated time of detection, $t(x_i)$, and a probability of detection, $P_d(x_i)$ that is derived from the sensor performance and observation geometry. The *supervisory loop* control action, CA1a enables the assignment corresponding track importance weighting, $\mu(x_i)$. All vertices are connected through an arc, forming a complete digraph. This means that the spacecraft can manoeuvre the camera boresight angle between any FOV within the FOR over the planning horizon. By traversing this graph, we produce a *path,* a sequence of vertex connected by arcs, in this case, an attitude manoeuvre sequence between FOV at a given time. **Table 25** provides an overview of the graph components in the context of the sensor tasking problem.

It is the job of the optimiser to determine the *optimal* path – a set of finite attitude manoeuvres between platform FOVs over the planning horizon as defined by the objective function U_p. In evaluating U_p, if a task (RSO) has been previously assigned it is not directly evaluated however may still be included in the schedule as a *duplicate opportunistic task*. An opportunistic task is defined as an observation (either a duplicate or unique) that has an estimated observation time between the first (manoeuvre in) and last (manoeuvre out) observation sequence of a specific FOV. Opportunistic tasks are passive observations the satellite platform can make, meaning the satellite does not have to perform an attitude manoeuvre to make the observation. The practical significance of a duplicate opportunistic task is that it supports the further reduction of uncertainty in the orbital environment (permitting resources permit e.g. computing). However, if in the case the duplicate task is estimated to occur first or last in the observation sequence of a specific FOV, the task is not opportune and is defined as a *deliberate duplicate*, as the ACO engine is constraining the satellite agent to move to a new FOV or stay in the current FOV. By penalising a duplicate observation that is observed at the beginning or end of an observation window, temporal resources are freed up and the ACO can schedule other tasks that would have initially conflicted. In this sense, the cost function aims to drive the behaviour (task selection) of the platform to observe the most likely detected highest-ranked RSO. **Figure 51** illustrates the relationship between deliberate, deliberate duplicate, opportune duplicates, and opportune tasks of a single satellite.

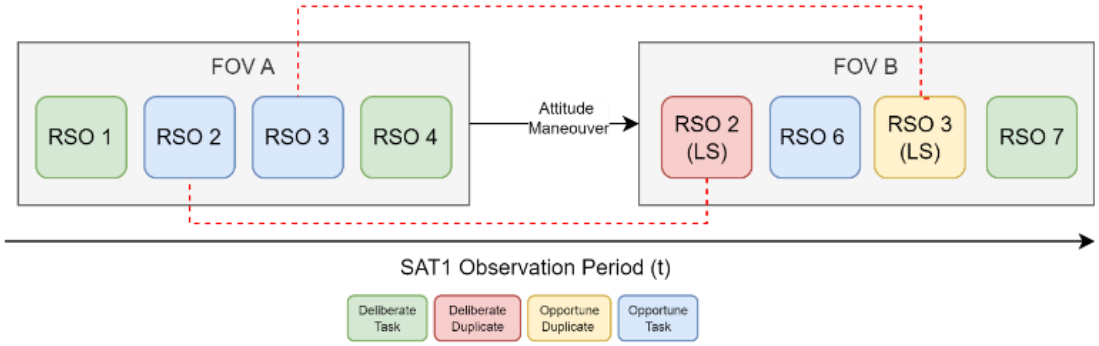

Figure 51. Graphical depiction of deliberate and opportune RSO observation of a single platform over the observation period. Red lines indicate the low-scoring relation between each observation

Table 25 Representation of graph components in sensor tasking problem

Graph Component	Representation	Symbol
Vertex ID	Field of View (FOV)	m_g
Vertex Weight	RSO ID, RSO weighting(s), Probability of detection	$x_i, \mu(x_i), P_d(x_i)$
Vertex Info	Timing information	$t(x_i)$
Arc	Attitude manoeuvre between FOV boresight	f, h
Arc Weight	Utility function evaluation of total attitude manoeuvre	$\tau_{f,h}$
Start Vertex	Not Specified	NA
End Vertex	Not Specified	NA
Max Vertex Selection	5	NA

6.1.2. Self-Adaptive Loop

The maturation of AI algorithms in conjunction with the significant advances in traditional Fault Detection, Isolation and Recovery (FDIR) techniques for space applications are supporting the development of Intelligent Health and Mission Management (IHMM) systems. These new intelligent systems are expected to support self-adaptation capabilities to the satellite through the assessment of safety and mission-critical subsystems health and provide an estimation of Residual Useful Life (RUL). Of particular benefit, will be the monitoring of the Attitude Determination and Control System (ADCS) to provide inputs to interfacing attitude optimisation autonomy. Figure 50 details this interaction between the IHMM and the onboard attitude optimisation through the provision of maximum torque and time threshold information (CA4). Time thresholds represent the maximum life that the ACDS systems can accrue over the planning horizon which corresponds to the number of manoeuvres a platform can perform (number of vertices/FOV selected). Torque

constraints limit the maximum torque an attitude manoeuvre can generate, corresponding to the potential degraded health of ACDS systems. In general, this increases the time taken to perform an attitude manoeuvre

Given these inputs from the IHMM autonomy module, it is the job of the onboard - attitude optimisation engine to take the outputs from the mission planning module - a set of rest-to-rest attitude manoeuvres that represent the boresight directions of each selected FOV (CA3) and generate an optimal torquing profile. In doing so, the objective of the optimisation is to minimise the time required by the manoeuvre, to meet both the self-adaptive information provided by the IHMM module (time thresholds) and the required time between each rest-to-rest manoeuvre to ensure observations can be performed.

As presented in Chapter 4, the optimal attitude manoeuvres between each FOV are determined by iteratively solving the following optimization problem[278]:

Minimize:

$$\mathrm{J} = \mathrm{t_f} \tag{214}$$

Subject to the dynamic and path constraints:

$$\mathbf{J}\dot{\boldsymbol{\omega}} = \mathrm{T}\mathbf{u} - \boldsymbol{\omega}^{\times}\mathbf{J}\boldsymbol{\omega} + \mathbf{M_{perturb}} \tag{215}$$

$$\mathbf{q}^{\mathbf{T}}\begin{bmatrix} -\mathbf{r}^{\mathrm{T}}\mathbf{x}' - \cos\theta_{\mathrm{F}} & [\mathbf{x}' \times (-\mathbf{r})]^{\mathrm{T}} \\ \mathbf{x}' \times (-\mathbf{r}) & [-\mathbf{r}\mathbf{x}'^{\mathrm{T}} + \mathbf{x}'(-\mathbf{r})^{\mathrm{T}} - (-\mathbf{r}^{\mathrm{T}}\mathbf{x}' + \cos\theta_{\mathrm{F}})]\mathbf{I_{3x3}} \end{bmatrix}\mathbf{q} < 0 \tag{216}$$

where:

$\boldsymbol{u} = [u_1 \quad u_2 \quad u_3]^T$ is the control vector.

$\boldsymbol{J}$ is the inertia matrix about its centre of mass in the body frame.

T is the maximum torque provided by the attitude actuators, so that the individual control variables are $-1.0 \leq u_i \leq 1.0$;

$\boldsymbol{\omega}^{\times}$ is the skew-symmetric matrix of angular velocity $\boldsymbol{\omega}$;

$\boldsymbol{M_{perturb}}$ are the perturbation moments (solar radiation pressure and drag);

$\boldsymbol{q}$ is the attitude quaternion with respect to the ECI frame.

$\boldsymbol{r}$ is the satellite position in ECI frame.

$\boldsymbol{x}'$ is the vector of the bright object in the ECI frame.

θ_F is the cone angle of the forbidden zone.

In our adopted solution method, the angular velocity follows a state parametrization adopting Bezier curves and Modified Rodrigues Parameters (MRP) as follows:

$$\boldsymbol{\omega} = 4\Psi^{-1}(\boldsymbol{p})\dot{\boldsymbol{p}} \tag{217}$$

$$\dot{\boldsymbol{\omega}} = 4\left(\Psi^{-1}(\boldsymbol{p})\dot{\boldsymbol{p}} + \Psi^{-1}(\boldsymbol{p})\ddot{\boldsymbol{p}}\right) \tag{218}$$

$$\Psi(\boldsymbol{p}) = [(1 - \boldsymbol{p}^T\boldsymbol{p})I + 2[\tilde{\boldsymbol{p}}] + 2\boldsymbol{p}\boldsymbol{p}^T] \tag{219}$$

$$\dot{\Psi} = \left[-(\dot{\boldsymbol{p}}^T\boldsymbol{p} + \boldsymbol{p}^T\dot{\boldsymbol{p}})I + 2[\dot{\tilde{\boldsymbol{p}}}] + 2(\dot{\boldsymbol{p}}\boldsymbol{p}^T + \boldsymbol{p}\dot{\boldsymbol{p}}^T)\right] \tag{220}$$

Where a seventh-order curve is used to ensure smoothness with differentiability class C^4:

$$\begin{aligned}\boldsymbol{p}(\tau) = \boldsymbol{p}_0(1-\tau)^7 + 7\boldsymbol{p}_1\tau(1-\tau)^6 + 21\boldsymbol{p}_2\tau^2(1-\tau)^5 + 35\boldsymbol{p}_3\tau^3(1-\tau)^4 \\ + 35\boldsymbol{p}_4\tau^4(1-\tau)^3 + \boldsymbol{p}_5\tau^5(1-\tau)^2 + \boldsymbol{p}_6\tau^6(1-\tau) + \boldsymbol{p}_7\tau^7\end{aligned} \tag{221}$$

$$\dot{\boldsymbol{p}} = \frac{d\boldsymbol{p}}{\mathrm{d}\tau}c; \quad \ddot{\boldsymbol{p}} = \frac{\mathrm{d}^2\boldsymbol{p}}{\mathrm{d}\tau^2}c; \quad c = \frac{d\tau}{dt} \tag{222}$$

and τ is the normalized time.

Based on the output of the attitude optimisation engine, feedback (FB3) is then provided to the mission planning autonomy on the candidate attitude plan in terms of its viability in meeting the dynamic constraints initially formulated from the IHMM module (CA4). FB3 then acts to penalise the attitude plan solution provided by the mission planning module if time thresholds are breached due to the number of and/or the magnitude of manoeuvres.

6.1.3. Mission Planning Module

6.1.3.1. Ant Colony Optimisation for the Sensor Tasking Problem

The ACO algorithm is a bio-inspired technique developed by Dorigo and Gambardella [279], based on the observation that an ant colony will find the shortest (optimal) path between the nest and a food source, based on the strength of pheromones left on the path. The ACO technique is based on treating the ants as software agents, that explore solutions of the optimisation utility function by traversing the problem space using a graphical representation. The exploration of each agent or ant, is dictated by two primary mechanisms, the amount of pheromone deposited by previous ants, $\tau_{f,\mathrm{h}}$, and a user-defined meta-heuristic, $\eta_{f,\mathrm{h}}$. Over time (each iteration), the pheromone strength reduces, according to a freely tuned evaporation constant $0 < \rho < 1$. In this chapter, the meta-heuristics value represents the number of common RSO between each FOV (vertex). The ACO algorithm follows three main steps, Path construction, Path Evaluation and Pheromone update.

Path Construction

Beginning from an initial vertex that is either pre-defined or randomly chosen, a set of ants begins a path construction between several vertices over the planning horizon. In our case, the maximum number of vertexes is set to 5, corresponding to 4 attitude manoeuvres. This was chosen to represent the upper bound of acceptable time constraints of the attitude control system provided by the IHMM module. During each

iteration, for each ant agent, the path chosen is dictated by the weighting factor $w_{f,h}(t)$ as shown in Equation (13).

$$w_{f,h}(t) = \frac{\left[\tau_{f,\mathrm{h}}(t,r)\right]^{\alpha} \cdot \left[\eta_{f,\mathrm{h}}(t,r)\right]^{\beta}}{\sum_{k=1}^{N}\left[\tau_{f,\mathrm{k}}(t,r)\right]^{\alpha} \cdot \left[\eta_{f,\mathrm{k}}(t,r)\right]^{\beta}} \tag{223}$$

In equation (4), f and h are the current and set of viewing directions (FOV), *N* is the total number of potential viewing directions, where *t* denotes the specific ant agent. α and β are the pheromone and heuristic weights respectively, where the value of each is chosen depending on whether a more exploratory or faster-converging solution is preferred. The proceeding grid field is chosen by evaluating the weighting factor probabilistically through a roulette wheel-type selection.

Path Evaluation

Upon constructing an attitude manoeuvre sequence (path), each ant agent evaluates the proposed path using the utility function, U_p and associated constraints.

Pheromone Update

After the evaluation of the utility function for each sequence generated by each ant, the pheromone map, $\tau_{f,\mathrm{h}}(t,r)$, is updated according to equation (14) where r represents the pheromones field for each attitude transition, i.e. $r(1)$ represents the transition between the first and second FOV. Having multiple pheromone fields is important as it allows us to represent the temporal dependency between the observed sets of RSO in each FOV sequence. Figure 52 illustrates the multi-pheromone map approach for an example transition between FOV A, D, F and B.

$$\tau_{f,\mathrm{h}}(t,r) = (1-\rho)\cdot\tau_{f,\mathrm{h}}(t-1) + \triangle\,\tau_{f,\mathrm{h}} \tag{224}$$

$$\triangle\,\tau_{f,\mathrm{h}} = \sum_{j=1}^{s(f,h)} \frac{U_P}{Q} \tag{225}$$

$\triangle\,\tau_{f,h}$ is the expected value gained by each agent for the selected FOV. $s(f,h)$ is the number of agents that chose the viewing window at that step (r) and Q is a scaling factor that is chosen as the total number of RSO in the catalogue. During this update, the pheromone strength from the previous map is decayed according to the evaporation rule, $(1-\rho)\cdot\tau_{f,\mathrm{h}}(t-1)$, to reduce the value of the pheromone growing uncontrollably. After each iteration the highest value of U_P generated by the set of ant agents is recorded and successively replaced when higher values are found. The output of this optimisation process is a sensor tasking plan for the DSS platform.

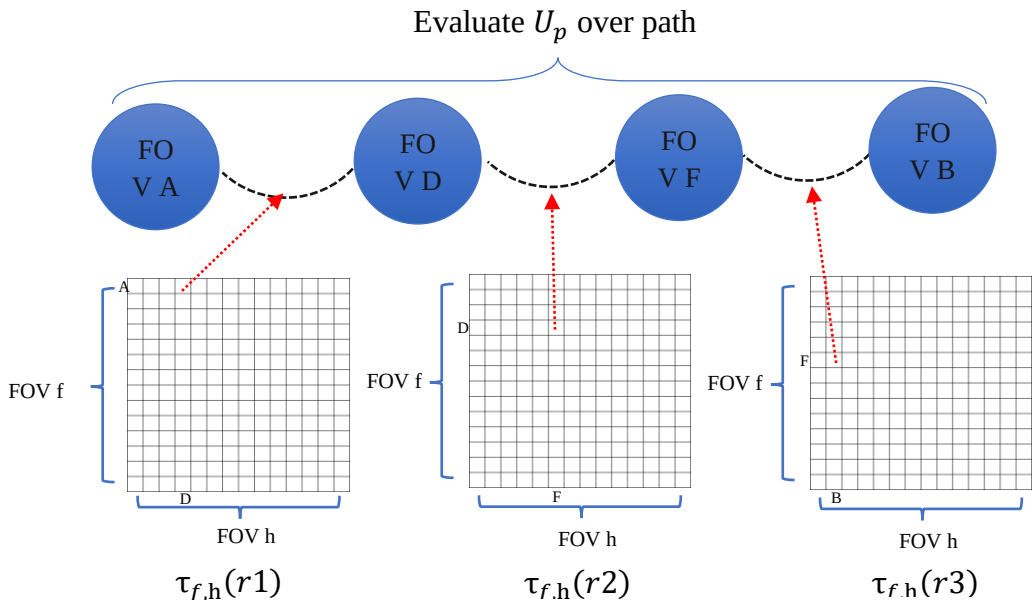

Figure 52 Relationship between graph components and multi-pheromone map approach.

6.1.4. Coordination Loop

While the supervisory controls introduced in the previous section establish a unified framework for mission goals and track weightings across the DSS SBSS mission, the inherent differences between individual satellite platforms—such as orbital positions, attitude control capabilities, and onboard resources—create distinct decision spaces for each. These differences mean that while all platforms aim toward the same global objective, their specific task schedules must account for unique operational contexts.

The coordination loop addresses this by synchronizing tasking plans across the DSS network. Each satellite represents the tasking problem as a graph, with vertices denoting Field of View (FOV) bins populated by a set of Resident Space Objects (RSOs). Although all platforms share consistent track importance weightings, variations in estimated detection times and probabilities arise due to differences in platform position and orientation, leading to diverse tasking solutions.

To optimize global performance and minimize redundant observations, the coordination loop employs a Distributed Ant Colony Optimization (ACO) approach. By sharing task schedules and performance metrics (e.g., detection probabilities) via intersatellite links or ground stations, satellites can identify and adjust low-scoring duplicate tasks. This fosters cooperation while enabling satellites to capitalize on unique, opportunistic observations within their decision spaces.

6.1.4.1. Distributed ACO for Dynamic DSS Coordination

Based on the dynamics of each platform, each satellite has a different view of the problem space, expressed as a graph, where each vertex contains the pool of available tasks. As described, these tasks populate the FOR of the spacecraft which is discretised into FOV "bins". Each bin is associated with a finite number of RSO, each with an ID and track importance weighting, estimated time of detection and probability of detection. The track importance weighting is a constant global parameter, common to all FOV (that the RSO appears in) for all spacecraft platforms, however the estimated time of detection $t(x_i)$ and probability of detection $P_d(x_i)$ are unique to each FOV bin for all spacecraft. In the context of this distributed SBSS mission, we are interested in coordinating the behaviour of all platforms to minimise task duplicates, and in turn, maximise the global DSS utility. In doing so, we extend the previously described local ant colony optimisation through the following multi-agent approach where each satellite agent's local ACO-based mission planning algorithm is synchronised through an outer coordination feedback loop.

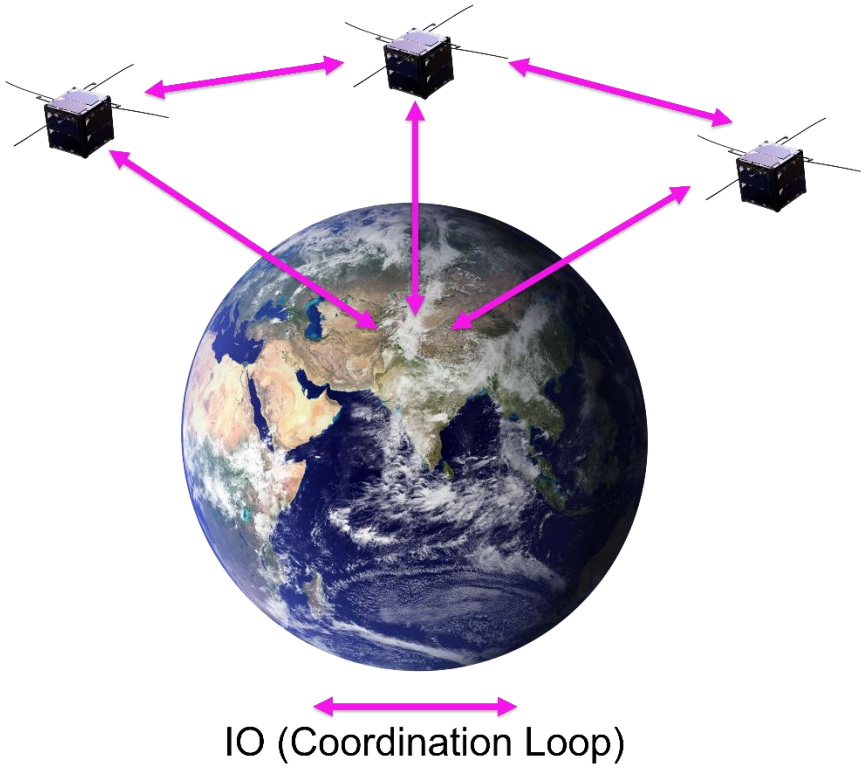

Figure 53 High-level communication architecture to support distributed coordination

Initially, each satellite agent generates their task schedule through the described ACO approach as illustrated in Figure 54, with no awareness of the task selection of other

platforms. The selected tasks and associated performance criteria (probability of detection) are then broadcasted (IOA of the ***coordination loop***) to all other platforms, either via the use of inter-satellite links or a network of ground station facilities (Figure 53). Each satellite agent than assesses the global schedule (IOB of the ***coordination loop***) and identifies if its own proposed schedule contains *low scoring* tasks - at this step, the information used as inputs for each satellite local ACO colony has been synchronised. We define a low-scoring task, as a duplicate RSO observation that has a lower *probability of detection*. If a satellite agent identifies that its proposed schedule includes a low-scoring task, it re-runs its local ACO planning algorithm, including an additional penalty on its lower-scoring tasks (set to zero). If the expected value of the low-scoring task is low, and the observation is *opportunistic*, the satellite will not alter its attitude schedule, as an attitude adjustment would remove other higher-scoring observations within that FOV. This balances cooperation and competition between each satellite agent, as the satellite agent assumes that the "competitor" satellite has found a satisfactory solution and does not actively search to find a higher-scoring version of the task. Figure 55 illustrates the multi-satellite relationship between deliberate, deliberate duplicates, opportune duplicates, and opportune tasks enabled by the coordination loop.

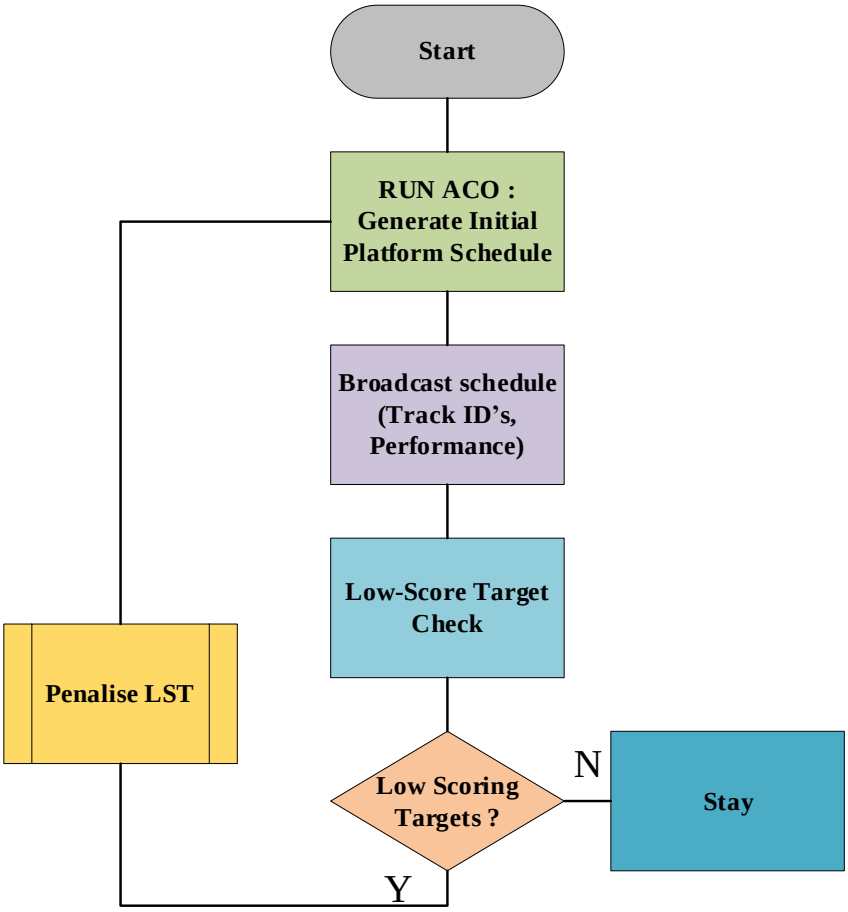

Figure 54 ACO coordination flow chart from the perspective a single satellite agent

However, the provision is also given in the case that a satellite agent does change its attitude manoeuvre sequence and finds a higher-performing version of the duplicate task opportunistically. It will include it in the evaluation of the utility function and its schedule. Another important aspect of the algorithmic design is that the satellite agent does not re-initialise the pheromone maps generated in previous global iterations but adapts the level of pheromone decay based on the number of low-scoring tasks i.e., the degree of change in the mission environment. This allows the satellite agent to dynamically "forget" as much as required about the problem space maintain consistency with previously generated schedules and converge to a global solution. The coordination loop defined by IOA and IOB is converged when each satellite tasking plan does not contain deliberate duplicate tasks.

The global solution can be represented as the utility function. U_g, that evaluates all spacecraft agent schedules, penalising lower-scoring duplicate tasks.

$$U_g = \sum_{k}^{p_s} U_P \tag{226}$$

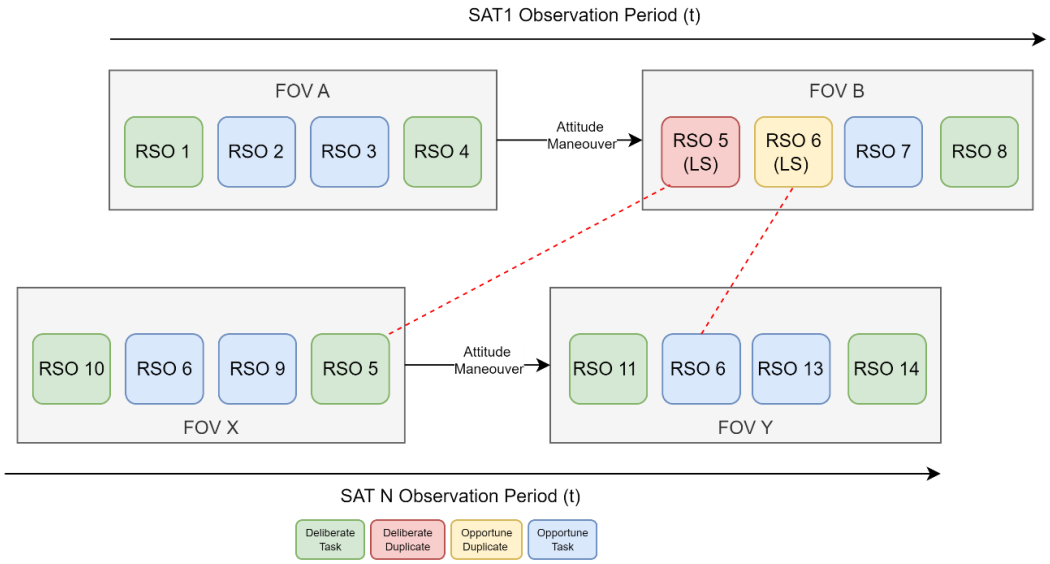

Figure 55 Graphical depiction of multiplatform deliberate and opportune RSO observation over the observation period. Red lines indicate the low-scoring relation between each observation

6.2. Verification Case Studies

The verification of the proposed Distributed Satellite System (DSS) architecture and its operational loops is demonstrated through two distinct case studies, each focusing on a critical component of the system: the self-adaptive loop and the coordination loop. These studies validate the feasibility of the methods developed, highlighting their ability to address the challenges posed by dynamic tasking and mission coordination in DSS environments.

The **self-adaptive loop** is verified through an **Attitude Reorientation Optimization** case study, which builds upon the trajectory optimization models developed in Chapter 4. This study demonstrates the system's ability to generate an optimal attitude manoeuvre under realistic observation constraints (e.g., forbidden zones for electro-optical instrumentation) and physical limits (e.g., maximum torque). By leveraging the previously developed optimization framework, this case study illustrates the efficacy of the proposed Particle Swarm Optimization (PSO) combined with Bézier shape functions in achieving a computationally efficient, rest-to-rest attitude manoeuvre while satisfying all imposed constraints.

The **coordination loop** is verified through a **Distributed Mission Planning** case study, which explores the multi-agent behaviour of the DSS in a dynamic tasking environment. Using a pseudo-pass prediction model for a constellation of satellites, this study evaluates the ability of the Ant Colony Optimization (ACO)-based coordination mechanism to minimize task duplication, optimize global utility, and balance cooperation and competition among satellite agents. Through iterative global

updates, the study demonstrates the emergence of self-organizing behaviour and the system's ability to converge toward an efficient, coordinated task allocation that maximizes the global tasking utility, representing STM goals.

Together, these case studies provide a comprehensive evaluation of the proposed DSS architecture, verifying its capability to dynamically adapt to platform-specific constraints while coordinating at a system-wide level to achieve greater STM goals.

6.2.1. Self-Adaptive Loop

This case study demonstrates the ability of the attitude reorientation optimization approach to generate a feasible, optimal attitude manoeuvre while adhering to observation constraints (e.g., forbidden zones for electro-optic instrumentation) and physical constraints (e.g., maximum torque). Building on the self-adaptive loop framework described earlier, the optimization accounts for critical inputs provided by the Intelligent Health and Mission Management (IHMM) module. These inputs, including maximum torque constraints and time thresholds, are reflective of the Attitude Determination and Control System (ADCS) health status and operational limits. As such, the optimization directly addresses the dynamic and physical constraints highlighted in the IHMM's role within the self-adaptive loop.

This study also builds upon the trajectory optimization models presented in Chapter 4, where a rest-to-rest attitude manoeuvre problem was formulated and solved using Bezier curves and Modified Rodrigues Parameters (MRP). The objective is to minimize the manoeuvre time, ensuring compliance with both dynamic constraints (e.g., angular velocity and torque) and path constraints (e.g., avoidance of forbidden zones for Earth and Sun). By adopting this optimization methodology, the onboard attitude optimization engine generates a torquing profile that not only minimizes time but also ensures safe and effective manoeuvring under real-world operational constraints.

6.2.1.1. Results

In the presented scenario, an example rest-to-rest manoeuvre is demonstrated. The spacecraft performs a near 180-degree manoeuvre about the across-track (W) axis Figure 56)., corresponding to the identity quaternion $q_0 = [1\ 0\ 0\ 0]$ to the final quaternion $q_f = [0.5592\ \ 0\ \ -0.5699\ \ -0.6021]$ over 15.5 minutes (Figure 57). The computed manoeuvre adheres to the maximum torque constraint M_{max} = 7 mNm, as illustrated in Figure 59, and satisfies rest-to-rest conditions with final angular velocities at 0 deg/s Figure 58. Moreover, the optimization avoids forbidden zones throughout the manoeuvre Figure 60, validating that all constraints are met.

Feedback (FB3) from this optimization process provides critical inputs to the mission planning autonomy, evaluating the viability of candidate attitude plans generated by the mission planning module. If any time thresholds (required time from rest-to-rest

manoeuvre) or torque constraints are breached, the mission planning autonomy is penalized, prompting the generation of an alternative solution. This feedback loop ensures that the self-adaptive capabilities of the DSS are dynamically maintained, enabling a robust balance between mission planning objectives and the operational health of the ADCS.

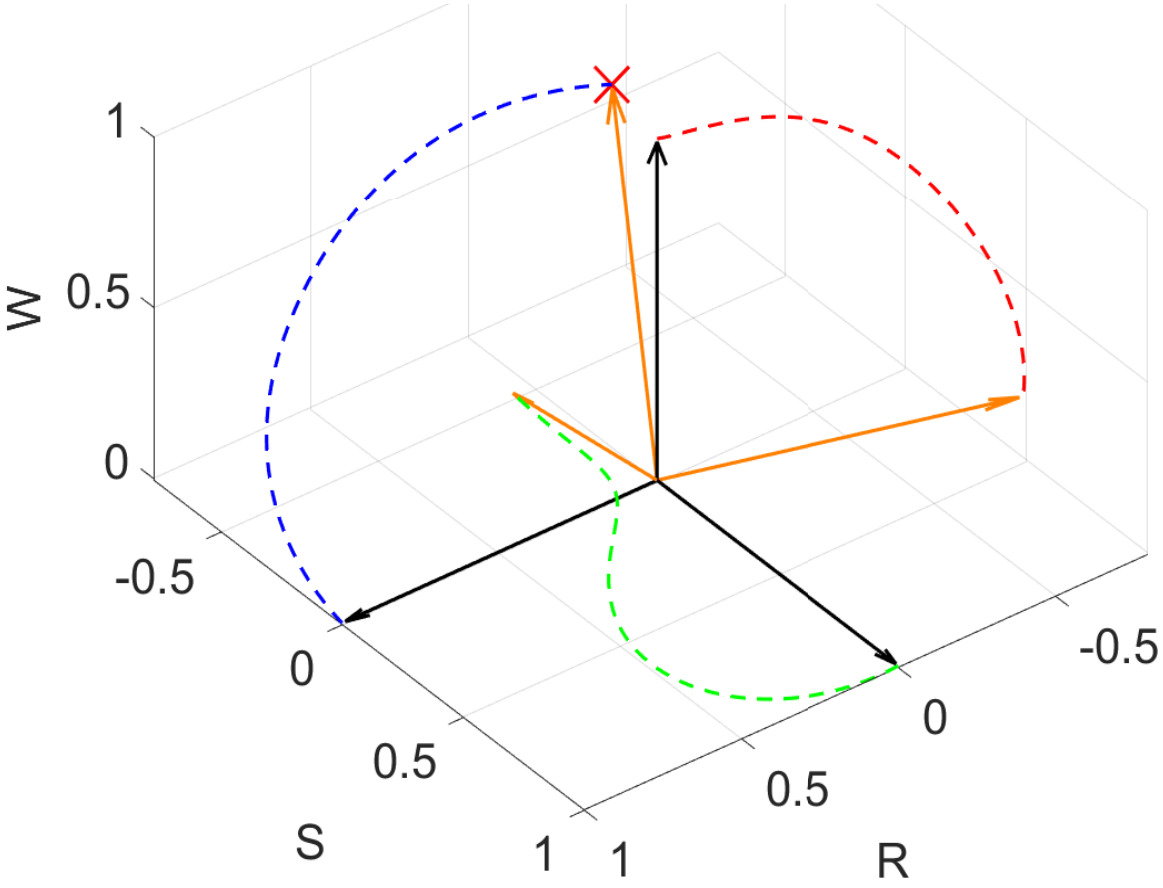

Figure 56 Optimal Attitude manoeuvre in RSW frame. The yellow axis represents the final orientation.

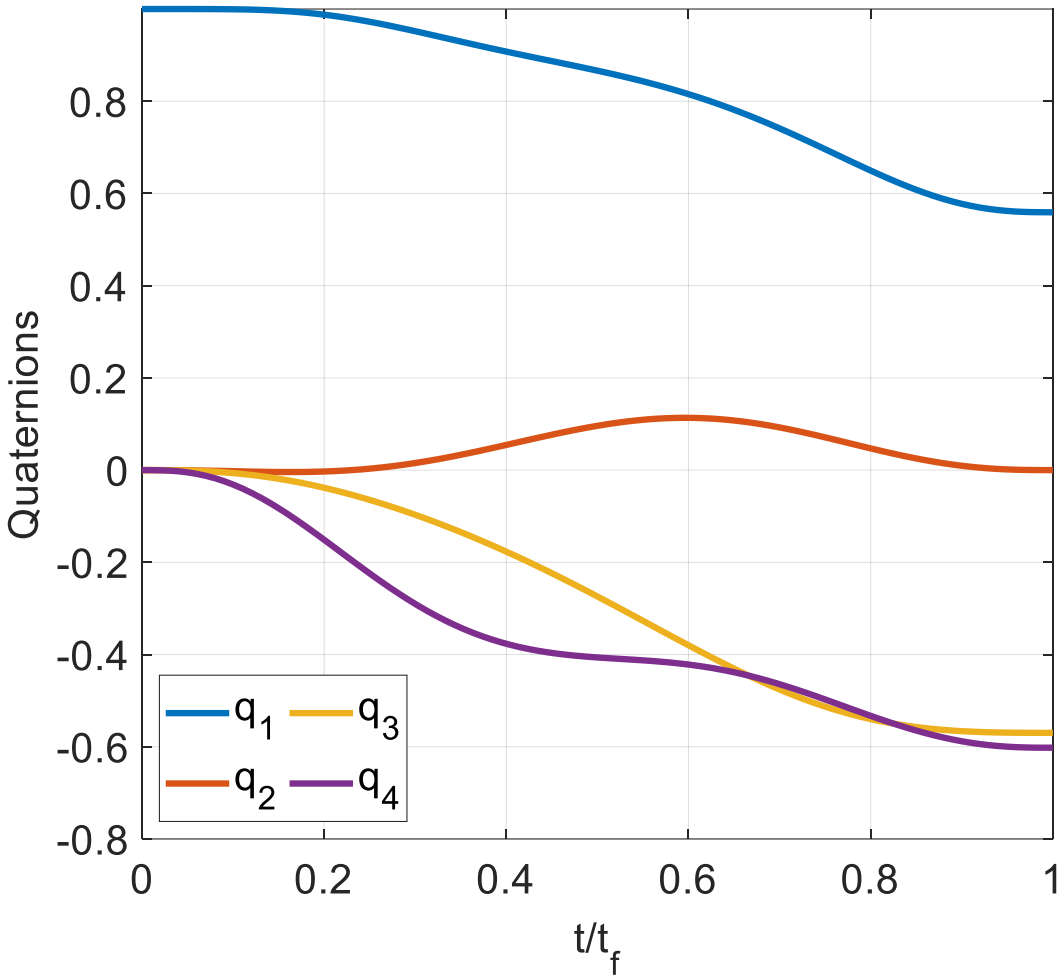

Figure 57 Quaternion time history. For the rest-to-rest attitude manoeuvre

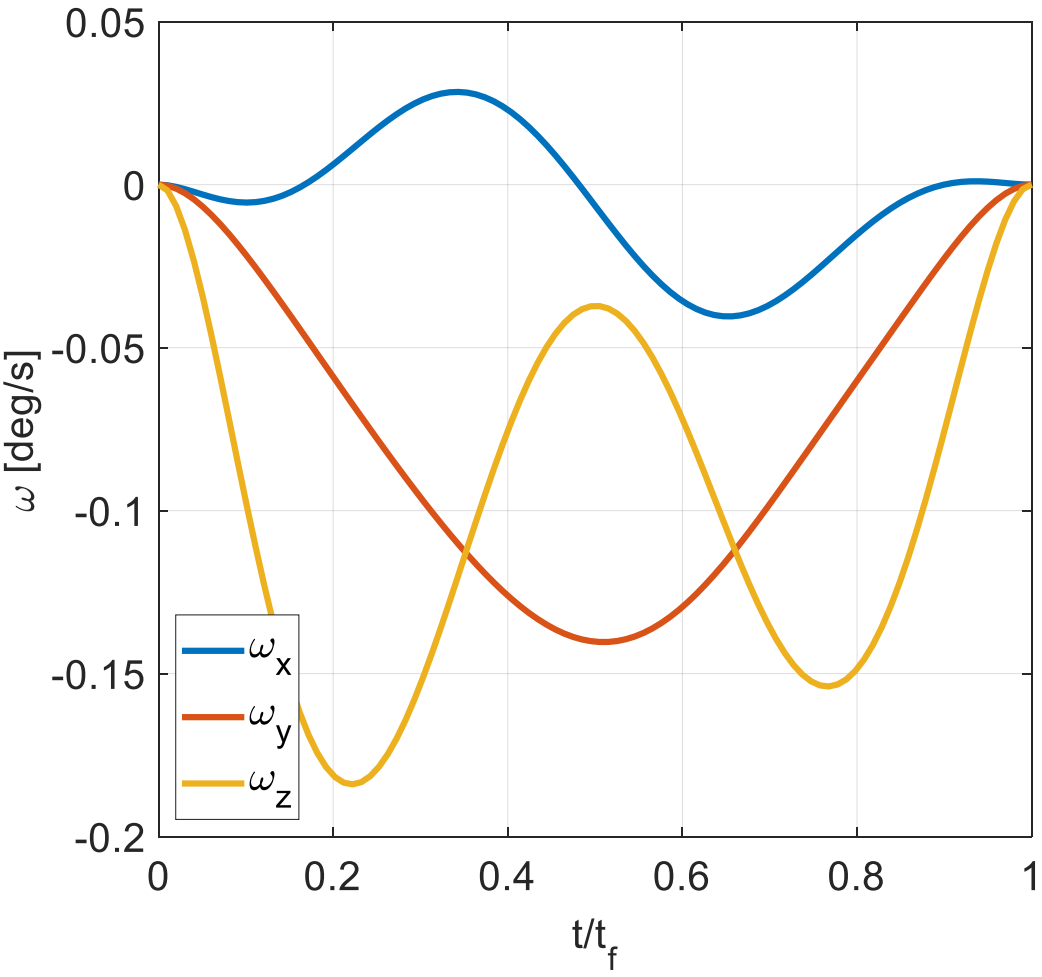

Figure 58 Angular velocity time history of manoeuvre, demonstrating adherence to rest to rest criteria.

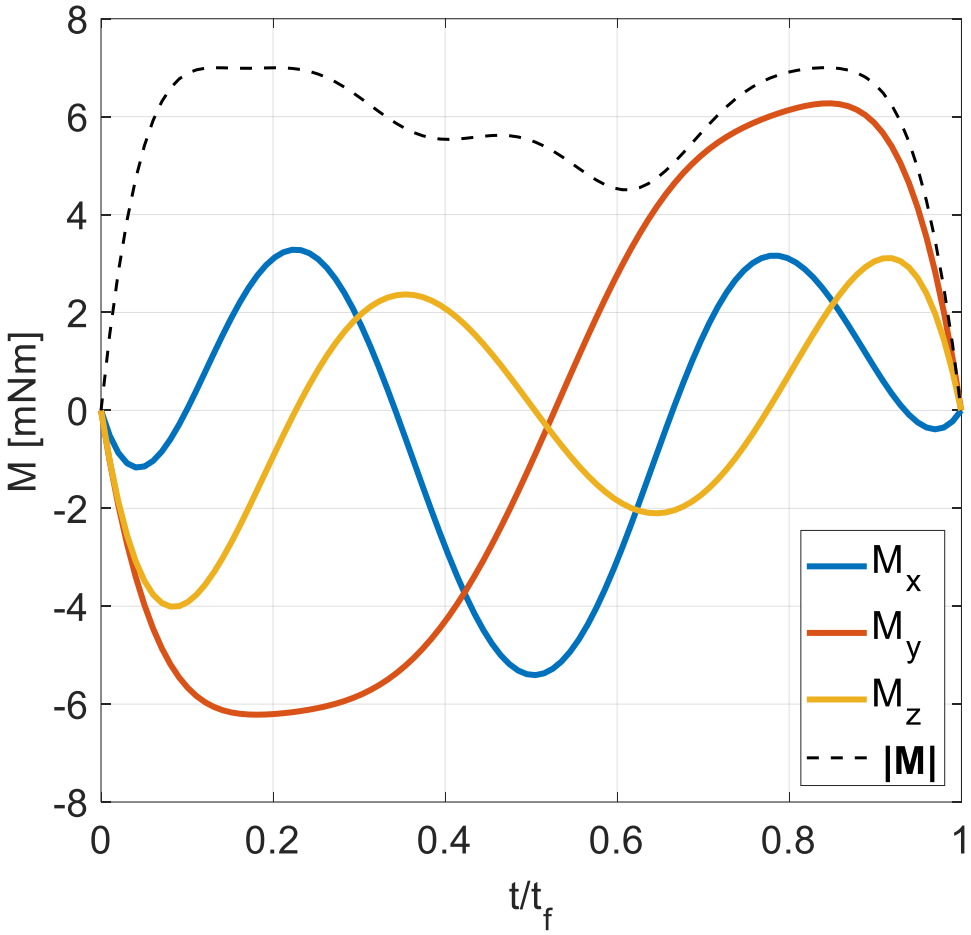

Figure 59 Torque time history and corresponding magnitude

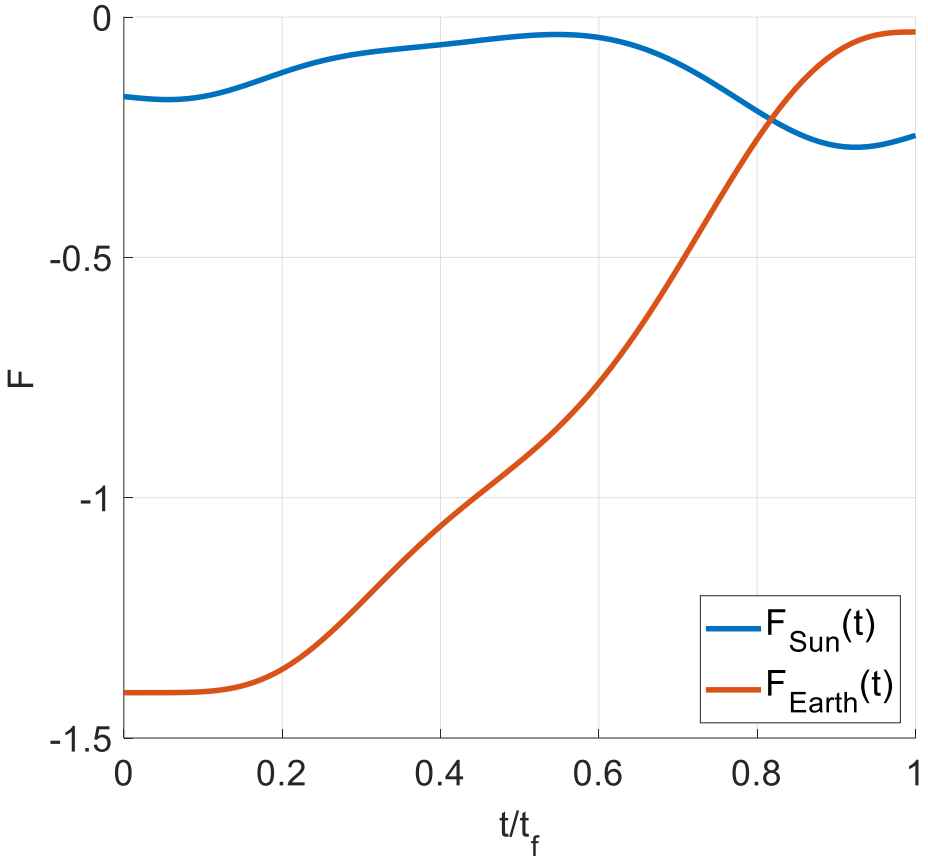

Figure 60 Evaluation of F functions for Sun and Earth over the manoeuvre

6.2.2. Coordination Loop

This case study focuses on verifying the coordination loop, a critical component of the Distributed Satellite System (DSS) architecture that facilitates system-wide behaviour alignment. The architecture achieves this coordination through a multi-agent Ant Colony Optimization (ACO) approach, where individual satellites act as autonomous agents that iteratively refine their tasking schedules. The coordination loop facilitates global synchronization by enabling satellites to exchange task schedules and performance metrics, such as probabilities of detection and task utility, through inter-satellite links or ground station networks. Supervisory control inputs, such as the track weighting and STM goals, guide this iterative process, ensuring that local decisions align with the global mission framework.

6.2.2.1. Experimental Setup

A pass prediction model is generated pseudo-randomly for 10 satellites. As described previously, the total FOR is discretised into a 10x10 FOV grid to represent 100 different boresight directions the payload can point towards by changing the attitude

of the spacecraft platform. From a total number of 1500 RSOs each with a unique ID a pass prediction model is generated pseudo-randomly that includes the number of RSOs that can be observed within each FOV (and the associated ID), the time of predicted observation (within the planning horizon), and a probability of detection. The track weighting for each RSO is also chosen pseudo-randomly but is common to all satellite pass prediction models generated. Table 26 outlines each of the above parameters for the verification case study.

Table 26 Pass prediction model generation parameters.

Number of satellite agents	10
Total number of unique RSOs	1500
Observation period (planning horizon)	21 hours
Number of RSO observed per FOV	1<n<10
Probability of detection	$0.1< P_d < 1$

Table 27 outlines the parameters chosen for each satellite agent ant colony. The pheromone and heuristic exponential weights, number of iterations and ant agents selected are chosen based on standard parameter values found within the similar-sized combinatorial optimisation problems found within the literature. Each ant colony begins with an initial pheromone evaporation rate of 0.02 (a common value for exploratory solutions) however is updated iteratively based on the stagnation of the pheromone field. The maximum path length is set to 5, corresponding to a possible 4 attitude manoeuvres over the planning horizon. In some cases, the spacecraft agent may decide to perform less than 4 manoeuvres depending on the expected return, and the ability to fit extra tasks within the specified planning horizon.

Table 27 ACO engine parameters

Pheromone exponential weight (α)	1
Heuristic exponential weight (β)	1.2
Number of ant agents	300
Initial pheromone evaporation	0.02
Number of local iterations	50
Max number of attitude manoeuvres between FOV per satellite	5

6.2.2.2. Results

To verify the proposed approach, this study examines the task selection behaviour of each satellite over successive global interactions. The objective of these interactions is to achieve a balanced system-wide behaviour among satellites that fulfils a shared global goal. This goal is represented in the form of the utility function U_p , which is common to all platforms. A utility function defines the system's intent—what it aims to accomplish—without prescribing how the goal should be achieved. In this case, the

goal is for each satellite agent to identify and prioritize its high-performing tasks while minimizing task duplication, only allowing duplicate tasks when they are opportunistic. The scenario concludes (exit condition) when all satellite agents have optimized their schedules to include only high-performing tasks without deliberate duplicates.

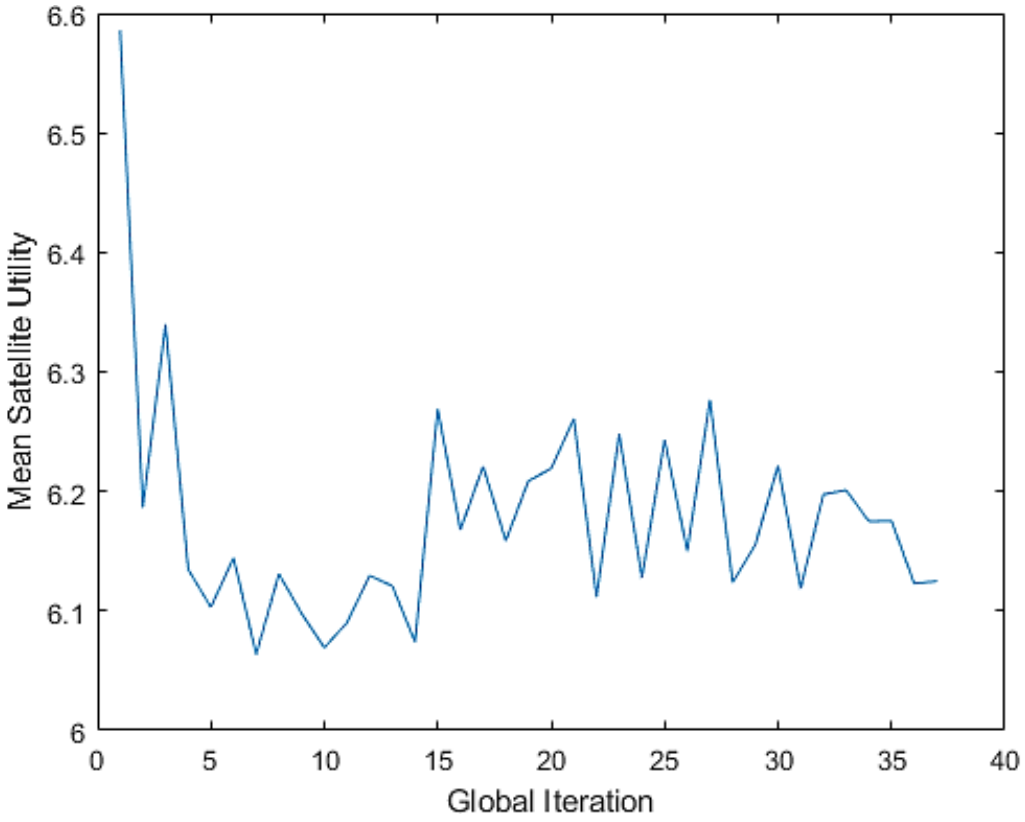

Figure 61 Mean satellite utility per global update through coordination loop

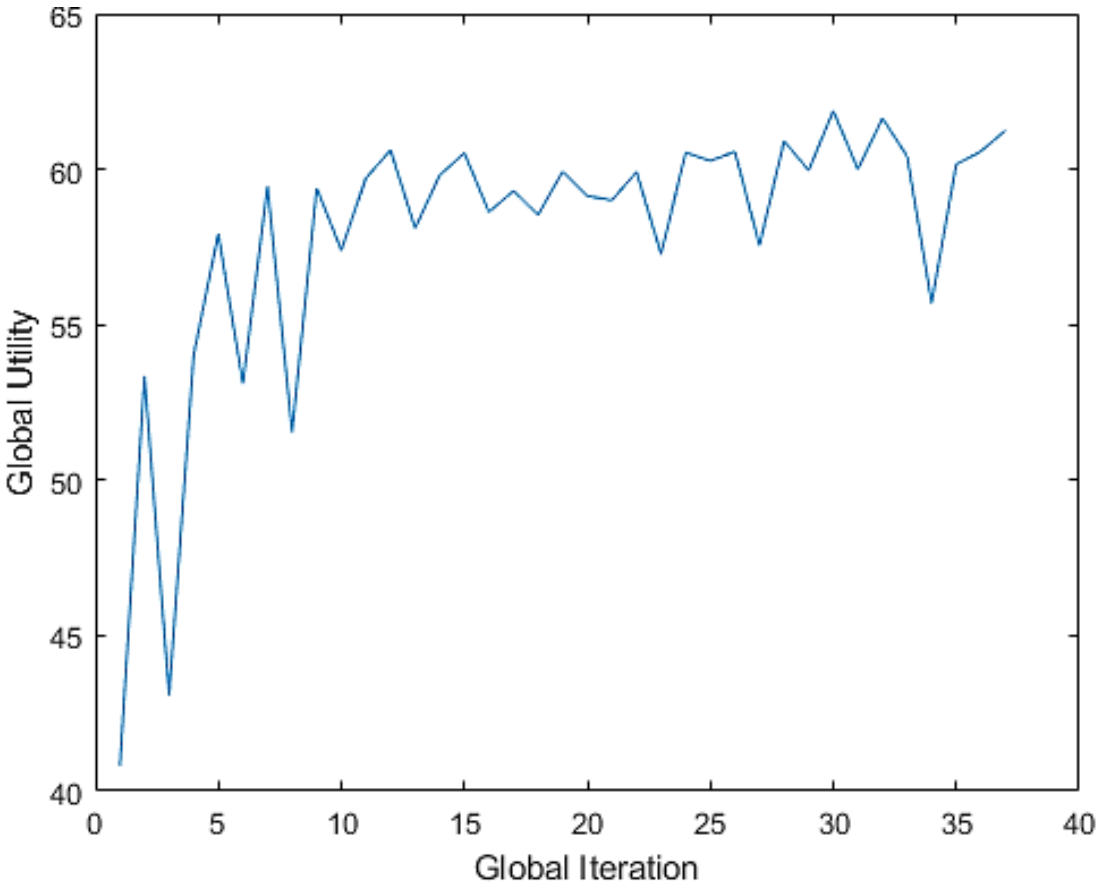

Figure 62 Global utility per global update through coordination loop

Figure 61 and Figure 62 illustrate the results of these global interactions. Figure 61 shows the mean utility of individual satellites over successive global updates, while Figure 62 highlights the overall global utility. A key insight from these figures is that as the mean satellite utility decreases (indicating local sacrifices in individual task prioritization), the global utility increases. This demonstrates effective coordination among satellite agents, where individual adjustments align with the system-wide optimization objective. Following an initial "position-fix" phase, where satellites align their local schedules, global utility steadily improves with each interaction.

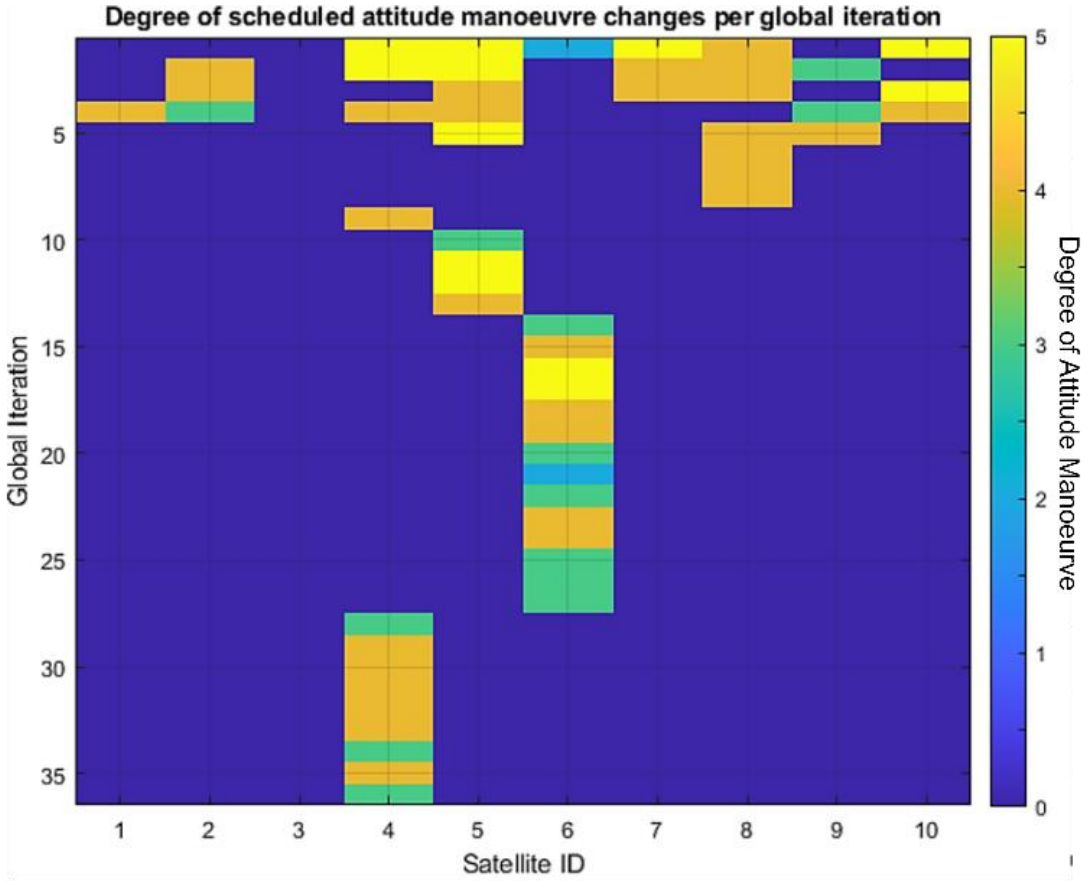

Figure 63 DSS behaviour over each global update provided by the coordination loop

Figure 63 provides further detail on the dynamic behaviour of individual satellite agents, showing the degree of attitude manoeuvre (task adjustments) during global interactions. Temporal constraints play a crucial role in this process. The degree of attitude manoeuvre is defined as the extent of change in the earliest scheduled Field of View (FOV) task in response to global updates. For example, if a satellite initially schedules a FOV sequence of [1, 2, 3, 4, 5] and later adjusts to [1, 2, 3, 4, 6], the degree of change is 1. Whereas an adjustment to [1, 6, 3, 4, 5], would indicate a degree of change of 4.

From Figure 63, we observe the initial "position-fix" phase where most satellites engage in significant re-planning to exclude low-performing tasks, as dictated by their internal utility functions. Over time, as global iterations progress, the self-organizing properties of the Ant Colony Optimization (ACO) approach become apparent. This is reflected in a reduced frequency of re-planning, as satellite agents stabilize their schedules. Interestingly, coupling effects between satellites, such as those observed between SAT5/SAT6 and SAT6/SAT4, emerge, where the re-planning of one platform triggers adjustments in others. This behaviour is driven by the opportunistic identification of higher-performing tasks rather than deliberate competition.

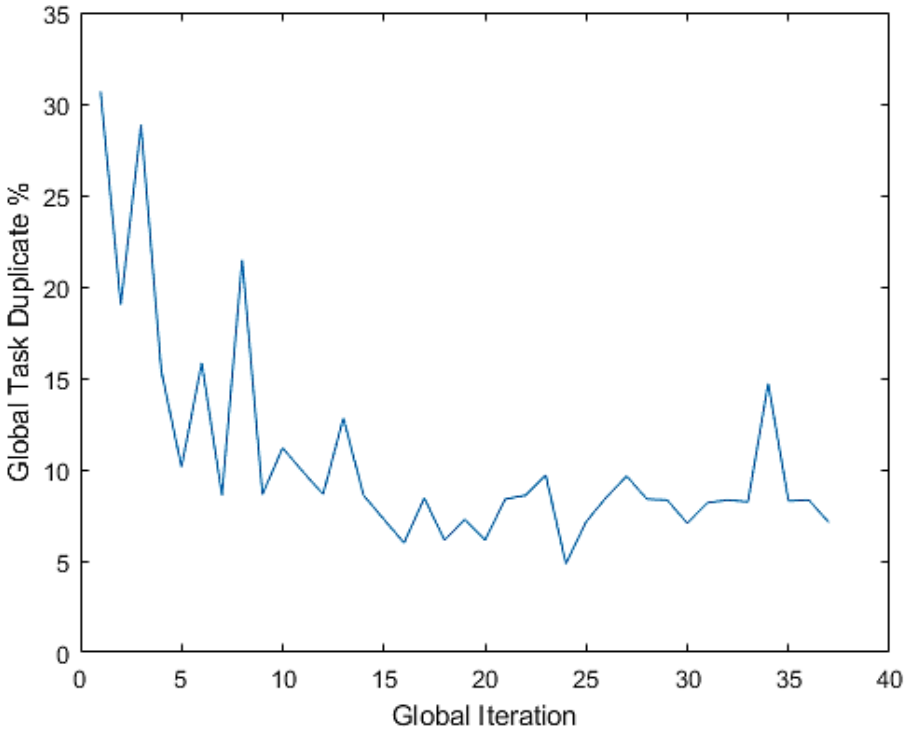

Figure 64 Task duplicate percentage per global update through coordination loop

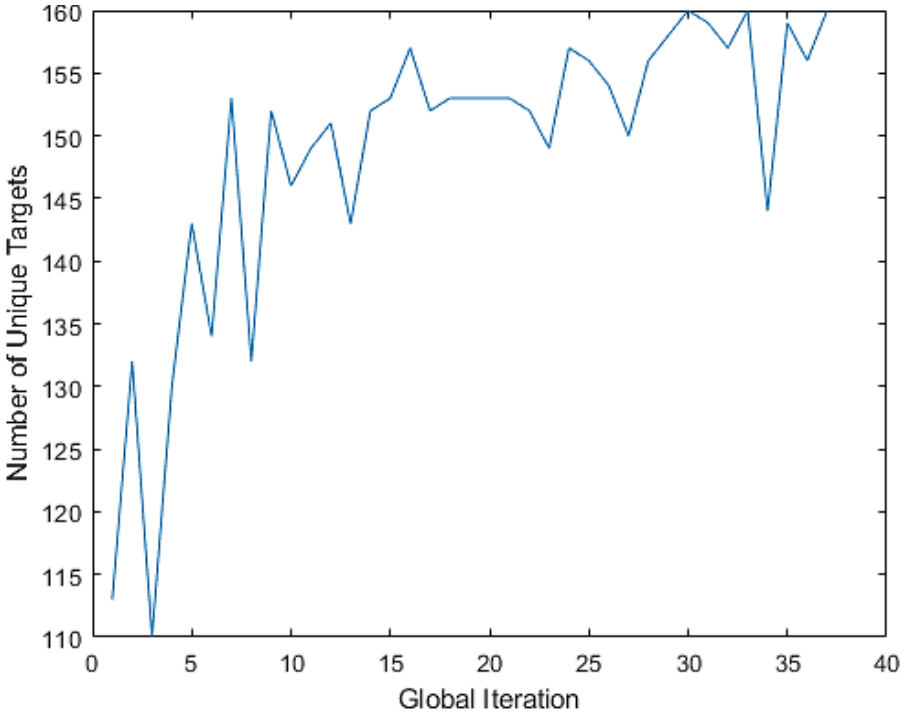

Figure 65 Unique RSO tasked per global update through coordination loop

Figure 64 and Figure 65 provide metrics on task performance over global iterations. Figure 64 shows a steady reduction in the percentage of duplicate tasks, converging toward a minimal duplication rate. Concurrently, Figure 65 highlights an increase in the number of unique RSOs observed across the system, reflecting the growing efficiency and coordination of the satellite network. These results validate the ability of the proposed approach to achieve system-wide optimization through coordinated, iterative task adjustments among distributed satellite agents.

6.3. Conclusions

This chapter has presented an extended architecture for Distributed Satellite Systems (DSS) tailored to Space-Based Space Surveillance (SBSS) operations, addressing the objective of designing a distributed mission planning strategy that optimizes task allocation, minimizes duplication, and maximizes global utility. Through the integration of onboard autonomy, and system-wide coordination, the chapter demonstrates a framework for achieving effective and efficient execution of SBSS missions using DSS.

The distributed mission planning autonomy employs a multi-agent Ant Colony Optimization (ACO) algorithm, which enables individual satellites to optimize their tasking schedules locally while achieving global coordination through iterative feedback. This approach ensures that satellites operate within unique decision spaces, determined by observation probabilities and task constraints while adhering to common supervisory control objectives such as minimizing task duplication and prioritizing high-utility Resident Space Object (RSO) observations.

Through integration a Particle Swarm Optimization (PSO)-based approach, leveraging high-order polynomial parameterizations to achieve computationally efficient, real-time attitude and orbital manoeuvres. By addressing constraints such as torque limits and forbidden zones and incorporating dynamic feedback from Intelligent Health and Mission Management (IHMM) modules, the self-adaptive loop ensures that task required task execution aligns with the targeted mission reliability highlighting the interplay between platform-level autonomy and system-wide coordination.

This chapter has presented a distributed mission planning strategy for Space-Based Space Surveillance (SBSS) operations, leveraging autonomous coordination among satellites to optimize task allocation, minimize duplication, and maximize global utility across collaborative platforms. Addressing the objectives of designing a distributed mission planning approach, integrating onboard trajectory optimization, and validating the methodology in a representative operational scenario, the study provides a robust framework for achieving these goals.

While the proposed methodology provides a flexible, computationally efficient, and timely solution for distributed mission planning and trajectory optimization, the proposed methodology is subject to the following key limitations:

Communication Infrastructure Assumptions: The coordination loop assumes the availability of inter-satellite links and ground station networks with sufficient bandwidth and minimal latency. Future research will explore the impact of communication delays, link availability, and interruptions, incorporating these factors into the simulation environment to provide a more realistic assessment of performance.

Global Optimality: The stochastic nature of metaheuristic solutions introduces challenges in guaranteeing proximity to the global optimum, particularly in high-dimensional problem spaces.

The sophistication of the Coordination Mechanism: The current architecture relies on autonomous decision-making at the platform level, guided by supervisory control inputs. However, the integration of supervisory intervention mechanisms could provide a safeguard for resolving conflicts to addressing scenarios where autonomous coordination fails to meet mission objectives and corresponding STM goals.

Chapter 7

Supervisory Decision Support Design

This chapter presents the design and simulation of a decision support tool tailored for supervisory control within the Intelligent DSS Architecture. By quantifying system autonomy outputs in terms of mission-level reliability, the simulation case study underscores the critical importance of a strategic, data-driven approach to mission planning, monitoring, and selection to achieve and sustain mission assurance targets. The findings offer valuable insights into the evolving role of future ground station operators, emphasizing their need to leverage advanced decision support systems to effectively manage complex missions and ensure optimal system performance under dynamic conditions.

7.1. Background

As spacecraft autonomy increases, a common misconception is that ground segment roles will diminish. Instead, traditional ground processes shift from low-level command sequences to higher-level supervisory roles focused on autonomous goal-based operations. This evolution involves monitoring and commanding onboard autonomous processes (e.g., orbital manoeuvres, mission planning), and supporting onboard autonomy with high-level decision-making inputs. This necessitates the development of Human-Machine Systems (HMS) that enable operators to interpret system-level responses and interject when intentions are not being fulfilled or guidance is required to safeguard mission objectives in the presence of cyber-physical threats.

Cyber-physical threats to autonomous Distributed Satellite Systems (DSS) encompass a diverse range of risks, as summarized in **Table 28**. These include software-based risks such as direct cyberattacks aimed at system control, and physical risks like orbital debris collisions (addressed in Chapter 5), space weather impacts (e.g., solar flares affecting electronics), and radio interference due to poor spectrum management. Operational risks such as human error and sensor degradation over time also pose challenges, alongside emerging risks from unintended intelligent system actions, where artificial intelligence or machine learning leads to unforeseen behaviours [280].

Table 28 Cyber-physical threat vectors for intelligent space operations [280]

Threat vectors	Description
Direct cyber attacks	Malicious efforts to subvert a system through software malware or intrusion to command and control a system

Orbital debris	Impacts of satellite debris colliding with spacecraft
Space weather impacts	Energetic particles from solar flares and coronal mass ejections impinging on space systems affecting electronics
Human error	Errant Commands, loss of situational awareness, programming glitches, design or manufacturing flaws
Sensor degradation	Change in sensor monitoring characteristics and performance over time affecting measurement and resulting actions
Component failure	Failures caused by age, excess temperature, excess current or voltage, ionizing radiation, mechanical shock, stress or impact, operating cycle and many other causes
Radio interference	Intentional or unintentional impact to system performance resulting from insufficient spectrum management
Unintended intelligent system actions	Unintended changes in system performance and actions over time resulting from artificial intelligence and/or machine-learning evolution

A particularly critical threat to satellite missions is component failure, which can result from factors such as excess temperature, radiation, mechanical stress, and operating cycles. Table 29 provides the results of recent analyses of historical satellite failure data using the Seradata and Telastra anomaly databases [281]. The results highlight that along with communication systems, Attitude Determination and Control System (ADCS), are among the most significant contributors to satellite reliability degradation. In the context of the described SBSS mission, these failures are particularly impactful because the ADCS is essential for maintaining precise orientation and control for RSO observation, making the reliability of reaction wheels a key determinant of overall mission success.

Table 29 Percentage of failures per satellite subsystems and components [281]

Spacecraft Subsystem	% Total Failures	Component
Communication	12%	Amplifiers (TWTA/SSPA) (29%) Channel (15%) Antenna (6%)

		Transmitter (6%)
		Receiver (4%)
		Spurious (2%)
		Noises and Interferences (2%)
		Unspecified (36%)
Attitude Determination and Control debris	10%	Attitude Reference Sensors (30%)
		Actuator System (18%)
		Attitude Control Processor (6%)
		Unspecified (46%)
Electrical Power System	9%	Solar arrays (37%)
		Batteries (36%)
		Unspecified (27%)
Payloads	8%	Instruments (70%)
		Atomic Clock (18%)
		Scan Mirrors (4%)
		Unspecified (8%)
Propulsion	4%	Thrusters/AKM (61%)
		Fuel System (22%)
		Unspecified (17%)
Telemetry, Command and Ranging	3%	Encoders/Decoders (18%)
		Transmitters/Receivers (12%)
		Telemetry Data (11%)
		Phantom Commands (7%)
		Unspecified (52%)
Mechanisms	3%	Solar Panels Deployment (41%)
		Antenna Deployments (24%)
		Others (35%)
On-Board Computer	2%	Software errors (21%)
		Tape recorder (27%)
		Data handling system (5%)
		Unspecified (47%)
Thermal Control	1%	
Unspecified Anomalies	48%	

As described in Chapters 3 and 6, system autonomy serves as a key controller of ADCS behaviour through the mission planning process and coupled trajectory optimization. These processes generate optimal sensor tasking plans and corresponding torquing profiles, ensuring precise attitude control for Resident Space Object (RSO) observation. This chapter focuses specifically on monitoring and guiding system

autonomy behaviour to mitigate ADCS failures, particularly those associated with critical components like reaction wheels, through effective supervisory control mechanisms. By addressing these vulnerabilities, the chapter aims to enhance the reliability and resilience of SBSS missions, ensuring mission success in the presence of cyber-physical threats.

7.2. System Development

Due to the high expense of launching and flying spacecraft, in conjunction with the space sustainability issues that dead spacecraft pose, providing a required level of space system reliability provides a means of assurance that a given mission architecture will survive and meet required risk tolerance expectations. As such, DSS missions are typically required to comply with requirements [240] that require the quantification of initial mission-level reliability. Nonetheless, in comparison to individual platform-level reliability estimations, mission-level DSS reliability necessitates a more stringent approach. Proposed DSS missions may become infeasible when mission assurance and system reliability are considered as individual platform reliability may (individually) meet defined risk tolerance, however, it may not be achieved at a system level. Fundamentally this is due to the extension from platform reliability considerations to functional mission configurations required to meet missions' objectives. As such mission level reliability modelling necessitates a Systems of Systems (SoS) perspective to determine representative reliability estimates, which are crucial to supporting mission assurance arguments.

However, the inherent uncertainty surrounding the actual operating behaviour and corresponding component usage represented by cycles/time of DSS elements used to derive initial reliability estimates poses significant challenges as continual deviations from this expected operating behaviour can have a detrimental compounding effect on continued mission reliability.

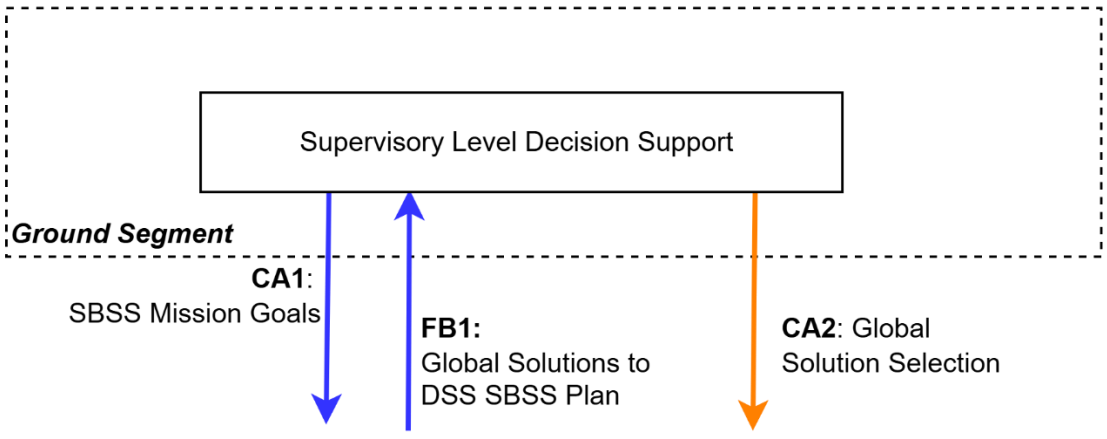

Figure 66 Supervisory Level Decision Support and DSS Interfaces

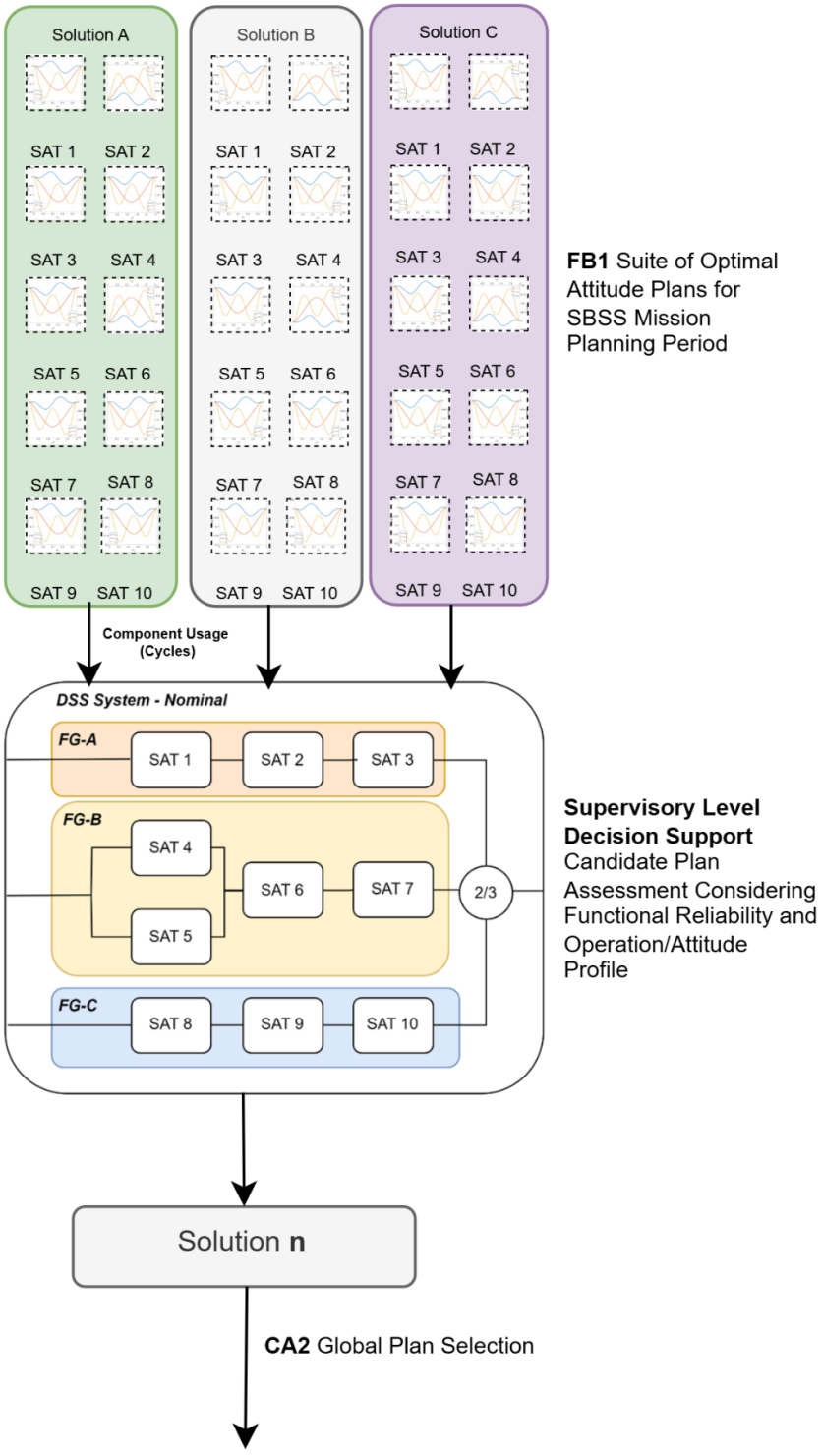

Figure 67 Detailed Illustration of Intelligent Plan Selection design, where each candidate SBSS plan solution (A,B, C) is assessed in terms of meeting system reliability objectives and a selection made based on reliability informed metric.

Given the importance of mission reliability in achieving DSS mission goals, we extend the Intelligent DSS framework described in Chapters 3 & 6 by focusing on the interfaces between the DSS system and Supervisory Level Decision Support (Figure 60) and the selection of global optimal plans (CA2) to provide system level reliability-informed selection to mitigate the likelihood of ACDS component failure.

Figure 67 illustrates the interactions and interfaces involved in the intelligent plan selection process. Specifically, it depicts how attitude torque profiles (described in Chapter 6) for each satellite platform (SAT n) are transformed into reaction wheel usage, quantified in terms of operating cycles. These cycles are then used to assess the mission-level reliability of each candidate plan. Based on predefined selection criteria, the most suitable plan is chosen for implementation by the Distributed Satellite System (DSS).

The following sections provide a detailed explanation of the models used in this process, followed by a verification case study employing a dynamic programming approach.

7.2.1. Initial Reliability Model Construction

The initial reliability model is developed to estimate the probability that at proposed DSS mission will survive for sufficient time to achieve a given science objective. This estimation is dependent on the following:

- Individual platform reliability
- Mission/orbit design (required mission functional configuration to achieve objectives)

7.2.1.1. Individual Platform Reliability

Platform reliability models represent a logical arrangement of systems required to perform a given platform-level function. In the context of the autonomous DSS SBSS mission described in previous chapters a simplified version of an ACDS system based on 3 axis reaction wheel system that provides attitude reorientation required for RSO observation. Each Reaction Wheel (RW) is modelled with the following Weibull reliability function:

$$R_{RW}(t) = e^{-\left(\frac{t-\gamma}{\eta}\right)^{\beta}} \tag{227}$$

where,

t is the number of wheel cycles (rotations)

β is the shape parameter (slope) = 1.81

γ is the location parameter (failure-free life) = 0 cycles

η is the scale parameter (characteristic life) = 4E9 cycles

The Weibull reliability function R_{RW} has been chosen to due to its suitability to capture an ageing "wear out" process typical of reaction wheels and other motor-type devices related to bearing failures, corrosion and lubrication decay[282] [283]. The effect of wearout is achieved through setting $1< \beta < 4$ where the scale parameter η has the effect setting where the bulk of the distribution lies representing the typical cycles to failure. A positive value of the location parameter γ enables the shifting of the distribution to represent a period of failure-free life, whereas a negative value indicates possible of failures before the start of a mission. The number of cycles t is an estimation of the operating usage of the reaction wheel over the total mission duration. For the SBSS mission, we formulate an estimate based on the mission and usage assumptions detailed in Table 30.

T**able 30**: Initial Reliability Model Usage Assumptions

Mission Duration	5 Years
Planning Interval	24 Hours
Total Planning Cycles	1825
Mean RW RPM	4500 RPM
Mean time of each Attitude Maneuver	15 minutes
Number of Attitude Maneuvers per plan	5
Cycles per planning interval	337500
Estimated Total Number of Cycles over 5 years (t)	615937500 cycles

To represent the functional configuration of each reaction wheel we assume that each RW system must function, corresponding to a series structure. Mathematically this is represented as the product of each RW reliability function:

$$R_{SAT} = R_{RWX} \cdot R_{RWY} \cdot R_{RWZ} \quad (228)$$

7.2.1.2. Mission Functional Configuration

Mission functional configuration represents the required platform structure to achieve science objectives. Generally, this is reflective of the required orbital arrangements and any required cooperation between heterogeneous satellite nodes. In the following example, a 10-satellite DSS SBSS system is represented. The science objectives in this

case would be to maximize the number of unique possible RSO observations over the mission lifetime, requiring a preliminary SBSS orbit design optimization [284]. To achieve this objective the SBSS mission configuration is separated into 3 functional groupings (FG-A, FG-B, FG-C) that each represent a given orbital plane (Figure 68). Within each functional grouping, the required orbit design of satellite platforms is logically arranged – representing a mission success path of each functional grouping. This success path defines the satellite nodes that must be functional to meet RSO observation requirements. The series arrangement of satellite nodes in FG-A and FG-C in Figure 68 is interpreted as "all satellite nodes must be functional to meet observation requirements of each orbital plane". In contrast to FG-B, which provides a level of redundancy due to the parallel arrangement between SAT 4 & SAT 5.

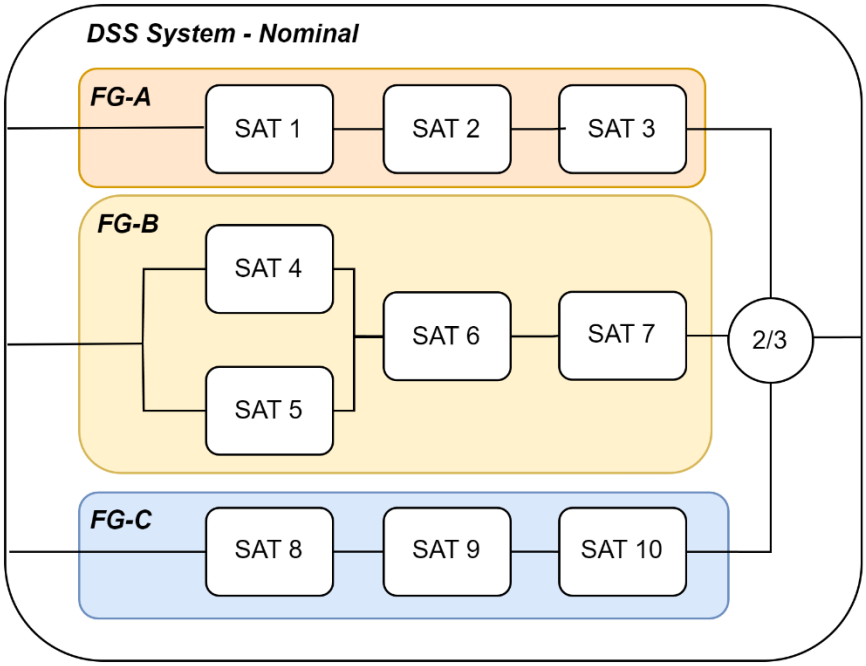

Figure 68. Nominal DSS KoN Mission Functional Configuration

At the DSS System level, we represent the required functional configuration between FG-A FG-B and FG-Cas a K out of N (KoN) redundancy configuration. In KoN systems all items are operating simultaneously at a certain capacity. When a redundant item/group fails, the remaining items can continue to carry the load. Failure occurs when enough items have failed such that the remaining items cannot carry the load (observation requirements). In the SBSS mission scenario, the KoN group is reflective of a performance requirement that "2 out of 3 functional groups must be operating to meet RSO observation requirements".

To calculate the reliability of KoN systems with i.i.d components (all components have the same reliability), the number of working components follows the binomial distribution with parameters n and p.

where

n is the number of components in the system

p is the reliability of each component when components are i.i.d

Therefore, the probability that exactly i component work is equal to:

$$\binom{n}{i} p^i q^{n-i}, \qquad i = 0,1,2 \ldots, n. \tag{229}$$

The reliability of the system is equal to the probability that the number of working components is greater than or equal to k:

$$R(k,n) = \sum_{i=k}^{n} \binom{n}{i} p^i q^{n-i} \tag{230}$$

However, where items are not identical (as in the case of heterogeneous functional groupings and differing satellite usage) enumerative methods are required. Using this approach, all operation combinations are enumerated to obtain systems reliability. Through the application of the mutually exclusive events axiom, the reliability is calculated as the probability of the union of all mutually exclusive events that meet system success criteria, defined by k number of working components. The following demonstrates the ESM method for the KoN DSS system through the application of a truth table:

Scenario	Component State			Success
	FG_A	FG_B	FG_C	
X_1	1	1	1	1
X_2	1	1	0	1
X_3	1	0	1	1
X_4	0	1	1	1
X_5	1	0	0	0
X_6	0	1	0	0
X_7	0	0	1	0
X_8	0	0	0	0

Therefore, the success scenarios are:

$$X_1 = FG_A FG_B FG_C \tag{231}$$

$$X_2 = FG_A FG_B \overline{FG_C} \tag{232}$$

$$X_3 = FG_A \overline{FG_B} FG_C \tag{233}$$

$$X_4 = \overline{FG_A} FG_B FG_C \tag{234}$$

The probability of success (reliability) of the K-out-of-N DSS system is then calculated as:

$$R_{DSS} = R(X_1 \cup X_2 \cup X_3 \cup X_4) \quad (235)$$

As X_1, X_2, X_3, X_4 are mutually exclusive:

$$R_{DSS} = R(X_1) + R(X_2) + R(X_3) + R(X_4) \quad (236)$$

Where:

$$R(X_1) = R_{FG_A} \cdot R_{FG_B} \cdot R_{FG_c} \quad (237)$$

$$R(X_2) = R_{FG_A} \cdot R_{FG_B} \cdot (1 - R_{FG_c}) \quad (238)$$

$$R(X_3) = R_{FG_A} \cdot (1 - R_{FG_B}) \cdot R_{FG_c} \quad (239)$$

$$R(X_4) = (1 - R_{FG_A}) \cdot R_{FG_B} \cdot R_{FG_c} \quad (240)$$

Based on the usage assumptions detailed in Table 30 The initial mission reliability estimate is then calculated as:

$$R_{DSS} = 0.857$$

7.2.2. Dynamic Reliability Model Construction

To capture the inherent uncertainty surrounding the actual operating behaviour and the potentially detrimental compounding effect on continued mission reliability, we extend the Weibull function for each reaction wheel defined by Eq (1) to conditional reliability. That is, given a certain amount of prior usage (and not failed), T, what is the probability of completing the remaining number of cycles, t, represented as the following:

$$R_{RW}(t|T) = \frac{R(T+t)}{R(T)} = e^{-\left[\left(\frac{T+t-\gamma}{\eta}\right)^{\beta} - \left(\frac{T-\gamma}{\eta}\right)^{\beta}\right]} \quad (241)$$

Practically this means that R_{DSS} becomes a function of T, t for each reaction wheel unit. This allows past cycle history and an estimation of future cycles (based on past usage and remaining usage (remaining planning cycles) to be captured in our dynamic reliability assessment. In the simulation $R_{RW}(t|T)$ is calculated at each planning interval, where given previous usage T, t is estimated using the following Bayesian average approach:

$$t = \overline{C_B} \cdot P_R + C_C \quad (242)$$

where,

P_R is the number of remaining planning cycles.

C_c is the number cycles for the current planning interval

$\overline{C_B}$ is the updated Bayesian average of RW cycles

$$\overline{C_B} = \frac{\overline{C_{BP}} \cdot N_{C_{BP}} + \bar{C} \cdot N_C}{N_{C_P} + N_C} \tag{243}$$

where,

$\overline{C_{BP}}$ is the prior Bayesian average RW cycles per planning period.

$N_{C_{BP}}$ is the number of prior planning periods to calculate prior Bayes average.

$\bar{C}$ is the new mean of RW cycles per planning period.

N_C is the number of planning periods used to calculate updated mean, equal to $N_{C_{BP}} + 1$

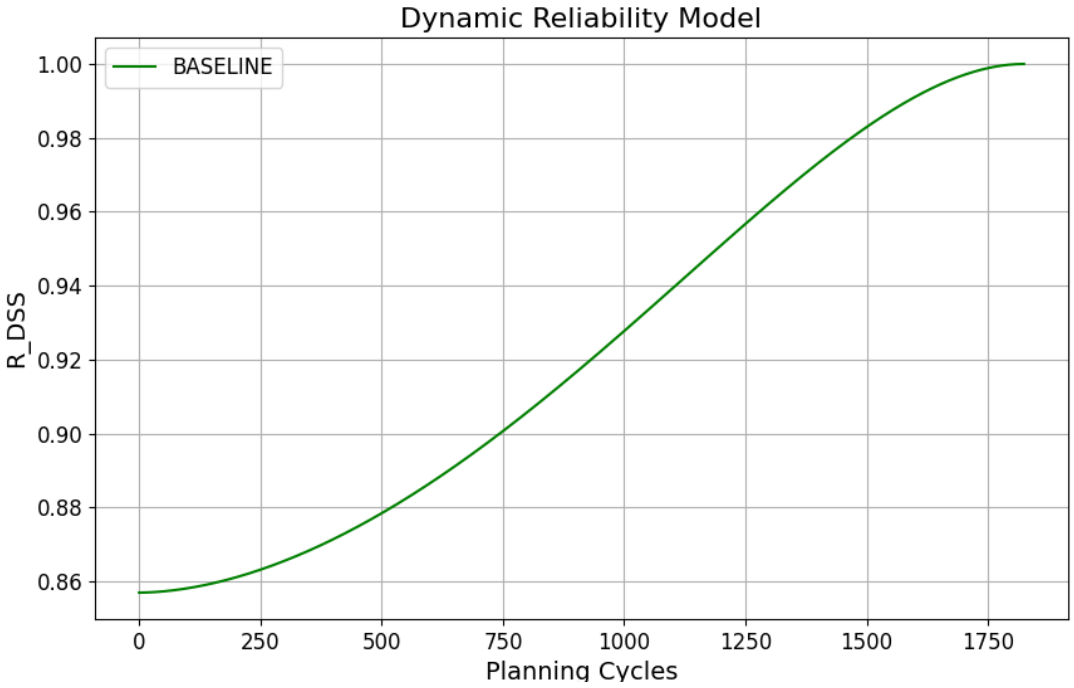

Figure 69 Results of System Level conditional reliability over mission duration with initial RW usage assumptions

When holding initial reliability usage assumptions detailed in Table 30 over the entire mission duration, a baseline dynamic mission reliability model is constructed. Figure 2 demonstrates the increasing conditional reliability over the mission due to the receding mission horizon. These conditional reliability values act as the baseline to achieve the desired mission assurance over the mission duration.

7.3. Verification Case Study

As discussed, we are interested in demonstrating the value of intelligent selection of plans that support reliability-informed mission assurance requirements. To

demonstrate our approach a Dynamic Programming simulation is implemented that is detailed in Figure 70.

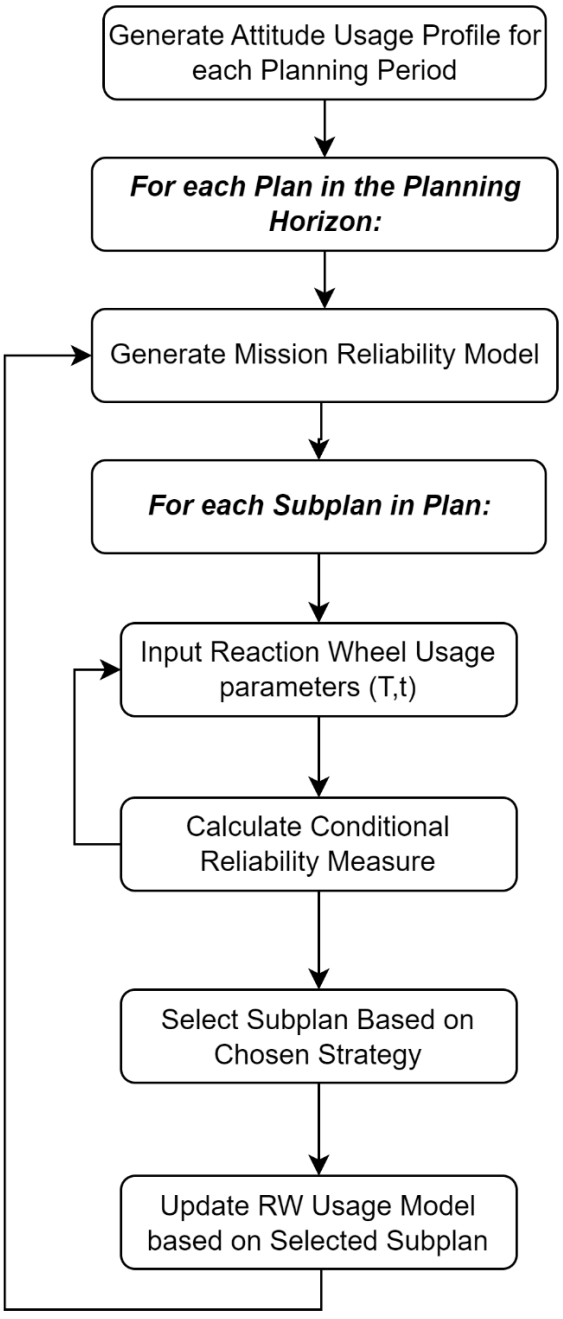

Figure 70 Dynamic Programming approach for reliability-based mission assurance strategy selection.

The key contribution of the approach is to show the effect of incorporating a systematic plan selection process for each planning cycle of the mission duration. In the simulation two plan selection rules are explored. The first is a MAX reliability plan

selection criterion – where for each planning cycle each possible plan (sub-plan) is evaluated in terms of its effect on remaining DSS mission level reliability $\mathbf{R_{DSS}}$.and the plan that provides the highest level of reliability is selected. The second is a RANDOM selection, that is, a subplan selection not based on considering past RW usage. Practically, the RANDOM selection represents plan selection purely based on the evaluation of the global utility function. U_g defined in Chapter 6, without any explicit consideration of mission reliability objectives. During the simulation, two failure conditions are injected creating an initial (Figure 71) and final degraded functional figuration (Figure 72).

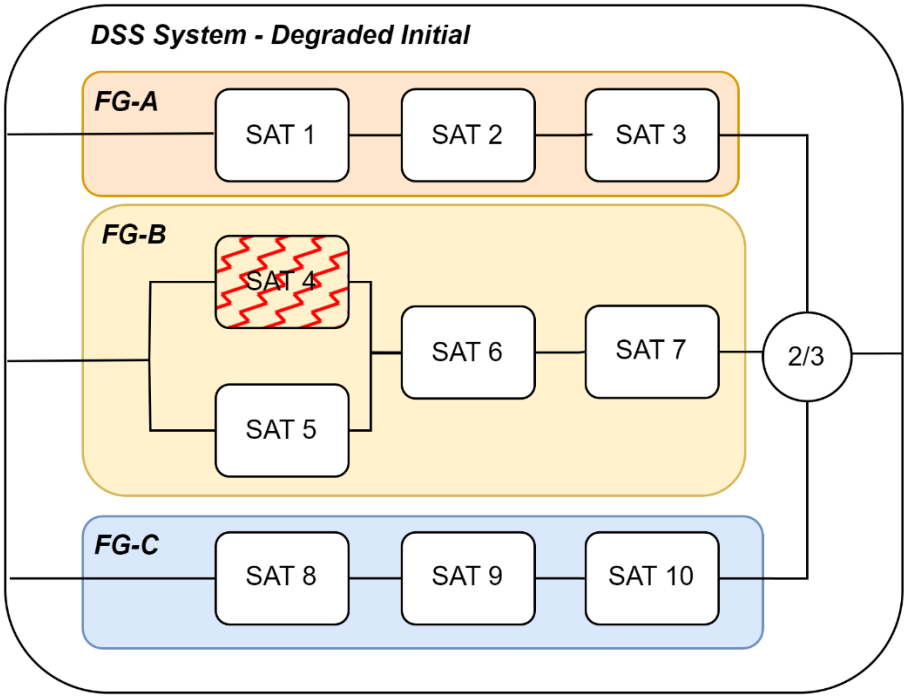

Figure 71 Degraded Initial Functional Configuration

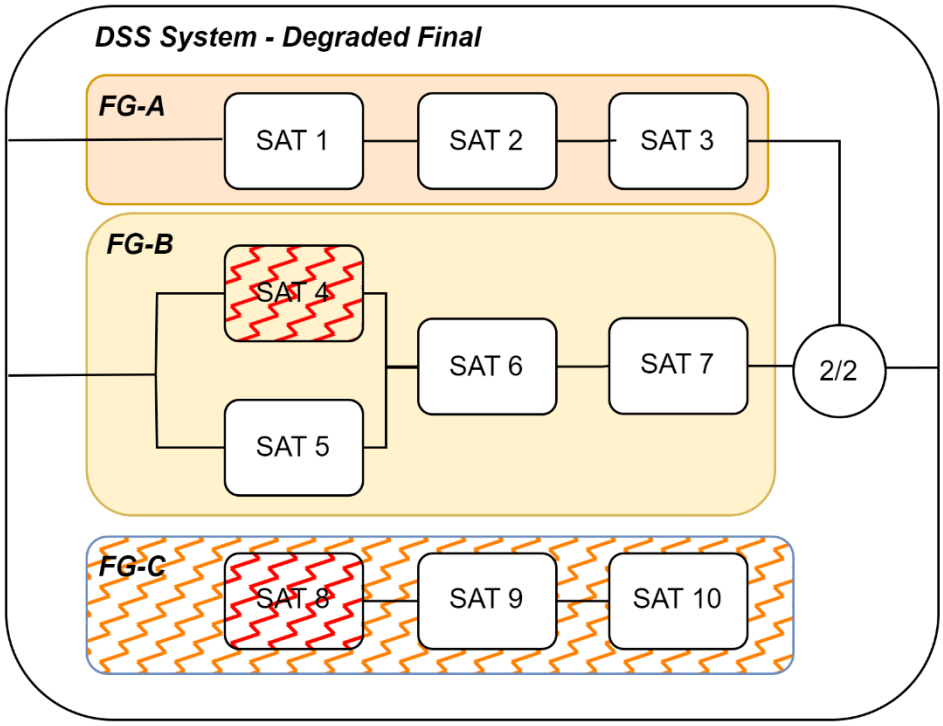

Figure 72 Degraded Final Functional Configuration

The initial degraded functional configuration represents a loss of SAT 4, where either one of its RWs has failed. Similarly, the Final degraded functional configuration represents the loss of SAT 8, reducing the system-level functional configuration to a 2/2 KoN system (series configuration). To represent the uncertainty in the operational cycle usage of the RW systems, we extend the initial reliability estimate assumptions in Table 30 to include stochastic behaviour. This enables a planning model generation that provides representative variability in each subplan and therefore the cumulative effect of plan selection to be shown. Table 31 each of the inputs to the simulation.

Table 31 Simulation Inputs

Planning Horizon	5 Years
Planning Interval	24 Hours
Total Plans	1825
Number of Subplans per planning interval	10
Mean RW RPM per planning interval	4500 RPM
RW RPM Standard Deviation	500 RPM
Number of Attitude Maneuvers per planning interval	RND (5,8)

Total Up Time Per Planning interval	RND (5,20) minutes
Ratio Between Reaction Wheels Usage in each planning interval (X, Y, Z)	[4,3,2] (shuffled)

7.3.1. Simulation Results

The results of each sub-plan selection strategy (MAX, Random) are illustrated below. Figure 73 demonstrates the approach under nominal conditions (failure-free mission) meaning that initial reliability model structure is maintained throughout the mission duration. In comparison to our baseline reliability generated from estimated conditions, the results show a significant (positive) deviation using the MAX plan selection strategy, in contrast to the random selection strategy that deviates negatively from the required reliability performance over the mission duration.

The approach is also demonstrated under the more likely conditions of system failure Figure 74, where the initial and final degraded configurations are then used to calculate DSS System Reliability. For each failure instance, the reliability of the system naturally drops, however, the MAX selection strategy significantly outperforms the random strategy, with a much smaller magnitude of mission reliability loss.

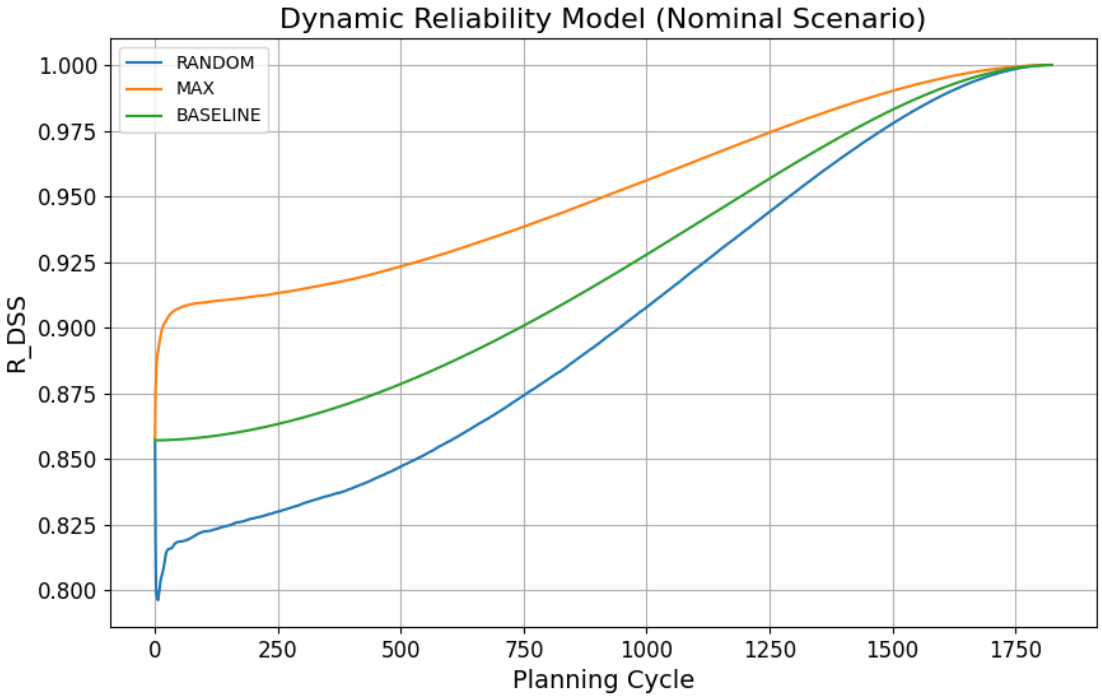

Figure 73 Conditional reliability of the DSS system under nominal conditions over the 5 year mission period

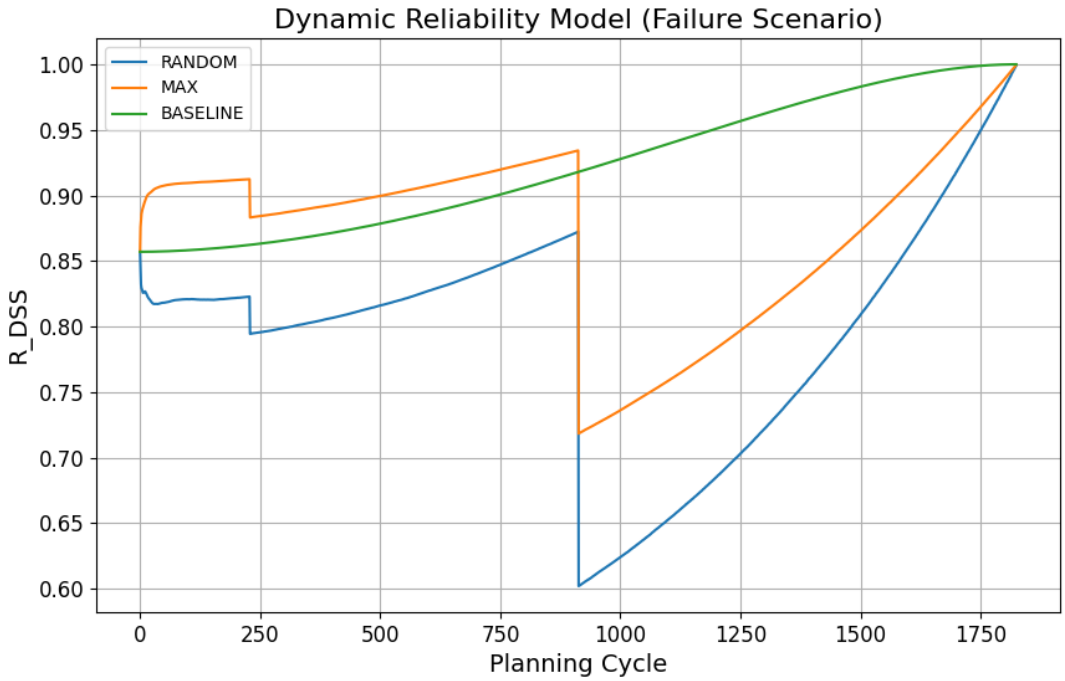

Figure 74 Conditional reliability of the DSS system under failure conditions over the 5 year mission period

To further quantify this relationship, we introduce a system resilience metric. System resilience is typically represented as a combination of survivability and recoverability. Survivability is concerned with the ability of a system to survive disruption and maintain function (drop in reliability without system failure), whereas recoverability is a measure of the system's ability to "Bounce back", i.e. return to a level of nominal performance over time given a disruption (baseline reliability) [285]. To represent this behaviour, the percentage difference between the baseline and the performance of each strategy is calculated.

In the nominal scenario illustrated by Figure 75, a clear positive buffer in resilience is demonstrated throughout the mission duration. In the failure scenario, Figure 76, it is demonstrated that the MAX strategy provides a lower deviation from the normal providing a greater performance in the level of recovery of failure events, due to the compounding effect of plan selection based on maximizing system reliability and building system resilience.

Notably, the positive "buffer" in resilience provided by the MAX strategy would allow for increased usage time, and subsequently constraints provided to the mission planning module, increasing the availability of potential RSO observations. This forms a critical component of the mission assurance constraint control action (CA1b), ensuring both operational effectiveness and adherence to reliability targets. Conversely, a negative buffer would trigger feedback into the DSS system to limit uptime for affected platforms, ensuring mission assurance constraints are maintained.

This dual control mechanism reinforces the system's ability to adapt dynamically to operational conditions while safeguarding reliability and resilience.

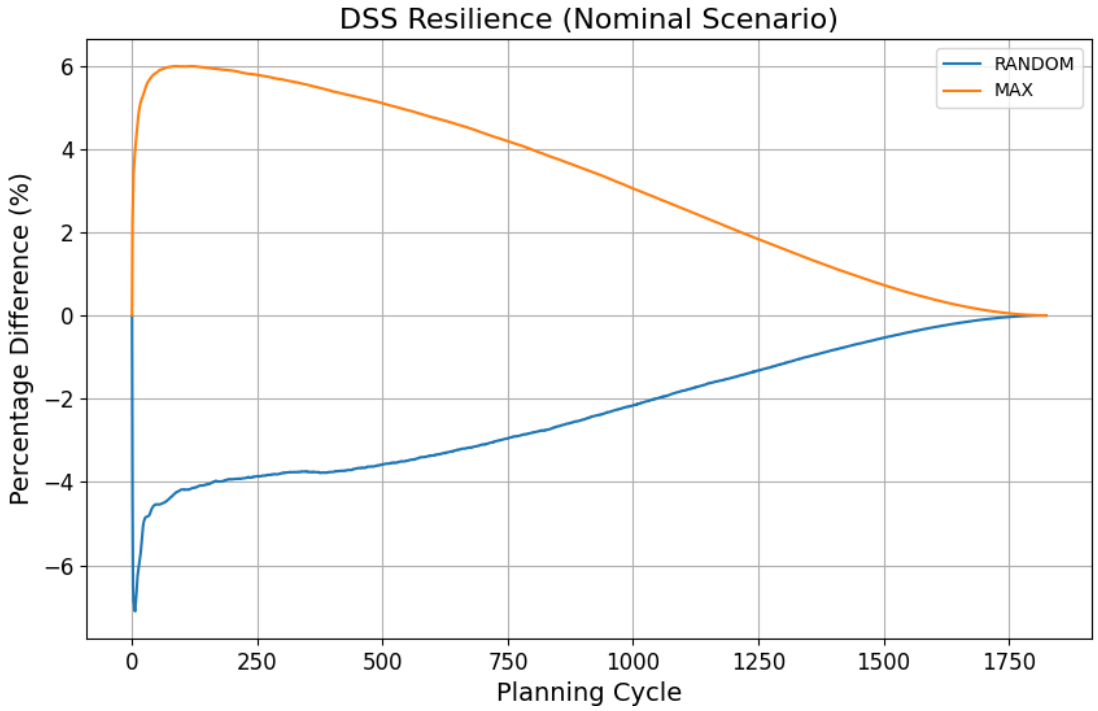

Figure 75 DSS Resilience in nominal conditions of the 5-year mission period, defined as the percentage difference between the baseline mission reliability objective

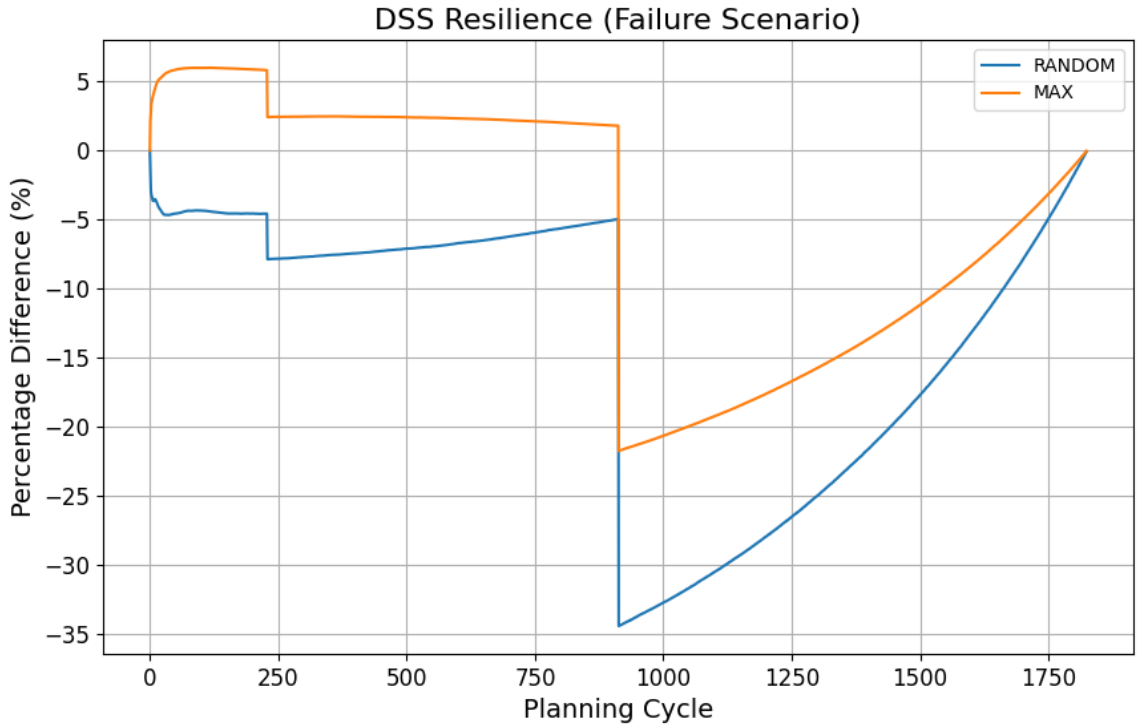

Figure 76 DSS Resilience in failure conditions of the 5-year mission period, defined as the percentage difference between the baseline mission reliability objective

7.4. Conclusions

A comprehensive framework integrating supervisory control mechanisms with dynamic system reliability models was developed, addressing Objective 6. This framework enhances mission assurance, operational reliability, and resilience in Distributed Satellite Systems (DSS) by systematically selecting plans that align with reliability-informed mission assurance requirements. Key contributions include the construction of initial and dynamic reliability models, incorporating Weibull-based reliability functions for platform-level components and extending these to system-level mission configurations using a Systems of Systems (SoS) perspective.

To support dynamic mission assurance, a plan selection methodology was proposed, enabling intelligent plan selection based on operational usage profiles. This approach aims to continually meet, build resilience, and optimize operational usage profiles to ensure reliability-based mission assurance requirements are upheld. Dynamic reliability modelling captured the effects of operational uncertainty and evolving system configurations, enabling real-time assessments of conditional reliability based on prior usage and projected operational demands.

Verification studies demonstrated the superiority of reliability-informed plan selection strategies over random selection, particularly in scenarios involving system degradation or failures. These strategies significantly improved mission survivability,

recoverability, and overall system resilience, ensuring continued DSS functionality under real-world operational constraints. Notably, the positive "buffer" in resilience provided by the MAX strategy would allow for increased usage time for given satellite platform reaction wheels, forming part of the mission assurance constraint control action (CA1b). Conversely, a negative buffer would trigger feedback into the DSS system to limit uptime for affected platforms, ensuring mission assurance constraints are maintained. This dual control mechanism reinforces the system's ability to adapt dynamically to operational conditions while safeguarding reliability and resilience.

.

.

Chapter 8

Conclusions and Recommendations

8.1. Conclusions

The conclusions of this research project are here summarised in terms of achieved research objectives:

1. **Identify the evolving goals of Space Traffic Management (STM) focusing on operational challenges and technological drivers that enable a safe and sustainable use of the space environment**

   An extensive review of STM of approximately 200 publications was performed that identified the key technical and operational challenges in Space Traffic Management (STM). In addition to two major publications, the critical review informed the design of an Intelligent DSS framework for STM that was implemented in subsequent chapters.

2. **Develop an integrated operational framework for intelligent Distributed Satellite Systems (DSS) that integrates key system autonomy functionalities.**

   An operational framework for intelligent Distributed Satellite Systems (DSS) to support Space Traffic Management (STM) was developed. Foundational STM goals were translated into specific autonomy functions, including mission planning, collision avoidance, and orbit/attitude optimisation. These functions were integrated into a hierarchical control structure featuring supervisory, coordination, and self-adaptive feedback loops. This structure facilitates task coordination, and supervisory control, and supports adaptive responses to dynamic space environments. The framework served as the basis for verifying and simulating the components and interactions of the proposed system.

3. **Develop an integrated approach to quantify and propagate uncertainty in Resident Space Object (RSO) tracking and establish probabilistic models for collision prediction and avoidance.**

   An integrated approach to quantify and propagate RSO uncertainty was developed, addressing Objective 3. Ground-based and space-based sensor-level uncertainty models were established, focusing on tracking and navigation system errors. Covariance realism at the sensor level was rigorously tested using statistical metrics, including the Average Mahalanobis Distance (AMD)

and Cramer–von Mises (CVM) goodness-of-fit tests, to validate the Gaussian assumptions underlying uncertainty representations. These models highlighted the required performance conditions for linearised uncertainty propagation methods for both ground-based radar systems and space-based millimetre-wave (MMW) radar platforms. By combining navigation and tracking uncertainties, a comprehensive framework for quantifying RSO uncertainty at the sensor level was developed, enabling reliable inputs for collision probability calculations and avoidance strategies This research, which advances the understanding of performance-based sensor-level uncertainty for Space Traffic Management (STM), was published in a major peer-reviewed publication, highlighting its contribution to the field of space surveillance and collision avoidance autonomy in Distributed Satellite Systems (DSS).

4. **Develop and implement onboard optimization algorithms for adaptive trajectory and attitude planning in Space-Based Space Surveillance (SBSS) mission and collision avoidance operations.**

   Optimization algorithms for adaptive trajectory and attitude planning in Space-Based Space Surveillance (SBSS) missions was developed and implemented, addressing Objective 4. Dynamic models incorporating perturbation effects were formulated, and adaptive metaheuristic algorithms, specifically Particle Swarm Optimization (PSO), were applied to solve complex trajectory and attitude optimization problems. The methodologies enable energy- and time-efficient manoeuvres for collision avoidance and attitude reorientation under real-world mission constraints. Key innovations include the use of Bézier curves for attitude path planning and Modified Equinoctial Elements (MEE) for orbital dynamics, ensuring robustness and accuracy. The integration of these onboard optimization capabilities into the DSS platform facilitates autonomous and adaptive decision-making enhancing the operational effectiveness of distributed satellite systems.

5. **Design a distributed mission planning strategy for Space-Based Space Surveillance (SBSS) operations, to optimize task allocation, minimize duplication, and maximize global utility across collaborative satellite platforms.**

   A distributed mission planning strategy for Space-Based Space Surveillance (SBSS) operations was developed and implemented, addressing Objective 4. The framework integrates Ant Colony Optimization (ACO)-based multi-agent coordination to optimize task allocation, minimize duplication, and maximize global utility across Distributed Satellite Systems (DSS). Supervisory control ensures alignment with mission goals, while onboard autonomy adapts to unique satellite constraints and dynamic environments. Key innovations include iterative feedback loops for coordinated tasking, and a self-adaptive loop using Particle Swarm Optimization (PSO) for real-time trajectory and

attitude optimization under operational constraints. Simulation-based case studies validate improvements in task efficiency, global utility, and duplication reduction. This work was published in a major journal and demonstrates significant potential to enhance SBSS mission planning in dynamic and complex operational environments.

6. **Develop a comprehensive framework that integrates supervisory control mechanisms with dynamic system reliability models to ensure mission assurance, operational reliability, and resilience in Distributed Satellite Systems (DSS)**

   A comprehensive framework integrating supervisory control mechanisms with dynamic system reliability models was developed and implemented, addressing Objective 6. This framework systematically aligns plan selection with reliability-informed mission assurance requirements to enhance mission assurance, operational reliability, and resilience in Distributed Satellite Systems (DSS) A plan selection methodology was proposed to enable intelligent, usage-profile-informed decision-making, with dynamic reliability modelling capturing the effects of operational uncertainty and evolving configurations. Verification studies demonstrated significant improvements in mission survivability, recoverability, and resilience under both nominal and degraded conditions, driven by the superior performance of the MAX selection strategy. This strategy facilitates enhanced platform usage availability through the dynamic adjustment of mission planning constraints while maintaining system reliability targets. Limitations include the reliance on representative reliability parameters and the absence of failure-reduction dynamics in simulations.

8.2. Recommendations for Future Work

The following key areas have been identified for performing further research and development activities.

- **Expand sensor studies** Extend covariance realism studies to space-based optical sensors, examining their performance under varying physical and geometric configurations.
- **Incorporate covariance realism into SBSS mission planning:** Validate sensor tasking plans based on covariance realism and integrate them into the mission planning process.
- **Address communication constraints:** Simulate the effects of communication delays, link interruptions, and bandwidth limitations on mission planning and coordination.

- **Enhance coordination loop:** Develop more sophisticated multi-agent coordination algorithms that integrate supervisory intervention. These mechanisms would support conflict resolution when autonomous coordination fails to meet mission objectives.
- **Expand platform reliability models:** Extend platform-level reliability models to include additional key functions and subsystems, such as communication links, thermal control, and propulsion systems, creating a more comprehensive representation of DSS functional reliability to enhance the plan selection approach.
- **Incorporate effects of plan selection on system reliability**: Develop discrete event simulation frameworks to model interactions between reliability improvements and reduced failure occurrences, offering a more detailed view of system behaviour and dependencies under intelligent plan selection approaches.
- **Refine plan selection mechanisms**: Explore enhanced plan selection criteria that balance immediate usage demands with long-term system resilience by integrating adaptive mission assurance constraint control mechanisms into mission planning simulations.
- **Incorporate adaptive functional configurations:** Implement adaptive functional architectures into plan assessments to represent evolving orbit designs and replacement platforms.
- **Investigate Human-in/on-the-Loop Integration**: Study the effects of human operators into the supervisory decision-making process including cognitive effects and human machine interface design.
- **Incorporate additional cyber physical threat vectors**: Development and simulation of additional supervisory control actions that support the mitigation of additional cyber physical threat vectors such as space weather and direct cyber-attacks.

References

[1] M. Sippel, "Introducing the SpaceLiner vision," 2007.

[2] M. Vozoff and J. Couluris, "SpaceX products-advancing the use of space," in *AIAA SPACE 2008 Conference \& Exposition*, 2008, vol. 9.

[3] R. D. Howard *et al.*, "Dream chaser commercial crewed spacecraft overview," in *17th AIAA International Space Planes and Hypersonic Systems and Technologies Conference*, 2011.

[4] D. Linehan, *Spaceshipone: An illustrated history*. Zenith Press, 2011.

[5] R. Longstaff and A. Bond, "The skylon project," *AIAA Journal*, 2011.

[6] R. A. M. Hunter, *Point-to-point Commercial Space Transportation in National Aviation System*. 2010.

[7] P. Duan, "ADS-B feasibility study for commercial space flight operations," in *Digital Avionics Systems Conference (DASC), 2010 IEEE/AIAA 29th*, 2010, pp. 3-A.

[8] R. VanSuetendael, A. Hayes, and R. Birr, "A common communications, navigation & surveillance infrastructure for accommodating space vehicles in the next generation air transportation system," in *AIAA 2008-6893, AIAA Atmospheric Flight Mechanics Conference and Exhibit*, 2008.

[9] M. J. Holzinger and M. K. Jah, "Challenges and Potential in Space Domain Awareness," ed, 2018.

[10] T. Flohrer, H. Krag, H. Klinkrad, and T. Schildknecht, "Feasibility of performing space surveillance tasks with a proposed space-based optical architecture," *Advances in space research*, vol. 47, no. 6, pp. 1029-1042, 2011.

[11] J. Utzmann and A. Wagner, "SBSS Demonstrator: A Space-Based Telescope for Space Surveillance and Tracking," ed.

[12] Y.-W. Chang, "The first decade of commercial space tourism," *Acta Astronautica*, vol. 108, pp. 79-91, 2015.

[13] D. J. Piatak, M. K. Sekula, and R. D. Rausch, "Ares Launch Vehicle Transonic Buffet Testing and Analysis Techniques," *Journal of Spacecraft and Rockets*, vol. 49, no. 5, pp. 798-807, 2012.

[14] J. P. W. Stark, "The Spacecraft Environment and its Effect on Design," in *Spacecraft Systems Engineering, 4th Edition*, P. W. Fortescue, G. G. Swinerd, and J. P. W. Stark Eds.: Wiley, 2011.

[15] Z. Shen and P. Lu, "Onboard generation of three-dimensional constrained entry trajectories," *Journal of Guidance, control, and Dynamics*, vol. 26, no. 1, pp. 111-121, 2003.

[16] Z. Shen and P. Lu, "On-board entry trajectory planning for sub-orbital flight," *Acta Astronautica*, vol. 56, no. 6, pp. 573-591, 2005.

[17] P. Lu and P. Rao, "An integrated approach for entry mission design and flight simulations," in *42nd AIAA Aerospace Sciences Meeting and Exhibit*, 2004, p. 702.

[18] P. Lu, "Entry guidance and trajectory control for reusable launch vehicle," *Journal of Guidance, Control, and Dynamics*, vol. 20, no. 1, pp. 143-149, 1997.

[19] P. Lu, "Asymptotic analysis of quasi-equilibrium glide in lifting entry flight," *Journal of Guidance, Control, and Dynamics,* vol. 29, no. 3, pp. 662-670, 2006.

[20] K. D. Mease, D. T. Chen, P. Teufel, H. Sch-ograve, and nenberger, "Reduced-order entry trajectory planning for acceleration guidance," *Journal of Guidance, Control, and Dynamics,* vol. 25, no. 2, pp. 257-266, 2002.

[21] A. Saraf, J. A. Leavitt, D. T. Chen, and K. D. Mease, "Design and evaluation of an acceleration guidance algorithm for entry," *Journal of Spacecraft and Rockets,* vol. 41, no. 6, pp. 986-996, 2004.

[22] K.-U. Schrogl, "Space traffic management: The new comprehensive approach for regulating the use of outer space — Results from the 2006 IAA cosmic study," *Space Policy,* vol. 62, pp. 272-276, 2008.

[23] C. Contant-Jorgenson, P. Lala, and K.-U. Schrogl, "The International Academy of Astronautics (IAA) Cosmic Study on Space Traffic Management," presented at the United Nations Committee on the Peaceful Uses of Outer Space (UNCOPUOS), Vienna, Austria, Jun 2006.

[24] H. Cukurtepe and I. Akgun, "Towards space traffic management system," *Acta Astronautica,* vol. 65, pp. 870-878, 2009.

[25] W. K. Tobiska, "The Space Environment," in *Space Mission Engineering: The New SMAD,* J. R. Wertz, D. F. Everett, and J. J. Puschell Eds.: Microcosm Press, 2011, ch. 7.

[26] B. Arbesser-Rastburg and N. Jakowski, "Effects on satellite navigation," in *Space Weather - Physics and Effects*, V. Bothmer and I. Daglis Eds.: Springer-Verlag Berlin Heidelberg, 2007, pp. 353-382.

[27] J.-G. Wu, L. Eliasson, H. Lundstedt, A. Hilgers, L. Andersson, and O. Norberg, "Space environment effects on geostationary spacecraft: Analysis and prediction," *Advances in Space Research,* vol. 26, no. 1, pp. 31-36, 2000.

[28] N. Iucci *et al.*, "Space weather conditions and spacecraft anomalies in different orbits," *Space Weather,* vol. 3, no. 1, pp. 1-16, 2005.

[29] Y.-z. Luo and Z. Yang, "A review of uncertainty propagation in orbital mechanics," *Progress in Aerospace Sciences,* vol. 89, pp. 23-39, 2017.

[30] S. Ramasamy, R. Sabatini, and A. Gardi, "A Unified Analytical Framework for Aircraft Separation Assurance and UAS Sense-and-Avoid," *Journal of Intelligent \& Robotic Systems,* pp. 1-20.

[31] I.-A. S. D. C. Committee, "IADC space debris mitigation guidelines," *IADC-02-01 Revision,* vol. 1, 2007.

[32] A. Kato, B. Lazare, D. Oltrogge, and P. Stokes, "Standardization by ISO to Ensure the Sustainability of Space Activities," in *Proceedings of the Sixth European Conference on Space Debris, ESOC, Darmstadt, Germany*, 2013, pp. 22-25.

[33] S. Winkler *et al.*, "GPS Receiver On-Orbit Performance for the GOES-R Spacecraft," 2017.

[34] B. Hudson, "AN/MPS-39 support of US space launch activities," in *Radar Conference, 1995., Record of the IEEE 1995 International*, 1995: IEEE, pp. 39-43.

[35] "Terminal Guidance System for Satellite Rendezvous," *Journal of the Aerospace Sciences,* vol. 27, no. 9, pp. 653-658, 1960/09/01 1960, doi: 10.2514/8.8704.

[36] J. E. Young, M. G. E. Kee, and C. M. Young, "Effects of Future Launch and Reentry Operations on the National Airspace System," *Journal of Air Transportation*, 2017.

[37] T. J. Colvin and J. J. Alonso, "Compact envelopes and SU-FARM for integrated air-and-space traffic management," in *AIAA Aerospace Sciences Meeting*, 2015.

[38] T. Kistan, A. Gardi, R. Sabatini, S. Ramasamy, and E. Batuwangala, "An evolutionary outlook of air traffic flow management techniques," *Progress in Aerospace Sciences*, Review vol. 88, pp. 15-42, 2017, doi: 10.1016/j.paerosci.2016.10.001.

[39] D. J. Kessler, N. L. Johnson, J. C. Liou, and M. Matney, "The kessler syndrome: implications to future space operations," *Advances in the Astronautical Sciences*, vol. 137, no. 8, p. 2010, 2010.

[40] D. J. Kessler, "Orbital debris environment for spacecraft in low earth orbit," *Journal of spacecraft and rockets*, vol. 28, no. 3, pp. 347-351, 1991.

[41] N. L. Johnson, "A new look at the GEO and near-GEO regimes: Operations, disposals, and debris," *Acta Astronautica*, vol. 80, pp. 82-88, 2012.

[42] H. Krag, S. Lemmens, T. Flohrer, and H. Klinkrad, "Global trends in achieving successful end-of-life disposal in LEO and GEO," in *SpaceOps 2014 Conference*, 2014, p. 1933.

[43] J.-C. Liou and P. Krisko, "An Update on the Effectiveness of Postmission Disposal in LEO," 2013.

[44] R. P. Patera, "General method for calculating satellite collision probability," *Journal of Guidance, Control, and Dynamics*, vol. 24, no. 4, pp. 716-722, 2001.

[45] J. L. Foster and H. S. Estes, "A parametric analysis of orbital debris collision probability and maneuver rate for space vehicles," *NASA JSC*, vol. 25898, 1992.

[46] R. P. Patera and G. E. Peterson, "Space vehicle maneuver method to lower collision risk to an acceptable level," *Journal of guidance, control, and dynamics*, vol. 26, no. 2, pp. 233-237, 2003.

[47] S. Alfano, "A numerical implementation of spherical object collision probability," *Journal of Astronautical Sciences*, vol. 53, no. 1, pp. 103-109, 2005.

[48] F. K. Chan, *Spacecraft collision probability*. Aerospace Press El Segundo, CA, 2008.

[49] R. Garcia-Pelayo and J. Hernando-Ayuso, "Series for Collision Probability in Short-Encounter Model," *Journal of Guidance, Control, and Dynamics*, pp. 1908-1916, 2016.

[50] R. Serra, D. Arzelier, M. Joldes, J.-B. Lasserre, A. Rondepierre, and B. Salvy, "Fast and accurate computation of orbital collision probability for short-term encounters," *Journal of Guidance, Control, and Dynamics*, pp. 1009-1021, 2016.

[51] A. Gardi, R. Sabatini, and S. Ramasamy, "Multi-objective optimisation of aircraft flight trajectories in the ATM and avionics context," *Progress in Aerospace Sciences*, Review Article vol. 83, pp. 1-36, 2016, doi: 10.1016/j.paerosci.2015.11.006.

[52] N. P. Y.Lim, A. Gardi and R.Sabatini, "Eulerian Optimal Control Formulation for Dynamic Morphing of Airspace Sectors," presented at the 31st Congress of the International Council of the Aeronautical Sciences, 2018.

[53] P. H. Kopardekar, "Safely enabling UAS operations in low-altitude airspace," presented at the NASA UAS Traffic Management (UTM), Moffett Field, CA, USA, 2015.

[54] NASA, "UTM: Air Traffic Management for Low-Altitude Drones," in "NASAfacts," National Aeronautics and Space Administration (NASA), Washington DC, USA, NASAfacts NF-2015-10-596-HQ, 2015.

[55] J. Homola, T. Prevot, J. Mercer, N. Bienert, and C. Gabriel, "UAS traffic management (UTM) simulation capabilities and laboratory environment," in *35th DASC Digital Avionics Systems Conference, DASC 2016*, 2016, vol. 2016-December: Institute of Electrical and Electronics Engineers Inc., doi: 10.1109/DASC.2016.7778078. [Online]. Available: https://www.scopus.com/inward/record.uri?eid=2-s2.0-85009483664&doi=10.1109%2fDASC.2016.7778078&partnerID=40&md5=9c22ea423428d93bd91b89b503278c8c

http://ieeexplore.ieee.org/document/7778078/?reload=true

[56] P. Kopardekar, J. Rios, T. Prevot, M. Johnson, J. Jung, and J. E. Robinson, III, "Unmanned aircraft system traffic management (UTM) concept of operations," in *16th AIAA Aviation Technology, Integration, and Operations Conference, 2016*, 2016: American Institute of Aeronautics and Astronautics Inc, AIAA. [Online]. Available: https://www.scopus.com/inward/record.uri?eid=2-s2.0-84980417654&partnerID=40&md5=3a6a3692f81ef8cbee74fd2b1c0a510d. [Online]. Available: https://www.scopus.com/inward/record.uri?eid=2-s2.0-84980417654&partnerID=40&md5=3a6a3692f81ef8cbee74fd2b1c0a510d

[57] T. Prevot, J. Homola, and J. Mercer, "From rural to urban environments: Human/systems simulation research for low altitude UAS traffic management (UTM)," in *16th AIAA Aviation Technology, Integration, and Operations Conference, 2016*, 2016: American Institute of Aeronautics and Astronautics Inc, AIAA. [Online]. Available: https://www.scopus.com/inward/record.uri?eid=2-s2.0-84980349695&partnerID=40&md5=7fd723d4e63ea62cb7f3e6b85eb5ffbc. [Online]. Available: https://www.scopus.com/inward/record.uri?eid=2-s2.0-84980349695&partnerID=40&md5=7fd723d4e63ea62cb7f3e6b85eb5ffbc

[58] E. Mueller, P. Kopardekar, and K. Goodrich, "Enabling airspace integration for high-density on-demand mobility operations," in *17th AIAA Aviation Technology, Integration, and Operations Conference, 2017*, 2017: American Institute of Aeronautics and Astronautics Inc, AIAA. [Online]. Available: https://www.scopus.com/inward/record.uri?eid=2-s2.0-85023633412&partnerID=40&md5=ed6253ecd08e8320b50f0bd214659b31. [Online]. Available: https://www.scopus.com/inward/record.uri?eid=2-s2.0-85023633412&partnerID=40&md5=ed6253ecd08e8320b50f0bd214659b31

[59] S. Ramasamy, R. Sabatini, A. Gardi, and J. Liu, "LIDAR obstacle warning and avoidance system for unmanned aerial vehicle sense-and-avoid," (in English), *Aerosp Sci Technol*, Article vol. 55, pp. 344-358, 2016, doi: 10.1016/j.ast.2016.05.020.

[60] S. Ramasamy, R. Sabatini, and A. Gardi, "A Unified Analytical Framework for Aircraft Separation Assurance and UAS Sense-and-Avoid," (in English), *J Intell Rob Syst Theor Appl*, Article vol. 91, no. 3-4, pp. 735-754, 2018, doi: 10.1007/s10846-017-0661-z.

[61] S. Ramasamy, R. Sabatini, and A. Gardi, "A Novel Approach to Cooperative and Non-Cooperative RPAS Detect-and-Avoid," (in English), *SAE Techni. Paper.*, Conference Paper vol. 2015-September, no. September, 2015, doi: 10.4271/2015-01-2470.

[62] E. Batuwangala, T. Kistan, A. Gardi, and R. Sabatini, "Certification Challenges for Next-Generation Avionics and Air Traffic Management Systems," *IEEE Aerospace and Electronic Systems Magazine*, vol. 33, no. 9, pp. 44-53, 2018, doi: 10.1109/MAES.2018.160164.

[63] S. Ramasamy, R. Sabatini, and A. Gardi, "Avionics sensor fusion for small size unmanned aircraft Sense-and-Avoid," in *2014 IEEE International Workshop on Metrology for Aerospace, MetroAeroSpace 2014*, Benevento, 2014: IEEE Computer Society, pp. 271-276, doi: 10.1109/MetroAeroSpace.2014.6865933. [Online]. Available:

https://www.scopus.com/inward/record.uri?eid=2-s2.0-84907305354&doi=10.1109%2fMetroAeroSpace.2014.6865933&partnerID=40&md5=2d8e8ea1b54eba12e2e0bd1f0c48acff

[64] S. Ramasamy, A. Gardi, J. Liu, and R. Sabatini, "A laser obstacle detection and avoidance system for manned and unmanned aircraft applications," in *2015 International Conference on Unmanned Aircraft Systems, ICUAS 2015*, 2015: Institute of Electrical and Electronics Engineers Inc., pp. 526-533, doi: 10.1109/ICUAS.2015.7152332. [Online]. Available: https://www.scopus.com/inward/record.uri?eid=2-s2.0-84941109082&doi=10.1109%2fICUAS.2015.7152332&partnerID=40&md5=a8ce715b3e8cc6b3943a2a7ed55cca1f

[65] R. Sabatini, T. Moore, and S. Ramasamy, "Global navigation satellite systems performance analysis and augmentation strategies in aviation," (in English), *Progress in Aerospace Sciences*, Review vol. 95, pp. 45-98, 2017, doi: 10.1016/j.paerosci.2017.10.002.

[66] R. Sabatini, T. Moore, and C. Hill, "A new avionics-based GNSS integrity augmentation system: Part 1 - Fundamentals," (in English), *J. Navig.*, Article vol. 66, no. 3, pp. 363-384, 2013, doi: 10.1017/S0373463313000027.

[67] R. Sabatini, T. Moore, C. Hill, and S. Ramasamy, "Investigation of GNSS Integrity Augmentation Synergies with Unmanned Aircraft Sense-and-Avoid Systems," (in English), *SAE Techni. Paper.*, Conference Paper vol. 2015-September, no. September, 2015, doi: 10.4271/2015-01-2456.

[68] M. Eineder, A. Moreira, and A. Roth, "Ten Years of TerraSAR-X—Scientific Results," ed: Multidisciplinary Digital Publishing Institute, 2019.

[69] B. Wille, M. T. Wörle, and C. Lenzen, "VAMOS–Verification of Autonomous Mission Planning On-board a Spacecraft," in *IFAC Proceedings Volumes*, 2013, vol. 46, no. 19: Elsevier, pp. 382-387.

[70] K. Thangavel *et al.*, "Trusted Autonomous Operations of Distributed Satellite Systems Using Optical Sensors," *Sensors*, vol. 23, no. 6, p. 3344, 2023. [Online]. Available: https://www.mdpi.com/1424-8220/23/6/3344.

[71] M. D. Graziano, "Overview of distributed missions," in *Distributed space missions for Earth system monitoring*: Springer, 2013, pp. 375-386.

[72] K. Thangavel *et al.*, "Artificial Intelligence for Trusted Autonomous Satellite Operations," *Progress in Aerospace Sciences*, vol. 144, p. 100960, 2024/01/01/ 2024, doi: https://doi.org/10.1016/j.paerosci.2023.100960.

[73] S. Hilton, A. Gardi, R. Sabatini, N. Ezer, and S. Desai, "Human-machine system design for autonomous distributed satellite operations," in *2020 AIAA/IEEE 39th Digital Avionics Systems Conference (DASC)*, 2020: IEEE, pp. 1-8.

[74] S. Mathavaraj and R. Padhi, *Satellite formation flying: high precision guidance using optimal and adaptive control techniques*. Springer Nature, 2021.

[75] J. Wang and S. Nakasuka, "Cluster flight orbit design method for fractionated spacecraft," *Aircraft Engineering and Aerospace Technology*, vol. 84, no. 5, pp. 330-343, 2012.

[76] C. Araguz, E. Bou-Balust, and E. J. S. E. Alarcón, "Applying autonomy to distributed satellite systems: Trends, challenges, and future prospects," vol. 21, no. 5, pp. 401-416, 2018.

[77] J. Guo, D. Maessen, and E. Gill, "Fractionated spacecraft: The new sprout in distributed space systems," in *60th International Astronautical Congress: IAC 2009, 12-16 October 2009, Daejeon, Republic of Korea*, 2009.

[78] A. Golkar and I. L. i Cruz, "The federated satellite systems paradigm: Concept and business case evaluation," *Acta Astronautica*, vol. 111, pp. 230-248, 2015.

[79] C. Araguz, E. Bou-Balust, and E. Alarcón, "Applying autonomy to distributed satellite systems: Trends, challenges, and future prospects," *Systems Engineering*, vol. 21, no. 5, pp. 401-416, 2018.

[80] G. Australia, "b. Sentinel Hotspots," ed, 2018.

[81] Z. Shabbir, A. Sarosh, and M. J. A. Nayyer, "Space Technology Applications for Maritime Intelligence, Surveillance, and Reconnaissance," vol. 17, no. 2, pp. 104-126, 2019.

[82] G. Sciré, F. Santoni, and F. Piergentili, "Analysis of orbit determination for space based optical space surveillance system," *Advances in Space Research*, vol. 56, no. 3, pp. 421-428, 2015.

[83] E.-J. Choi *et al.*, "Performance analysis of sensor systems for space situational awareness," *Journal of Astronomy Space Sciences*

vol. 34, no. 4, pp. 303-313, 2017.

[84] K. F. Hussain, K. Thangavel, A. Gardi, and R. Sabatini, "Passive electro-optical tracking of resident space objects for distributed satellite systems autonomous navigation," *Remote Sensing*, vol. 15, no. 6, p. 1714, 2023.

[85] L. Felicetti and M. R. Emami, "A multi-spacecraft formation approach to space debris surveillance," *Acta Astronautica*, vol. 127, pp. 491-504, 2016.

[86] X. Vanwijck and T. Flohrer, "Possible contribution of space-based assets for space situational awareness," vol. 4, pp. 2466-2472, 01 2008.

[87] M. Gruntman, "Passive optical detection of submillimeter and millimeter size space debris in low Earth orbit," *Acta Astronautica*, vol. 105, no. 1, pp. 156-170, 2014.

[88] J. Utzmann *et al.*, "Space-based space surveillance and tracking demonstrator: mission and system design," 2014.

[89] H. Yunpeng, L. Kebo, L. Yan'gang, and C. Lei, "Review on strategies of space-based optical space situational awareness," *Journal of Systems Engineering and Electronics*, vol. 32, no. 5, pp. 1152-1166, 2021.

[90] J. Du, J. Chen, B. Li, and J. J. A. A. Sang, "Tentative design of SBSS constellations for LEO debris catalog maintenance," vol. 155, pp. 379-388, 2019.

[91] M. D'Errico, *Distributed space missions for earth system monitoring*. Springer Science & Business Media, 2012.

[92] E. Vassev and M. Hinchey, *Autonomy requirements engineering for space missions*. Springer, 2014.

[93] E. J. E.-E. Secretariat, Requirements and T. N. E.-E.-S.-.-C. Standards Division Noordwijk, "Space engineering: space segment operability," 2008.

[94] D. Dvorak, M. Ingham, J. R. Morris, and J. Gersh, "Goal-based operations: an overview," *Journal of Aerospace Computing, Information, Communication*, vol. 6, no. 3, pp. 123-141, 2009.

[95] P. Grandjean, T. Pesquet, A. Muxi, and M. Charmeau, "What on-board autonomy means for ground operations: an autonomy demonstrator conceptual design," in *Space OPS 2004 Conference*, 2004, p. 267.

[96] J. G. Reed *et al.*, "Performance Efficient Launch Vehicle Recovery and Reuse," presented at the AIAA SPACE 2016, Long Beach, CA, Sep 2016.

[97] D. E. Koelle and R. Janovsky, "Development and transportation costs of space launch systems," presented at the DGLR/CEAS European Air and Space Conference 2007, Berlin, Germany, Sep 2017.

[98] L. A. Davis, "First Stage Recovery," *Engineering*, vol. 2, pp. 152-153, 2016.

[99] T. A. Heppenheimer, "The Space Shuttle Decision: NASA's Search for a Reusable Space Vehicle," NASA, NASA/SP-1999-4221, 1999.

[100] E. Seedhouse, *Virgin Galactic: The First Ten Years*. Springer International Publishing, 2015.

[101] M. Hempsell and A. Bond, "Skylon: An Example of Commercial Launcher System Development," *Journal of the British Interplanetary Society*, vol. 67, pp. 434-439, 2014.

[102] S. Lentz, M. Hornung, and W. Staudacher, "Conceptual Design of Winged Reusable Two-Stage-to-Orbit Space Transport Systems," in *Basic Research and Technologies for Two-Stage-to-Orbit Vehicles*: Wiley, 2006.

[103] S. Paul and T. Westbrook, "Tesla chief Musk's latest idea: Intercity rocket travel." [Online]. Available: https://www.reuters.com/article/us-space-mars/tesla-chief-musks-latest-idea-intercity-rocket-travel-idUSKCN1C40MF

[104] T. Masson-Zwaan and S. Freeland, "Between heaven and earth: The legal challenges of human space travel," *Acta Astronautica*, vol. 66, pp. 1597-1607, 2010.

[105] A. Tewari, *Atmospheric and space flight dynamics*. Springer, 2007.

[106] T. Wekerle, J. B. P. Fiho, L. E. V. L. da Costa, and L. G. Trabasso, "Status and Trends of Smallsats and Their Launch Vehicles - An Up-to-date Review," *Journal of Aerospace Technology Management*, vol. 7, no. 3, pp. 269-286, 2017.

[107] C. Niederstrasser and W. Frick, "Small Launch Vehicles - A 2016 State of the Industry Survey," presented at the 67th International Astronautical Congress, Guadalajara, Mexico, Sep 2016.

[108] M. Sippel, J. Klevanski, A. van Foreest, l. G\"u, Ali, B. Esser, and M. Kuhn, "The SpaceLiner Concept and its Aerothermodynamic Challenges," 2006.

[109] F. G. von der Dunk, "The integrated approach — Regulating private human spaceflight as space activity, aircraft operation, and high-risk adventure tourism," *Acta Astronautica*, vol. 92, pp. 199-208, 2013.

[110] P. E. Davies, *North American X-15* (X-Planes). Osprey Publishing, 2017.

[111] K. J. Stroud and S. E. Jacobs, "Dream Chaser Integrated Spacecraft and Pressure Suit Design," presented at the 45th International Conference on Environmental Systems, Bellevue, WA, Jul 2015.

[112] R. Varvill and A. Bond, "A Comparison of Propulsion Concepts for SSTO Reusable Launchers," *Journal of the British Interplanetary Society*, vol. 56, pp. 108-117, 2003.

[113] K. Gee and S. L. Lawrence, "Launch vehicle debris models and crew vehicle ascent abort risk," presented at the 2013 Proceedings Annual Reliability and Maintainability Symposium (RAMS), Orlando, FL, Jan 2013.

[114] R. Daines and C. Segal, "Combined rocket and airbreathing propulsion systems for space-launch applications," (in English), *J Propul Power,* vol. 14, no. 5, pp. 605-612, 1998, doi: 10.2514/2.5352.

[115] S. Walker, M. Tang, and C. Mamplata, "TBCC Propulsion for a Mach 6 Hypersonic Airplane," presented at the 16th AIAA/DLR/DGLR International Space Planes and Hypersonic Systems and Technologies Conference, Bremen, Germany, Oct 2009.

[116] U. Hueter, "Rocket-Based Combined-Cycle Propulsion Technology for Access-to-Space Applications," presented at the 9th International Space Planes and Hypersonic Systems and Technologies, Norfolk, VA, Jan 1999.

[117] G. Norris, "Skunk Works Hints At SR-72 Demonstrator Progress." [Online]. Available: http://aviationweek.com/defense/skunk-works-hints-sr-72-demonstrator-progress

[118] G. Hagemann, H. Immich, T. V. Nguyen, and G. E. Dumnov, "Advanced Rocket Nozzles," *J Propul Power,* vol. 14, no. 5, pp. 620-634, 1998.

[119] W. Huang, Z.-G. Wang, D. B. Ingham, L. Ma, and M. Pourkashanian, "Design exploration for a single expansion ramp nozzle (SERN) using data mining," *Acta Astronautica,* vol. 83, pp. 10-17, 2013.

[120] Z. Liang, J. Yu, Z. Ren, and Q. Li, "Trajectory Planning for Cooperative Flight of Two Hypersonic Entry Vehicles," in *21st AIAA International Space Planes and Hypersonics Technologies Conference*, 2017, p. 2251.

[121] N. X. Vinh, A. Busemann, and R. D. Culp, "Hypersonic and planetary entry flight mechanics," *NASA STI/Recon Technical Report A,* vol. 81, 1980.

[122] C. D. Johnson and P. S. Wilke, "Protecting Satellites from the Dynamics of the Launch Environment," presented at the AIAA Space 2003 Conference & Exposition, Long Beach, CA, Sep 2003.

[123] D. M. Van Wie, D. G. Drewry Jr., D. E. King, and C. M. Hudson, "The hypersonic environment: Required operating conditions and design challenges," *Journal of Materials Science,* vol. 39, no. 19, pp. 5915-5924, 2004.

[124] J. C. Harpold and C. A. Graves Jr, "Shuttle entry guidance," in *American Astronautical Society, Anniversary Conference, 25th, Houston, Tex., Oct. 30-Nov. 2, 1978, 35 p.*, 1978, vol. 1.

[125] J. C. Harpold and D. E. Gavert, "Space shuttle entry guidance performance results," *Journal of Guidance, Control, and Dynamics,* vol. 6, no. 6, pp. 442-447, 1983.

[126] F. J. Regan, *Dynamics of atmospheric re-entry*. Aiaa, 1993.

[127] Y. Xie, L. Liu, J. Liu, G. Tang, and W. Zheng, "Rapid generation of entry trajectories with waypoint and no-fly zone constraints," *Acta Astronautica,* vol. 77, pp. 167-181, 2012.

[128] W. L. Pritchard and J. A. Sciulli, *Satellite communication systems engineering*. Prentice Hall Englewood Cliffs, New Jersey, 1993.

[129] A. Dalgarno, R. J. W. Henry, and A. L. Stewart, "The photoionization of atomic oxygen," *Planetary and Space Science,* vol. 12, no. 3, pp. 235-246, 1964.

[130] E. Doornbos and H. Klinkrad, "Modelling of space weather effects on satellite drag," *Advances in Space Research,* vol. 37, no. 6, pp. 1229-1239, 2006.

[131] R. L. Walterscheid, "Solar cycle effects on the upper atmosphere - Implications for satellite drag," *Journal of Spacecraft and Rockets*, vol. 26, pp. 439-444, 1989.

[132] D. M. Prieto, B. P. Graziano, and P. C. E. Roberts, "Spacecraft drag modelling," *Progress in Aerospace Sciences*, vol. 64, pp. 56-65, 2014.

[133] A. Hilgers, A. Glover, and E. Daly, "Effects on spacecraft hardware and operation," in *Space Weather - Physics and Effects*, V. Bothmer and I. Daglis Eds.: Springer-Verlag Berlin Heidelberg, 2007, pp. 353-382.

[134] A. K. Singh, D. S. Siingh, and R. P. Singh, "Space Weather: Physics, Effects and Predictability," *Surveys in Geophysics*, vol. 31, no. 6, pp. 581-638, 2010.

[135] L. J. Lanzerotti, "Space weather effects on communications," in *Space Weather - Physics and Effects*, V. Bothmer and I. Daglis Eds.: Springer-Verlag Berlin Heidelberg, 2007, pp. 247-268.

[136] K. K. de Groh, B. A. Banks, C. E. McCarthy, R. N. Rucker, L. M. Roberts, and L. A. Berger, "MISSE PEACE Polymers Atomic Oxygen Erosion Results," NASA/TM-2006-214482, 2006.

[137] W. A. D. Greer, J. P. W. Stark, and N. H. Pratt, "Surface-induced luminescence in a high-velocity rarefied atomic oxygen flow regime," *Journal of Geophysical Research - Space Physics*, vol. 100, no. A5, pp. 7821-7828, 1995.

[138] E. Grossman and I. Gouzman, "Space environment effects on polymers in low earth orbit," *Nuclear Instruments and Methods in Physics Research Section B: Beam Interactions with Materials and Atoms*, vol. 208, pp. 48-57, 2003.

[139] J.-C. Liou and N. L. Johnson, "Risks in space from orbiting debris," *Science*, vol. 311, no. 5759, pp. 340-341, 2006.

[140] M. Stanford and J. A. Jones, "space radiation concerns for manned exploration," *Acta Astronautica*, vol. 45, no. 1, pp. 39-47, 1999.

[141] R. Facius and G. Reitz, "Space weather impacts on space radiation protection," in *Space Weather - Physics and Effects*, V. Bothmer and I. Daglis Eds.: Springer-Verlag Berlin Heidelberg, 2007, pp. 289-352.

[142] *RTCA DO-340: Concept of Use (CONUSE) for Aeronautical Information Services (AIS) and Meteorological (MET) Data Link Services*, RTCA DO-340, RTCA, 26/9/2016 2012.

[143] *RTCA DO-324: Safety and Performance Requirements (SPR) for Aeronautical Information Services (AIS) and Meteorological (MET) Data Link Services*, RTCA DO-324, RTCA, 8/12/2010 2010.

[144] *RTCA DO-308: Operational Services and Environment Definition (OSED) for Aeronautical Information Services (AIS) and Meteorological (MET) Data Link Services*, RTCA DO-308, RTCA, 6/12/2016 2007.

[145] ICAO, "Annex 3 to the Convention on International Civil Aviation - Meteorological Service for International Air Navigation," The International Civil Aviation Organization (ICAO), Montreal, Canada, 2010.

[146] A. Gardi, Y. Lim, T. Kistan, and R. Sabatini, "Planning and negotiation of optimized 4D-trajectories in strategic and tactical rerouting operations," in *30th Congress of the International Council of the Aeronautical Sciences, ICAS 2016*, 2016: International Council of the Aeronautical Sciences. [Online]. Available: https://www.scopus.com/inward/record.uri?eid=2-s2.0-85013685109&partnerID=40&md5=0eed388f7f280d3c68a4aa6c52f4f701. [Online]. Available:

https://www.scopus.com/inward/record.uri?eid=2-s2.0-85013685109&partnerID=40&md5=0eed388f7f280d3c68a4aa6c52f4f701

[147] E. Canuto, C. Novara, L. Massotti, D. Carlucci, and C. P. Montenegro, "Chapter 8 - Orbit and Attitude Sensors," in *Spacecraft Dynamics and Control*: Butterworth-Heinemann, 2018, pp. 389-461.

[148] M. D. Griffin, *Space vehicle design*. AIAA, 2004.

[149] Y. Sun and M. Kumar, "Uncertainty propagation in orbital mechanics via tensor decomposition," *Celestial Mechanics and Dynamical Astronomy*, vol. 124, no. 3, pp. 269-294, 2016.

[150] A. Gelb, *Applied optimal estimation*. MIT press, 1974.

[151] A. Gelb and R. S. Warren, "Direct statistical analysis of nonlinear systems: CADET," *AIAA Journal*, vol. 11, no. 5, pp. 689-694, 1973.

[152] T. C. O.Brown, M. Gleason M. Hallax A. Long E. Rivera D. Finkleman T. Hitchens M. Jah D. Koplow R. Sedwick, "Orbital Traffic Management Study: Final Report," 2016.

[153] P. B. Larsen, "Space Traffic Management Standards," *Journal of Air Law and Commerce*, vol. 83, no. 2, p. 359, 2018.

[154] Inter-Agency Space Debris Coordination Committee, "Support to the IADC space debris mitigation guidelines," *IADC-04-06 Rev 5.5*, vol. 1, 2014.

[155] N. L. Johnson, "Medium Earth Orbits: is there a need for a third protected region?," 2010.

[156] D. S. McKnight and F. R. Di Pentino, "New insights on the orbital debris collision hazard at GEO," *Acta Astronautica*, vol. 85, pp. 73-82, 2013.

[157] R. S. Jakhu, "Regulatory Process for Communications Satellite Frequency Allocations," *Handbook of Satellite Applications*, pp. 359-381, 2017.

[158] Y. Henri, "Orbit/Spectrum INternational Regulatory Framework: Challenges in the 21st Century," presented at the 6th Nandasiri Jasentuliyana Keynote Lecture, Geneva, Switzerland, 2014.

[159] J. Hoffman and J. N. Pelton, "Regulatory procedures and standards for launch range safety for manned and unmanned launches-Chapter 9."

[160] A. G. Karacalioglu and A. Bukley, "Examining the Underlying Causes of Space Launch Failures," in *Space Safety is No Accident*: Springer, 2015, pp. 179-188.

[161] P. D. Wilde and C. Draper, "Aircraft protection standards and implementation guidelines for range safety," in *Proc. 48 th AIAA Aerospace Sciences Meeting, Paper AIAA*, 2010, vol. 1542.

[162] S. Kaltenhaeuser, F. Morlang, and D.-R. Schmitt, "A concept for improved integration of Space Vehicle Operation into ATM," 2017.

[163] E. Seedhouse, *Suborbital: Industry at the Edge of Space*. Springer Science \& Business Media, 2014.

[164] "SkyVector: Flight Planning / Aeronautical Charts." https://skyvector.com (accessed.

[165] K. D. Bilimoria and M. Jastrzebski, "Space transition corridors in the National Airspace System," in *Aviation Technology, Integration, and Operations Conference, Los Angeles, CA*, 2013.

[166] P. Llanos, E. Seedhouse, and C. Hays, "Nominal SpaceShipTwo Flights conducted by Scientist-Astronaut Candidates in a Suborbital Space Flight Simulator," 2018.

[167] T. J. Colvin and J. J. Alonso, "Near-elimination of airspace disruption from commercial space traffic using compact envelopes," in *AIAA SPACE 2015 Conference and Exposition*, 2015, p. 4492.

[168] T. Standfuß, I. Gerdes, A. Temme, and M. Schultz, "Dynamic airspace optimisation," *CEAS Aeronautical Journal*, vol. 9, no. 3, pp. 517-531, 2018.

[169] M. Shan, J. Guo, and E. Gill, "Review and comparison of active space debris capturing and removal methods," *Progress in Aerospace Sciences*, vol. 80, pp. 18-32, 2016.

[170] N. R. Council and others, *Protecting the Space Shuttle from Meteoroids and Orbital Debris*. National Academies Press, 1997.

[171] H. Klinkrad, *Space debris: models and risk analysis*. Springer Science & Business Media, 2006.

[172] S. Alfano, "Review of Conjunction Probability Methods for Short-Term Encounters (AAS 07-148)," *Advances in the Astronautical Sciences*, vol. 127, no. 1, p. 719, 2007.

[173] a.-P. Garc\'\i, Ricardo and J. Hernando-Ayuso, "Series for Collision Probability in Short-Encounter Model," *Journal of Guidance, Control, and Dynamics*, pp. 1908-1916, 2016.

[174] J. Hernando-Ayuso, C. Bombardelli, and J. L. Gonzalo, "OCCAM: OPTIMAL COMPUTATION OF COLLISION AVOIDANCE MANEUVERS."

[175] S. Alfano, "Eliminating assumptions regarding satellite conjunction analysis," *The Journal of the Astronautical Sciences*, vol. 59, no. 4, pp. 676-705, 2012.

[176] I. Grande-Olalla, N. Sanchez-Ortiz, J. A. Pulido, and K. Merz, "Collision risk assessment and avoidance manoeuvre strategies for satellites: new tool CORAM for ESA," in *Sixth European Space Debris Conference*, 2013, vol. 1, p. 2013.

[177] R. Schneider, "Convex bodies: the Brunn-Minkowski theory, volume 151 of Encyclopedia of Mathematics and its Applications," ed, 2014.

[178] G. Peterson, M. Sorge, and W. Ailor, "Space Traffic Management in the Age of New Space," 2018.

[179] T. S. Kelso and others, "Analysis of the Iridium 33-Cosmos 2251 collision," *Advances in the Astronautical Sciences*, vol. 135, no. 2, pp. 1099-1112, 2009.

[180] T. S. Kelso and S. Alfano, "Satellite orbital conjunction reports assessing threatening encounters in space (SOCRATES)," in *Modeling, Simulation, and Verification of Space-based Systems III*, 2006, vol. 6221, p. 622101.

[181] D. Vallado, P. Crawford, R. Hujsak, and T. S. Kelso, "Revisiting spacetrack report# 3," in *AIAA/AAS Astrodynamics Specialist Conference and Exhibit*, 2006, p. 6753.

[182] J. Chan, "Current State of Conjunction Monitoring for Satellite Operators and the Steps Forward," in *24th International Symposium on Space Flight Dynamics*, 2014.

[183] T. S. Kelso and others, "Improved conjunction analysis via collaborative space situational awareness," 2008.

[184] D. A. Vallado and P. J. Cefola, "Two-line element sets--practice and use," in *63rd International Astronautical Congress, Naples, Italy*, 2012.

[185] T. Flohrer, H. Krag, and H. Klinkrad, "ESA's process for the identification and assessment of high-risk conjunction events," *Advances in Space Research*, vol. 44, no. 3, pp. 355-363, 2009.

[186] T. S. Kelso, "How the Space Data Center Is Improving Safety of Space Operations," CENTER FOR SPACE STANDARDS AND INNOVATION COLORADO SPRINGS CO, 2010.

[187] R. J. Rovetto and T. S. Kelso, "Preliminaries of a space situational awareness ontology," *arXiv preprint arXiv:1606.01924*, 2016.

[188] A. P. Cox, C. K. Nebelecky, R. Rudnicki, W. A. Tagliaferri, J. L. Crassidis, and B. Smith, "The space object ontology," in *Information Fusion (FUSION), 2016 19th International Conference on*, 2016, pp. 146-153.

[189] J. Spurbeck, M. K. Jah, D. Kucharski, J. C. Bennett, and J. G. Webb, "Satellite Characterization, Classification, and Operational Assessment Via the Exploitation of Remote Photoacoustic Signatures," 2018.

[190] M. Jah *et al.*, "Space Traffic Management (STM): Balancing Safety, Innovation, and Growth," *AIAA Institute Position Paper*, 2017.

[191] B. D. Little and C. E. Frueh, "Space Situational Awareness Sensor Tasking: Comparison of Machine Learning with Classical Optimization Methods," *Journal of Guidance, Control, and Dynamics*, vol. 43, no. 2, pp. 262-273, 2020, doi: 10.2514/1.G004279.

[192] P. Grandjean, T. Pesquet, A. M. M. Muxi, and M.-C. Charmeau, "What on-Board Autonomy Means for Ground Operations: An Autonomy Demonstrator Conceptual Design," 2004.

[193] C. Iacopino, P. Palmer, N. Policella, A. Donati, and A. Brewer, "How ants can manage your satellites," *Acta Futura*, vol. 9, pp. 57-70, 2014.

[194] D. D. Dvorak, M. D. Ingham, J. R. Morris, and J. Gersh, "Goal-based operations: an overview," *Journal of Aerospace Computing, Information, and Communication*, vol. 6, no. 3, pp. 123-141, 2009.

[195] C. Araguz, E. Bou-Balust, and E. Alarcón, "Applying autonomy to distributed satellite systems: Trends, challenges, and future prospects," *Systems Engineering*, vol. 21, no. 5, pp. 401-416, 2018, doi: 10.1002/sys.21428.

[196] H. V. D. Parunak, "Making swarming happen," Citeseer.

[197] D. Aleva and J. McCracken, "Jspoc cognitive task analysis," in *Advanced Maui Optical and Space Surveillance (AMOS) Conference Proceedings*, 2009.

[198] J. D. Ianni, "Human-system interfaces for space cognitive awareness," in *Proceedings of the Advanced Maui Optical and Space Surveillance Technologies Conference, Maui, HI, USA*, 2008, pp. 17-19.

[199] A. D. Jaunzemis, "Predictive sensor tasking and decision support for space situational awareness using evidential reasoning," Georgia Institute of Technology, Atlanta, GA, USA, 2018.

[200] M. Jenkins, M. G. Catto, and M. Bird, "Increased Space Situational Awareness through Augmented Reality Enhanced Common Operating Pictures," in *Proceedings of the Advanced Maui Optical and Space Surveillance Technologies Conference, Maui, HI, USA*, 2018, pp. 11-14.

[201] J. D. Ianni, D. L. Aleva, and S. A. Ellis, "Overview of human-centric space situational awareness science and technology," in *Proceedings of the Advanced Maui Optical and Space Surveillance Technologies Conference, Maui, HI, USA*, 2012: Citeseer, pp. 11-14.

[202] N. G. Leveson, *Engineering a safer world: Systems thinking applied to safety*. The MIT Press, 2016.

[203] N. G. Leveson, *STPA Handbook*. 2018.

[204] A. Shirazi, J. Ceberio, and J. A. Lozano, "Spacecraft trajectory optimization: A review of models, objectives, approaches and solutions," *Progress in Aerospace Sciences*, vol. 102, pp. 76-98, 2018/10/01/ 2018, doi: https://doi.org/10.1016/j.paerosci.2018.07.007.

[205] B. Conway, *Spacecraft Trajectory Optimization* (Cambridge Aerospace Series). Cambridge: Cambridge University Press, 2010.

[206] O. v. Stryk and R. Bulirsch, "Direct and indirect methods for trajectory optimization," *Ann. Oper. Res.*, vol. 37, no. 1–4, pp. 357–373, 1992, doi: 10.1007/bf02071065.

[207] D. White, "Optimal Control Theory with Aerospace Applications," *The Aeronautical Journal*, vol. 114, p. 521, 08/01 2010, doi: 10.1017/S0001924000088151.

[208] K. Graham and A. Rao, "Minimum-Time Trajectory Optimization of Low-Thrust Earth-Orbit Transfers with Eclipsing," *Journal of Spacecraft and Rockets*, vol. 53, pp. 1-15, 02/22 2016, doi: 10.2514/1.A33416.

[209] K. F. Graham and A. V. Rao, "Minimum-Time Trajectory Optimization of Multiple Revolution Low-Thrust Earth-Orbit Transfers," *Journal of Spacecraft and Rockets*, vol. 52, no. 3, pp. 711-727, 2015, doi: 10.2514/1.A33187.

[210] M. A. Patterson and A. V. Rao, *GPOPS-II: A MATLAB Software for Solving Multiple-Phase Optimal Control Problems Using hp-Adaptive Gaussian Quadrature Collocation Methods and Sparse Nonlinear Programming* (no. 1). Association for Computing Machinery, 2014, p. Article 1.

[211] J. W. Sales, "Trajectory optimization for spacecraft collision avoidance," Aerospace Engineering, Air Force Institute of Technology, 2013.

[212] C. Blum and A. Roli, "Metaheuristics in combinatorial optimization: Overview and conceptual comparison," *ACM Comput. Surv.*, vol. 35, no. 3, pp. 268–308, 2003, doi: 10.1145/937503.937505.

[213] N. Xiong, D. Molina, M. L. Ortiz, and F. Herrera, "A Walk into Metaheuristics for Engineering Optimization: Principles, Methods and Recent Trends," *International Journal of Computational Intelligence Systems*, vol. 8, no. 4, pp. 606-636, 2015/07/04 2015, doi: 10.1080/18756891.2015.1046324.

[214] J. Kennedy and R. Eberhart, "Particle swarm optimization," in *Proceedings of ICNN'95 - International Conference on Neural Networks*, 27 Nov.-1 Dec. 1995 1995, vol. 4, pp. 1942-1948 vol.4, doi: 10.1109/ICNN.1995.488968.

[215] J. A. Kechichian, "The treatment of the earth oblateness effect in trajectory optimization in equinoctial coordinates," *Acta Astronautica*, vol. 40, no. 1, pp. 69-82, 1997/01/01/ 1997, doi: https://doi.org/10.1016/S0094-5765(97)00025-8.

[216] J. A. Kéchichian, *Applied Nonsingular Astrodynamics*. 2018.

[217] J. Yang and E. Stoll, *Time-optimal Spacecraft Reorientation with Attitude Constraints Based on A Two-stage Strategy*. 2018.

[218] G. A. Boyarko, M. Romano, and O. A. Yakimenko, "Time-optimal reorientation of a spacecraft using a direct optimization method based on inverse dynamics," *2010 IEEE Aerospace Conference*, pp. 1-13.

[219] D. Spiller, F. Curti, and L. Ansalone, *Inverse dynamics particle swarm optimization for spacecraft minimum-time maneuvers with constraints*. 2015.

[220] M. J. H. Walker, B. Ireland, and J. Owens, "A Set of Modified Equinoctial Orbit Elements," *Celestial Mechanics* vol. 36, no. 4, pp. 409-419, August 1985, doi: 10.1007/BF01227493.

[221] R. A. Braeunig. "Atmospheric models." http://www.braeunig.us/space/atmmodel.htm (accessed.

[222] V. D.A., *Fundamentals of Astrodynamics and Applications*. Springer Science & Business Media, 2001.

[223] U. S. N. Observatory, *Astronomical phenomena for the year 2019*. Washington: U.S. Government Pubishing Office, 2016.

[224] A. Bani Younes, J. Turner, D. Mortari, and J. Junkins, *A Survey of Attitude Error Representations*. 2012.

[225] M. Shuster, "A survey of attitude representation," *Journal of astronautical sciences*, vol. 41 No.4, pp. 439-517, 1993.

[226] S. Hilton, R. Sabatini, A. Gardi, H. Ogawa, and P. Teofilatto, "Space traffic management: towards safe and unsegregated space transport operations," (in English), *Progress in Aerospace Sciences*, Review vol. 105, pp. 98-125, 2019, doi: 10.1016/j.paerosci.2018.10.006.

[227] M. Holzinger and M. Jah, "Challenges and Potential in Space Domain Awareness," ed: American Institute of Aeronautics and Astronautics, 2018.

[228] Y.-p. Hu, J.-y. Huang, and L. Chen, "Space-based visible observation strategy for beyond-LEO objects based on an equatorial LEO satellite with multi-sensors," *Advances in Space Research*, vol. 59, no. 7, pp. 1751-1762, 2017.

[229] M. Davis, "Technology challenges in affordable space based radar," in *Record of the IEEE 2000 International Radar Conference [Cat. No. 00CH37037]*, 2000: IEEE, pp. 18-23.

[230] M. Davis, "Space based radar moving target detection challenges," 2002.

[231] J. T. Horwood, J. M. Aristoff, N. Singh, A. B. Poore, and M. D. Hejduk, "Beyond covariance realism: a new metric for uncertainty realism," in *Signal and Data Processing of Small Targets 2014*, 2014, vol. 9092: International Society for Optics and Photonics, p. 90920F.

[232] A. B. Poore *et al.*, "Covariance and uncertainty realism in space surveillance and tracking," Numerica Corporation Fort Collins United States, 2016.

[233] G. R. J. N. Curry, MA, "radar System Performance Modeling, ARTECH HOUSE," pp. 23-25, 2005.

[234] D. Woffinden, S. Robinson, J. Williams, and Z. R. Putnam, "Linear Covariance Analysis Techniques to Generate Navigation and Sensor Requirements for the Safe and Precise Landing Integrated Capabilities Evolution (SPLICE) Project," in *AIAA Scitech 2019 Forum*, 2019, p. 0662.

[235] P. C. Mahalanobis, "On the generalized distance in statistics," 1936: National Institute of Science of India.

[236] P. Vanicek and E. J. Krakiwsky, *Geodesy: the concepts*. Elsevier, 2015.

[237] M. Mezian, B. Vallet, B. Soheilian, and N. Paparoditis, "Uncertainty propagation for terrestrial mobile laser scanner," *Int. Arch. Photogramm. Remote Sens. Spatial Inf. Sci.*, vol. 41, pp. 331-335, 2016.

[238] F. L. Markley, "Approximate Cartesian state transition matrix," *The journal of the Astronautical Sciences*, vol. 34, no. 2, pp. 161-169, 1986.

[239] A. P. Chiaradia, H. Kuga, and A. Prado, "Comparison between Two Methods to Calculate the Transition Matrix of Orbit Motion," *Mathematical Problems in Engineering*, vol. 2012, 01/01 2012, doi: 10.1155/2012/768973.

[240] H. Kuga, "Adaptive orbit estimation applied to low altitude satellites," *Masters Thesis*, p. 7, 1982.

[241] F. K. Chan, *Probability of collision*. Aerospace Press, 2008, p. 365.

[242] M. R. Akella and K. T. Alfriend, "Probability of Collision Between Space Objects," *Journal of Guidance, Control, and Dynamics*, vol. 23, no. 5, pp. 769-772, 2000, doi: 10.2514/2.4611.

[243] A. Hauschild, M. Markgraf, and O. Montenbruck, "The Navigation and Occultation Experiment - GPS Receiver Performance On Board a LEO Satellite," *Inside GNSS*, pp. 48-57, 07/01 2014.

[244] H. Klinkrad, J. Alarcon, and N. Sanchez, "Collision avoidance for operational ESA satellites," in *4th European Conference on Space Debris*, 2005, vol. 587, p. 509.

[245] S. Hilton, K. Thangavel, A. Gardi, and R. Sabatini, "Intelligent mission planning for autonomous distributed satellite systems," *Acta Astronautica*, vol. 225, pp. 857-869, 2024.

[246] T. Uhlig, F. Sellmaier, and M. Schmidhuber, *Spacecraft operations*. Springer.

[247] *CCDS 529.0-G-1: Mission Planning and Scheduling*, CCSDS, Washington, DC, USA, 2018.

[248] S. Chien *et al.*, "ASPEN-Automating space mission operations using automated planning and scheduling," in *SpaceOps 2000*, 2000.

[249] S. Chien, "A generalized timeline representation, services, and interface for automating space mission operations," in *SpaceOps 2012*, 2012, p. 1275459.

[250] S. Chien *et al.*, "Using autonomy flight software to improve science return on Earth Observing One," vol. 2, no. 4, pp. 196-216, 2005.

[251] S. Damiani, G. Verfaillie, and M.-C. Charmeau, "An earth watching satellite constellation: How to manage a team of watching agents with limited communications," in *Proceedings of the fourth international joint conference on Autonomous agents and multiagent systems*, 2005: ACM, pp. 455-462.

[252] J. Bonnet, M.-P. Gleizes, E. Kaddoum, S. Rainjonneau, and G. Flandin, "Multi-satellite mission planning using a self-adaptive multi-agent system," in *2015 IEEE 9th International Conference on Self-Adaptive and Self-Organizing Systems*, 2015: IEEE, pp. 11-20.

[253] G. Bonnet and C. Tessier, "Coordination despite constrained communications: a satellite constellation case," in *3rd National Conference on Control Architectures of Robots*, 2008, pp. 89-100.

[254] P. Skobelev, E. Simonova, A. Zhilyaev, and V. Travin, "Application of multi-agent technology in the scheduling system of swarm of earth remote sensing satellites," vol. 103, pp. 396-402, 2017.

[255] C. Lenzen, M. T. Wörle, F. Mrowka, M. P. Geyer, and R. Klaehn, "Automated scheduling for TerraSAR-X/TanDEM-X," in *IWPSS-11*, 2011.

[256] W. Pitz and D. Miller, "The TerraSAR-X satellite," vol. 48, no. 2, pp. 615-622, 2010.

[257] M. P. Geyer, F. Mrowka, and C. Lenzen, "TerraSAR-X/TanDEM-X Mission Planning Handling Satellites in Close Formation," in *SpaceOps 2010 Book*: Space Operations: Exploration, Scientific Utilization & Technology Development, 2011.

[258] S. Tonetti, S. Cornara, A. Heritier, and F. Pirondini, "Fully Automated Mission Planning and Capacity Analysis Tool for the DEIMOS-2 Agile Satellite," in *Workshop on Simulation for European Space Programmes (SESP)*, 2015, vol. 24, p. 26.

[259] S.-w. Baek *et al.*, "Development of a scheduling algorithm and GUI for autonomous satellite missions," vol. 68, no. 7-8, pp. 1396-1402, 2011.

[260] G. Beaumet, G. Verfaillie, and M. C. Charmeau, "Feasibility of autonomous decision making on board an agile earth-observing satellite," *Computational Intelligence*, vol. 27, no. 1, pp. 123-139, 2011.

[261] C. Iacopino, P. Palmer, N. Policella, A. Donati, and A. Brewer, "How ants can manage your satellites."

[262] R. Grasset-Bourdel, G. Verfaillie, and A. Flipo, "Planning and replanning for a constellation of agile Earth observation satellites," in *Proc. of the ICAPS-11 Workshop on «Scheduling and Planning Applications»(SPARK-11), Freiburg, Germany*, 2011: Citeseer.

[263] M. Lemaître, G. Verfaillie, F. Jouhaud, J.-M. Lachiver, and N. Bataille, "Selecting and scheduling observations of agile satellites," vol. 6, no. 5, pp. 367-381, 2002.

[264] N. Bianchessi, J.-F. Cordeau, J. Desrosiers, G. Laporte, and V. J. E. J. o. O. R. Raymond, "A heuristic for the multi-satellite, multi-orbit and multi-user management of earth observation satellites," vol. 177, no. 2, pp. 750-762, 2007.

[265] G. Wu, W. Pedrycz, H. Li, M. Ma, and J. Liu, "Coordinated planning of heterogeneous earth observation resources," *IEEE Transactions on Systems, Man, Cybernetics: Systems*, vol. 46, no. 1, pp. 109-125, 2015.

[266] A. R. Carrel and P. L. Palmer, "An evolutionary algorithm for near-optimal autonomous resource management," in *8th International Symposium on Artificial Intelligence, Robotics and Automation in Space*, 2005.

[267] J. A. Englander, B. A. Conway, and T. Williams, "Automated mission planning via evolutionary algorithms," *Journal of Guidance, Control, Dynamics*, vol. 35, no. 6, pp. 1878-1887, 2012.

[268] M. A. Mansour and M. M. Dessouky, "A genetic algorithm approach for solving the daily photograph selection problem of the SPOT5 satellite," vol. 58, no. 3, pp. 509-520, 2010.

[269] A. Globus, J. Crawford, J. Lohn, and A. Pryor, "Scheduling earth observing satellites with evolutionary algorithms," 2003.

[270] I. Czarnowski, P. Jędrzejowicz, and J. Kacprzyk, *Agent-based optimization*. Springer, 2013.

[271] J. Ocon, "Multi-agent frameworks for space applications," in *SpaceOps 2010 Conference Delivering on the Dream Hosted by NASA Marshall Space Flight Center and Organized by AIAA*, 2010, p. 2069.

[272] J. Vago *et al.*, "ExoMars-searching for life on the Red Planet," vol. 126, pp. 16-23, 2006.

[273] E. Friis-Christensen, H. Lühr, D. Knudsen, and R. Haagmans, "Swarm–an Earth observation mission investigating geospace," *Advances in Space Research*, vol. 41, no. 1, pp. 210-216, 2008.

[274] L. Kaltenegger and M. Fridlund, "The Darwin mission: Search for extra-solar planets," *Advances in Space Research*, vol. 36, no. 6, pp. 1114-1122, 2005.

[275] D. Bernard *et al.*, "Spacecraft autonomy flight experience: The DS1 Remote Agent experiment," 1999.

[276] J. Aschbacher and M. P. Milagro-Pérez, "The European Earth monitoring (GMES) programme: Status and perspectives," *Remote Sensing of Environment*, vol. 120, pp. 3-8, 2012.

[277] J. Bang-Jensen and G. Z. Gutin, *Digraphs: theory, algorithms and applications*. Springer Science & Business Media, 2008.

[278] E. Lagona, S. Hilton, A. Afful, A. Gardi, and R. Sabatini, "Autonomous Trajectory Optimisation for Intelligent Satellite Systems and Space Traffic Management," *Acta Astronautica*, 01/25 2022, doi: 10.1016/j.actaastro.2022.01.027.

[279] L. M. Gambardella and M. Dorigo, "Solving symmetric and asymmetric TSPs by ant colonies," in *Proceedings of IEEE international conference on evolutionary computation*, 1996: IEEE, pp. 622-627.

[280] S. R. M. Ronald J. Birk, "Framework for Trusted Operations of Autonomous Systems," in *Ground Systems Architecture Workshop*, 2019.

[281] J. N. Buitrago-Leiva, M. E. K. Ramouz, A. Camps, and J. A. Ruiz-de-Azua, "Towards a second life for Zombie Satellites: Anomaly occurrence and potential recycling assessment," *Acta Astronautica*, 2024.

[282] J. Bouwmeester, A. Menicucci, and E. K. Gill, "Improving CubeSat reliability: Subsystem redundancy or improved testing?," *Reliability Engineering & System Safety*, vol. 220, p. 108288, 2022.

[283] Y. Yun, J. Lee, H.-s. Oh, and J.-H. Choi, "Remaining useful life prediction of reaction wheel motor in satellites," *JMST Advances*, vol. 1, pp. 219-226, 2019.

[284] J. Davis, T. Jennings-Bramly, J. Symons, and F. Waltho, "Sensor Management for Space-Based Sensing Constellations," in *Proceedings of the Advanced Maui Optical and Space Surveillance (AMOS) Technologies Conference*, 2022.

[285] P. Uday and K. Marais, "Designing resilient systems-of-systems: A survey of metrics, methods, and challenges," *Systems Engineering*, vol. 18, no. 5, pp. 491-510, 2015.